TH Wildau Engineering and Natural Sciences Proceedings
1 | 2021

2nd German-West African Conference on Sustainable, Renewable Energy Systems - SusRES

6th April 2021 – Kara, Togo

Conference Proceedings

Editors:

Jörg REIFF-STEPHAN

Kou´santa AMOUZOU

Assiongbon ADANLETE

sponsored by:

TH Wildau Engineering and Natural Sciences Proceedings

TH Wildau Engineering and Natural Sciences Proceedings (TH Wildau ENSP) are the home for various proceedings of conferences organized by researchers of the TH Wildau.

The TH Wildau as one of the top research universities in Germany specialises in the research fields of applied biosciences, information technology/telematics, optical technologies/photonics, production and materials, transport and logistics as well as management and law.

These proceedings give a manifold insight into the technical and scientific research output and present the latest advancements of the university's research fields.

ISSN (online): 2748-8829

TH Wildau Engineering and Natural Sciences Proceedings are published by TIB Open Publishing (Technische Informationsbibliothek, Welfengarten 1 B, 30167 Hannover) on behalf of Technische Hochschule Wildau.

2nd German-West African Conference on Sustainable, Renewable Energy Systems SusRes – Kara 2021

April 6th 2021, University of Kara

“Decentralized Systems as a Key Factor in Clean Energy Production for Locations with Limited Infrastructure”

Poster contributions

2nd German-West African Conference on Sustainable, Renewable Energy Systems SusRES – Kara 2021

https://doi.org/10.52825/thwildauensp.v1i.30

Published: 15 June 2021

Preface

Jörg Reiff-Stephan[1], Kou´santa AMOUZOU[2], and Assiongbon ADANLETE[2]

[1] Technical University of Applied Sciences Wildau, Germany

[2] University of Kara, Togo

Renewable energy sources are more important today than ever before, as they represent a key factor in reducing greenhouse emissions and fossil fuel consumption. Avoiding excessive burdens on future generations has now become the declared challenge of this century and justifies the efforts we must undertake to reduce global warming. This can only be achieved by conceiving new technical approaches, exploiting alternative resources and by raising people's awareness of the sustainable use of their own livelihoods. However, this change in awareness is a process that needs to be driven forward, especially in the field of research and education, and is therefore the declared aim of the Joint German-West African Conference on Sustainable, Renewable Energy Systems – SusRES. This annual conference provides a platform for exchange between scientists, students and many other interested parties, with technological progress at the forefront of the event. The SusRES conference is known as an accelerator for an ever-growing international network, not limited to the circumstances of a single country or even continent, which strives to take on and meet the global challenges of the present and future.

This year's guiding theme of the event -Decentralized systems as a key factor in clean energy production for locations with limited infrastructure- of the event is primarily based on the consideration of how the energy supply of the future is to be designed. For some years now, a paradigm shift towards decentralised energy supply has been observed, which opens up new possibilities especially in areas with weak infrastructural supply. This is not just about providing energy from renewable resources, but also about exploiting this energy we have today efficiently and sustainably, whereby intelligent and interconnected systems play an ever-increasing role.

The reader is provided with exciting insights into these topics within this conference proceedings elaborated by stakeholders from twelve time zones and four continents. In their contributions, the authors address important findings, especially from research but also from teaching, which represent an important milestone in their activities and thus make a significant contribution to our declared goals.

2nd German-West African Conference on Sustainable, Renewable Energy Systems SusRES – Kara 2021

Photovoltaic

https://doi.org/10.52825/thwildauensp.v1i.4

Published: 15 June 2021

Design and implementation of a photovoltaic characterization platform at FaST

Moudjibatou AFODA [1], N'detigma KATA [1,2], Dambé. DOUTI[1,] Hodo-Abalo SAMAH[1], Amadou Séidou MAIGA[2]

[1] Faculté des Sciences et Techniques (FaST), Université de Kara, Togo

[2] Laboratoire d'Électronique Informatique Télécommunication et Énergies Renouvelables, Université Gaston Berger, 32000 Saint-Louis, Sénégal

Abstract. The site that houses the FaST faces high dusty winds and considerable temperature variation. Weather conditions such as solar radiation, temperature, and wind speed greatly affect the performance of PV modules. But the data from PV equipment manufacturers do not allow for proper sizing. Therefore, a rigorous study is needed to find the most suitable PV module technology for the study area. For this purpose, platforms for the acquisition of meteorological parameters and module characterization are indispensable. This platform project at FaST will serve training and pedagogy because its configuration will allow master and bachelor students to carry out practical work, to carry out studies on new cell technologies under the influence of external factors specific to the sub-Saharan zone and will bring an added value by providing additional information on real conditions and especially the influence of local external factors. Our study consisted first of all in the realization of the platform on the roof of the FaST, then in the design and the programming of a module of acquisition of the measured parameters on the basis of the Arduino microcontroller card and finally in the test of characterization of the modules used for the platform thanks to an electronic load on the basis of MOSFET of power controlled by a microcontroller that we realized.

Keywords: platform, acquisition, electronic load.

Introduction

The performance of PV modules is highly dependent on weather conditions such as solar radiation, temperature and wind speed. To provide energy continuously over a long period of time, a PV system must be correctly dimensioned. This requires a fairly rigorous study in order to make the right choice. To do this, platforms for acquiring meteorological parameters and characterizing the panels are indispensable. This platform project at the FaST will achieve the following objectives: the platform at the service of training and pedagogy: with the instantaneous taking of measurements, the platform will allow learners and visitors to observe the behavior of the modules according to the conditions in which the modules are located. Its configuration will allow practical work to be carried out without influencing the long-term measurements. Thus, master and bachelor students will be able to carry out their practical work. The platform at the service of research: In the research of photovoltaic technologies best adapted to the sub-Saharan zone, the platform will allow to realize studies on new cell technologies with the influence of external factors specific to the sub-Saharan zone. The PV modules sold to the local market can be characterized through this platform to reassure investors and customers. The platform at the service of projects: most projects in the northern part of Togo are based on software data that may not correspond to the reality on the ground. This platform will bring an added value by providing additional information on real conditions and especially the influence of local external factors. Our work consisted in

the realization of the platform on the roof of the Faculty of Sciences and Technologies (FaST), then in the design of a variable electronic load based on MOSFET and finally in the design, the realization and the programming of the acquisition module based on the Arduino microcontroller.

Methodology

We have defined the parameters that must be acquired by making a bibliographic study. During a visit to meteorological centers, we noticed that the available data are the ambient temperature, relative humidity, wind speed and direction. These centers do not acquire solar irradiation. From these researches, we have established a list of materials [1] of the platform and the right way to make their different assemblies. We have thus realized a diagram presenting in a general way the platform.

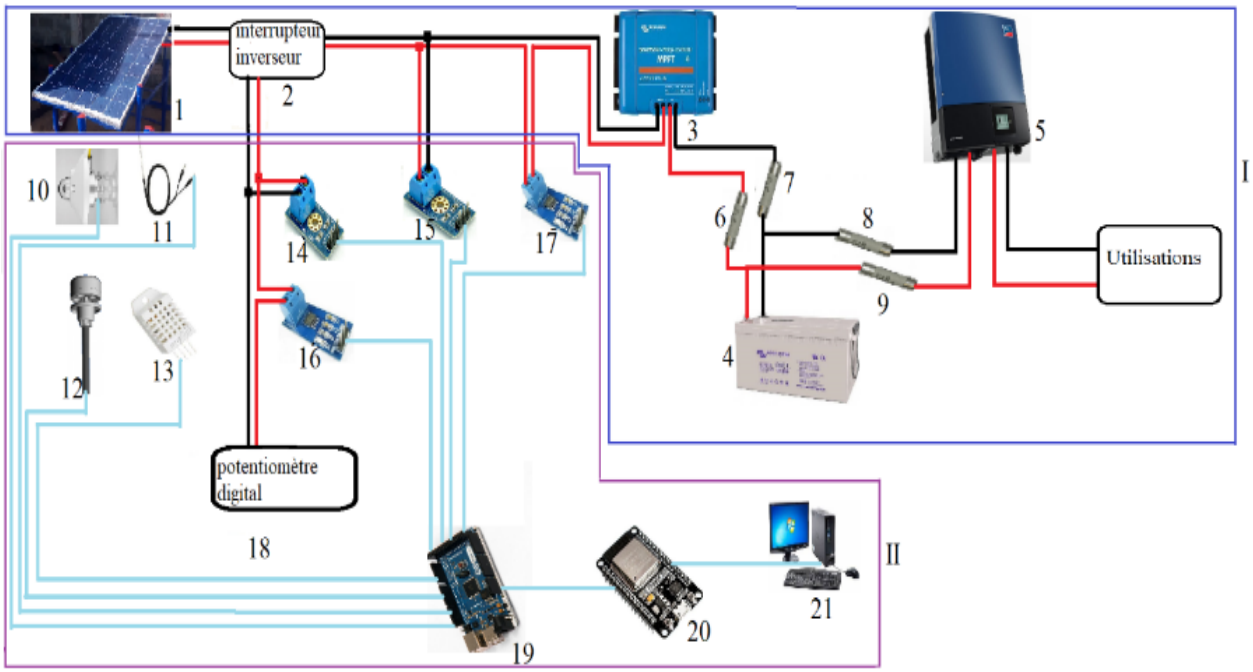

Figure 1: Schematic of the whole system

I-Power block

1-Solar modules

2-Inverter switch

3-Regulator

4- Battery

5- Inverter

6-7-8-9-Fuses

II-Acquisition block

10-Pyranometer

11-Temperature sensor

12-Wind vane-anemometer

13- DHT22 sensor

14-15- Voltage sensors

16-17- ACS712 current sensors

18-Digital potentiometer

19-Arduino board

20-ESP32 MCU node

21-Computer

As illustrated by the block diagram in Figure 1, the I-V measurement platform for photovoltaic modules consists of two main parts: the production block and the acquisition block. These two blocks are controlled by a programmable changeover switch that serves as a flip-flop.

Production block

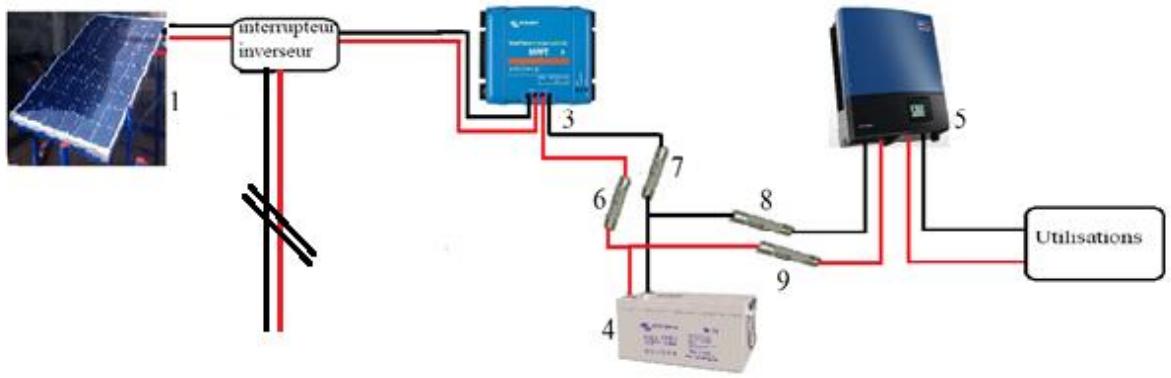

Figure 2: Production block

The production block allowing to feed the laboratory of physics of the Faculty of Sciences and Technologies (FaST), is constituted of:

A small photovoltaic field consisting of four solar modules placed on a metal structure that we have made (Figure 3) and installed (Figure 4 and 5) on the roof of the Faculty of Sciences and Technologies.

Figure 3: Assembly of metal structures

Figure 4: Installation of metal structures

Figure 5: Photovoltaic field installed on the roof of the FaST

- A regulator to control the charge of the batteries and limit their discharge

- Batteries to store energy for times of no sunlight

- An inverter to convert the direct current from the solar modules into alternating current that can be used to power the physics laboratory

Acquisition block

This block consists of different devices for the measurement of solar irradiation (pyranometer), of the temperature of the modules in operation (temperature probes), of the direction and speed of the wind (wind vane-anemometer), of the ambient temperature and relative humidity (DHT22), of the measurement of the current (ACS712) and of the voltage. For the representation of the I-V characteristic from the current and voltage measurements, it is necessary to vary the impedance in order to have different voltage and current values, hence the usefulness of the digital potentiometer.

Digital potentiometer

The characteristics of potentiometers available on the market do not correspond to those of the modules we have for this study, it was therefore important to opt for a variable electronic load.

Electronic load

Photovoltaic modules are usually tested using direct current electronic loads. These loads are often very expensive. However, with the help of very simple and much cheaper circuits, it is possible to build an electronic load. It varies the resistance over the entire measurement range in a very short time.

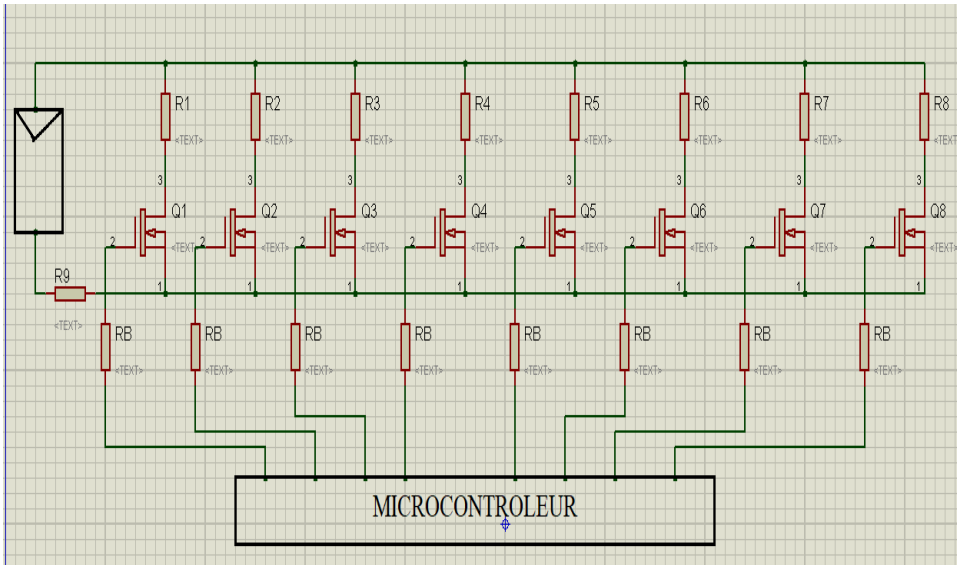

Figure 4: Circuit of the electronic load

For this electronic load, we have connected in parallel resistors that are controlled by a microcontroller that generates control signals. We have used the PIC microcontroller for its efficiency and its availability on the market, to generate the signals that applied to the transistors allow to define the value of the resistance [2]. The MOSFET transistors are chosen for their simplicity, their speed and their lower cost and used in this case as electronic switches.

Data acquisition

Measurements made by the pyranometer, the vane anemometer, the temperature and humidity sensor, the thermocouples, the temperature sensor, the voltage and current sensors are retrieved by the Arduino board and then transferred to the MCU node. Potentiometers to adjust the periodicity of sending data to the Node MCU, the MAX485 module, a data receiver to transmit the data from the pyranometer to the Arduino, the RTC module, a real time clock to give the time at any time and an LCD screen to display the date, time and ambient temperature are added to allow a better understanding of the data to be acquired.

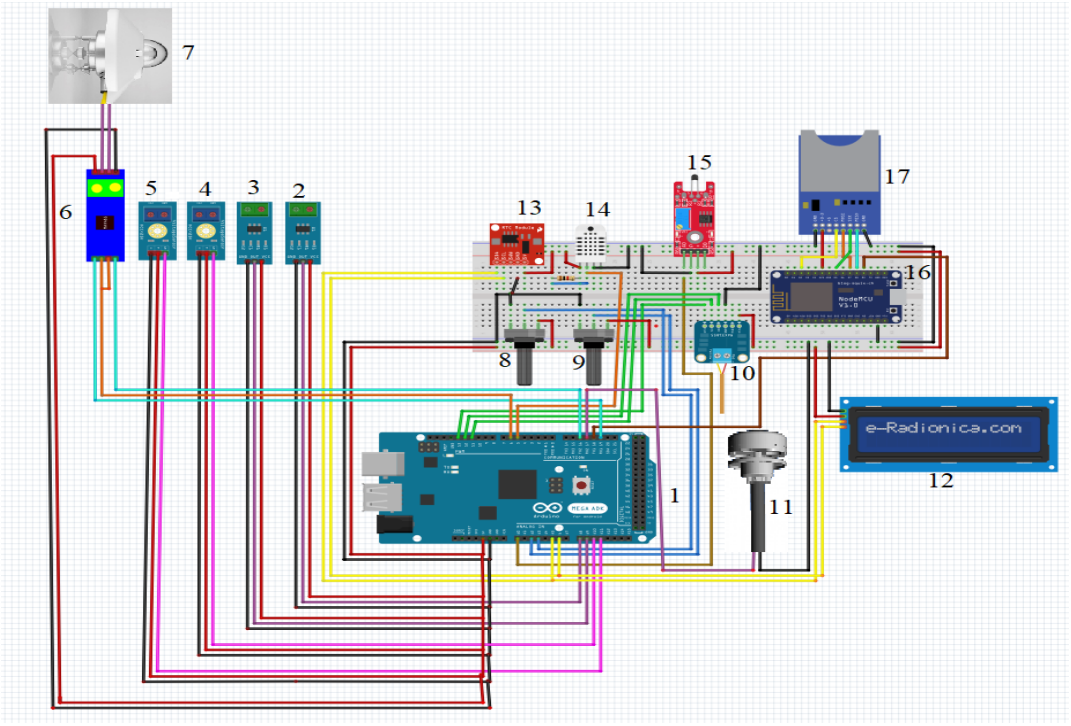

Figure 5: Assembly of the different Arduino sensors

1-Arduino	11- Anemometer- Wind vane
2,3-Current sensors ACS712	12- LCD screen
4,5-Voltage sensors	13- RTC module
6-Max485 module	14- DHT22 humidity and temperature sensor
7-Pyranometer Temperature sensors	15- Temperature sensor KY-028
8-9- Potentiometers	16-ESP32 MCU node
10-Thermocouples MAX31855	17-SD card

In order to acquire the data from the different sensors, we created two programs [3]. A first program that we uploaded on Arduino [4], [5] to recover the measurements made by the different sensors and then transmit them to the Node MCU. The second program is uploaded on the Node MCU allowing it to recover the data, to transfer them on a web server and on a SD card while allowing to download them.

Flowcharts

The following figure shows the execution steps of the algorithm that we used to develop the programs in C language that we uploaded on the Arduino board and on the Node MCU.

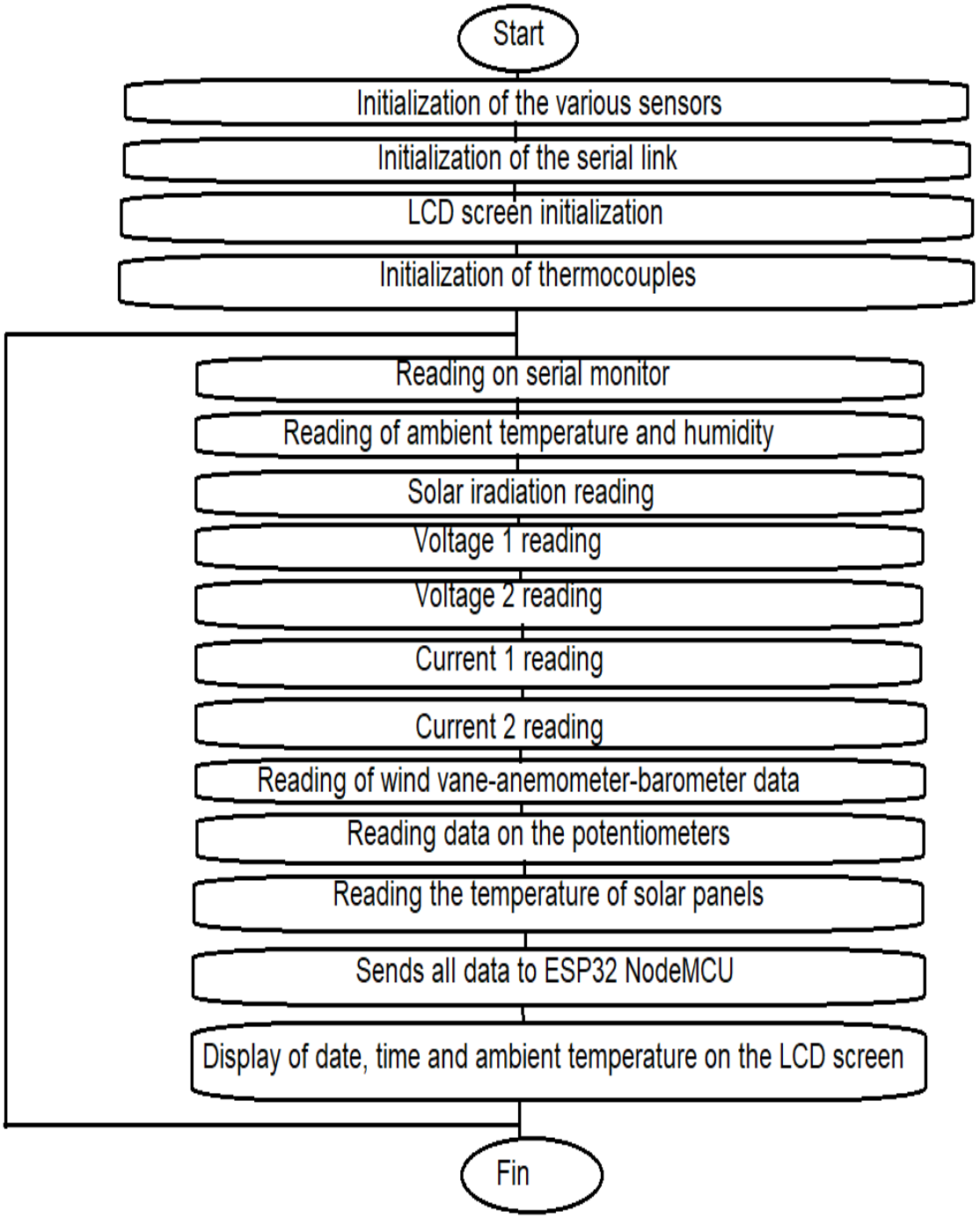

Figure 5a: Flowchart of the program driving the Arduino board

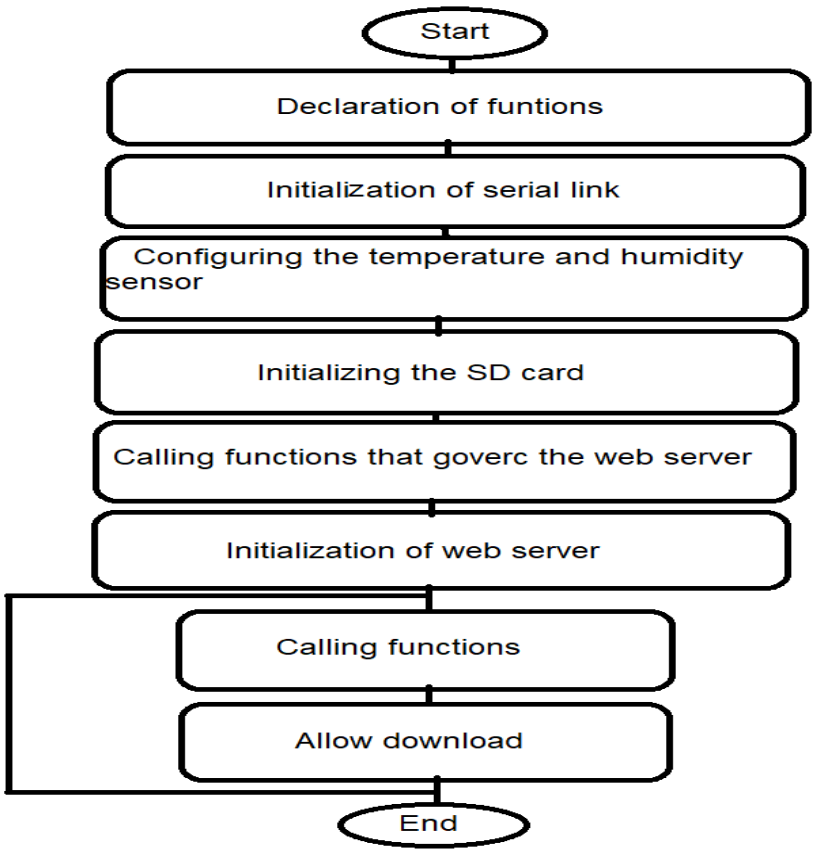

Figure 5 b: Flowcharts of the programs driving the ESP32 Node MCU

Results and discussions

This project of characterization platform being in progress, in this part, we present only the variation of some climatic parameters according to time. A test was carried out on 26/03/2021 from 8h30 am to 7h30 pm on the characterization platform allowing us to present these results.

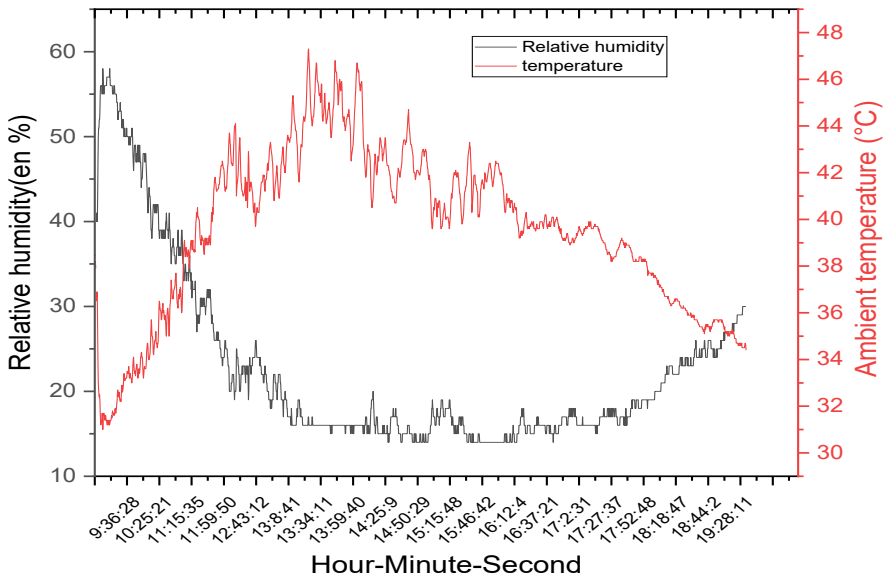

Figure 6 a: Variation of relative humidity and ambient temperature

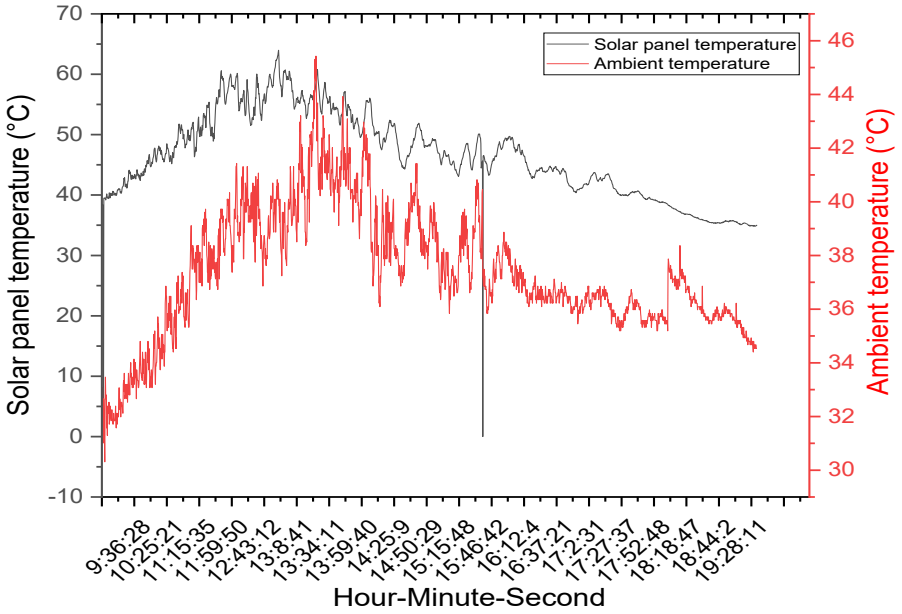

Figure 6b: Variation of the temperature of the solar modules and the ambient temperature

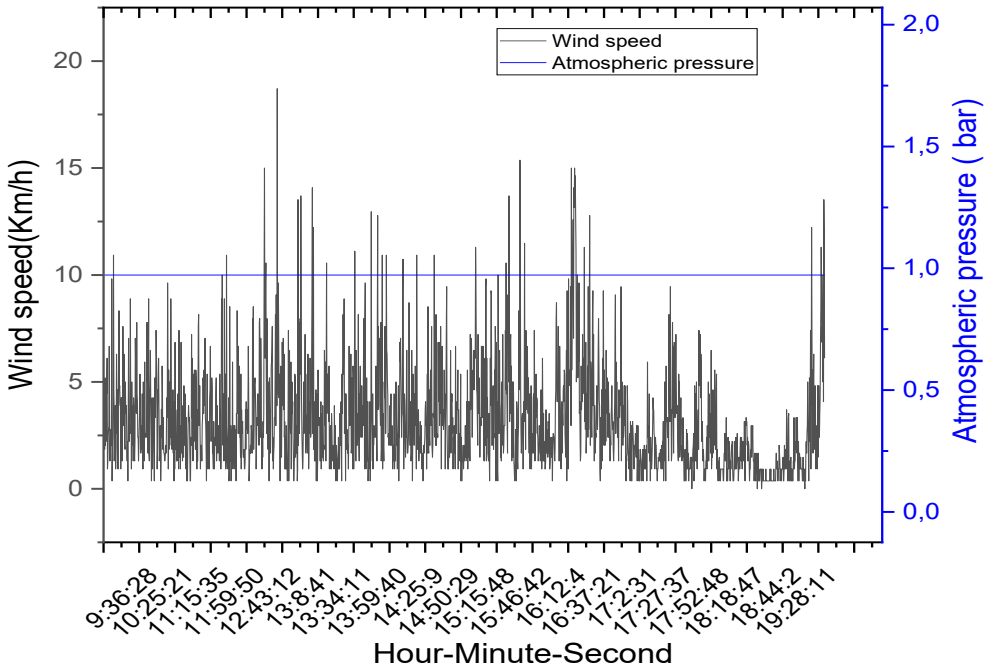

Figure 6c: Variation of wind speed and atmospheric pressure

Figure 6a shows a decrease in humidity, reaching an almost constant value around 2pm and starting to increase around 5pm. The ambient temperature increases until it reaches its maximum value around 2:00 pm, a critical time used in the environment for air conditioning projects.

Curve 6b shows that the temperature of the modules is generally higher than the ambient temperature during the day because these panels absorb light and heat up.

The atmospheric pressure at the platform site is about 1 bar (Figure 6c), which is roughly equal to normal atmospheric pressure (101.3mbar). The wind speed varies a lot with several

spikes during this day carrying a lot of dust on the solar modules. The impact of dust will be studied when all the characterization sensors are installed.

Conclusion

This article presents the work done for the realization of the solar module characterization platform implemented at FaST. Currently, it is possible to acquire meteorological data. However, the work continues in order to acquire the current-voltage characteristics of the solar modules as well as the solar irradiation in order to evaluate the consequences of the effect of the climatic conditions (temperature and dust) on the production of solar modules.

Acknowledgements

We offer all our recognitions to German Academy Exchange Service DAAD for financially supporting this project through WILDAU University

References

[1] Asch G, Poussery B. Les capteurs en instrumentation industrielle. 8e édition. Malakoff: Dunod; 2017.

[2] Akoro E, Tevi G, Faye M, Sene M, Maiga A. Modelling and simulation of an automatic solar module characteristics data acquisition system. OAJ Materials and Devices. 2019. https://doi.org/10.23647/CA.MD20191602

[3] Asch G, Néel L. Acquisition de données : du capteur à l'ordinateur. 1 Vol.. 3e édition. Paris: Dunod; 2011.

[4] Nfaoui M, El-Hami K. Conception et réalisation d'un système de métrologie et supervision des paramètres météorologiques et électriques d'une installation photovoltaïque . https://www.openscience.fr/IMG/pdf/iste_incertfia17v2n5.pdf. 2017;

[5] Tavernier C. Arduino : Applications avancées. Dunod; 2012.

2nd German-West African Conference on Sustainable and Renewable Energy Systems SusRES - Kara 2021

Photovoltaic

https://doi.org/10.52825/thwildauensp.v1i.8

Published: 15 June 2021

Evaluation of power losses in a DC-DC Boost converter

Komi Boniface EHLAN[1], Edjadessamam AKORO [1,2], Hodo-Abalo SAMAH [1], N'detigma KATA[1,2], Amadou Séidou MAIGA [2]

[1] Faculté des Sciences et Techniques (FaST), Université de Kara, Togo

[2] Département de Physique Appliquée, Université Gaston Berger, Saint-Louis, Sénégal

Abstract. DC-DC converters are dynamic systems consisting of the passive components. These components under the effect of thermal stress in a PV system generate power losses. The knowledge of these power losses is necessary to evaluate the conversion efficiency of the system. Using the polynomial approximation method, the equations for calculating losses in the different components were determined. The system is implemented under the MATLAB / Simulink software. The results show that for a PV application of 240 W supplied to the load, 18% are lost, only 82% are transferred

Keywords: Photovoltaic conversion chain, DC-DC converter, Power losses.

Introduction

Photovoltaic solar energy comes from the direct conversion of solar radiation into electrical energy through Photovoltaic (PV) cells. Depending on the desired power, these cells are connected in series and or in parallel to give a photovoltaic generator (GPV) [1], [2]. Nevertheless, the production of this energy varies according to the light intensity and the temperature of the cell. On the other hand, [3] states that a direct connection of the PV generator to the load does not guarantee the transfer of the maximum available power. In order to extract the maximum power available at each moment at the terminals of the PVG, the technique classically used is the insertion of a matching stage composed of a DC-DC converter and a MPPT (maximum power point tracking) controller between the GPV and the load [2]. The latter acts as an interface between the GPV and the load by ensuring, through a control action, the transfer of the maximum power supplied by the GPV so that it is as close as possible to the maximum available power. Therefore, several works on photovoltaic systems have led to the development of algorithms to extract the maximum energy from the GPV to increase the system efficiency. Therefore, the main objective of this paper is to shed light on the different losses generated by a converter in a PV conversion chain. To do this, we have based ourselves on the polynomial approximation method and on the manufacturer's, data sheets to derive the equations of the losses as a function of the global current. In order to confirm our theory, we proceeded by programming these equations under the MATLAB / Simulink software. The rest of the paper is organized as follows: the block diagram of the studied PV conversion chain is described in section 2 and the loss equations are established in section 3. Section 4 presents the discussions on the obtained results and section 5 concludes the paper.

Synoptic diagram of a PV conversion chain connected to a DC load

A photovoltaic system consists of four (04) blocks as shown in Figure 2. The first block represents the energy source (PV panel), the second block is a static DC-DC converter, the third block represents the load and the fourth block represents the control system. This MPPT control system is in charge of modifying the cyclic ratio of the converter's switching cell in order to force the panel to deliver the maximum of its energy at each moment.

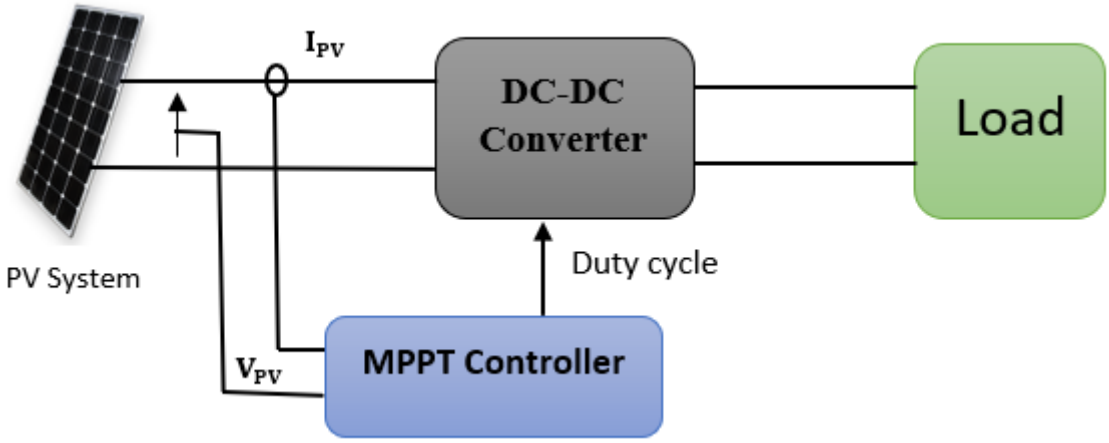

Figure 1: Synoptic diagram of the photovoltaic system

Global study of the losses for a static converter

As described in the previous section, the constituents of the Boost converter are: MOSFET, Diode, Inductance and Capacitance. The conversion efficiency can be written as:

$$\eta_{Conversion} = \frac{P_{out}}{P_{in}} = \frac{P_{in}-P_{losses}}{P_{in}} \quad (1)$$

With P_{in} and P_{out} the powers respectively at the input and output of the converter, P_{losses} the power lost in the converter

Losses in the MOSFET

The transistor dissipates energy during the firing phase W_A, the conduction phase W_C, and the blocking phase W_B corresponding to a Total energy W_T: per switching period. For a MOSFET, the behavior in conduction regime is similar to that of a resistor, the powers dissipated during this phase and during the switching phases are defined according to [4] by the following equations:

$$P_{Cond} = f.W_{Cond} = \frac{T_{Cond}}{T}.V_{on}.I_{in} = \alpha.I^2_{in}.R_{DSon} \quad (2)$$

$$P_{Cond} = (W_A + W_B).f = \frac{1}{2}.V_{in}.I_{in}(t_{com} + t_{Bloc})f + \frac{1}{2}.V_{in}.I_{RM}.f.t_{com} \quad (3)$$

With : W_A: Energy dissipated during the firing phase, W_B: Energy dissipated during the blocking phase, W_{Cond}: Energy dissipated during the conduction phase, W_T: Total energy dissipated by the MOSFET, R_{DSon}: Source drain resistance of the MOSFET, V_{in}: Voltage at the terminals of the transistor in the blocked state, I_{in} : current delivered by the generator, I_{RM}: amplitude of the diode's overlay current, α: the duty cycle, f: the switching frequency of the MOSFET, t_{com}: duration of the switching phase, and t_{Bloc}: duration of the blocking phase.

In summary, the total losses at the MOSFET can be evaluated by:

$$P = f.W_T = \alpha.I^2_{in}.R_{DSon} + \frac{1}{2}.V_{in}.I_{in}(t_{com} + t_{Bloc})f + \frac{1}{2}.V_{in}.I_{RM}.f.t_{com} \quad (4)$$

Losses in the diode

When the diode is blocked, it behaves like a perfect capacitor because there is virtually no current flowing through it and only the voltage across it varies. When it is on, the voltage and the current vary. The other losses of the diode have been taken into account in the switching losses of the MOSFET, only the conduction losses are considered here. These are in the form of:

$$P_F = V_d . I_{out} \text{ with } V_d = R_d . I_{in} + V_F \quad (5)$$

$$\mathbf{P_F = (1-\alpha)\,[R_d . I^2_{in} + I_{in} . V_F\,]} \quad (6)$$

with R_d : differential resistance or dynamic resistance et V_F : direct voltage.

Losses in the capacitor

In most cases, a capacitor is a simple capacitance C expressed in Farad but as a component the capacitor is not limited to its simple capacity:

$$\mathbf{P_{Cap} = R_C . I^2_{RMS}} \quad (7)$$

We can rewrite (7) thanks to the expressions of the effective currents in the various components of the circuit developed in [5] in the form:

$$\mathbf{P_{capacitor} = R_c \alpha(1-\alpha) I^2_{in} + \frac{R_c}{12}(1-\alpha)\left(\frac{\alpha * V_{in}}{L * f}\right)^2} \quad (8)$$

Losses in the inductor

The equivalent electrical model of a wound inductor can be reduced to an ideal inductor in series with a resistor $\mathrm{R_L}$. The presence of the latter generates direct losses by Joule effect linked to the conductors and to the losses induced in the magnetic core (losses by hysteresis and by eddy currents) which depend on the frequency and the variation of the flux.

$$\mathbf{P_{Inductor}} = \mathrm{R_L . I^2_{L,RMS}} \quad (9)$$

$$\mathbf{P_{Inductor} = R_L I^2_{in} + \frac{R_L}{12}\left(\frac{\alpha * V_{in}}{f * L}\right)^2} \quad (10)$$

The expressions (11) and (12) of the average voltage of the inductance and the average current of the capacitor of a boost converter, make it possible to establish a relation showing the influence of the losses generated by $\mathrm{R_L}$ of the inductance on the output of this converter according to the electric quantities of the circuit [6].

$$\langle V_L \rangle = 0 = V_{in} - R_L I_{in} - (1-\alpha).V \quad (11)$$

$$\langle i_C \rangle = 0 = (1-\alpha).I_{in} - \frac{V}{R} \quad (12)$$

$$\boldsymbol{\eta = \frac{P_{out}}{P_{in}} = \frac{1}{1 + \frac{R_L}{R.\alpha'^2}}} \quad (13)$$

For application, we used a MOSFET type IRFZ44E [7], a Standard silicon rectifier diodes1N 5059...1N 5062 [8], a capacitor APSA100ESS680MFA5S [9] and an inductor muRata|Ps 49101sc [10].

Using the datasheets of all these components, the equations for calculating the losses as a function of the current through them are summarized in Table 1.

Table 1: Loss evaluation equations

Parameters	Equations
$\mathbf{P_{Mosfet}}$	$\mathbf{(8.625e^{-3})I_{in}^2 + (0.234)I_{in} + 34.53e^{-3}}$
$\mathbf{P_{Diode}}$	$\mathbf{(2.562e^{-2})I_{in}^2 + 0.688I_{in}}$
$\mathbf{P_{Capacitor}}$	$\mathbf{(5.86e^{-3})I_{in}^2 + 0.0732}$
$\mathbf{P_{Inductor}}$	$\mathbf{(0.165)I_{in}^2 + 0.938}$

Loss calculation method

From the equations listed in Table 1, the block model in Figure 2 has been developed in Simulink to calculate the losses generated by a single-inverter PV system. Each of its blocks modeling the losses whose sum represents the total loss of the converter receives at its input the current $\boldsymbol{I_{in}}$ which is the equivalence of the current $\boldsymbol{I_{PV}}$. This calculation block is associated with the MPPT control system that is implemented in the converter.

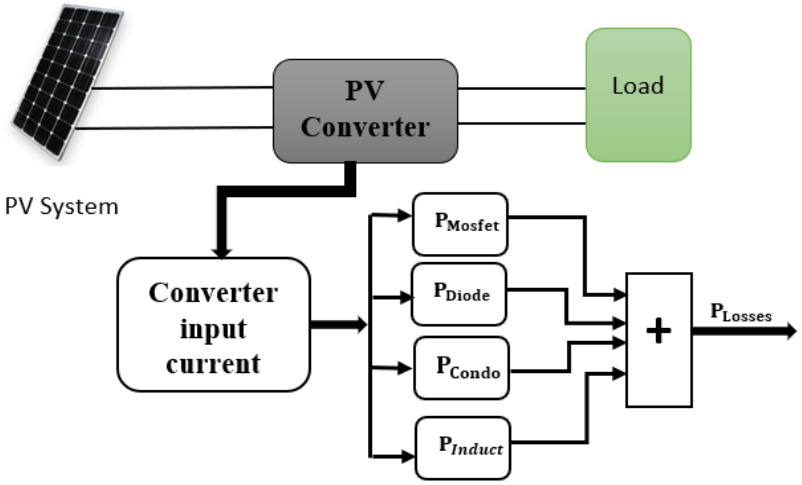

Figure 2: Total loss calculation blocks of a DC-DC converter in a PV system.

Results and discussions

We have evaluated the losses in the components including the switching cells (MOSFET, diode) and passive components of a DC-DC converter. On figure 3 showing the characteristic curves of the losses generated by these components as a function of the global current, we can notice that the losses in the capacitor, the MOSFET and in the diode are almost linear while the losses in the inductor evolve exponentially with the global current. In terms of efficiency, a cross analysis between figure 3 and 4 shows that the influence of these losses on the conversion efficiency is directly proportional to the losses generated by each component of the converter.

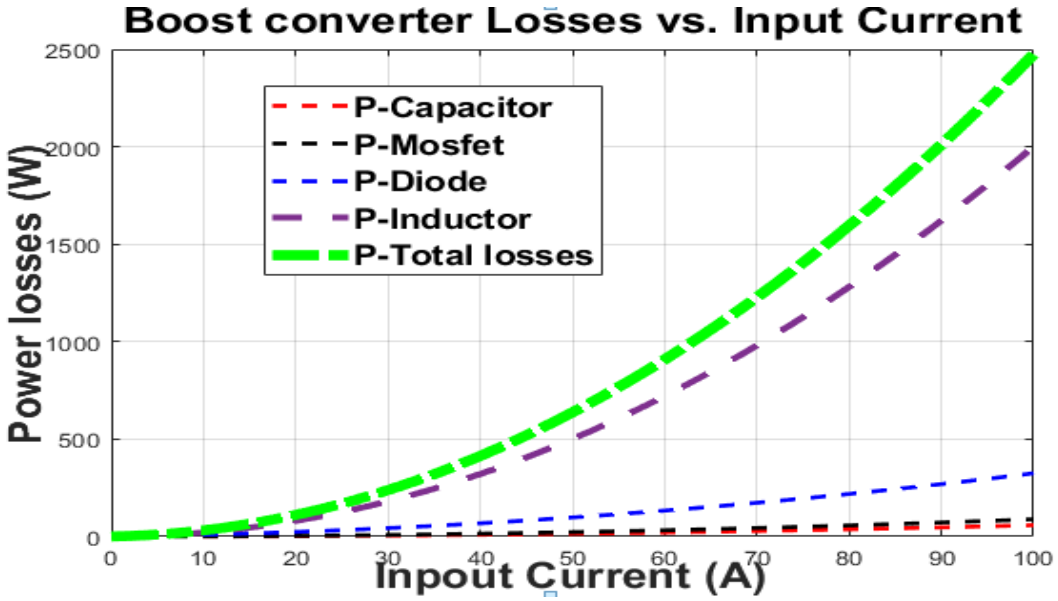

Figure 3: Changes in losses based on global current

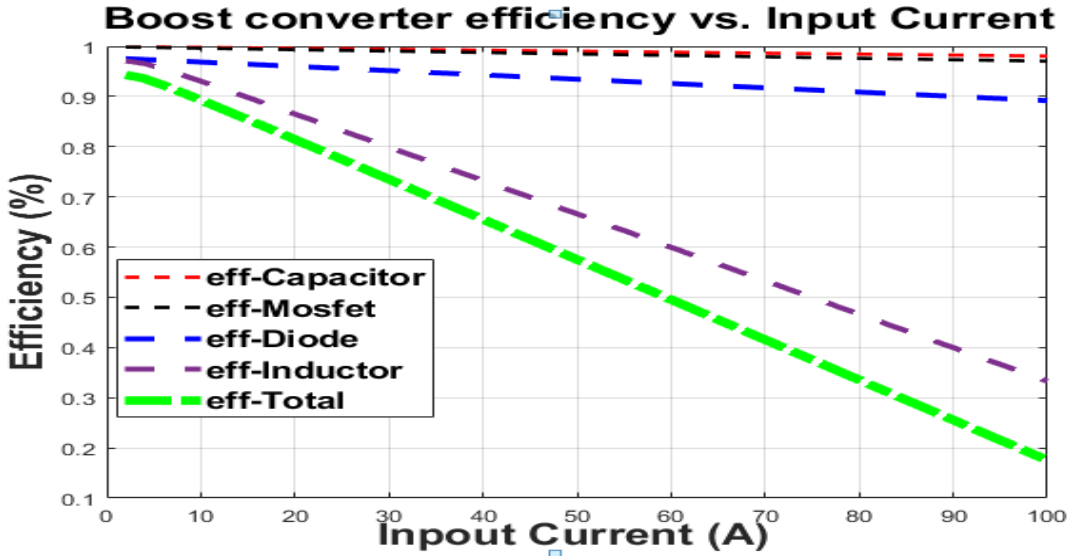

Figure 4: Influence of losses on efficiency

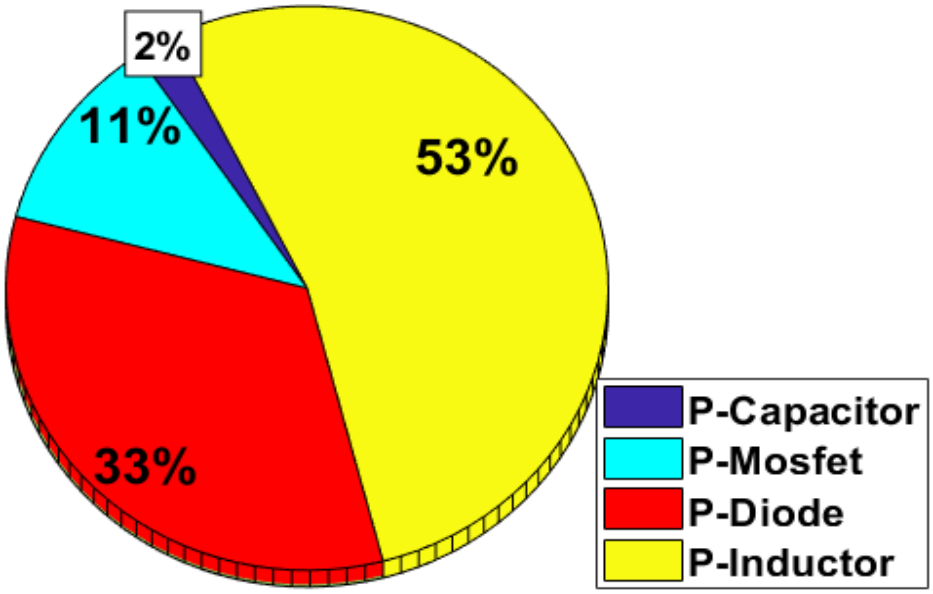

Figure 5: Loss distribution diagram

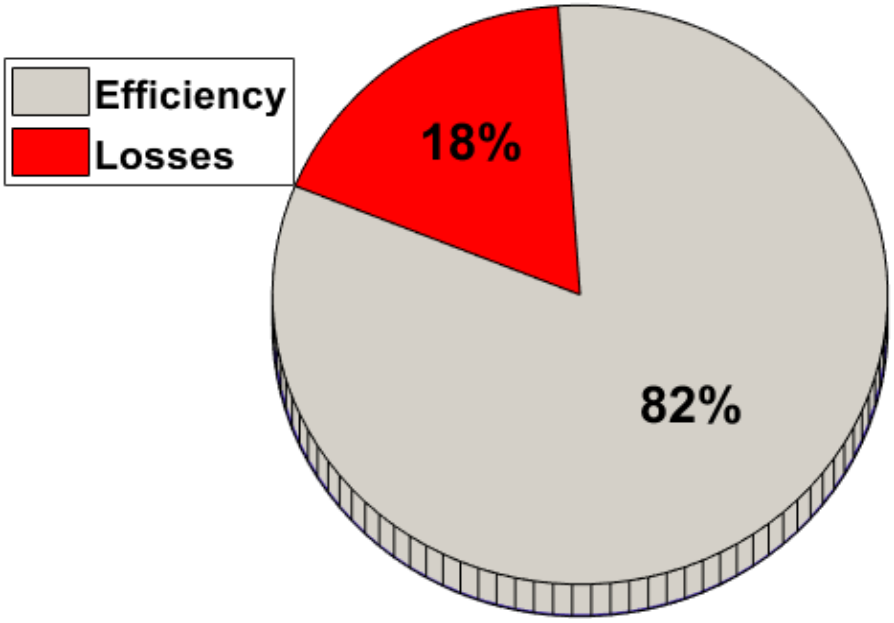

Figure 6: Total loss diagram.

Then, the simulation is performed under MATLAB / Simulink with a 240 KW PV generator and a purely resistive charge of 9.6 Ω. By applying the Figure 1 loss calculation block, Figure 6 shows that for a 240W PV source, a converter can encroach on conversion output up to 18% of the total power available at its in, reducing conversion power to 82%. Figure 5 shows that 53% of its losses are caused by the inductor, 33% by the diode, 11% by the MOSFET and only 2% by the capacitor.

Conclusion

The total efficiency of the converter is strongly influenced by the efficiency of the induction since the efficiency of the capacitor and MOSFET always remain above 95% and 90% respectively. While the efficiency of the diode which is 67% is still acceptable, the induction seems to impose its losses on the converter we simulated. Thus, in order to boost the efficiency of the converter, we must try to work a lot on the effectiveness of the inductor.

ACKNOWLEDGEMENTS

The authors offer their sincere thanks to the German Academic Exchange Service DAAD through the Technical University of Applied Sciences (WILDAU) for their unwavering support throughout the implementation of this work.

References

[1] Dileep G, Singh S. Selection of non-isolated DC-DC converters for solar photovoltaic system. *Renewable and Sustainable Energy Reviews*. 2017 Sep;76:1230-1247. https://doi.org/10.1016/j.rser.2017.03.130

[2] Azab M. A new maximum power point tracking for photovoltaic systems. *World Academy of Science, Engineering and Technology*. 2008;44:571–574.

[3] Akoro E, Gabriel Jean-Philippe T, Faye M, Doumbia M, Amadou SM. Artificial Neural Network Photovoltaic Generator Maximum Power Point Tracking Method using Synergetic

Control Algorithm. *Akoro et al.,International Journal on Emerging Technologies11(2): 590-594(2020) 590International Journal on Emerging Technologies* . 2020;11(2):590–594.

[4] Cabal C. Optimisation énergétique de l'étage d'adaptation électronique dédié à la conversion photovoltaïque.:188.

[5] Walker G. Evaluating MPPT converter topologies using a Matlab PV model. *Australian Journal of Electrical & Electronics Engineering*. 2001;21(1):49-55.

[6] Erickson RW. *Fundamentals of power electronics*. New York: Chapman & Hall; 1997.

[7] IRFZ44E MOSFET Datasheet pdf - Equivalent. Recherche de références croisées. https://alltransistors.com/mosfet/transistor.php?transistor=3395. Accessed 2021 March 27.

[8] 1N 5059...1N 5062. https://www.terraelectronica.ru/pdf/show?pdf_file=%252Fz%252FDatasheet%252F1%252F1N5061.pdf. Accessed 2021 March 27.

[9] Cha E. *PART NUMBERING SYSTEM, p.2*.

[10] *Magnetic Products, p. 20*. M. P. Solutions;

2nd German-West African Conference on Sustainable, Renewable Energy Systems SusRES – Kara 2021

Photovoltaic

https://doi.org/10.52825/thwildauensp.v1i.7

Published: 15 June 2021

Study of the decentralized electrification by a micro-wind power plant: Case of Ahouandji locality in southern Benin

Hagninou E. V. Donnou[1,2] [https://orcid.org/0000-0002-2207-0398], Gabin Koto N'Gobi [1,2] [https://orcid.org/0000-0001-7322-138X], Hilaire Kougbéagbédè [2] [https://orcid.org/0000-0002-1962-9680], Germain Hounmenou[3], Aristide B. Akpo[1,2] [https://orcid.org/0000-0002-4318-0123], and Basile B. Kounouhewa[1]

[1]Laboratoire de Physique du Rayonnement (LPR), Université d'Abomey-Calavi, 01 BP 526 Cotonou

[2]Laboratoire de Physique de l'Atmosphère (LPA), Université d'Abomey-Calavi, 01 BP 526 Cotonou

[3] Institut National Supérieur de Technologie Industrielle, Université Nationale des Sciences, Technologies, Ingénieries et Mathématiques, Abomey, Bénin

Abstract. Access to energy is a major challenge for the socio-economic well-being of populations. In Benin, the electric energy sector is characterized by a low rate of access to energy in rural area (6.6% in 2017) and dependence on the outside at 40%. In the village of Ahouandji (Ouidah commune) located on the coast of Benin and far from the conventional network, the surface winds are regular and permanent. However, this wind resource is untapped despite the unavailability of electrical energy. To cope with this difficulty, this study therefore addresses the design and sizing of a micro-wind power plant to supply the region. Wind data at 10 m above the ground recorded over the period January 1981 to December 2014 by the Agency for the Safety of Air Navigation in Africa (ASECNA) were used. Based on the socio-economic study of the locality and the statistical study of the winds by the Weibull distribution and the power law, the sizing of the wind power plant components was carried out. The economic study of the system then made it possible to assess the profitability of the project. It emerges from this study that at 25 m above the ground the Weibull shape parameter is estimated at 2.94 and the scale parameter at 6.07 m/s. The most frequent speed is estimated at 5 m/s and the one giving the maximum energy at 10.2 m/s. The micro-power plant is made up of two wind turbines with a nominal power of 29.7 kW for a daily production estimated at 355 kWh, a three-phase converter rated at 30 kW, 06 inverters/chargers with a power of 11.5 kW and 120 batteries (3000Ah/2V). The selling price of kilowatt-hour estimated at 0.17 euro/kWh is quite competitive. The establishment of this micro-wind power plant is therefore an asset for these rural populations.

Keywords: Electrical energy, Weibull distribution, Power law, Wind turbine, Kilowatt-hour price

Introduction

Energy plays an essential role in the socio-economic development of people and its demand is growing exponentially in the world [1], [2]. In order to reconcile development policies in this sector with environmental protection strategies, renewable energies now constitute a sustainable alternative. Their share in the global energy mix has been steadily increasing [3], [4] and they will become the largest source of electricity generation by 2025, surpassing coal according to the International Energy Agency's Renewable Energy 2020 report (IEA, 2020). Among these sources, wind power has experienced a remarkable growth in recent decades. Its production capacity has increased from 23,900 MW in 2001 to 591,549 MW at the end of 2018 [5], [6], [7] and wind power production exceeded 1,200 TWh over the year 2018,

contributing to 4.6% of the world's electricity production (all sources combined) [7]. This source therefore deserves to be valorized especially in developing countries. Moreover, the production of electricity in rural communities is an acute problem that militates against the socio-economic well-being of the population of these underdeveloped countries [8], [9].

In Benin, several studies such as Awanou et al [10], Houekpoheha et al [11], Akpo et al [12],Salami et al [13], Donnou et al [2] agree that the exploitation of wind energy in the coastal region is suitable at small and large scale. However, despite the many efforts made by leadersin the energy sector, this source of energy is still not exploited and many rural areas still livewithout electricity, especially on the coast of Benin. The electrification rate in rural areas is6.6%. To cope with these challenges of electricity production, several authors have addressed the issue of rural electrification through the installation of micro wind power plants or the assessment of wind potential to overcome the energy deficit observed in these regions especially rural. Thus, in the work of Abdelhady et al [14], the authors give an overview of the wind potential in different regions of Egypt, along the Mediterranean and the Red Sea, and in the Western Desert. The techno-economic evaluation of the annual electricity production from 8 small wind turbines was performed. The net present value and payback period by analyzing the profitability of the selected wind turbines were addressed. The results obtained show that, in the locations considered, the reduced value of the feed-in tariff is a detrimental factor affecting the profitability of small wind turbines. Okeniyi et al [8] studied the assessment of wind power potential at selected sites in three major geopolitical zones in Nigeria. It was found that the simulation of electrical energy at different hub heights of low wind speed wind systems showed that the cost of electrical energy production at the three study sites converged to an affordable cost per kWh of electrical energy (0.0507 Euro in Kaduna, 0.0774 Euro in Warri and 0.0819 Euro in Calabar). Rural electrification by renewable energy source (wind) in these study sites was suggested by the authors. Ajayi et al [15] evaluated the wind power potential of two sites (Shaki, Iseyin) in Oyo State, Nigeria. Three wind energy conversion systems were used and it was found from the statistical study of the winds, that the sites have a capacity to generate in MWh and GWh of electricity at an average cost/kWh between (0.025 and 0.049) Euro. Furthermore, turbines with technical parameters of start-up speed, cut-off speed and rated speed (3m/s, 25m/s and 11.6 m/s) are suitable for these sites. In Turkey, Gökçeka et al [16] analyzed the wind energy potential of Kirklareli province in the northwestern Marmara region. The economic evaluation of wind energy at the site was performed using the discounted cost method. The results showed that the energy production cost per kWh for the site concerned varies between 0.0537 and 0.119 euro and that an increase in operation and maintenance costs from 0 to 10%, leads to an increase in the unit energy cost of about 6%. Similarly, the analysis of the wind characteristics in the city of Ras Benas located on the east coast of the Red Sea in Egypt using measured data (wind, pressure and temperature) and the Weibull function was performed by Ahmed [17]. This station has a huge potential of wind power for electricity generation and was selected to install a wind farm of 30 MW consisting of 20commercial wind turbines (Nordex S 77). The production costs have been estimated at 0.013 euro/kWh, which is a competitive price in the global wind energy market. In the work of Ajayi et al [18], a study assessed the wind power potential of ten selected sites in the southwestern region of Nigeria and conducted a cost-benefit analysis of wind power generation at these sites. The energy cost analysis shows that the production cost can be as low as 0.02 Euro/kWh and as high as 5.03 Euro/ kWh, depending on the turbine model used. Faida et al [19], after processing and simulating wind data from a site in Morocco, designed a wind farm and evaluated its electrical production based on a judicious choice of wind turbines. The installed capacity is 140 MW, i.e. 140 wind turbines, for an annual production of 516.6 GWh. Kassem et al [20] undertook an economic evaluation of a grid-connected 12 MW wind farm and PV plant in two regions of northern Cyprus for electricity generation. The production costs of the wind farm obtained by the authors ranged from 0.023 to 0.04 Euro/kWh. Gaddada and Kodicherla [21] selected three commercial wind turbines as large-scale wind energy conversion systems (WECS) for the technical evaluation of power generation through the present value cost (PVC) method in eight selected locations in the Tigray region of Ethiopia. The minimum average cost per kWh obtained in Mekele was $0.0011/kWh with VESTAS

V110-2. while the highest average cost was $7.3148/kWh with POLARIS P15-50 in Shire. Bagiorgas et al [22] estimated the Weibull parameters by three different methods on four meteorological stations in the central region of Western Greece to estimate the wind potential in this area. An analysis of the specific cost per kilowatt-hour of electrical energy, obtained for several wind turbines at different hub heights was performed for each station. The result of this study is that the specific cost per kWh decreases as the size of the wind turbine increases for comparable systems designed by the same manufacturer with similar performance but with different power ratings (size).

The diversity of this work and the results obtained, notably on the competitive cost of the wind power kilowatt-hour, reveal the interest in this energy source and the importance of its exploitation on appropriate sites for a better profitability. The interest of this study, which consists of supplying electric energy from a wind source to the households of Ahouandji, is therefore justified in this locality. To achieve this, a statistical study of wind speeds in the study area was conducted at 10 and 25 m to estimate the available wind resource. Then, based on the socio-economic study of the Ahouandji locality and the wind speed profile, the characteristics of the components of the micro power plant were determined. Finally, the financial evaluation of the project was carried out in order to assess its profitability.

Material and Methods

Material

Study area

Benin's 125 km long coastal zone extends from Hillacondji in the west to Kraké in the east. It is located between latitude 6°15 'N and 7°00' N and longitude 1°40′ E and 2°45′ E. The site of our study is the village of Ahouandji located in the district of Avlékété (commune of Ouidah) on the coast of Benin. Figure 1 provides an overview of the geographical location of the coastal region of Benin and the study site.

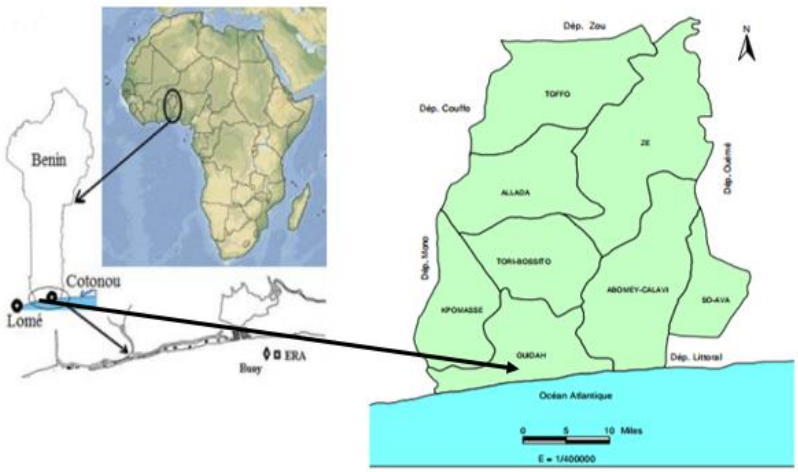

Figure 1. Geographic location of the coastal region of Benin. Location of the commune of Ouidah [23], [24].

Data collection

The data used in this study include wind speed measured at 10 m from the ground during the period from January 1981 to December 2014. They were recorded every hour by the Cotonou Airport meteorological station. Figure 2 shows the experimental site of the meteorological station where the data were collected.

Figure 2. Experimental site of the Cotonou-Airport meteorological station. Anemometer with cup and wind vane located on a 10 m mast (left panel). Experimentation site (right panel) [25]

Methods

Statistical study of the wind at the study site

Weibull distribution

The Weibull function is used to characterize the frequency distribution of wind speeds over a given period (a year, a month, or a day). It is defined by equation [2], [17], [26], [27], [28], [29]:

$$f(v) = \frac{k}{c}\left(\frac{V}{C}\right)^{k-1}\exp\left[-\left(\frac{V}{C}\right)^{k}\right] \quad (1)$$

With f(v) the Weibull probability density function which is the probability of observing a wind speed V in m/s, c in m/s is the scale factor of the Weibull distribution. It is related to the mean wind speed by the Weibull form factor k describing the wind speed distribution. The relationship between the scale factor of the Weibull law and the mean wind speed is established by the following formula [2], [11], [12], [22]:

$$C = \frac{V}{\Gamma\left(1+\frac{1}{k}\right)} \quad (2)$$

With Γ the Gamma function, V the average wind speed. The relationship to determine the form factor is given by [11], [12], [19], [30]:

$$k = \left(\frac{\sigma}{V}\right)^{-1.086} \quad (3)$$

With σ the standard deviation.

The velocity giving the maximum energy V_{me} and the most frequent velocity V_f on the site are given by [2], [18]:

$$V_{me} = \left(1+\frac{2}{k}\right)^{1/k} c \quad (4)$$

$$V_f = \left(1-\frac{1}{k}\right)^{1/k} c \quad (5)$$

The power law

The power law is an equation that allows to determine from a known wind speed data (usually 10 m from the ground), the speed at an altitude higher than 10 m. It is the most commonly used equation for the extrapolation of wind speeds [25]. It is given [25], [31], [32], [33], [34].

$$V_2 = V_1 \left(\frac{z_2}{z_1}\right)^{\alpha} \quad (6)$$

with z_1 the height of the initial observation of the wind speed (m), V_1 is the observed speed ataltitude z_1, z_2 is the height at which we want to estimate the wind speed (m), V_2 is the speed that we estimate at the height z_2 (m/s).

Sizing of the micro wind power plant

The energetic study of the micro wind power plant consists in sizing the different components necessary for the implementation of the plant. It is thus a question of determining:

- the socio-economic study of the locality to be supplied;
- the power of the wind farm to be set up and able to cover the energy needs;
- the capacity of the batteries to be installed while taking into account the number of days
  or hours of autonomy;
- the characteristics of the converters to be used to satisfy the electrical energy needs;
- the system protection and control devices

Socio-economic study of the locality of Ahouandji

The socio-economic study of the Ahouandji locality was carried out according to the following steps

- Data collection

First, a study of the number of inhabitants of the Ahouandji village was conducted. Indeed, from the notebooks of villages and city districts of the Atlantic department published by the National Institute of Statistics and Economic Analysis (INSAE) [24], the population of the said village in the years 2004 and 2013 was obtained. In order to estimate the current number of inhabitants of the village considered in this study, we extrapolated from the year 2004 to the year 2020 using the following expression [24]:

$$P_{2020} = P_{2004}(1+\tau)^{(m-a)} \quad (7)$$

With m the future year (2020), a : the base year (2004).

The rate of increase τ is determined by [24]:

$$\tau = \left(\frac{P_{2013}}{P_{2004}}\right)^{\frac{1}{m}} - 1 \quad (8)$$

Avec P_{2013} : Population in 2013= 851 inhabitants
P_{2004} : Population in 2004 = 566 inhabitants

m : 2013-2004

The number of persons being estimated on average at 6 per household from the field surveys, we have the number of household N which is given by:

$$N = \frac{P_{2020}}{6} \quad (9)$$

In view of the demographic data obtained from the extrapolation to the year 2020, in this case the number of households, we have constituted a sample of households to be surveyed in the locality. The size of the sample is determined from the following relationship [24]:

$$n_e = t^2 * p * (1-p)/\alpha^2 \quad (10)$$

With n_e the minimum sample size for obtaining significant results for a given event and risk level, t the confidence level (the standard value of the 95% confidence level will be 1.96), p the estimated proportion of the number of households that have the characteristic (10% of the total number of households), α the margin of error (usually 5%). Based on the sample size of the population, a field survey was conducted in these households to learn about their different energy needs.

- Analysis of collected data

The analysis of the data consisted in making a synthesis of the receivers used by the households with their respective powers and then to proceed to the energy balance.

Power of the wind farm

To determine the power of the wind farm, the daily energy needs of the population must be less than or equal to the daily energy produced by the wind turbines. The useful energy E_u provided by the wind farm to supply the locality was obtained from equations (11), (12) and (13):

$$E_u = P_u * T \quad (11)$$

Its useful power P_u is given by the formula [9], [22]:

$$Pu = fc\ P_n \quad (12)$$

With:

$$fc = \left\{ \frac{\exp\left[-\left(\frac{V_d}{c}\right)^k\right] - \exp\left[-\left(\frac{V_n}{c}\right)^k\right]}{\left(\frac{V_n}{c}\right)^k - \left(\frac{V_d}{c}\right)^k} - \exp\left[-\left(\frac{V_c}{c}\right)^k\right] \right\} \quad (13)$$

fc is the capacity factor, P_n is the nominal power (W), T is the time (h), V_d is the starting speed,V_n he nominal speed and V_c the stop speed. The choice of V_n is made from the speed V_{me} and V_f. We have then $V_f < V_n \leq V_{me}$ [8].

1.2.2.3 Battery capacity

The capacity C_b in Ah of the battery bank is determined by the following relationship [35]:

$$C_b = \frac{E_{cons} * N}{D * U} \quad (14)$$

With E_{cons} the total daily energy to be satisfied, N number of autonomy days equal to 2 in the case of this study, D the deep discharge of the battery (80%), U the battery voltage is fixed at 48V in this study.

Characteristics of converters

- Sizing of the DC/AC converter

The use of an inverter in the wind power plant is essential because the loads will be supplied with alternating current. Indeed, its dimensioning is done essentially on the basis of the nominal power supplied by the wind field. Thus, the power of the DC/AC converter is equal to the power of the wind field.

- Sizing of the battery charger inverter

The battery charger inverter is an essential device in a wind power plant, since it not only allows to recharge the batteries that will be used as energy source for the loads during the periods when there is not enough wind, but also to create a primary AC voltage network

related to the synchronization of the central converter (DC/AC). It is usually sized based on the maximum power demand of the load. In fact, it is desirable to apply a safety coefficient equal to 1.25 to the maximum basic power in order to have a wide power range. The power of the inverter is given by [35]:

$$P_{ond} = \frac{P_{max} * 1.25}{\eta} \quad (15)$$

With P_{max} the maximum power demand, P_{ond} is the power of the inverter, η is the efficiency of the inverter (98%).

Economic calculation

Calculation of the annuity

The annuity which represents the annual repayment of a loan with interest by a constant amount is given by the relation [35]:

$$A = \frac{Ii}{1-(1+i)^{-n}} \quad (16)$$

With I : Initial investment, i Interest rate (12% in the case of this study), n Lifetime of the plant components (between 10 and 25 years).

Overall discounted cost

This cost takes into account maintenance, operating costs and annuity. Maintenance and operating costs are estimated at between 3 and 5% of the initial investment cost of the plant.

- Calculation of the cost per kilowatt hour

The cost per kilowatt-hour is given by the ratio of the discounted gbobal cost Cg to the annual energy production P_E [35]:

$$C_k = \frac{C_g}{P_E} \quad (17)$$

Return on investment time

Also known as the payback period, this is the time that must elapse before the operating profit streams can fully cover the initial capital. The initial investment is divided by the empirical average of the annual cash flows (profits). Then, we multiply the remainder of the quotient thus obtained by 360 days.

Results and discussion

Wind speed distribution

Variation of the Weibull parameters

In Figure 3, the Weibull shape k and scale c parameters are shown at the monthly scale.

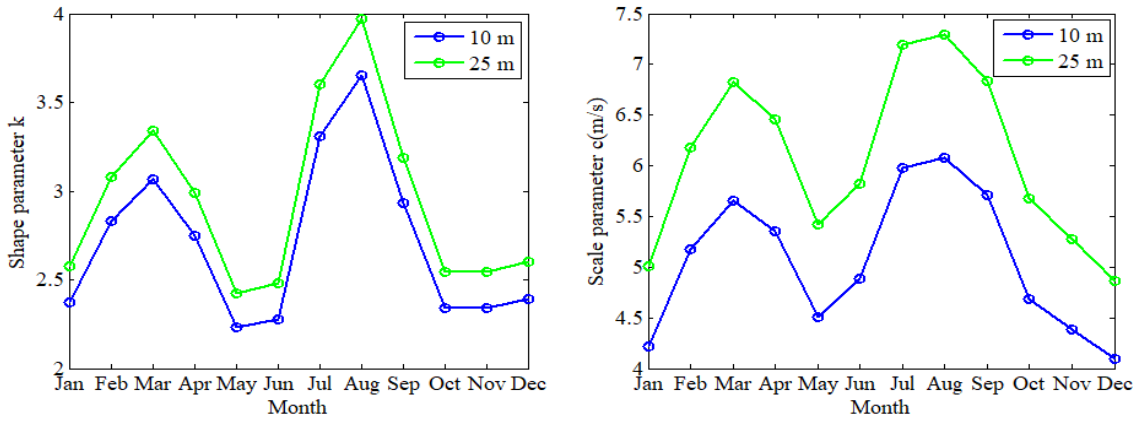

Figure 3. Monthly variation of Weibull parameters at 10 m from the ground (1981-2014)

We note that both Weibull parameters show seasonal variation. The shape parameter k varies from 2.23 (May) to 3.65 (August) at 10 m and from 2.3 (May) to 3.98 (August) at 25 m. As for the scale parameter c, it varies from 4.10 m/s (December) to 6.08 m/s (August) at 10 m and 4.75 m/s (December) to 7.30 m/s (August). The highest values of k are observed during the windiest months while the lowest are obtained during the least windy months. These results are in agreement with the work of Donnou et al [2] who used wind data at a smaller time scale (every 10min) in the same study area.

Speed giving the maximum energy

Figure 4 shows the monthly variation of the wind speed giving the maximum energy at altitudes of 10 and 25 m above ground.

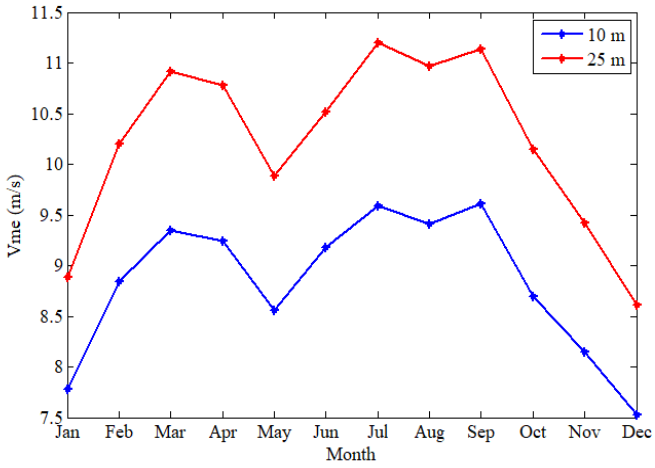

Figure 4. Variation of the wind speed giving the maximum energy as a function of the altitude (1981-2014)

The wind speed giving the maximum energy varies from 7.53 m/s (December) to 9.60 m/s (September) at 10 m and from 8.61 m/s (December) to 11.19 m/s (July) at 25 m. Referring to the studies of Adaramola et al [36], the wind speed carrying the maximum energy were evaluated at the coastal sites of Adafoah, Anloga, Aplaku, Mankoadze, Oshiyie and Warabeba in Ghana and are respectively estimated at 8.46 $m.s^{-1}$, 7.18 $m.s^{-1}$, 6.81 $m.s^{-1}$, 6.82 $m.s^{-1}$, 5.79 $m.s^{-1}$ and 6.5 $m.s^{-1}$ at 12 m. These values obtained are close to those obtained at our site at 10 m from the ground, notably at Adafoah and Anloga.

Variation of the Weibull distribution

The variation of the Weibull probability function at 10 m and then at 25 m from the ground is shown in Figure 5.

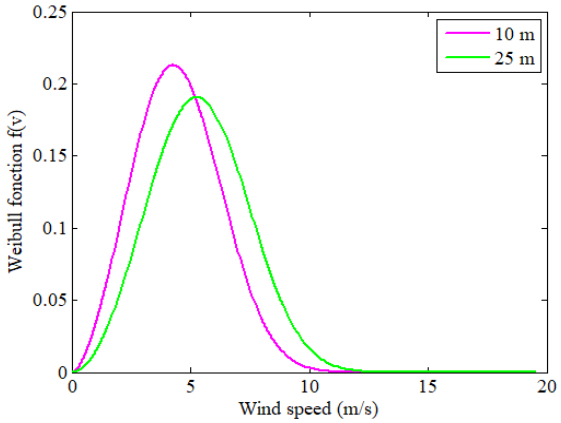

Figure 5. Annual frequency distribution of wind speeds from Weibull model (1981-2014)

Analysis of Figure 5 indicates that the most frequent wind speed at the study site is estimatedto be 4 m/s at 10 m. A large proportion of the winds above 10% are between 2 m/s and 7 m/s. Wind speeds above 10 m/s have a frequency of occurrence of less than 1%. At 25 m, the most frequent wind speed is 5 m/s. Wind speeds above 12 m/s have a frequency of less than 1%. Wind speeds between 3 and 8 m/s have a frequency of occurrence of more than 10%. We also notice that the most frequent speeds on the site are different from those that carry the maximum energy. These results are confirmed by the work of d'Adaramola et al [36] who obtained on the coastal sites of Adafoah, Anloga, Aplaku, Mankoadze, Oshiyie and Warabeba in Ghana frequent velocities of 4.23 m. s^{-1}, 3.59 m. s^{-1}, 4.34 m. s^{-1}, 3.88 m. s^{-1}, 3.39 m. s^{-1} and 3.07 m. s^{-1} at 12 m from the ground, which are different from the maximum energy speeds obtained at the same sites. The values of the most frequent wind speed observed on the Beninese coast were then compared to those recorded on some coastal sites of the West African sub-region. Thus, in analyzing the work of Udo et al [37] who investigated the wind energy potential of four coastal sites in Nigeria, the authors observed that the most frequent wind speed expected in Calabar, Uyo, Warri and Ikeja is about 3m/s, 4.5m/s, 3.5m/s and 5 m/s. Similarly, in the work of Youm et al [38], the authors evaluated the wind potential on the northern coast of Senegal along the Atlantic Ocean, particularly at the sites of Mboro, Ndandekhou, Pékesse, Pôtou and Makhana. The observed frequencies increase steadily, reaching a maximum value of wind speed of 4 m/s especially at the sites of Pôtou, Mboro and Makhana which are near the coast and where sea breezes can influence the wind regime. It can be seen that these values obtained on these Nigerian and Senegalese coastal sites at 10 m above ground level are close to those observed in Cotonou.

Characteristics of the micro wind power plant

Energy balance of the Ahouandji locality

Figure 6 presents the results of the socio-economic survey. Thirteen households represent the sample surveyed at the site out of a total of 195 households in the village. The energy and power balance for this sample of households is presented in Figure 6.

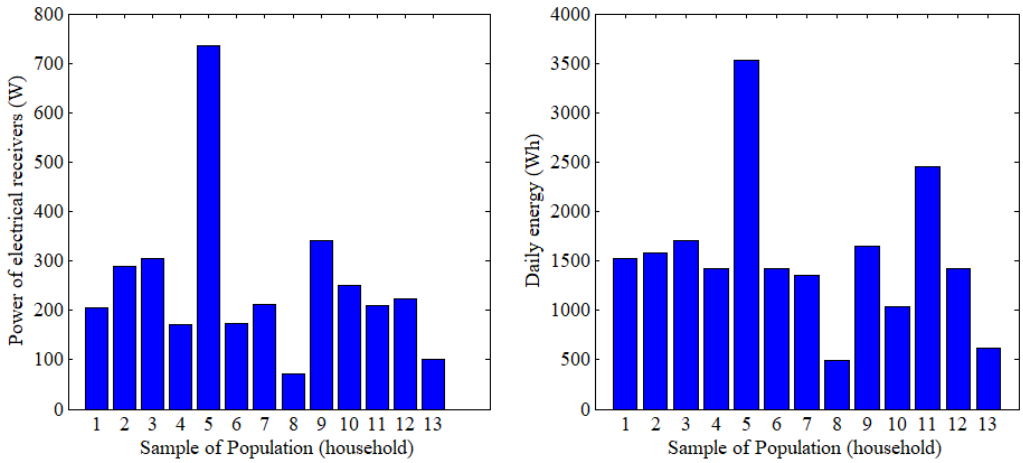

Figure 6. Energy balance by household sample

It can be seen that the energy requirements vary from one household to another. The total power of the receivers varies from 71 W to 736 W and the average daily energy consumption from 616 Wh to 2456 Wh. The power and energy that would be consumed by all households in the Ahouandji locality is presented in Table 1. The total power of the load is estimated at 49,275 kW and the average daily energy consumption is 303,150 kWh.

Table 1. Average daily energy balance of the village

Total power (kW)	Average energy consumption (kWh)
49. 275	303.150

Selection of the micro wind power plant components

The characteristics of the electrical equipment of the micro wind power plant are summarized in Table 2. The size of the wind farm is at least 24.5 kW. The capacity of the battery bank is estimated at 15,790 Ah. The DC/AC converter has a power of at least 24.5 kW. The power of the inverter-charger is estimated to be 62.85 kW

Table 2. Essential characteristics of the micro wind power plant components

Designation	Quantity	Characteristics		
Wind turbine	03	Operating Parameters	Starting wind speed V_d (m/s)	2.5
			Nominal wind speed V_n (m/s)	6.8
			Wind speed at cut-off V_c (m/s)	16
		Generator	Type	Permanent magnet synchronous
			Nominal power Pn (kW)	9.9
		Blade	Number of blades	3
			Blade length (m)	6.6
			Surface swept by the propeller (m²)	136.7
Converter DC/AC three-phase	03		Nominal power Pn (kW)	10
			Maximum input voltage (V)	1000
			Rated voltage AC (V)	380-400

Inverter-Charger	06		Maximum AC input power (kW)	11.5
			Maximum charge and discharge current of the batteries (A)	51
Battery	120		Capacity (Ah)	3000
			Operating voltage (V)	2
Cable			Section (mm²)	6, 16 et 50
Device for protection	03		Three-phase differential circuit breaker (A)	60
	01		DC protection box	
	01		AC protection box	

Based on the power curve of the selected wind turbine (TN 535 from the manufacturer Tozzi Green), the monthly energy production of the micro wind power plant has been evaluated and presented in figure 7.

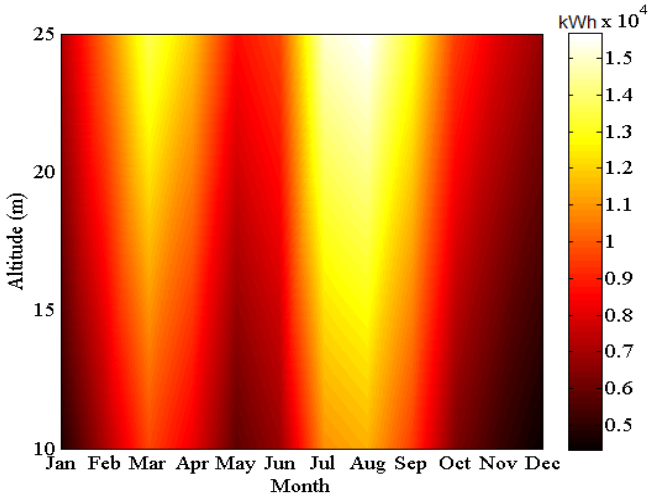

Figure 7. Monthly energy production of the micro wind power plant

It can be seen in Figure 7 that the energy production of the wind turbines varies from 4338 kWh to 11424 kWh at 10 m and from 6792 kWh to 15663 kWh at 25 m. The total annual energy production of the micropower plant is estimated at 129,528 kWh, or 355 kWh on average per day. This production largely covers the average daily consumption of the village estimated at 303.15 kWh.

Financial evaluation

Annual expenses

The annual expenses for the construction of this micro wind power plant are summarized in Table 3. The initial investment takes into account the components of the micro wind power plant, the construction of a technical platform, the accessories of the low voltage network and the public lighting.

Table 3. Annual expenses of the micro wind power plant

Designation	Initial investment (euro)	Maintenance and operating costs (3% of the investment)	Annuity (euro)	Overall discounted cost (euro)
Micro power plant	123779.30	3713.38	17272.47	20985.85

Project Sustainability

The result of the operation indicates that the cost price per kilowatt hour of electricity is 0.16 euro. For the operation of the plant, we have set the selling price of the kilowatt-hour at 0.17 euro for all social classes. This cost is quite competitive when compared to the tariff of the Société Béninoise d'Energie Electrique (SBEE) (0.19 euro/kWh), which is responsible for marketing energy in Benin. However, when comparing the cost per kilowatt hour obtained in this study to other costs observed in the literature by other authors on sites suitable for the installation of a wind power generation unit or plant, we note that the amounts vary according to the available potential, the size of the plant and the characteristics of the wind generators. Thus, by analyzing the work of Okeniyi et al [8] in Nigeria (Kaduna, Warri, Calabar), Ajayi et al [15] in Nigeria (Shaki and Iseyin in Oyo State), Gökçeka et al [16] in Turkey, Ahmed [17] in the East Red Sea coast of Egypt, Ajayi et al [18] in the southwestern region of Nigeria, Kassem et al [20] in two northern regions of Nigeria, and Kassem, et al [20] in the northwestern region of Nigeria. [22] in two regions of northern Cyprus, Gaddada and Kodicherla [21] in the Tigray region of Ethiopia, it is noted that the price of the kilowatt-hour has been evaluated respectively at (0.0.0507, 0.0774, 0.0819) euro; (0.025, 0.049) euro; (0.0537 to 0.119); (0.013) euro; (0.02 to 5.03) euro, (0.023, 0.04) euro; (0.000093 to 6.21) euro. These different costs are mostly much lower than the cost obtained in this study. These differences would therefore be due to the fact that the sites do not have the same meteorological characteristics. Moreover, in the present study, except for the investment costs of the micro power plant, the costs related to the construction of a low voltage distribution network of the produced energy were taken into account in the calculation of the cost price of the kilowatt-hour contrary to the works met in the literature. The amortization time of the invested capital for the project was estimated at 06 years 184 days.

Conclusion

The characteristics of the components of a micro wind power plant were determined in the present study in order to supplying electrical energy to the populations of the locality of Ahouandji on the coast of Benin. Based on the statistical study of wind speeds recorded on this site and the socio-economic study of the population, the size of the micro wind power plant was sized. From the annual expenses generated by the construction, operation and maintenance of the plant, the price per kWh of electrical energy was estimated in order to assess the profitability of the project. The main results of this study are as follows:

(1) The mean annual wind speed is estimated at 4.51 m/s at 10 m and 5.41 m/s at 25 m. The Weibull parameters (shape parameter k) vary from 2.23 to 3.97 and the scale parameter from 4.10 m/s to 7.29 m/s between 10 and 25 m from the ground. The mostfrequent velocity on the study site is 4 m/s at 10 m and 5 m/s at 25 m from the ground.
The speed giving the maximum energy varies from 7.53 m/s to 11.19 m/s between 10 and 25 m.

(2) The micro power plant is composed of 03 wind generators with a respective power of 9.9 kW, 03 three-phase DC/AC converters of 10 kW each, 06 inverter-chargers with a respective power of 11.5 kW, 120 batteries of 3000Ah/2V, DC and AC protection boxes
and 03 three-phase differential circuit breakers of 60A.

(3) The annual energy production of the plant has been estimated at 129,528 kwh and fully
covers the village's loads.

(4) The price per kilowatt hour of electricity is estimated at 0.17 euro and is quite competitive.

Based on these results, the installation of this micro power plant will be an asset for the locality of Ahouandji.

References

[1] Soulouknga MH, Oyedepo SO, Doka SY, Kofane TC. Assessment of Wind Energy Potential in the Sudanese Zone in Chad. *Energy and Power Engineering*. 2017;09(07):386-402. https://doi.org/10.4236/epe.2017.97026

[2] Donnou H, Akpo A, Nonfodji G, Kounouhewa B. Variability of Onshore Wind Energy Potential in the 60 m above the Ground under Convective Atmosphere in Southern Benin. *American Journal of Energy Research*. 2019 July;7(1):19-30. https://doi.org/DOI:10.12691/ajer-7-1-3

[3] Shawon M, El Chaar L, Lamont L. Overview of wind energy and its cost in the Middle East. *Sustainable Energy Technologies and Assessments*. 2013 06;2:1-11. https://doi.org/10.1016/j.seta.2013.01.002

[4] Qolipour M, Mostafaeipour A, Rezaei M. A mathematical model for simultaneous optimization of renewable electricity price and construction of new wind power plants (case study: Kermanshah). *International Journal of Energy and Environmental Engineering*. 2017 Nov 29;9(1):71-80. https://doi.org/10.1007/s40095-017-0254-4

[5] Wind Power Monthly. https://www.windpowermonthly.com/10- biggest-turbines. Accessed 2017 December 15.

[6] Global Wind Energy Council. http://gwec.net/wp content/uploads/2018/02/Global_Cumulative_Installed_Wind_Capacity_2001-2017.jpg. Accessed 2017 December 15.

[7] Global Wind Report 2018. www.gwec.ne. Accessed 2019 April.

[8] Okeniyi JO, Ohunakin OS, Okeniyi ET. Assessments of Wind-Energy Potential in Selected Sites from Three Geopolitical Zones in Nigeria: Implications for Renewable/Sustainable Rural Electrification. *The Scientific World Journal*. 2015;2015:1-13. https://doi.org/10.1155/2015/581679

[9] Donnou HEV, Boro D, Abode D, Capo-Chichi B, Akpo AB. Design of Vertical Axis Wind Turbine Darrieus Type (H- Darrieus Rotor) of 0.20 KW from the Software Topsolid. *Physical Science International Journal*. 2020 Dec 31;:52-70. https://doi.org/10.9734/psij/2020/v24i1130227

[10] Awanou CN, Degbey JM, Ahlonsou E. Estimation of the mean wind energy available in Benin (Ex Dahomey). *Renewable Energy*. 1991 01;1(5-6):845-853. https://doi.org/10.1016/0960-1481(91)90037-p

[11] Houekpoheha M, Kounouhewa B, Tokpohozin B, Awanou C. Estimationde la puissance énergétique éolienne à partir de la distribution de weibull sur la côte béninoise de Cotonou dans le golfe de guinée. *Revue des Energies Renouvelables*. 2014 September;13(3):489-495.

[12] Akpo A, Damada J, Donnou H, Kounouhewa B, Awanou C. Estimation de la production énergétique d’un aérogénérateur sur un site isolé dans la région côtière du Bénin. *Revue des Energies Renouvelables*.18(3):457-468.

[13] Salami AA, Ajavon ASA, Kodjo MK, Bedja K. Evaluation of wind potential for an optimum choice of wind turbine generator on the sites of Lomé, Accra, and Cotonou located in the gulf of Guinea. *International Journal of Renewable Energy Development*. 2016 Nov 04;5(3):211-223. https://doi.org/10.14710/ijred.5.3.211-223

[14] Abdelhady S, Borello D, Santori S. Economic Feasibility of Small Wind Turbines for Domestic Consumers in Egypt Based on the New Feed-in Tariff. *Energy Procedia*. 2015 08;75:664-670. https://doi.org/10.1016/j.egypro.2015.07.482

[15] Ajayi O, Fagbenle O, Katende J. Assessment of Wind Power Potential and Wind Electricity Generation Using WECS of Two Sites in South West, Nigeria. *International Journal of Energy Science*. 2011 January;1(2):78-92.

[16] Gölçek M, Erdem HH, Bayülken A. A Techno-Economical Evaluation for Installation of Suitable Wind Energy Plants in Western Marmara, Turkey. *Energy Exploration & Exploitation*. 2007 Dec;25(6):407-427. https://doi.org/10.1260/014459807783791791

[17] Ahmed AS. Wind energy as a potential generation source at Ras Benas, Egypt. *Renewable and Sustainable Energy Reviews*. 2010 Oct;14(8):2167-2173. https://doi.org/10.1016/j.rser.2010.03.006

[18] Ajayi O, Fagbenle R, Katende J, Ndambuki J, Omole D, Badejo A. Wind Energy Study and Energy Cost of Wind Electricity Generation in Nigeria: Past and Recent Results and a Case Study for South West Nigeria. *Energies*. 2014 Dec 22;7(12):8508-8534. https://doi.org/10.3390/en7128508

[19] Faida H, Saadi J, Khaider M, El Alami S, Monkade M. Etude et Analyse des Données du vent en Vue de Dimensionner un Système de Production d’Energie Eolienne: Cas d’un Site au Nord du Maroc. *Revue des Energies Renouvelables*. 2010 June;13(3):477-483.

[20] Kassem Y, Gökçekuş H, Çamur H. Economic assessment of renewable power generation based on wind speed and solar radiation in urban regions. *Global Journal of Environmental Science and Management*. 2018 Oct;4(4). https://doi.org/10.22034/gjesm.2018.04.007

[21] Gaddada S, Kodicherla SPK. Wind energy potential and cost estimation of wind energy conversion systems (WECSs) for electricity generation in the eight selected locations of Tigray region (Ethiopia). *Renewables: Wind, Water, and Solar*. 2016 03 17;3(1). https://doi.org/10.1186/s40807-016-0030-8

[22] Bagiorgas H, Assimakopoulos M, Theoharopoulos D, Matthopoulos D, Mihalakakou G. Electricity generation using wind energy conversion systems in the area of Western Greece. *Energy Conversion and Management*. 2007 05;48(5):1640-1655. https://doi.org/10.1016/j.enconman.2006.11.009

[23] Hounguè GH, Kounouhéwa BB, Tokpohozin BN, Houékpohéha MA, Madogni VI, Almar R. Wave Energy Impact on Benin’s Coastline Dynamics, Gulf of Guinea. *Current Journal of Applied Science and Technology*. 2018 Nov 13;30(4):1-12. https://doi.org/10.9734/cjast/2018/44341

[24] *Cahier des villages et quartiers de ville du département de l’Atlantique, Bénin*. INSAE; 2016.

[25] Donnou HEV, Akpo AB, Kouchadé CA, Kounouhewa BB, Hounguè GH, Nonfodji GF, Djossou J. Vertical Profile of Wind Diurnal Cycle in the Surface Boundary Layer over the Coast of Cotonou, Benin, under a Convective Atmosphere. *Advances in Meteorology*. 2019 04 01;2019:1-18. https://doi.org/10.1155/2019/7530828

[26] Akinsanola A, Ogunjobi K, Abolude A, Sarris S, Ladipo K. Assessment of Wind Energy Potential for Small Communities in South-South Nigeria: Case Study of Koluama, Bayelsa State. *J Fundam Renewable Energy Appl*. 2017 February;7(2):1-6. https://doi.org/10.4172/20904541.1000227

[27] Fadare A. A statistical analysis of wind energy potential in Ibadan, Nigeria, based on Weibull distribution function. *Pac J Sci Technol*. 2008;9(1):110-119.

[28] Koukpémédji A. Sur le potentiel énergétique éolien en milieu tropical: Cas du Bénin. Porto Novo, Bénin: Université d’Abomey-Calavi, Institut de Mathématiques et de Sciences de Physiques; 2015.

[29] Weisser D. A wind energy analysis of Grenada: an estimation using the ‘Weibull’ density function. *Renewable Energy*. 2003 09;28(11):1803-1812. https://doi.org/10.1016/s0960-1481(03)00016-8

[30] Merzouk N, Merzouk M. Estimation du Potentiel Energétique Eolien Utilisable Application au Pompage dans les Hauts Plateaux. *Revue des Energies Renouvelables*. 2006 January;9(3):155-163.

[31] Gnandji M, Fifatin F, Dubas F, Espanet C, Vianou A. *Etude du Potentiel Energétique Eolien Offshore du Bénin*. Cotonou, Benin: Colloque International Francophone portant sur l’Energétique et la Mécanique; 2018 November.

[32] Newman J, Klein P. The Impacts of Atmospheric Stability on the Accuracy of Wind Speed Extrapolation Methods. *Resources*. 2014 01 23;3(1):81-105. https://doi.org/10.3390/resources3010081

[33] Gualtieri G. Atmospheric stability varying wind shear coefficients to improve wind resource extrapolation: A temporal analysis. *Renewable Energy*. 2016 03;87:376-390. https://doi.org/10.1016/j.renene.2015.10.034

[34] Okorie ME, Inambao F, Chiguvare Z. Evaluation of Wind Shear Coefficients, Surface Roughness and Energy Yields over Inland Locations in Namibia. *Procedia Manufacturing*. 2017;7:630-638. https://doi.org/10.1016/j.promfg.2016.12.094

[35] Morel Aolo S. Etude de l’électrification décentralisée par une microcentrale solaire photovoltaïque: cas de la localité de Koutè, commune de Ségbana. Abomey-Calavi, Bénin: Energies Renouvelables et Systèmes Energétiques, Université d’Abomey-Calavi; 2014.

[36] Adaramola MS, Agelin-Chaab M, Paul SS. Assessment of wind power generation along the coast of Ghana. *Energy Conversion and Management*. 2014 01;77:61-69. https://doi.org/10.1016/j.enconman.2013.09.005

[37] Udo N, Oluleye A, Ishola K. Investigation of Wind Power Potential over Some Selected Coastal Cities in Nigeria. *Innovative Energy & Research*. 2017;06(01). https://doi.org/10.4172/2576-1463.1000156

2nd German-West African Conference on Sustainable, Renewable Energy Systems SusRES – Kara 2021

Photovoltaic

https://doi.org/10.52825/thwildauensp.v1i.5

Published: 15 June 2021

Bi-facial Open-Space Photovoltaic Systems versus Conventional Systems using Mono-facial Modules

A Technical and Economic Comparison

Marcus Schmidt[1,2], Martin Hinneburg[2], Lutz B. Giese[3]

[1] Technische Hochschule Wildau (Graduate), Germany

2 SUNfarming GmbH Erkner, Germany

3 Technische Hochschule Wildau, Germany

Abstract: As part of a scientific work within the solar company Sunfarming GmbH, the aim was to find out whether bi-facial modules on open spaces deliver better results economically than conventional mono-facial solar modules. In this context, an already installed 750 kW_p PV system with mono-facial solar modules was compared directly with a structurally identical PV system with bi-facial modules, which, however, does not exist in practice but was only simulated with PV software. The second part of the investigation includes the comparison of four different assembly systems or elevation variants in order to determine the system with the best relationship between system yield and costs.

The final result of the first investigation showed that the use of bi-facial modules reduced the specific costs per kWh by approximately 5 %. In order to improve this effect, the use of compact assembly systems is recommended, e.g. five rows of modules per table with horizontal alignment.

Keywords: Bi-facial photovoltaics, open-space PV systems, Renewable Energy Sources

Introduction

For many years, photovoltaics have been one of the most important players in renewable power generation in Germany. The PV modules have been optimized in terms of production and quality, especially in the last 10 years, which at the same time increased customer demands, prices have fallen and the degree of efficiency depending on the design has already reached over 20 %. With the aim of placing as much power as possible in a small area, the trend of bi-facial modules developed on the market in 2018/2019. The technology is able to convert solar radiation into electrical energy on both the front and rear of the module. According to the suppliers and manufacturers, additional energy yields of 5-30 % compared to mono-facial modules are possible depending on the orientation, inclination and shading [1].

In this context, the question arises to what extent the bi-facial standard modules compare to mono-facial modules in terms of additional power and whether these can generally replace the conventional modules in open spaces. For this consideration, the actual costs and energy yields of a current open-space system were examined and compared with the costs and yields of a simulated system with bi-facial modules.

PV Open Space Systems

A ground-mounted PV system basically consists of the following main components:

- Mounting system / substructure
- Solar modules
- Generator connection boxes
- Inverter
- Transformer and transfer station

Figure 1. PV system with bi-facial modules.

The **mounting system** is used to hold and align modules (Figure 1). The modules are inclined to a certain angle (15°-30°) with the aid of the frames, while this is already guaranteed by the roof inclination in roof systems. The more module rows a table has, the lower the inclination must be selected in order to minimize the effect of wind loads. The mounting system is one of the most important factors influencing the effectiveness of the PV system [2].

A conventional mono-facial **solar module** usually consists of several crystalline solar cells with silicon as the starting material. The solar cells form the heart of a PV system, as the actual photovoltaic effect takes place in these or convert the energy of the photons into electricity. In practice, mainly polycrystalline (light blue appearance) and monocrystalline (dark blue appearance) are used, which differ only in terms of the type of production and the degree of efficiency. While polycrystalline solar modules have an efficiency of 13-17 %, monocrystalline modules can have an efficiency of more than 20 %, but this is associated with higher costs. In a PV system, the solar modules are connected in series, creating so-called strings that are then led to the generator junction box [3].

The nominal output of a solar module is specified in kilowatt-peak (kW_p) and indicates the maximum output of the module, which is also optimized with half-cell technology (Figure 2). If the cells are halved after production, the peak performance can be improved by 2-3 % according to the Fraunhofer Institute for Solar Energy Systems, since the electrical resistance and thus the energy losses are reduced within the cell connectors [4].

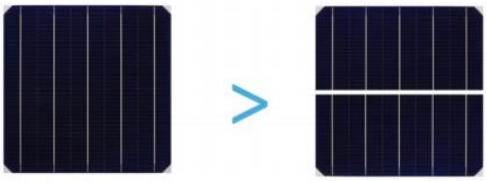

Figure 2. Half-cell technology [4].

The **generator junction boxes** have the task of bringing the individual solar cables or strings together and, if necessary, of separating the load from the rest of the system by means of a switch disconnector (e.g. for maintenance work). By merging the strings, cable runs and costs can be saved [2].

The solar generator generates direct current and can therefore not feed into the power grid with alternating current. Therefore, all PV modules must be connected to one or more inverters depending on the generator power. This converts the direct current (DC) into alternating current (AC). In addition to the conversion, the inverters also perform the following tasks [3]:

- Performance optimization
- Plant monitoring
- Power feed-in

Performance optimization: The inverter detects the point of maximum power (MPP = Maximum Power Point) per module string. This point is different at any time depending on the irradiance, shading and module temperature, which is why the MPP is constantly searched for and tracked (MPP tracking) [5].

Plant monitoring: Thanks to the independent operation, inverters can switch to stand-by mode when the voltage is too low in order to save energy and switch on again when there is sufficient incidence of light. They can also automatically disconnect themselves from the network in the event of network faults or failures using a disconnection device. With the help of a communication interface, the inverters and thus the yields of the PV system can be remotely monitored at any time, e.g. to quickly identify any loss of yield [6].

Power feed-in: After a successful conversion, the electricity is fed into the corresponding electricity network. While this process takes place in small PV systems (e.g. 5 kW_p) via the house connection with 230 V, larger systems (e.g. 750 kW_p open-space systems) feed into the medium-voltage network between 1 kV and 35 kV via the transformer or the transfer station [2].

The **transformer** is connected to the PV generator via the inverter and transforms the output voltage of the inverter to the required medium-voltage level. In addition, with the help of a switchgear within the station, it is possible to disconnect the transformer from the power grid [2].

However, the energy from the PV system is fed into the public grid with the help of the transfer station. This also takes over the counting of the energy generated by the generator and at the same time forms the property boundary of the PV operator and the responsible network operator [7].

Bi-facial Modules PV Open Space System

In contrast to the mono-facial cell, the bi-facial solar cell can convert the solar radiation on the front as well as on the back into electricity. However, these are not two separate areas, but simply the same item. The bi-facial PERC cell (PERC = Passivated Emitter Rear Cell) is characterized by its dielectric layer (dielectric = non-conductive). The illustration in Figure 3 shows both a conventional solar cell and a PERC cell. The standard cell (left) has a full-surface aluminum metallization on the back, which serves as a conductive contact for the cell. The PERC technology, on the other hand, involves the creation of a dielectric layer that has several small holes with the help of a laser. This means that the silicon wafers only have contact with the aluminum metallization through the tiny holes [1].

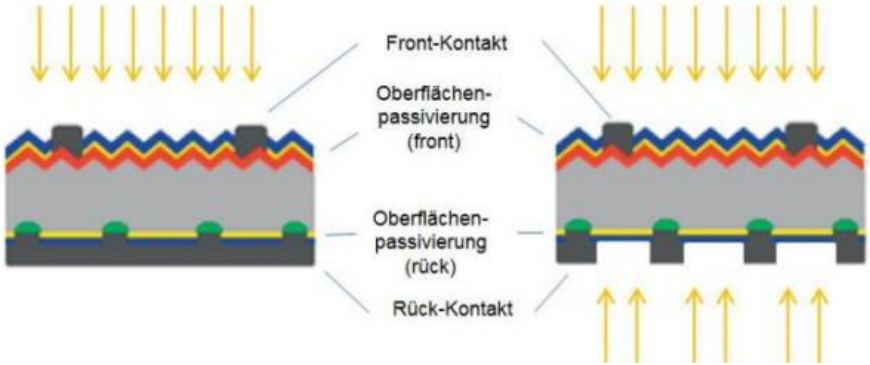

Figure 3. PERC cell technology [8] (in German).

By modifying the back of the cell, the radiation can also be received from the back. In order to fulfill this function, there must also be a transparent back [8].

The back is not symmetrical with the front and for this reason can only partially absorb the radiation as efficiently. The ratio between back and front performance is called the bi-facial factor and is approximately 70 % under standard test conditions [1].

In addition, there are the following influencing factors that influence the rear side yield of bi-facial modules:

The **reflection factor** (albedo) is a percentage of the reflection radiation that hits the back of the module and depends on the color and nature of the surface. While light colors have an albedo value of approximately 60-90 % (e.g. snow), grass, for example, guarantees a value of approximately 23 % [1].

The higher the **angle of installation**, the more diffuse radiation can reach the rear, and the same applies to the installation height of the module tables [1].

The **row spacing between the module tables** also has an influence on the radiation behind the modules. At short distances, the horizon is narrowed down, so that the diffuse radiation decreases. Self-shading can also occur at low positions in the sun if a module table is too close to the rear one [1].

The last influencing factor is the shading from the solar cables and the mounting system. The profiles of the mounting system should therefore not cover the rear of the bi-facial modules [1].

Economics of Bi-facial PV Systems

Economic Comparison of Two 750 kW_p PV Systems

A 750 kW_p PV system that had already been built by SUNfarming GmbH was used as the basis for the investigation, and its investment costs were compared with the annual energy yields in order to calculate the specific costs in €/ kWh. In the study, these specific costs should represent a measure of the profitability of a PV system.

With the help of the simulation software PV-Sol, it was then possible to simulate the same PV system with the same technical configurations that instead contains bi-facial solar modules. For the simulation system, the theoretical investment costs and yield data were also put in relation and the specific costs were calculated. According to the comparison, the specific costs when using bi-facial modules decreased by 3.17 %. However, it should be noted here that it is not certain whether the simulation software can calculate the actually possible energy yield through the rear. An additional energy yield of approximately 5 % was output in the simulation, which can therefore differ slightly from reality.

Economic Comparison of Different System Concepts

In the second part of the investigation, the standard assembly system used was compared economically with four other elevation concepts. An area of approximately 4 hectares was used as the basis, which was covered by the concepts below in full simulation.

The fundamental data set of the installation concepts and their technical configuration is shown in Table 1.

Table 1. Comparison of the system concepts [own illustration].

Concepts/ Reference	Concept 1	Concept 2	Reference	Concept 3	Concept 4
Orientation of modules	Vertical	Horizontal	horizontal	horizontal	horizontal
Module rows per table	2	3	4	5	6
Installation angle	30°	30°	25°	20°	15°
Elevation (in m)	0.6	0.6	0.6	0.6	0.6
Row spacing (in m)	3	3	3	3	3

In Figure 4 sketches of the configurations can be seen.

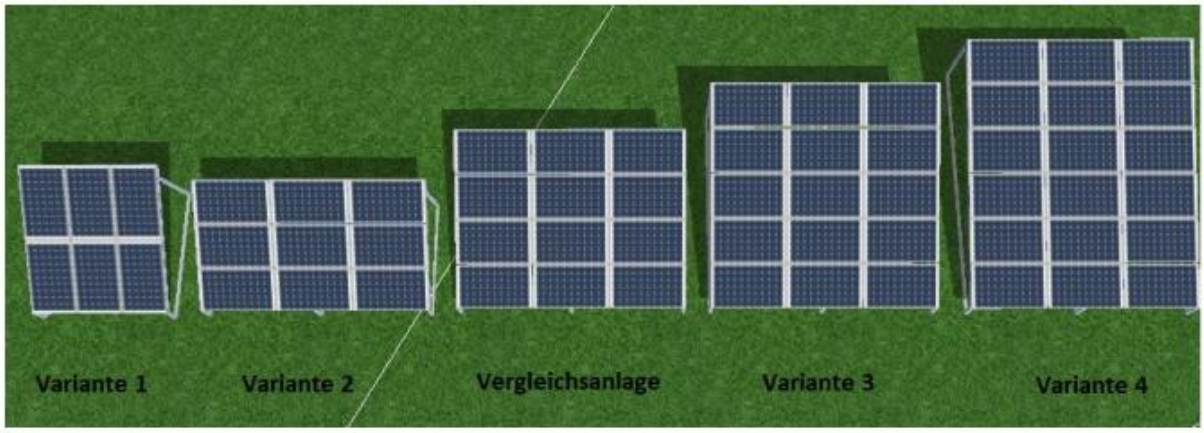

Figure 4. System concepts 1 to 4 and reference [own illustration; in German].

During the simulations of the individual concepts, it turns out that the space utilization increases with the size of the module tables and that, despite the lower elevation angle, a higher energy yield is possible with concepts 3 and 4. At the same time, however, the possible reverse side yield decreases by up to 4 % compared to concept 1.

Following the same procedure as mentioned above, where the investment costs and energy yields are used to calculate the specific costs, the end result shows that the specific costs of the first two variants are slightly more than for the comparison system.
Variants 3 and 4, on the other hand, have lower specific costs. Of the four different concepts, variant 4, with an optimization of 0.84 % compared to the reference system, at least in theory, represents the most economical PV system.

In the investigations, the bi-facial modules turned out to be the more economical variant for elevated PV ground-mounted systems. The additional yield of the bi-facial modules is high enough in the simulations to compensate for the additional costs and to achieve a positive benefit. Since it was not possible to determine whether the simulation software can realistically calculate the additional yield from bi-facial modules, it is nevertheless advisable to carry out a precise yield report in order to achieve a final result.

Conclusions

The bi-facial modules have not yet fully achieved the market breakthrough, but due to the ever increasing demands on solar modules, the trend is likely to continue to rise until the bi-facial modules may have replaced the mono-facial modules for the most part on the market. Here, however, one can only assume speculation.

The increase in yield can be of great advantage, especially in regions such as in the African area, as the solar radiation is about twice as high as in the European area, whereby the profitability could probably be optimized again.

In addition to the pure increase in yield, the transparency and the longer shelf life due to the glass-glass construction speak for the use of bi-facial solar modules, as this opens up completely new applications for photovoltaics, in which conventional mono-facial modules could not be used efficiently. At the moment, the modules are mainly used as roof-integrated in greenhouses, in order to serve as both a power generator and a roof at the same time. The modules are also suitable for multi-purpose use for facades, balconies, noise barriers and carports. In addition, they can also be erected on flat roofs with the lightest possible foil as a substrate in order to increase the albedo value. In this case, the high reflection factor could achieve an additional energy yield on the back that clearly exceeds 5 %. For this reason, it is advantageous to examine the economic viability of bi-facial modules in other areas of application and to test them in practice.

References

[1] Frontini F, Caccivio M, Renken C. *Anwendung von bifazialen Solarmodulen – Einsatzmöglichkeiten an Gebäuden, Dimensionierung der Anlagenkomponenten*. EnergieSchweiz; 2019 August.

[2] Sperling P. Masterarbeit - Ertrags- und Kostenoptimierung von PVFreiflächenanlagen. 2016.

[3] Antony F, Dürschner C, Remmers KH. *Photovoltaik für Profis: Verkauf, Planung und Montage von Solarstromanlagen*. 2. vollständ. überarb. Edition. Solarpraxis; 2009.

[4] Alpha Solar & Heizungstechnik GmbH. Halbzellenmodule – Der neue Trend bei den Modulherstellern 2019. http://docplayer.org/129827504- Halbzellenmodule-der-neue-trend-bei-den-modulherstellern-2019.html. Accessed 2020 December 17.

[5] ET-SYSTEM. MPP-Tracking. https://www.etsystem.de/fileadmin/user_upload/Applikationen_Sondergeraete/MPP-Tracking_HPSMP_de.pdf. Accessed 2020 December 17.

[6] SMA Solar Technology AG. Wechselrichter: Leistungselektronik für eine saubere Energieversorgung. https://www.sma.de/partner/expertenwissen/wechselrichter-leistungselektronikfuer-eine-saubere-energieversorgung.html

[7] Solibra System Montage Gmbh. Baubeschreibung für den geplanten Bau einer Photovoltaik-Freiflächenanlage auf der ehemaligen Kasernenanlage in Zerbst. *http://docplayer.org/62688876-Baubeschreibung-fuer-den-geplanten-bau-einer-photovoltaik-freiflaechenanlage-auf-der-ehemaligen-kasernenanlage-in-zerbst.html*. 2017;

[8] Kutzer M, Fülle A, Jahnke A, Becker J, Hahn H, Wendt S, Neuhaus D, Witzig A, Kunath L, Stöckli U. Ertragssteigerung durch bi-faciale Modultechnologie. *https://www.velasolaris.com/wpcontent/uploads/2018/12/solarworld_otti_beitrag_final_1.pdf*.

2nd German-West African Conference on Sustainable, Renewable Energy Systems SusRES – Kara 2021

Photovoltaic

https://doi.org/10.52825/thwildauensp.v1i.3

Published: 15 June 2021

Simulation study of perovskite cell performance in real conditions of sub-Saharan Africa

Essodossomondom Anate[1], N'Detigma Kata[1,2], Hodo-Abalo Samah[1], Amadou Seidou Maiga[2]

[1] Faculté des Sciences et Techniques, Université de Kara, Togo.

[2]Laboratoire Électronique, Informatique, Télécommunication et Énergies Renouvelables,

Saint-Louis, Sénégal

Abstract. Perovskite is certainly the material of the future of photovoltaics for terrestrial applications. With high efficiencies and advances in stability, perovskite solar cells, modules and mini-modules have already made their appearance in the laboratory and are being tested under real-world conditions to evaluate their real performance. In our study, we predict the performance of perovskite-based photovoltaic panel technology under the conditions of the Sub-Saharan African region by simulation. We started from the current-voltage characteristic of a real perovskite-based module to extract the cell parameters through MATLAB analysis software. These parameters were used to model a cell and then a module in the LTSpice XVII software for simulation. The impact of temperature is studied to evaluate the performance ratio (PR) of a clear day. This study allowed us to evaluate the PR of the perovskite solar module. Displaying PR reaching 90%, perovskite is a future candidate with high potential in the list of the most suitable technologies for our sub-region.

Keywords: PV module, perovskite, simulation, extraction, performance ratio.

Introduction

This study is situated in the context of forecasting photovoltaic production in real sub-Saharan conditions. The challenge is to evaluate the influence of climatic factors, in particular temperature, on the photovoltaic performance of a perovskite-based solar photovoltaic module. To ensure the effectiveness of this new technology of photovoltaic panels in the sub-region, it is important to estimate their production in real conditions compared to standard test conditions (STC; 25°C and AM1.5 G with 1000W/m^2).

Considered as the "black gold" [1] for photovoltaic cells, the perovskite-based cell reached in 2020 an efficiency of 25.5% [2] in laboratory. The ease of its synthesis, its low production cost and its integration to various substrates make this technology one of the most accessible to a wide range of users. The crucial issue is its industrialization. Perovskite degrades at temperatures above 40°C and is soluble in water [1]. Several studies on these two aspects have been done and are being actively pursued: the introduction of 2-methylbenzimidazole (MBIm) by C. Longeaud between the electron transport layer (ETL) SnO_2 and the perovskite layer as a passivating layer has improved the stability of the cell [3], S. Sonmezoglu et S. Akin showed that the introduction of Triethyl Citrate (TEC) between the perovskite and PCBM forming the PCBM/TEC retained up to 84% of the cell performance after 1000 hours of exposure without encapsulation [4]. The improvement of the strontium titanate ($SrTiO_3$) electron transport layer by M. Neophytou et al. also shows this [5] etc. At present, perovskite-based modules/mini-modules are available in laboratories with yields, for a small module, of 17.9% (*Panasonic*) in 2020 [2] [6]. The same company having reached in May 2019 an efficiency of 16.1% with a module of 55 cells [7]. All these very encouraging results show the progress made in terms of stability and efficiency. This technology is

eagerly awaited to prove itself in real-life conditions and will soon appear on the world market. In view of all this, it seems obvious to foresee the efficiency of the perovskite solar cell technology in real conditions in the Sub-Saharan African zone.

We study the impact of temperature on the performance and the performance ratio of the perovskite solar cell in the climatic conditions of Sub-Saharan Africa. The results are presented and discussed in this paper.

Methodology

Figure 1 presents the flow chart of the method adopted to conduct our study.

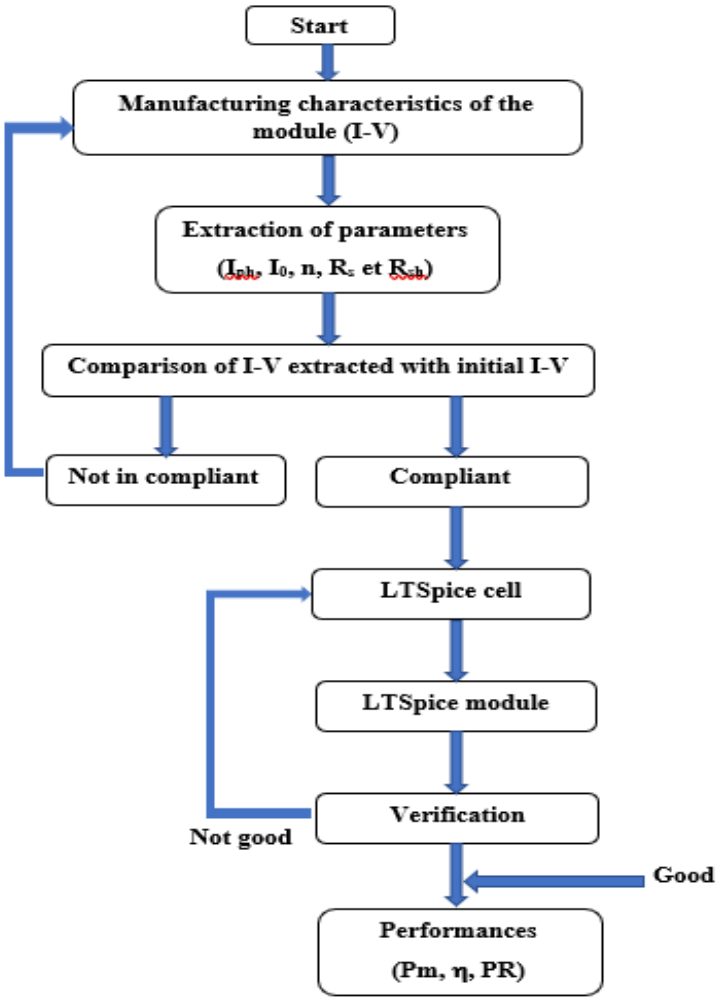

Figure 1. Organization chart of the study

From the current-voltage characteristic of the manufacturer Panasonic (Table 1.) [7], we extracted the data of the one-diode model with five parameters I_{ph}, I_0, n, R_s, and R_{sh}, respectively the photo-generated current, saturation current, ideality factor, series resistance and the parallel resistance to carry out our study. The hybrid Levenberg-Marquardt-analytical algorithm proposed by Kata et al. [8] is used to extract these parameters. This algorithm combines the analytical [9] and empirical method to calculate the initial values needed by the Levenberg-Marquardt algorithm making it not only fast and robust but also accurate as shown in [8].

Table 1. Manufacturing characteristics of the module

Open circuit voltage of the module (Voc)	57.3 V
Short circuit current (Isc)	321 mA
Module efficiency (η)	16.1 ± 0.5 %
Fill factor (FF)	70.3 %
Module area (S)	802 cm^2

At the end of the extraction the algorithm plots the I-V characteristic corresponding to the extracted data and compares it with the initial I-V characteristic. The algorithm resumes the extraction if there is no conformity of the new I-V characteristic with the initial one. In case of conformity, the data are collected to go to the next step.

This new step consists in modeling a photovoltaic cell in the LTSpice software. The algorithm at the beginning is adapted to the electrical model of the cell with one diode (figure 2.), it is thus this model which will be made in LTSpice, model which we call the "LTSpice cell". This model is shown in Figure 3. Using this model, the current delivered by the cell to a load is given by the equation (1).

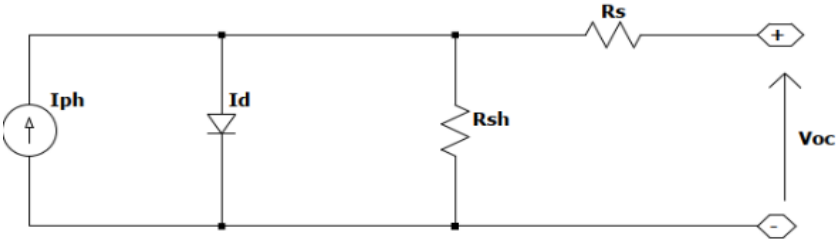

Figure 2. Electrical model equivalent to a diode of a solar cell

$$I = I_{ph} - I_0 \left[exp\left(q \frac{V_{Cell}+I_{Cell}R_s}{nk_BT}\right) - 1 \right] - \left(\frac{V_{Cell}+I_{Cell}R_s}{R_{sh}}\right) \quad (1)$$

Where I_{ph} is the photo-generated current, I_0 the saturation current, n the ideality factor, T the temperature of the cell, q the elementary charge (1,602 *10^{-19}C), V_{Cell} the voltage at the terminals of the cell and k_B the Boltzmann constant (1,38*10^{-23}J/°K).

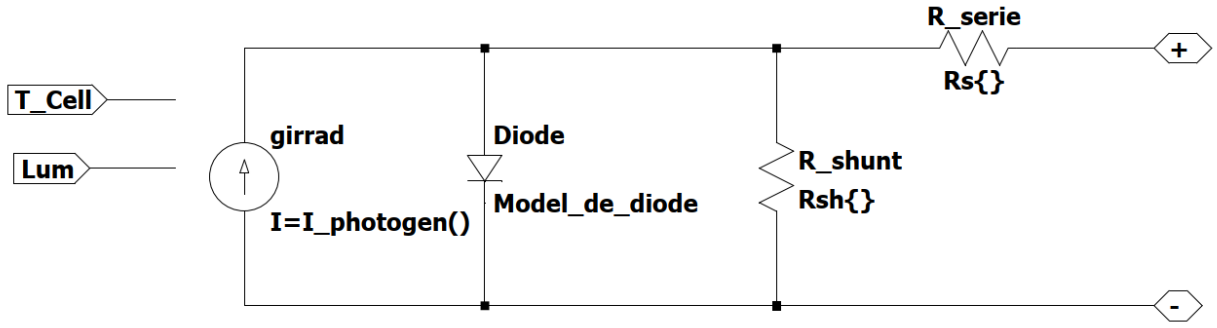

Figure 3. Behavioral model of a photovoltaic cell under LTSpice.

As the maximum power and the arrangement mode were not given, we obtained them (Table 2) by using the relation (2) for the maximum power and the relation (3) for the cell arrangement mode.

$$\eta_{STC} = {}^{p_m}/_{S_{Module*}} G_{STC} \quad (2)$$

$$\begin{cases} I_{ph} = N_p * I_{scCell} \\ V_{oc} = N_s * V_{ocCell} \end{cases} \quad (3)$$

Table 2. Module details

Maximum power (Pm)	12.9 W
Arrangement of the cells	Serial

The LTSpice cells are then connected in series to form an LTSpice module.

It is in this module that we introduce the temperature and irradiance measurements. The measurements are made during a clear day with a measurement time step of 5 minutes on which we assume that the measured value is a constant.

Results and discussion

The real performance ($\eta_{\text{réel}}$) of the LTSpice module is determined for each measurement of the day using equation (4). Like the yield, the performance ratio allows the comparison of performances between different technologies and also within the same technology with respect to the conditions in which they are installed. It is defined as the ratio between the real performance under real conditions and the performance under STC conditions (η_{STC}) in equation (5).

$$\eta_{\text{réel}} = \frac{P_{m\text{réel}}}{S * G_{\text{réel}}} \quad (4)$$

$$\text{PR} = \frac{\eta_{\text{réel}}}{\eta_{STC}} \quad (5)$$

Figure 4 shows the evolution of the performance ratio, temperature and irradiance as a function of time of day.

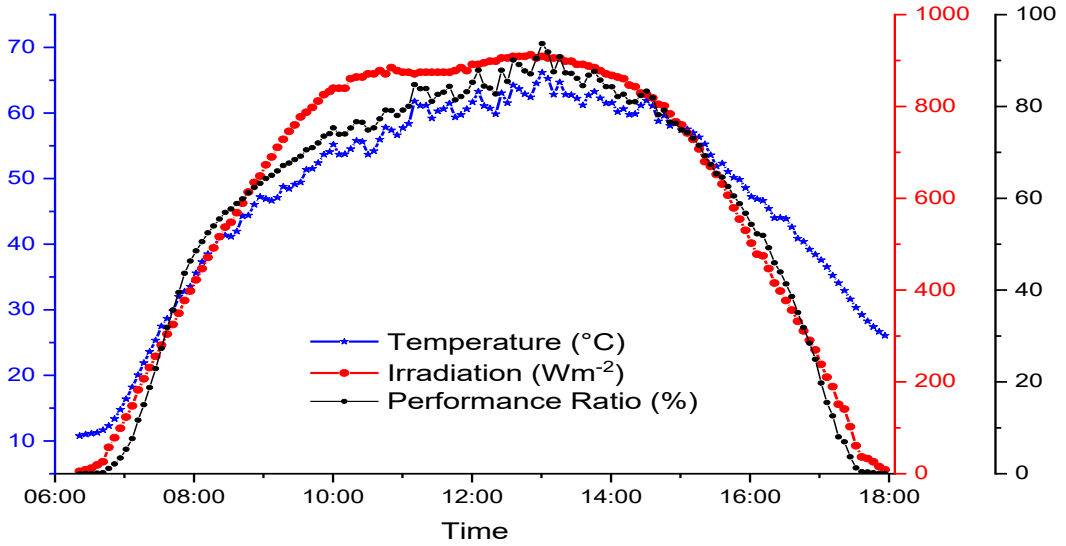

Figure 4. Evolution of the performance ratio during the day under clear sky

We can notice through the graph of figure 4 a performance ratio exceeding 70% between 10 am and 3 pm, period on which often appear high irradiation and high temperatures of the day. The highest PR is obtained at the highest temperature point of the day with of course an irradiation close to the maximum of the day. This means that the perovskite-based solar cell shows only a small decrease in efficiency with high temperature and thus agrees with the finding of Tress et al. in [10]. These results seem obvious when we know that perovskite is not very sensitive to temperatures above ambient [11]

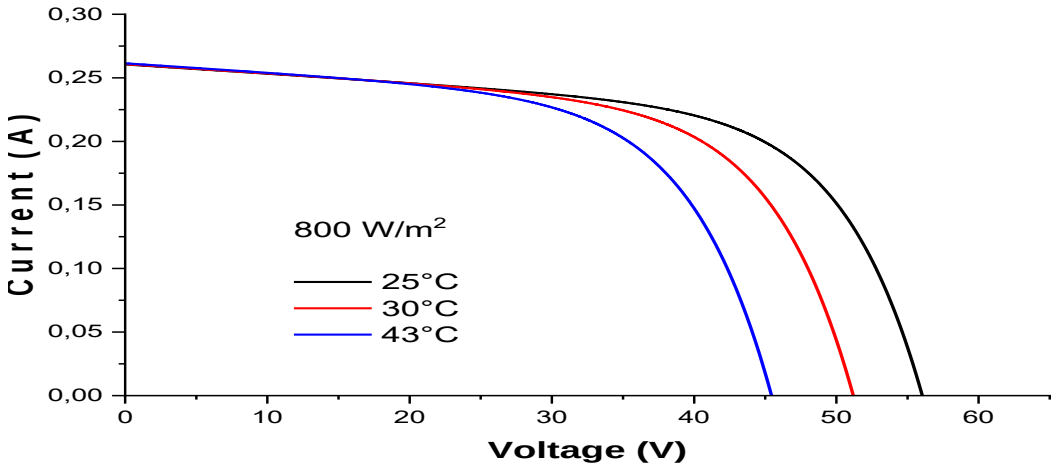

Figure 5. I-V curve showing the effect of temperature

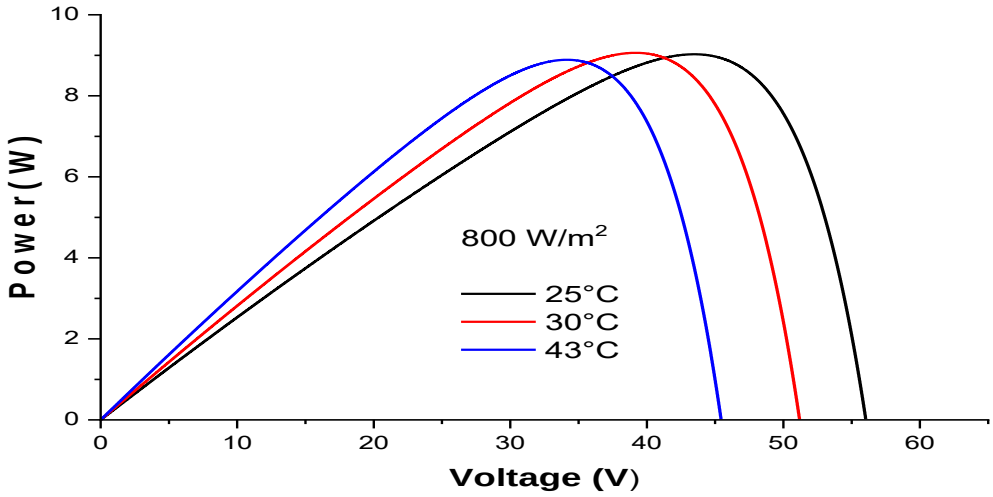

Figure 6. P-V curve showing the effect of temperature

We show here the effect of temperature on the voltage and also on the power. By fixing the irradiation we see that it is the voltage that is responsible for the decrease in performance when the temperature increases in the cell. The current remaining constant and a decreasing voltage leads to a decrease of the power according to equation (6).

$$P_m = V_m * I_m \quad (6)$$

As shown by J. A. Schwenzer et al., the voltage decreases with temperature. This is justified by a negative temperature coefficient of the voltage. [12] [13]

Conclusion

In this paper we have evaluated the performance of a perovskite based photovoltaic module in the climatic conditions of Sub-Saharan Africa by simulation. We used the Levenberg-Marquardt-analytical hybrid extraction method proposed by Kata et al. to retrieve the data that allowed us to model a LTSpice PV module. Thus, we have collected the performances that we compare with those of the STC conditions. These results are inferior to those of STC conditions but remain encouraging for a young and very promising technology. With low temperature coefficients, perovskite is a potential future candidate of the most suitable technologies for our sub-region

References

[1] Jemli K. Synthése et auto-assemblage de molécules de pérovskite pour la photonique et le marquage. Université Paris-Saclay; Faculté des Sciences de Bizerte (Tunisie); 2016.

[2] Green M, Dunlop E, Hohl-Ebinger J, Yoshita M, Kopidakis N, Hao X. Solar cell efficiency tables (version 57). Progress in Photovoltaics: Research and Applications. 2021 Jan 1;29(1):3-15. https://doi.org/10.1002/pip.3371

[3] Longeaud C. Study of transport parameters and defect states in thin film perovskites under different environments − air or vacuum − and after light-soaking. Guenier-Farret M, Alvarez J. EPJ Photovoltaics. 2020;11:5. https://doi.org/10.1051/epjpv/2019009

[4] Sonmezoglu S, Akin S. Suppression of the interface-dependent nonradiative recombination by using 2-methylbenzimidazole as interlayer for highly efficient and stable perovskite solar cells. Nano Energy. 2020;76:105127.

[5] Neophytou M, De Bastiani M, Gasparini N, Aydin E, Ugur E, Seitkhan A, Moruzzi F, Choaie Y, Ramadan AJ, Troughton JR. Enhancing the charge extraction and stability of perovskite solar cells using strontium titanate (SrTiO3) electron transport layer. ACS Applied Energy Materials. 2019;2(11):8090-8097.

[6] Ren A, Lai H, Hao X, Tang Z, Xu H, Jeco BMFY, Watanabe K, Wu L, Zhang J, Sugiyama M. Efficient Perovskite Solar Modules with Minimized Nonradiative Recombination and Local Carrier Transport Losses. Joule. 2020;4(6):1263-1277.

[7] Green MA, Dunlop ED, Hohl-Ebinger J, Yoshita M, Kopidakis N, Ho-Baillie AW. Solar cell efficiency tables (Version 55). Progress in Photovoltaics: Research and Applications. 2019 Dec 20;28(1):3-15. https://doi.org/10.1002/pip.3228

[8] N’Detigma K, Djicknoum D, Y. MS, Arouna D, Amadou SM. Module parameter extraction and simulation with LTSpice software model in sub-Saharan outdoor conditions. African Journal of Environmental Science and Technology. 2018 Dec 31;12(12):523-531. https://doi.org/10.5897/AJEST2018.2566

[9] Ibrahim H, Anani N. Evaluation of Analytical Methods for Parameter Extraction of PV modules. Energy Procedia. 2017 Oct;134:69-78. https://doi.org/10.1016/j.egypro.2017.09.601

[10]

Tress W, Domanski K, Carlsen B, Agarwalla A, Alharbi EA, Graetzel M, Hagfeldt A. Performance of perovskite solar cells under simulated temperature-illumination real-world operating conditions. Nature energy. 2019;4(7):568-574.

[11] Kata N, Diouf D, Darga A, Seidou Maiga A. The effect of the recombination mechanisms location on the temperature sensitivity of thin-film photovoltaic cells. EPJ Photovolt.. 2019;10. https://doi.org/10.1051/epjpv/2019008

[12] Schwenzer JA, Rakocevic L, Gehlhaar R, Abzieher T, Gharibzadeh S, Moghadamzadeh S, Quintilla A, Richards BS, Lemmer U, Paetzold UW. Temperature variation-induced performance decline of perovskite solar cells. ACS applied materials & interfaces. 2018;10(19):16390-16399.

[13] Jošt M, Lipovšek B, Glažar B, Al-Ashouri A, Brecl K, Matič G, Magomedov A, Getautis V, Topič M, Albrecht S. Perovskite Solar Cells go Outdoors: Field Testing and Temperature Effects on Energy Yield. Advanced Energy Materials. 2020 05 28;10(25):2000454. https://doi.org/10.1002/aenm.202000454

2nd German-West African Conference on Sustainable, Renewable Energy Systems SusRES – Kara 2021

Photovoltaic

https://doi.org/10.52825/thwildauensp.v1i.31

Published: 15 June 2021

Advances in Conversion Efficiency and Thermal Stability of the Perovskite-based Solar Cell: Review

N'Detigma Kata[1,2] [https://orcid.org/0000-0001-8757-9825], Hodo-Abalo SAMAH [2], Kodjo Kpode [2] and Amadou Seidou Maiga[1]

[1] Laboratoire Electronique, Informatique, Télécommunication et Energies Renouvelables, Saint-Louis, Senegal,

[2] Faculté des Sciences et Techniques, Université de Kara, Togo.

Abstract. This paper presents a small review on the technological advances made on the perovskite-based solar cell. Through this summary of the results of the research on perovskite, the reader will have an overview of the perovskite material, the different structures of a perovskite solar cell, and the opto-electrical properties of such cell as well as the electrical models used in its simulation. Finally, the paper presents in a very brief way the challenges that this technology will have to overcome before finding its place in the photovoltaic market.

Keywords: perovskite solar cell, review, thermal stability.

Introduction

Among the photovoltaic cell technologies, perovskite solar cell technology has become probably the hottest topic in photovoltaics as can be seen in the number of publications and conference topics on the subject. In 2009, Miyasaka et al. developed a perovskite-based cell with an efficiency of 2.2%. But, by replacing Boron with Iodine, the efficiency improved to 3.8%. Ten years later, the confirmed efficiency of the single junction cell of a perovskite-based cell was 21%. In 2020, a perovskite-based solar cell with a conversion efficiency of 25.5% was achieved by Jeong M. and all. Several models of perovskite –based solar cell structure, elaboration and optimization method and simulation models have been proposed in the published studies. In spite of the visible advances in terms of structure stability and conversion performance, much research effort remains to be done to ensure the thermal stability of this cell which will guarantee its commercial success. The objective of this paper is to highlight these advances and to review the manufacturing and simulation models of the perovskite cell in order to bring together the similarities in the methods and structure that will ensure its thermal stability.

Structure of the perovskite solar cell

Perovskite mineral is used as a photovoltaic solar cell absorber. It can be elaborated from a variety of materials and different synthesis methods. Perovskite was discovered in 1839 in the Ural Mountains in Russia and named after the Russian mineralogist L.A.Perovskite [1]. The chemical formula of this mineral is CaTiO3 (calcium titanium oxide). Compounds that have a similar structure to CaTiO3 (ABX3) are called perovskites. In general, in the ABX3 structure of perovskite, A is a large monovalent cation that occupies the cubooxctahedral sites in a cubic space. B is a small divalent metal cation that occupies the octahedral sites and X is an anion (typically a halogen, however, X can be oxygen, carbon or nitrogen). The

structure of perovskite and its stability is quantified by two crucial parameters: the tolerance factor (t) given by equation 1 and the octahedral factor (μ).

$$t = \frac{(R_A + R_X)}{\sqrt{2(R_B + R_X)}} \qquad (1)$$

This factor is a ratio of the ionic radius of the divalent cations R_A, R_B and the radius of the anion R_X. These two parameters are generally between 0.81 and 1.11 for t and then 0,44 and 0.90 for μ μ [1]. The perovskite-based solar cell has a variety of architecture. As in other photovoltaic cell technologies, the perovskite cell has an electron transport layer (ETL) and a hole transport layer (HTL) in addition to the perovskite absorber layer. Thus, the configuration of the cell is very crucial to expect a high-performance perovskite cell. From the literature, two configurations stand out for perovskite based cells: the planar configuration and the mesoporous configuration. Each configuration can be elaborated according to the conventional structure (N-i-P) or the inverse structure (P-i-N). The following figures illustrates its two configurations.

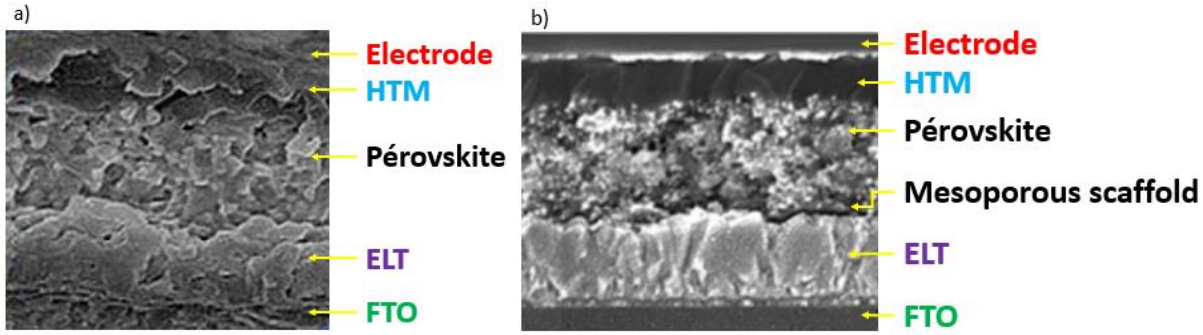

Figure 1. The perovskite-based solar cell configuration: a) the planar configuration and b) the mesoporous configuration.

The evolution of this technology is meteoric with a yield that has evolved from 3.3% in 2009 to 25% in 2020 (figure 2).

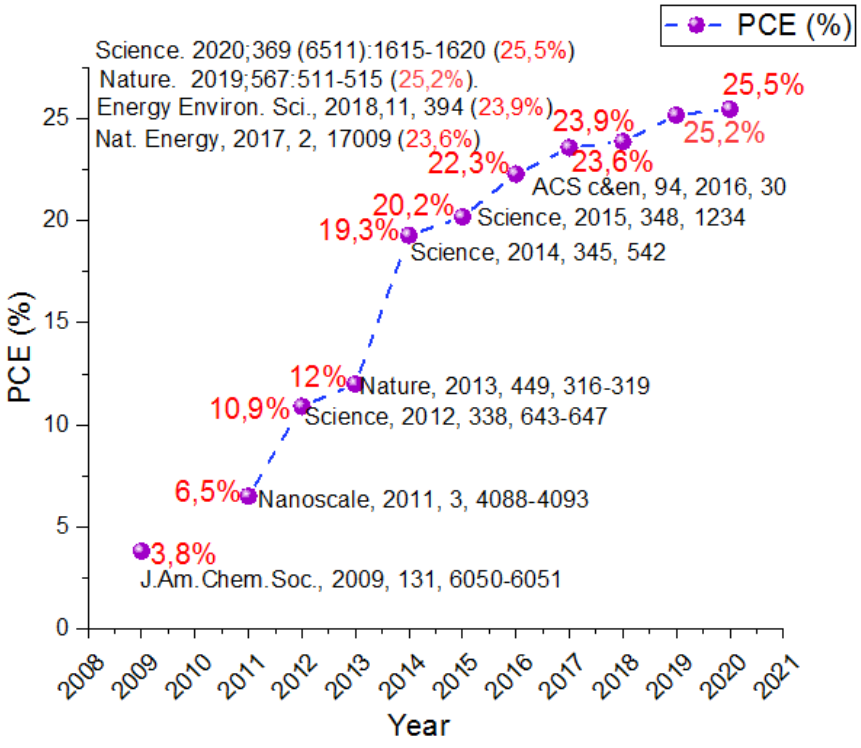

Figure 2. The best annual yield of solar cells based on perovskite.

This performance is partly due to the understanding in the structure of the layers of this cell, the treatment reserved to their interface and the interest that this technology arouses in research. The following table summarizes the different structures of the perovskite-based cell studied in the literature. It is necessary to recall that the choice of a structure aims at the improvement and the stability of the existing cell.

Table 1. The different structures of the perovskite-based cell studied in the literature.

Structures	**PCE**	**Stability time**	**Ref**
FTO / TiO_2-Cl / $MAPbI_3$ / Spiro-OMeTAD / Au	21%	2000 h	[3]
FTO / Doped C_{60} / mixed perovskite / Spiro-OMeTAD / Au	17%	650 h	[4]
Glass / ITO / PEDOT:PSS / $MAPbI_3$ / PCBM / EFGnPs-F / Al	14.3%	30 days	[5]
FTO / LBSO / $MAPbI_3$ / PTAA / Au	21.2%	120 h	[6]
FTO / TiO_2 / $MAPbI_3$ / PTAA / Au	19.6%	120 h	
FTO / LBSO / $MAPbI_3$ / NiO / Au	-	100 h	
GlassFTO / c-TiO_2 / mp-TiO_2 / mixed perovskite / Spiro-OMeTAD-SWCNT	15%	580 h	
FTO / c-TiO_2 / m-TiO_2 / perovskite / Spiro-OMeTAD / Au	14.6%	300 h	[7]
FTO / c-TiO_2 / m-TiO_2 / perovskite / ZrO_2 / Carbon	11.9%	12000 h	[8]
FTO / c-TiO_2 / m-TiO_2 / Cs_5M / HTL / Au	21.2%	250 h	[8]
FTO / c-TiO_2 / m-TiO_2 / Cs_0M / HTL / Au	-	250 h	
ITO / cp-TiO_2 / ms-TiO_2 / perovskite / PTAA / Au	20.6%	160 h	[9]
ITO / cp-TiO_2 / ms-TiO_2 / perovskite / Spiro-mF / Au ITO / cp-TiO_2 / ms-TiO_2 / perovskite / Spiro-oF/ Au	24.8%	500 h	[10]
FTO / bl-TiO_2 / mp-TiO_2 / $MAPb(I_{1-x}Br_x)$ / PTAA / Au	16.2%	-	[11]
FTO / PEDOT:PSS / $MAPb(I_{3-x}Cl_x)$ / PCBM / Al	17.7%	-	[12]
ITO / PEIE / TiO_2 / perovskite / Spiro-OMeTAD / Au	19.3%	-	[13]
FTO / bl-TiO_2 / mp-TiO_2 / $FAPbI_3$ / PTAA / Au	20.2%	-	[14]

If these different structures of the perovskite cell are inexpensive to develop, it should be noted that the structural, electrical and optical properties of the perovskite cell degrade when exposed to the ambient air. This degradation, which is one of the major challenges to overcome if the technology is to appear on the photovoltaic market, is simply due to the reaction of the perovskite layer with the oxygen in the air and with water vapor.

Electrical and optical properties of the perovskite solar cell

The optical band gap of the halide-based perovskite materials used is about 1.6 eV. The absorption of these materials covers only a fraction of the ultraviolet and visible light; 45% to 50% of the entire solar spectrum [15] [16].

However, the absorption range of single crystal perovskite is red-shifted [17]. The absorption in single crystal perovskite starts from 850 nm while it starts at 780 nm for polycrystalline thin films [18].

This absorption shift in the single crystal is due to the enhanced use of below-bandgap absorption attributed mainly to the indirect-bandgap absorption transition with a bandgap of 60 meV smaller than the direct bandgap. The absorption coefficient of the below bandgap is small compared to that of the above-gap transition making the below bandgap absorption negligible in polycrystalline thin films but abvious in thick single crystals [19].

Z. Cheu showed that the absorption coefficient of single crystal perovskite is an order of magnitude higher than those of conventional ruthenium dyes. Liu et al., have shown that perovskite material is an excellent absorber in the visible spectrum, but very transparent in the near infrared spectrum [19].

Blessing E. et al [20], observed similar results to those demonstrated by Aharon et al [21], concerning the improvement of the absorption of the perovskite cell and the decrease of the optical conductivity when the volumetric ration of methylammonium lead bromine introduced in a fixed volume of MAPbI3 increases. The knowledge of the different optical properties and absorption limits and the search for methods to extend the absorption range will contribute to the improvement of the performance of the perovskite technology. This quest for performance improvement also involves simulation studies using electrical models of the solar cell.

Electrical model of the perovskite cell

The current-voltage characteristic of a cell does not provide reasonable insight into the actual mechanisms of charge transport, recombination and storage. As such, an evaluation of the response of a solar cell to a small perturbation of various real inputs such as voltage or light in the frequency domain of the cell remains an essential method. These mechanisms are summarized in the form of an equivalent circuit that describes the actual physical processes in terms of the passive electrical element and the voltage and current sources. The perovskite cell has been treated theoretically as an ordinary direct band gap semiconductor [22]. Therefore, it is considered as a simple p-i-n diode governed by the equivalent circuit equations of the said diode. Many authors have used the one-diode (figure 3a) and two-diode models for the equivalent circuit of the perovskite-based solar cell [23] [24]. In addition to these commonly encountered models, other models often used for organic cells have been used to model perovskite solar cell.

Huang et al. have developed for a perovskite-based solar cell, an equivalent circuit model very close to the one developed by Mazhai for organic cells. The model is shown in Figure 3b.

Ebadi et al, proposed an equivalent circuit model for the perovskite cell including electrical components and ionic components [25] (figure 3c).

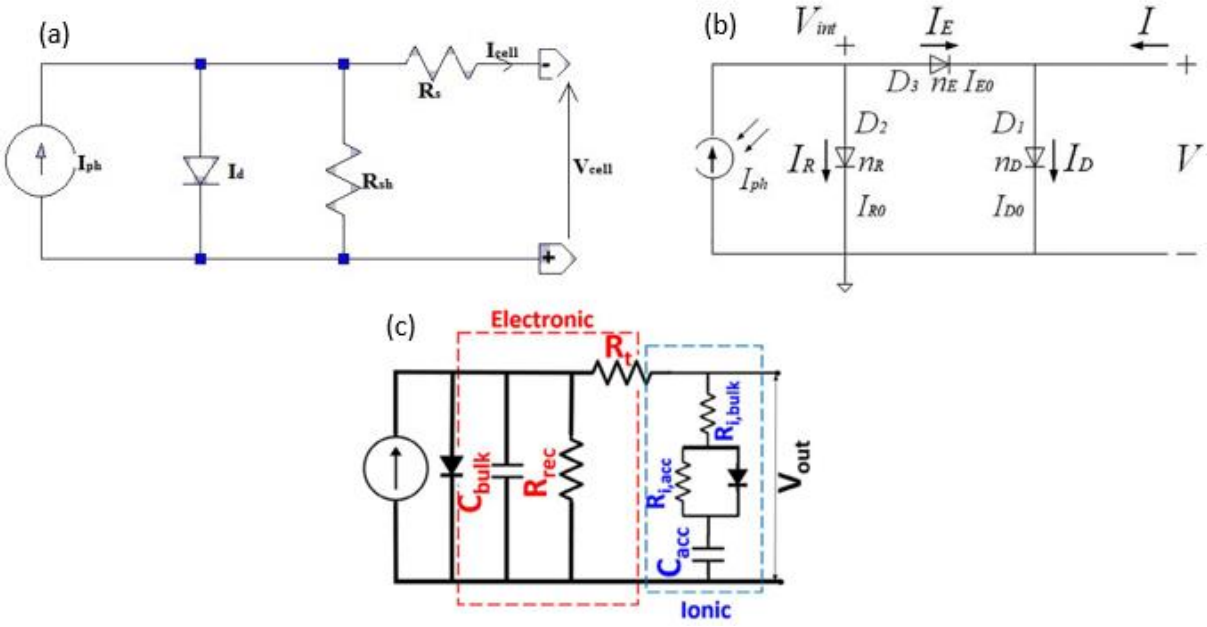

Figure 3. Electrical model of perovskite solar cell: (a) one diode equivalent circuit model, Figure (b) The solar cells' lumped-parameter equivalent circuit model proposed by Mazhari [26] and (c) Equivalent circuit for the fitting photo-voltage rise and decay plots [25]

Future challenges in perovskite solar cell

The commercialization of the perovskite-based solar cell remains closely linked to the improvement and stability of its performance. If its efficiency reached 25% in 2020, the future challenge of the cell remains its stability.

J. Zhang et al., have shown that the Spiro-OMeTAD hole transport layer used in the elaboration of the perovskite cell contributes to its poor stability when exposed to ambient air [27].

Much effort has been made to develop hole transport layer to replace the Spiro-OMeTAD layer [28] [29] [30]. This layer could be replaced by a Cu:NiOx layer. However, Damian et al., have shown in their study that using Cu:NiOx as the hole transport layer results in a huge drop in open circuit voltage and short circuit current. On the other hand, by using Cu:NiOx/PTAA, the quality of the cell improves as well as its efficiency [31]. In 2020, Mingyu J. et al., replaced the Spiro-OMeTAD hole transport layer with two fluorinated isomers. This process resulted in a perovskite-based cell with 24.8% efficiency stable at 87% of its efficiency after 500 hours under humidity conditions without encapsulated [10]. Based on this observation, Yanjie Wu sought to improve the stability of the perovskite-based cell and the mobility of the holes by replacing this layer with a MoO3 layer. In addition, they sought to improve the performance of the cell through the extension of the absorption range to the infrared. For this purpose, a PBDB-TF:BTP-4Cl bulk-heterojunction layer was integrated into the cell [32].

In 2018, Constantina E. et al, developed a perovskite cell with ambition to improve its performance and stability. Thus, by varying the cations (A= Cs, FA, MA) and halogen (X= I, Br, Cl) in the perovskite APbX3, the authors noted not only an improvement in efficiency to 17%, but also a high stability of the cell, low presence of impurity, and low hysteresis when Cesium is used as a cation [33].

The other challenge in perovskite-based cell research is the substitution of Pb in perovskite with a non-toxic metal. The metals of group 14 of the Mendeleyev table are possible candidates, but their major problem is their chemical instability in the required oxidation state [34]. Considering the enthusiasm that researchers have for this technology, it is certain that in a few years to come, these barriers will be lifted.

Conclusion

There is no doubt about the performance that perovskite cell can achieve, which rivals crystalline silicon with 25.5% efficiency in 2020. The major future challenge facing research on perovskite before its commercialization is the stability of its current structure in outdoor conditions, as it reacts with oxygen in the air and water vapor.

References

1 Habibi M, Zabihi F, Ahmadian-Yazdi MR, Eslamian M. Progress in emerging solution-processed thin film solar cells – Part II: Perovskite solar cells. Renewable and Sustainable Energy Reviews. 2016 09;62:1012-1031. https://doi.org/10.1016/

2 Green MA, Ho-Baillie A, Snaith HJ. The emergence of perovskite solar cells. Nature Photonics. 2014 06 27;8(7):506-514. https://doi.org/10.1038/nphoton.2014.134.

3 Pitchaiya S, Natarajan M, Santhanam A, Asokan V, Yuvapragasam A, Madurai Ramakrishnan V, Palanisamy SE, Sundaram S, Velauthapillai D. A review on the

classification of organic/inorganic/carbonaceous hole transporting materials for perovskite solar cell application. Arabian Journal of Chemistry. 2020 01;13(1):2526-2557. https://doi.org/10.1016/j.arabjc.2018.06.006.

4 Wang Z, McMeekin DP, Sakai N, van Reenen S, Wojciechowski K, Patel JB, Johnston MB, Snaith HJ. Efficient and Air-Stable Mixed-Cation Lead Mixed-Halide Perovskite Solar Cells with n-Doped Organic Electron Extraction Layers. Advanced Materials. 2016 Dec 01;29(5):1604186. https://doi.org/10.1002/adma.201604186.

5 Kim G, Jang H, Yoon YJ, Jeong J, Park SY, Walker B, Jeon I, Jo Y, Yoon H, Kim M, Baek J, Kim DS, Kim JY. Fluorine Functionalized Graphene Nano Platelets for Highly Stable Inverted Perovskite Solar Cells. Nano Letters. 2017 09 14;17(10):6385-6390. https://doi.org/10.1021/acs.nanolett.7b03225

6 Shin SS, Yeom EJ, Yang WS, Hur S, Kim MG, Im J, Seo J, Noh JH, Seok SI. Colloidally prepared La-doped BaSnO3 electrodes for efficient, photostable perovskite solar cells. Science. 2017 03 30;356(6334):167-171. https://doi.org/10.1126/science.aam6620

7 K Aitola K, Domanski K, Correa-Baena J, Sveinbjörnsson K, Saliba M, Abate A, Grätzel M, Kauppinen E, Johansson EMJ, Tress W, Hagfeldt A, Boschloo G. High Temperature-Stable Perovskite Solar Cell Based on Low-Cost Carbon Nanotube Hole Contact. Advanced Materials. 2017 02 23;29(17):1606398. https://doi.org/10.1002/adma.201606398

8 Grancini G, Roldán-Carmona C, Zimmermann I, Mosconi E, Lee X, Martineau D, Narbey S, Oswald F, De Angelis F, Graetzel M, Nazeeruddin MK. One-Year stable perovskite solar cells by 2D/3D interface engineering. Nature Communications. 2017 06 01;8(1). https://doi.org/10.1038/ncomms15684

9 Duong T, Wu Y, Shen H, Peng J, Zhao S, Wu N, Lockrey M, White T, Weber K, Catchpole K. Light and elevated temperature induced degradation (LeTID) in perovskite solar cells and development of stable semi-transparent cells. Solar Energy Materials and Solar Cells. 2018 Dec;188:27-36. https://doi.org/10.1016/j.solmat.2018.08.017

10 Jeong M, Choi IW, Go EM, Cho Y, Kim M, Lee B, Jeong S, Jo Y, Choi HW, Lee J, Bae J, Kwak SK, Kim DS, Yang C. Stable perovskite solar cells with efficiency exceeding 24.8% and 0.3-V voltage loss. Science. 2020 09 24;369(6511):1615-1620. https://doi.org/10.1126/science.abb7167

11 Jeon NJ, Noh JH, Kim YC, Yang WS, Ryu S, Seok SI. Solvent engineering for high-performance inorganic–organic hybrid perovskite solar cells. Nature Materials. 2014 07 06;13(9):897-903. https://doi.org/10.1038/nmat4014

12 Nie W, Tsai H, Asadpour R, Blancon J, Neukirch AJ, Gupta G, Crochet JJ, Chhowalla M, Tretiak S, Alam MA, Wang H, Mohite AD. High-efficiency solution-processed perovskite solar cells with millimeter-scale grains. Science. 2015 01 29;347(6221):522-525. https://doi.org/10.1126/science.aaa0472

13 Kong L, Ma J, Huang H, Zhang R. Crystallization of magnesium niobate from mechanochemically derived amorphous phase. Journal of Alloys and Compounds. 2002 06;340(1-2):L1-L4. https://doi.org/10.1016/s0925-8388(02)00003-8

14 Yang WS, Noh JH, Jeon NJ, Kim YC, Ryu S, Seo J, Seok SI. High-performance photovoltaic perovskite layers fabricated through intramolecular exchange. Science. 2015 05 21;348(6240):1234-1237. https://doi.org/10.1126/science.aaa9272

15 Bi W, Wu Y, Chen C, Zhou D, Song Z, Li D, Chen G, Dai Q, Zhu Y, Song H. Dye Sensitization and Local Surface Plasmon Resonance-Enhanced Upconversion Luminescence for Efficient Perovskite Solar Cells. ACS Applied Materials & Interfaces. 2020 05 07;12(22):24737-24746. https://doi.org/10.1021/acsami.0c04258

16 Wu Y, Bi W, Shi Z, Zhuang X, Song Z, Liu S, Chen C, Xu L, Dai Q, Song H. Unraveling the Dual-Functional Mechanism of Light Absorption and Hole Transport of Cu2CdxZn1–xSnS4 for Achieving Efficient and Stable Perovskite Solar Cells. ACS Applied Materials & Interfaces. 2020 03 20;12(15):17509-17518. https://doi.org/10.1021/acsami.0c00607

17 Ezealigo BN, Nwanya AC, Ezugwu S, Offiah S, Obi D, Osuji RU, Bucher R, Maaza M, Ejikeme P, Ezema FI. Method to control the optical properties: Band gap energy of mixed halide Organolead perovskites. Arabian Journal of Chemistry. 2020 01;13(1):988-997. https://doi.org/10.1016/j.arabjc.2017.09.002

18 Liu Y, Zhang Y, Yang Z, Yang D, Ren X, Pang L, Liu SF. Thinness- and Shape-Controlled Growth for Ultrathin Single-Crystalline Perovskite Wafers for Mass Production of Superior Photoelectronic Devices. Advanced Materials. 2016 08 29;28(41):9204-9209. https://doi.org/10.1002/adma.201601995

19 Liu F, Zhu J, Wei J, Li Y, Lv M, Yang S, Zhang B, Yao J, Dai S. Numerical simulation: Toward the design of high-efficiency planar perovskite solar cells. Applied Physics Letters. 2014 06 23;104(25):253508. https://doi.org/10.1063/1.4885367

20 Ezealigo BN, Nwanya AC, Ezugwu S, Offiah S, Obi D, Osuji RU, Bucher R, Maaza M, Ejikeme P, Ezema FI. Method to control the optical properties: Band gap energy of mixed halide Organolead perovskites. Arabian Journal of Chemistry. 2020 01;13(1):988-997. https://doi.org/10.1016/j.arabjc.2017.09.002.

21 Aharon S, Cohen BE, Etgar L. Hybrid Lead Halide Iodide and Lead Halide Bromide in Efficient Hole Conductor Free Perovskite Solar Cell. The Journal of Physical Chemistry C. 2014 05;118(30):17160-17165. https://doi.org/10.1021/jp5023407

22 Miyano K, Tripathi N, Yanagida M, Shirai Y. Lead Halide Perovskite Photovoltaic as a Model p–i–n Diode. Accounts of Chemical Research. 2016 01 12;49(2):303-310. https://doi.org/10.1021/acs.accounts.5b00436

23 Cappelletti M, Casas G, Cédola A, Peltzer y Blancá E, Marí Soucase B. Study of the reverse saturation current and series resistance of p-p-n perovskite solar cells using the single and double-diode models. Superlattices and Microstructures. 2018 Nov;123:338-348. https://doi.org/10.1016/j.spmi.2018.09.023

24 Reza MN, Mominuzzaman SM. Extraction of Equivalent Circuit Parameters for CNT incorporated Perovskite Solar Cells Using Newton-Raphson Method. 2018 10th International Conference on Electrical and Computer Engineering (ICECE). 2018 10th International Conference on Electrical and Computer Engineering (ICECE). 2018 Dec. https://doi.org/10.1109/icece.2018.8636738

25 Ebadi F, Aryanpour M, Mohammadpour R, Taghavinia N. Coupled Ionic-Electronic

Equivalent Circuit to Describe Asymmetric Rise and Decay of Photovoltage Profile in Perovskite Solar Cells. Scientific Reports. 2019 08 19;9(1). https://doi.org/10.1038/s41598-019-48505-6

26 Huang G, Yu F, Xu C. An Analytical Solution to Lumped Parameter Equivalent Circuit Model of Organic Solar Cells. Crystals. 2018 05 18;8(5):224. https://doi.org/10.3390/cryst8050224

27 Zhang J, Tan HS, Guo X, Facchetti A, Yan H. Material insights and challenges for non-fullerene organic solar cells based on small molecular acceptors. Nature Energy. 2018 07 02;3(9):720-731. https://doi.org/10.1038/s41560-018-0181-5

28 Jeon NJ, Lee HG, Kim YC, Seo J, Noh JH, Lee J, Seok SI. o-Methoxy Substituents in Spiro-OMeTAD for Efficient Inorganic–Organic Hybrid Perovskite Solar Cells. Journal of the American Chemical Society. 2014 05 23;136(22):7837-7840. https://doi.org/10.1021/ja502824c

29 Jeon NJ, Na H, Jung EH, Yang T, Lee YG, Kim G, Shin H, Il Seok S, Lee J, Seo J. A fluorene-terminated hole-transporting material for highly efficient and stable perovskite solar cells. Nature Energy. 2018 07 09;3(8):682-689. https://doi.org/10.1038/s41560-018-0200-6

30 Saliba M, Orlandi S, Matsui T, Aghazada S, Cavazzini M, Correa-Baena J, Gao P, Scopelliti R, Mosconi E, Dahmen K, De Angelis F, Abate A, Hagfeldt A, Pozzi G, Graetzel M, Nazeeruddin MK. A molecularly engineered hole-transporting material for efficient perovskite solar cells. Nature Energy. 2016 01 18;1(2). https://doi.org/10.1038/nenergy.2015.17

31 Głowienka D, Zhang D, Di Giacomo F, Najafi M, Veenstra S, Szmytkowski J, Galagan Y. Role of surface recombination in perovskite solar cells at the interface of HTL/CH3NH3PbI3. Nano Energy. 2020 01;67:104186. https://doi.org/10.1016/j.nanoen.2019.104186

32 Wu Y, Gao Y, Zhuang X, Shi Z, Bi W, Liu S, Song Z, Chen C, Bai X, Xu L, Dai Q, Song H. Highly efficient near-infrared hybrid perovskite solar cells by integrating with a novel organic bulk-heterojunction. Nano Energy. 2020 Nov;77:105181. https://doi.org/10.1016/j.nanoen.2020.105181

33 Gkini KE, Antoniadou M, Balis N, Kaltzoglou A, Kontos AG, Falaras P. Mixing cations and halide anions in perovskite solar cells. Materials Today: Proceedings. 2019;19:73-78. https://doi.org/10.1016/j.matpr.2019.07.660

34 Vidyasagar CC, Muñoz Flores BM, Jiménez Pérez VM. Recent Advances in Synthesis and Properties of Hybrid Halide Perovskites for Photovoltaics. Nano-Micro Letters. 2018 09 24;10(4). https://doi.org/10.1007/s40820-018-0221-5

2nd German-West African Conference on Sustainable, Renewable Energy Systems SusRES – Kara 2021

Biomass Energy

https://doi.org/10.52825/thwildauensp.v1i.24

Published: 15 June 2021

Factual Quantification Methods of Energy Consumption for Transmission Nodes in Cellular Communication Systems : Experimental case study in Lome

Kodjovi Semenyo Agbosse [1], Koffi Agbeblewu Dotche [2] [https://orcid.org/0000-0002-5945-0036], Adekunlé Akim Salami [3] [https://orcid.org/0000-0002-0917-1231], Koffi Mawugno Kodjo [4] [https://orcid.org/0000-0001-5674-2212] and Ayité Sénah Akoda Ajavon [5] [https://orcid.org/0000-0002-6318-2396]

[1, 2, 3,4, 5] Department of Electrical Engineering, CERME (ENSI), University of Lome, Lomé- Togo

[2] Department of Electrical Technology, Akenten Appiah Menka-University of Skills Training and Entrepreneurial Development (AAMUSTED), Kumasi-Ghana

Abstract. The energy efficiency for wireless communication technology standard is very important for the current and the future generation ones. Noting that the energy consumption in communication systems is constantly increasing due to the exponential number of subscribers and high data services demand. In this regard, it becomes necessary to quantify this energy consumption with respect to the communication technology standard at the site. This article presents an evaluation of the factual quantifications methods for the energy consumption of transmission nodes in cellular communications systems. The data collection was obtained on three types of communication technology standards namely second generation (2G), 3G, 4G and their combination using the direct and indirect (the utility records) methods power measurement on the field installation of a mobile telephone operator in Togo. These data have undergone a preprocessing in the Microsoft Excel software (version 2019), then sent in the Matlab software (Matlab R2020b) for further analysis. The results showed that the energy consumption observed at the site is around 124 kWh, 254, kWh and 362 kWh on monthly average respectively for 2G, 2G/3G, and 2G/3G/4G typology used. It further indicated that when more communication standards are used on a given site, its power consumption is much more increasing. The power profile distribution has been investigated, and the analysis revealed that the normal distribution closely fitted the data. However, more parameters related to the number of utilised channels and climatic conditions need to be considered in future research works.

Keywords: cellular communication systems, distribution fitting tool, energy consumption, power profile quantification

Introduction

Please notice The cellular networks rely on the efficient use of the spectrum therefore the service area may be divided into smaller cells, ideally with no gaps or overlaps. Each cell, is served by its own base station and a set of frequencies. The goal behind this concept was to increase capacity so the network can provide service to a large number of subscribers while maintaining optimal system performance. The Groupe Spéciale Mobile acronym GSM was first used in 1982 by the European Standardization organization, the task group (GSM) was mandated to define a new standard of mobile communication in the band of 900MHz. This name was changed to Global System for Mobile Communication (GSM) in 1989 and has since remained GSM's name. The air interface of GSM is a combination of Time Division

Multiple Access and Frequency Division Multiple Access [1]. GSM is known as second-generation network. GSM technology has some limitations in high data application and bandwidth efficiency. This is explained by the introduction of the Code Division Multiple Access (CDMA). The CDMA is an alternative to GSM, because of the delivery of high-speed data packets such as multimedia, video, call conference etc., as required for the Third Generation (3G) networks. The greatest advantage of CDMA compared to other wireless cellular systems was the potentially enhanced voice capacity and its ability to work effectively in noisy environments.

The name of the access network is related to the generation of the cellular system, subsequently Network Sub-System (NSS) for 2G, Universal Terrestrial Access Network (UTRAN) for 3G. A 4G evolved-UTRAN (eUTRAN) has a simplified architecture (compared to a 3G-UTRAN), which integrates the eNode B base stations’ control functions that were previously implemented in base station controllers called RNC (Radio Network Controller of 3G) and Base Station Controllers (BSC) of RAN (Radio Access Network) networks. The main improvements of LTE-Advanced (LTE-A) residing in the 4G mobile network standard [2] are :

- carrier aggregation : consists of serving a user on several carriers at the same time, this allows to obtain a bandwidth of about 100 MHz (aggregation of five carriers of 20 MHz bandwidth) while one can achieve a 1 Gbits / s downstream speed;
- support for a heterogeneous network: this is an important advantage of LTE-A, which consists in deploying low-power stations (pico, femto, relay) in macro cells; this improves the quality of service (speed in particular) in areas with high population density or poorly covered;
- multiple antenna use: LTE-A and future mobile communications networks use a transmission mode that supports downlink MIMO configuration.

It will be recalled that the traditional macrocell base stations do consume some significant amount of energy at the network access due to the power amplifier low efficiency. The evolution to subsequent technology aims at reducing this energy consumption by introducing natural cooling. In regard to the sustainable technological development and free emission of dioxide of carbon policy, the renewable energy to supply the transmission nodes are gained much interest in the scientific community [3]. Thus, in practical network, different typologies are used at a cell site depending on the geographical area. It becomes necessary therefore to quantify the energy consumption by these typologies with respect to the communication technology standards that are used at the site. This article presents an evaluation of the factual quantifications methods for the energy consumption of transmission nodes in cellular communications systems.

The rest of this paper is structured as follows, the section 2 presents the theory behind the power modelling of a cluster-group of transmitters. In section 3, the methodology of the data collection is given and the results are in section 4. The last section is the conclusion.

The Model

The linear model of power consumption $P_{i,k}$, at a transmission node [3] is given as follows :

$$P_{i,k} = \frac{1}{\eta} P_{t,i} + \alpha P_c + P_0 \tag{1}$$

η is the efficiency of power amplifier, p_t, the transmit power of the node, α the number of antennas at the node, the circuit power P_c, and P_0 is the non-transmission power consumption including P_{DP} baseband signal processing, P_{Conv}, AC-DC converter ; P_{Cool} , cooling ; P_{LB} , the lighting system; E_{bb}, battery backup (uncharged), etc...

The non-transmission power, P_0 , is given by

$$P_0 = P_{DP} + P_{Conv} + \sum_{i}^{m} P_{Cool_i} + \sum_{j}^{n} P_{LB_j} + E_{bb} + P_{link} \quad (2)$$

Thus for a cluster group of base station the total power consumption, P_{To} of the system is given as:

$$P_{To} = \sum_{k=1}^{K} n_k . P_k + P_{Bach} \quad (3)$$

where K is the number of base station types used in the network, n_k is the total number of base stations of a specific type k-th (e.g., Macro base stations), P_k is the power consumption of a base station of type k, and P_{Bach} is the backhaul power loss [4].

Methodology

This section presents the data collection, sampling and processing steps

Data Collection

The power measurements were conducted on Moov-Africa cellular network’s installation in Togo. The power level against the top-level KPIs obtained by a Nokia Siemens Network Statistics tool.

Sample size and data processing

The data sampling size has consisted in the averaging of the raw data over a monthly basis. That implied that, the arithmetic average values were considered.

The measured power data’s collection spans over a 9 month, and has considered the following observation time intervals :

- hour: the hourly statistics gives a detailed picture of the network performance and are useful to help spot temporary problems and identify trends.
- peak or busy hour : Peak hour statistics are of great significance because they correspond to the time of heavy utilization of network resources. In a way, they provide the “worst-case” scenario.
- day: daily statistics are introduced to provide a way of averaging temporary fluctuations of hourly data.

The data were processed into excel spreadsheet, and saved as a cascaded sheet .CSV file before been processed into the Matlab software (Matlab R2020b) where the distribution fitting tool (dftool) was used for further analysis to help in quantifying the power profile distribution observed.

Results and discussion

In this section the results are presented and discussed.

In Figure 1, it shows that the power consumption based on the typologies of technology used on given a site may subsequently vary. It may however be stated when the three typologies are been deployed the consumption could be high. This high value may strongly depend on the geographical area by then on the subscribers’ density.

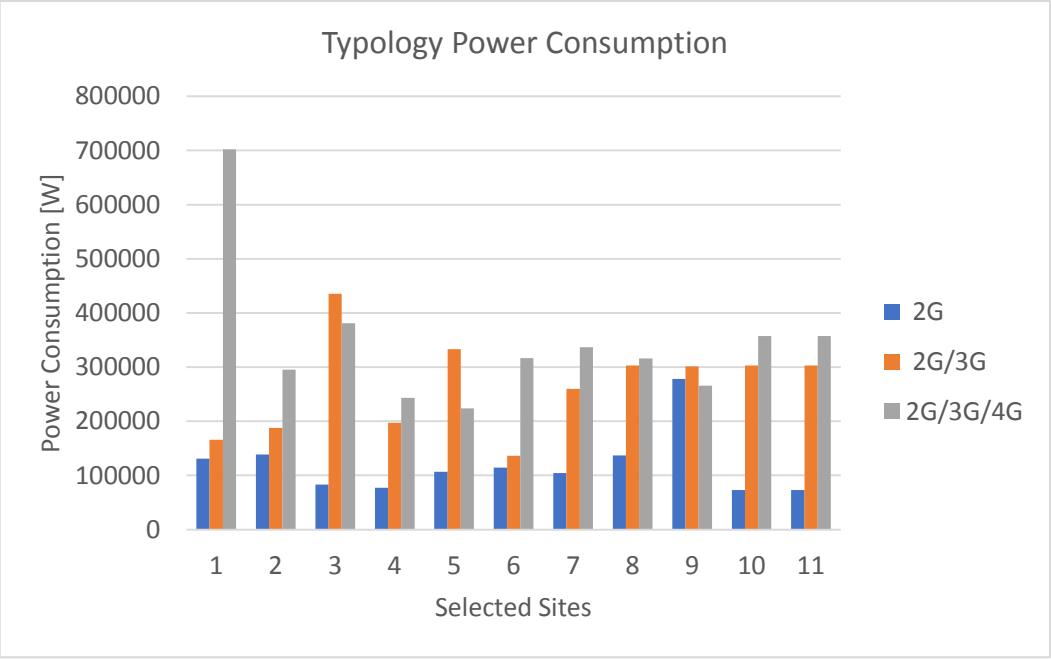

Figure 1 : Power Consumption of different typology

It is also observed in the particular case of the site 9 that the power consumption of 2G, the GSM technology, is equally high as compared to other two typologies. This could prompt a reserved decision of the telecom operators for the necessary need to go toward the advanced technology standard.

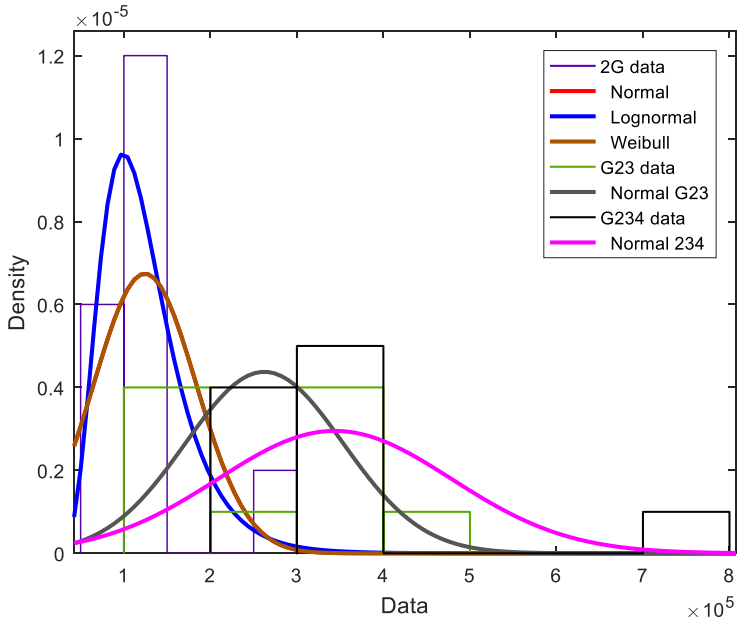

Figure 2 : Power Profile distribution

Instead the results observed (see Figure 1) on the site 1 and 5 may be quantified to be important due to the fact that the high power consumption is observed from the three typologies which in turn, the telecoms operators may not patronize.

Further analysis of the results in Figure 1, may indicate that the power consumption of the mixed typology is definitely high, however if the cost of site acquisition for each standalone typology is considered, it may be argued that the mixed typology should be commendable for the telecom operators.

In Figure 2, it has been illustrated the power profile distribution’s characteristic of the various typologies considered. The analysis indicated that the power profile could be described by the normal distribution. Thus, the normal distribution could be used to quantify the power consumption of the respective transmission nodes that were considered in the study with a monthly mean value 124 kWh, 254, kWh and 362 kWh respectively for 2G, 2G/3G, and 2G/3G/4G.

Conclusion

The energy efficiency for wireless communication systems is very important for the current and the future generation ones. It should be stated that the energy consumption in communication systems is constantly increasing due to the exponential number of subscribers and high data services demand.

This article presents an evaluation of the factual quantifications methods for the energy consumption of transmission nodes in cellular communications systems. The data were collected on Moov-Africa installation in Togo. These data have undergone a preprocessing in the Microsoft Excel software, then sent in the Matlab software for further analysis. The results showed that the energy consumption observed at the site is around 124 kWh, 254, kWh and 362 kWh on monthly average respectively for 2G, 2G/3G, and 2G/3G/4G typology used. It further indicated that when more communication standards are used on a given site, its power consumption is much more increasing. The power profile distribution has been investigated, and the analysis revealed that the normal distribution closely fitted the data. However, more parameters related to the number of utilised channels and climatic conditions need to be considered in future research works.

References

[1] Gyamfuaa JM, Ofosu WK, Dotche K, Diawu K. Investigation of the User Redial and its Effect on the Network Congestion in Call Admission : A Case Study in Ghana. In: Arai K, Bhatia R, Kapoor S, eds. *Advance in Artificial Intelligent Systems (Proceedings of the Future Technologies Conference (FTC) 2018)*. 881. Switzerland: Springer Nature; 2019:598-607. https://doi.org/https://doi.org/10.1007/978-3-030-02683-7_42

[2] Qian Li, Hu RQ, Yi Qian, Geng Wu. Cooperative communications for wireless networks: techniques and applications in LTE-advanced systems. *IEEE Wireless Communications*. 2012 04;19(2). https://doi.org/10.1109/mwc.2012.6189409

[3] Dotche K, Salami A, Kodjo K, Sekyere F, Bedja K. Studying the Impacts of the Renewable Energy Integration in Telecommunication Systems: A Case Study in Lome. In: Arai K, Bhatia R, Kapoor S, eds. *Advances in Intelligent Systems and Computing (Proceedings of the Future Technologies Conference (FTC) 2019)*. 1070. Switzerland: Springer Nature ; 2020:758-780.

[4] Tombaz S, Monti P, Kun Wang, Vastberg A, Forzati M, Zander J. Impact of Backhauling Power Consumption on the Deployment of Heterogeneous Mobile Networks. *2011 IEEE Global Telecommunications Conference - GLOBECOM 2011*. 2011 IEEE Global Communications Conference (GLOBECOM 2011). 2011 Dec. https://doi.org/10.1109/glocom.2011.6133999

2nd German-West African Conference on Sustainable, Renewable Energy Systems SusRES – Kara 2021

Biomass Energy

https://doi.or/10.52825/thwildauensp.v1i.14

Published: 15 June 2021

The LabTogo-Project

Analysis of the biomass potential and set-up of research capacities for the development of a biogas sector in Togo

Engler, Nils[1], Komi Agboka [2][https://orcid.org/1111-2222-3333-4444], Edem K. Koledzi[3][https://orcid.org/0000-0002-9078-7630], Jérémie Kokou Fontodji[4], Sena Alouka[5], Bellot, Franz-Fabian [1], Fischer, Peter[1], Helka, Josephin[1], Kalcher, Jasmin[1], Krüger, Dennis[1], Lenhart, Markus[1], Majer, Stefan[1], Mutlu,Özge Cepeloigullar[1], Naegeli de Torres, Friederike[1], Pohl, Marcel[1], Schaller, Sven[1], Steinert, Diana[1]

[1] DBFZ, Deutsches Biomasseforschungszentrum gemeinnützige GmbH

[2] West African Science Service Center on Climate Change and Adapted Land Use (WASCAL), Université de Lomé, Togo

[3] Laboratory GTVD, University of Lomé, Laboratory of Wastes Management, Treatment and Valorization; Po. Box 1515, Bd Eyadema, Lomé-Togo

[4] Laboratory of Forest Research, University of Lomé, Po. Box 1515, Bd Eyadema, Lomé-Togo

[5] Jeunes volontaires pour l'environnement (JVE)

Abstract. A joint project between West African Science Service Center on Climate Change and Adapted Land Use (WASCAL), the University of Lomé and the German Biomass Research Center (Deutsches Biomasseforschungszentrum; DBFZ) was initiated in 2020. The project aims at evaluating alternative and regenerative energy sources for rural areas and creating the basis for successful implementation. In three different work packages, therefore, biomass potentials should be quantified, technologies should be examined with regard to their suitability and - in the case of biogas application - a research structure, pilot biogas laboratory, should be created that is necessary to enable the sustainable implementation of technologies.

Keywords: biomass resource mapping, sustainable development, biogas research capacities

Introduction

Togo is one of the West African countries that is establishing research activities for sustainable development in the context of the German-African research cooperation West African Science Service Center on Climate Change and Adapted Land Use (WASCAL). The development of research infrastructure and transfer of knowledge for the bioenergetic use of agricultural, forestry and organic residues are essential in order to implement measures against climate change and to significantly reduce deforestation or, at best, to stop it.

In 2020, the Federal Ministry of Education and Research (BMBF) initiated a joint project between WASCAL, the University of Lomé and the DBFZ. The project aims at evaluating alternative and regenerative energy sources for rural areas and creating the basis for successful implementation.

In a first step, therefore, biomass potentials should be quantified, technologies should be examined with regard to their suitability and - in the case of biogas application - a research structure should be created that is necessary to enable the sustainable implementation of technologies. Accordingly, the project focuses on three subject areas and sets the following objectives:

- Analysis of the potential system contribution of biogenic resources
- Construction and commissioning of a biogas laboratory as well as corresponding training courses
- Studies on alternative methods for cooking stoves

A kick-off meeting was held in July 2020 as a virtual web meeting due to the COVID-19 pandemic. Since then, all partners involved have worked together on the implementation of the project goals. Despite the ongoing complex situation, which for example severely restricts travel opportunities, progress has been made in all work three work packages. The project structure is shown in **Figure 1**.

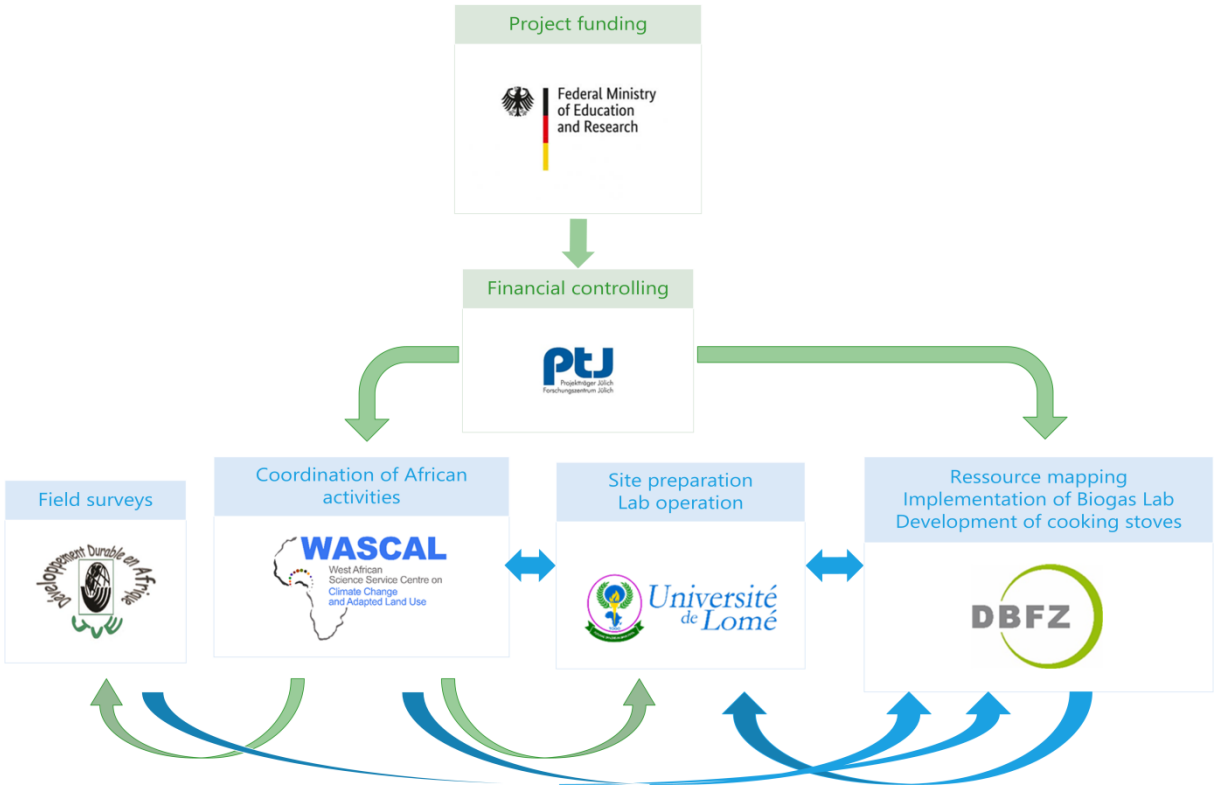

Figure 1: Structure of the project (green arrows: funding, blue arrows: information and product flow)

Work package 1: Analysis of the potential system contribution of biogenic resources

The system contribution of biomass depends largely on the availability and mobilization potential of existing resources. Therefore, work package 1 aims at a comprehensive systematic assessment of the expected impacts that the technologies considered in the project would achieve if they were established on a broad scale in Togo. To achieve this, three main activities have been defined: Acquisition of spatial information on biomass availability, assessment of suitable technologies and estimation of potential GHG emission savings.

Acquisition of Spatial Information for the Identification of Preference Regions

In a first step, freely available MODIS MOD12Q1 satellite datasets captured between 2001 and 2019 were acquired and analyzed in order to identify land-cover/land-use changes in Togo. We used Change Detection analyses to quantify the extent of relevant changes as well as to locate areas exposed to significant expansion of agricultural fields, urbanization or the loss and degradation of natural vegetation. Due to the high level of thematic detail in MODIS MOD12Q1 datasets, changes between 17 individual land-cover types can be identified on a yearly basis.

In addition to that, open geospatial data products derived from Global Forest Watch (GFW) as well as the International Food Policy Research Institute’s (IPFRI) global database on 42 spatially-disaggregated crop production statistics are used to determine locations exposed to significant tree cover losses and intense utilization of farm land. Agricultural production values extracted from IFPRI’s Spatial Production Allocation Model (SPAM) support the quantification and identification of areas with high biogenic residues. Furthermore, information about temporal changes and trends in agricultural production can be extracted and evaluated.

Additionally, the biomass potential, particularly that of agricultural by-products and organic wastes generated by markets and the food industry, will be mapped and evaluated in terms of quantity and spatial availability. To this end, the Togolese partners conducted extensive field work following a methodological procedure joint prepared with DBFZ to establish a sound database on point sources of large production sites. The objective of the current activity is to update data collected during the feasibility studies on the biomass potential in different regions of Togo. Data to be collected with high accuracy include local primary data (primary data on biogenic residues from agriculture, food processing and municipal waste) and the characterization of household wastes for the construction of biogas plants and pyrolysis.

Table 1 below summarizes the type of wastes to be collected in each region and their priority and Table 2 the farm/livestock/industries scales to be considered regarding each category of waste. The data are collected per point source with their coordinates and the amounts of wastes, byproducts, etc. were estimated based on conversion factors.

Table 1 Types of prioritized wastes in each region

Region	Types of wastes	Priority
Savanes	▪ Animal husbandry wastes/animal market ▪ Slaughterhouses wastes ▪ Rice bales/cooperatives/industries ▪ Rice straws ▪ Market ▪ others	Priority 1
	▪ Human sludge	Priority 2
Kara	▪ Animal husbandry wastes/animal market ▪ Rice bales/cooperatives/industries ▪ Rice straws ▪ Industries (brewery) ▪ Slaughterhouses wastes ▪ Market (Ketao) ▪ others	Priority 1
	▪ Human sludge ▪ Household waste characterization	Priority 2

Region	Types of wastes	Priority
Plateaux	▪ Animal husbandry wastes/animal market ▪ Rice bales/cooperatives/industries ▪ Rice straws ▪ Slaughterhouses wastes ▪ Fruits market ▪ Cotton industries ▪ Pineapple residues from farms ▪ Palm nut residues ▪ Wastes from woodwork ▪ Others	Priority 1
	▪ Human sludge ▪ Household waste characterization	Priority 2
Maritime	▪ Animal husbandry wastes/animal market ▪ Rice bales/cooperatives/industries ▪ Rice straws ▪ Slaughterhouses wastes ▪ Palm nut residues ▪ Market ▪ Fruit industries (Gbatope, Adangbe, etc.) ▪ Pineapple residues from farms ▪ Waste from woodwork ▪ Others	Priority 1
	▪ Slaughterhouses wastes ▪ Human sludge	Priority 2
Lomé	▪ Animal husbandry wastes/animal market ▪ Slaughterhouses wastes ▪ Human sludge ▪ Fruit market ▪ Cereal flour industry ▪ Fruit/juice industries ▪ Oil industries ▪ BB/SNB- breweries ▪ others	Priority 1
	▪ Household waste characterization	Priority 2

Table 2 Minimum size of the farm/livestock and other type of data scales

Types of wastes	Scale	Surveys’ procedures
Animal Farms/market	A minimum of: 1000 heads of poultry or 50 heads of cows or 200 heads of cattle/goats	- identify the farms through regional authorities or ongoing projects - number of farms to survey/markets - type of use of the waste
Industries (rice, fruits/juice, cashew fruit, cotton, oil, cereals)	All producing food-processing industries producing organic wastes	- identify the farms - quantitative evaluation of wastes and current uses
Rice straws (rice farms)	>30 ha in one set	- identification - quantification of the residues - type of use of the waste

Pineapple farms	>1 ha in one set	- identification - quantification of the residues - type of use of the waste
Fruits market; Industries (brewery); Slaughterhouses wastes		- systematic surveys - type of use of the waste
Human sludge	No scale	- Type of use of the waste

All gathered information will contribute to the identification of priority areas for preferential regions for the construction of biogas plants and regions for the mobilization of biomass for pyrolysis. A GIS-based hot spot analysis based on the point sources obtained in the field will further provide important spatial information to narrow down potential locations for sustainable biomass conversion and therewith an effective production of biogas and for pyrolysis. Advanced site assessments will analyze the respective catchment area, availability of agricultural residues and biomass by-products as well as infrastructural parameter (i.e. electrification, transport distances). Based on this information, biomass supply curves will be calculated for the identified sites, representing the relationship between biomass availability and transport distances. The biomass supply curves enable assumptions on which plant size classes would be suitable for the identified sites.

Assessment of Suitable Conversion Technologies

In a second step, different technologies including pyrolysis will be assessed. The aim is to provide general assumptions on the specific biomass substrates regarding their specific utility for the biogas process and for the pyrolysis cooker and to point out the necessary technical preconditions (e.g. substrate preparation). In this context, a broad regionalization for different technological concepts aligned to specific local needs (e.g. electricity supply, heat generation, cooking gas) will be carried out, so that appropriate technical solutions can be presented to the respective local stakeholders. Cost calculations for the establishment of the identified technological concepts and investments for indispensable required infrastructure are then developed in dependence of the site conditions. The derivation of specific production costs will enable an evaluation of the different technological solutions and a statement of their cost-effectiveness for each site and their competitiveness taking into account local market conditions. Subsequently, an economic technology impact assessment is needed to be aware of possible negative side effects.

Estimation of the GHG Emission Savings Potential

In a third step, local a national emission reduction effects are estimated for the identified material flows. Thereon, saving effects are determined that result from the substitution of the energy sources used to date in the different sectors (e.g. energy production, energy for cooking, etc.). The quantification of these saving effects in combination with the estimated amounts of available biogenic resources then allow for assumptions to be made about the potentially achievable energy savings at the national level and about the possible benefits of using biogenic resources in the various sectors of use. Finally, a calculation tool will be developed that will enable the evaluation of the energy savings and the relevance of substituting energy sources in the various sectors of use.

Work package 2: Construction and commissioning of a biogas laboratory and capacity building

The establishment of a ready-to-use biogas laboratory at the Université de Lomé is a central component of the project. The laboratory will serve to implement the results of work package 1 and to accompany and support the development of an own biogas sector in Togo through applied research. In addition, it will be used for the training of students at the University of Lomé and other stakeholders in West Africa.

The basic concept and the details of the equipment were designed in close cooperation with the University of Lomé. In order to save costs, the laboratory building is designed as a container construction. The individual containers will be largely pre-assembled in Germany and connected to form a complete building at the final location. The building will consist of six 20-foot laboratory containers as well as a refrigerated container that will serve as a cold storage room for samples. Each container contains a special laboratory area such as sample preparation, analysis room or biogas test reactors. The equipment will represent the current state of the art and includes:

- a biogas test laboratory with continuously stirred tank reactors (CSTR) and batch test reactors.

- a gas chromatography laboratory for measuring organic acids and alcohols in the biogas process

- a laboratory for the determination of total organic Nitrogen (crude protein, XP), cellulose, hemicellulose and lignin (crude fibre, XF) and lipids (crude fat, XL)

- a laboratory for general analyses with drying technology, centrifuge and weighing technology

- a special area for sample preparation such as sorting and grinding

Examples of the respective equipment at the DBFZ are shown in Figure 2 to Figure 5. The container lab will be equipped accordingly.

The entire container building will be equipped with a central exhaust air system and de-ionised water will be provided by a central treatment plant at several tap points.

Figure 2: Lab reactors (CSTR) with 15 L working volume

Figure 3: Batch test system for automated determination of Biomethane potential

Figure 4: automated system for analysis of lipids (crude fat, XL)

Figure 5: system for automated disintegration to determine cellulose, hemicellulose and lignin (crude fiber, XF)

The biogas laboratory will contain essentially the same equipment as the biogas laboratory at the DBFZ site in Leipzig. Before the end of this year, a group of scientists and technicians from the University of Lomé will travel to Leipzig and receive comprehensive training and hands-on training at the biogas laboratory of the DBFZ. The aim of this training is not only to provide the colleagues from Togo with analytical training, but also to teach them basic maintenance and repair skills. The second part of the training will then take place in the completed laboratory building in Lomé. DBFZ scientists and technicians will then start up the laboratory together with their Togolese colleagues and support them in establishing the respective methods.

The planning of the container construction has been completed, all details of the furnishing and equipment have been specified. The layout of the entire container building is shown in Figure 6. The dimensions and dates for the preparation of the foundation and the necessary connections (electrical, water, sewage) have been determined.

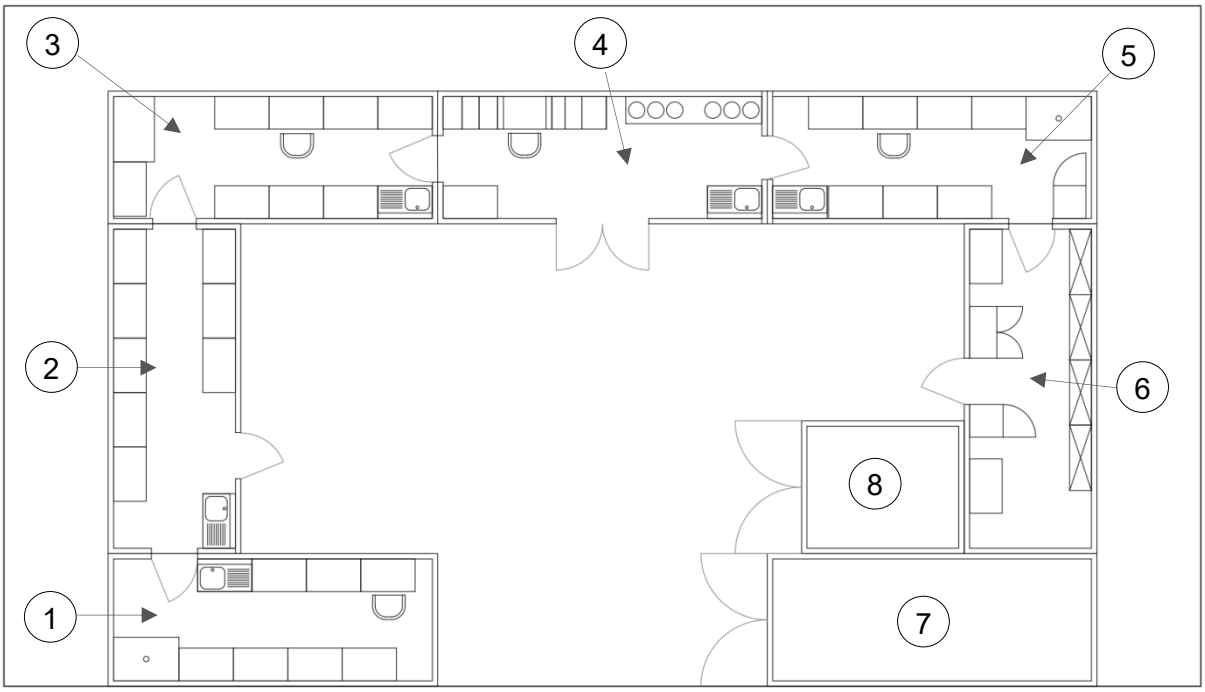

Figure 6: floor plan of the lab container building

1: lab for XF, XP, XF

2: sample preparation and milling are

3: lab with drying ovens, muffle furnace and general working area

4: Biogas lab with CSTR and Batch-Test-Systems

5: analytic lab witch GC-FID

6: store for chemicals, gas cylinders, samples / water purification unit

7: cold store (refrigerated container)

8: central energy hub

Work package 3: Studies on alternative methods for cooking stoves

Most of the people in Togo are currently still cooking with traditional open fire. This causes not only health problems due to the emissions but also a financial burden since the fuel has to be purchased in the form of wood or charcoal. In addition, direct use of wood is not sustainable considering the higher risks of deforestation and is therefore also problematic for ecological diversity and the climate.

In the meantime, a large number of stoves have been developed and used in field tests all over the world. Particularly in poorer regions, however, these are too expensive for the population due to the high selling price, depending on the type of the required material for the production (e.g. steel). Within the project, it is aimed to develop a low-cost and fuel-flexible stove which is easy to produce in the country and generates low emissions.

For this reason, a burner based on the use of liquid ceramic and with active ventilation is to be developed, which will be included in the existing pot holder of the usual used three-stone-fire. Although the use of active ventilation increases the costs, it is possible to enable lower emissions and better controlled combustion process. The extensive substitution of steel by ceramics should result in significantly lower production costs, which should compensate the use of active ventilation, so that a lower overall price can be achieved.

Since stoves with active ventilation require electricity, both a low-cost power control unit for the fan and the complete decentralized electrical infrastructure based on solar energy will be planned and tested on site.

Project status and first results

Project progress was significantly delayed in the first year, largely due to national and international constraints related to the COVID-19 pandemic. Despite these difficulties, progress was made in the crucial points of the individual work packages, which represent important building blocks for further successful project processing.

Outcomes of WP1

Figure 7 visualizes the methodological approach of change detection analysis, which is used for the identification of preference regions for biogas and pyrolysis activities. The detailed map shown in the upper circle exemplarily highlights areas exposed to large scale agricultural (red color) and urban (purple color) expansions.

First results of the change detection analysis between years 2001 and 2019 show, that extensive urban expansions especially appear around northern suburbs of the capital city Lomé. Nevertheless, smaller patches of urbanization can also be found in other regions. Newly established farmland can be detected in all regions with varying extents and is predominately established on woody areas and tree-savannas. Nevertheless, forests are degraded and converted to savannas and therefore, the expansion of arable land has to be regarded as a dominant driver for tree cover losses. The direct conversion of primary forests to agricultural areas cannot be detected at large scale.

Even though, global datasets derived from National Aeronautics and Space Administration (NASA) satellite imagery with international land cover classification schemes were used to identify relevant changes, the methodological approach of change detection analysis could also be repeated with locally explicit spatial information, if provided to the project, in order to enhance the level of detail.

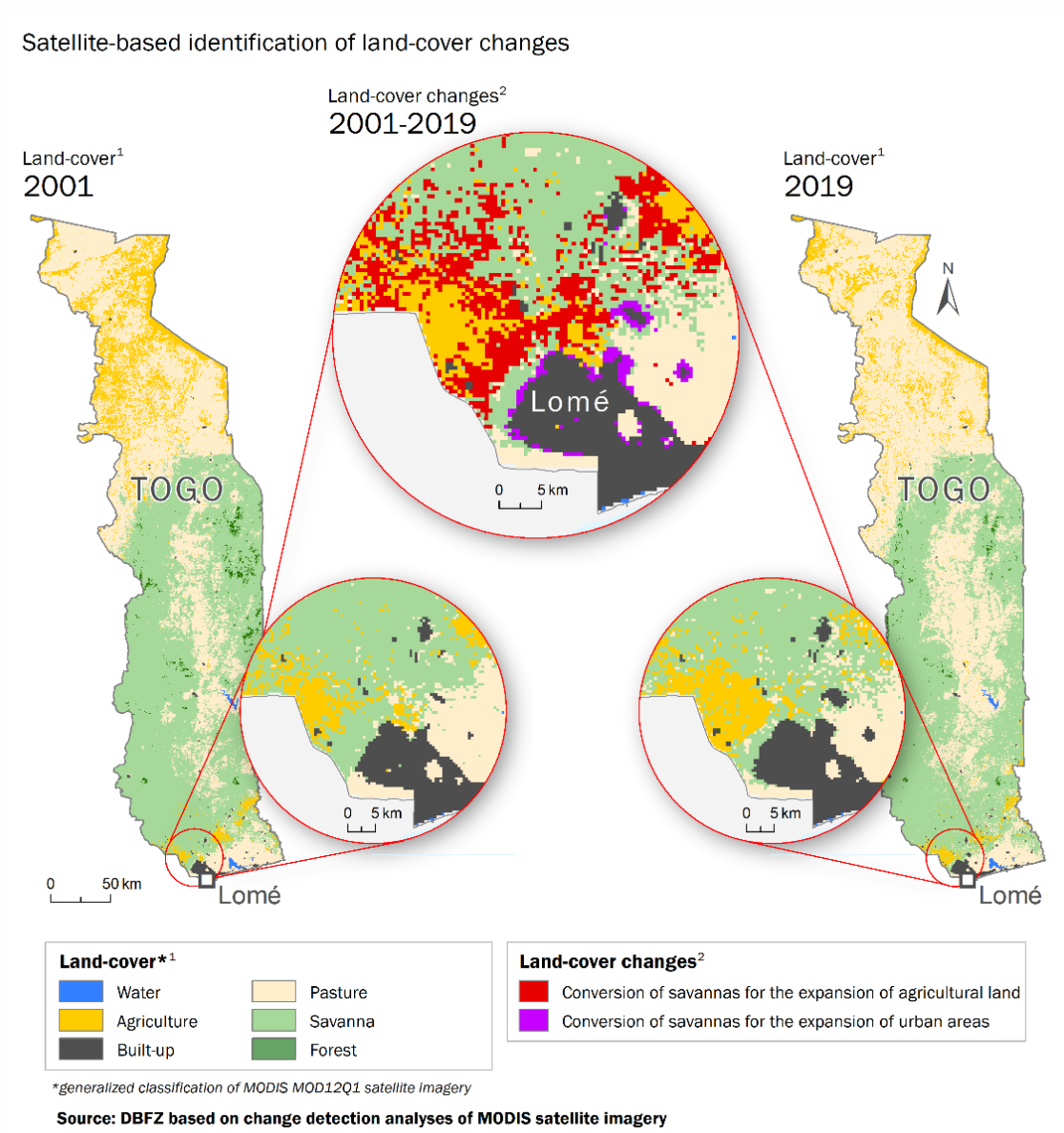

Figure 7 Simplified visualization of Change Detection analysis for the identification of preference region for biogas production

Outcomes of WP 2

The equipment for the laboratory has been specified in detail and the procurement process is underway. The first equipment has already been purchased and further devices will follw step by step. The initial commissioning of the laboratory equipment will take place in Leipzig. The equipment will be transported to Lomé in a refrigerated container once the entire equipment has been purchased. The refrigerated container will then remain in Lomé as part of the biogas laboratory (container No. 7 in Figure 6).

At the Université de Lomé, the granted site for the container Laboratory instalment is being prepared according to its specifications provided by the DBFZ. Main works done is the earth work and excavation including site clearance, leveling of the platform by removing soil layer with plant at a depth of at least 30 cm, backfill with laterite, backfill with crushed sand. The concrete and masonry and the remaining of the work to complete the site preparation will start before the end of March 2021 as the contractor selected provided detailed

documents which is submitted to the finance office for control before the go ahead of continuing.

Outcomes of WP3

So far, studies have been carried out about the production process with liquid ceramics and on the determination of the parameters for the combustion technology.

In the field of electronics and energy supply, the power control for the fan was developed and tested and the electrical infrastructure was planned.

Project outlook and summary

It is expected that substantial progress will be made in all three work packages this year. The field surveys, as shown in Table 1 and Table 2, have started and will provide extensive data for WP1. By including also biogenic waste, these data will also be important for further national strategic plans such as waste management concepts. As soon as the resource mapping delivers first results, the technology assessment for the identification of optimal utilisation strategies will be started. The main points of WP2 are to be completed before the end of 2021.

The execution of the container construction for the biogas lab has been put out to tender. It is expected that the contract will be awarded by mid-2021 and that the container construction will be completed in 2021. Transport to Togo and final assembly are planned for early 2022.

Later this year, a group of scientists and laboratory technicians from Togo will travel to Leipzig for a comprehensive training programme. The programme will include the methodology of various experimental and analytical investigations as well as a practical part including the maintenance and repair of laboratory equipment.

After the container construction in Lomé is completed, the second part of the training programme will be carried out there by scientists and laboratory technicians from Leipzig in the first half of 2022. Together with the Togolese colleagues, the complete commissioning of the laboratory will thus be carried out.

The prototype of the pyrolysis cooker will be tested and optimised in the coming months with real fuels, such as those available in Togo. The results of the field survey will also provide important data on the fuels used and their potential use. As soon as the final design has been determined, preparations for the production of the cookers in Togo will begin. Substantial progress is also expected here in the course of 2021.

2nd German-West African Conference on Sustainable, Renewable Energy Systems SusRES – Kara 2021

Biomass Energy

https://doi.or/10.52825/thwildauensp.v1i.13

Published: 15 June 2021

Estimation of the Amount of Electrical Energy Available From the Biogas Produced in the City of Sokodé

Nitale M'Balikine KROU[1][https://orcid.org/0000-0001-7091-3559], Gnon BABA [2][https://orcid.org/0000-0003-0168-0362], Ogouvidé AKPAKI [1][https://orcid.org/000-0001-9816-5580]

[1] University of Kara, Togo

[2] University of Lomé, Togo

Abstract. The purpose of this study is to estimate the amount of energy produced from biogas at the faecal sludge treatment plant in the city of Sokodé. The methodological approach consisted in producing biogas by co-digestion of faecal sludge with the fermentable fractions of solid waste then in estimating the quantity of energy available from the produced biogas. Tests of co-digestion of faecal sludge and fermentable fractions of solid waste, showed that from 2258 tons/DM of biomass in one year, 44476 m3 of biogas, or 29177 m3 of methane could be produced. The methane content, which is 65.6 %, is a very interesting source of energy. Several techniques for producing energy from biogas exist, one of which is the production of electricity. In this study, it is a question of making the choice of an adequate electric motor which will allow to produce electric energy from the biogas on the faecal sludge treatment plant. Thus, it was necessary to estimate the quantity of energy available from the biogas produced. To do so, it was calculated the quantity of energy that can be produced by the biogas in one year, the quantity of recoverable energy produced in a year and the quantity of energy supplied by biogas in one hour. The results showed that by 2035, the co-digestion of fermentable solid waste and faecal sludge from the city of Sokodé, would produce 534,246 kWh. The recoverable part would be 507,534 kWh and the energy supplied is 58 kWh.

Keywords: Biomass, biogas, electrical energy, faecal sludge.

Introduction

Non-traditional biomass to be used to improve electricity production by biogas processes in Africa seems to be innovative whereas decentralized small-scale biogas units locally are used. The widespread application of big scale biogas digesters still is missed. Faecal residues of human origin fermentation usually requires addition of co-substrates such as corn or wheat to improve the feasibility, what is not adequate for Africa. Hereby, traditional biomass as straw etc. as well as bio-waste or other organic waste could be suitable.

In Togo, as in most developing countries, the amount of energy produced is less than consumption [1]. Biomass, which is the main source of energy, represents 76 % of final energy consumption, with mainly wood fuels, in particular fuelwood, charcoal and certain agricultural residues. Despite the fact that energy production remains below demand, the energy supplying countries in Togo only reduce the amount over time as the demand only exacerbates. In order to fill this vacuum which continues to widen further, the use of renewable energies has become essential [2]. In this context, the production of biogas from fermentable waste is an opportunity for the diversification of energy resources and sustainable management of the environment. The production of biogas through organic

waste and its use could increase the economic feasibility of sanitation projects through the production of electricity. The use of biogas will directly contribute to meeting the challenges of climate change and responding to Togo's current energy challenges. Indeed, biogas is a renewable fuel gas resulting from the degradation of animal or plant organic matter by microorganisms under anaerobic conditions. This gas is mainly composed of methane (CH_4) and carbon dioxide (CO_2). The energy potential of biogas results from its methane content, the lower calorific value (LCV) of which is 9.94 kWh / Nm [3]. First used for the stabilization of sludge, anaerobic digestion has advantages for today's society. Upstream, this is a relevant way to treat waste, and downstream, it is a response to the pollution problems generated by the consumption of fossil fuels and the depletion of these resources. Biogas is an interesting source of energy since, on the one hand, it comes from a renewable resource (e.g organic waste) and on the other hand, its recovery ensures a reduction in GHG emissions, methane having a power of global warming greater than carbon dioxide. Its use therefore has a double environmental advantage [3]. Biogas is usually burned to produce heat and electricity in cogeneration [4]. Thanks to the combined production of heat and electricity, energy losses could be reduced significantly [5]. The combustion of biogas in an engine or turbine produces mechanical energy called primary energy. This energy is recovered and then used as electrical energy and heat with an overall efficiency of up to 90 % [6]. This technology can meet the needs of industrial applications, rural electrification, district heating and large-scale power generation. However, the water saturation of the biogas as well as the presence of CO_2 and possible H_2S are likely to make the biogas corrosive. In addition, biogas contains other compounds in trace amounts such as volatile organic silicon compounds or halogenated compounds. These trace compounds present in biogas are a brake on its energy recovery. Thus, upstream of its conversion into energy, extensive treatment of the biogas is therefore essential for such an application. It will therefore be necessary to include at least a stage of condensation of the water vapor or to go through a stage of purification.

According to the principle of converting biogas into electrical energy, the biogas is burned and the energy released feeds a generator which produces electricity. Indeed, the main composition of biogas is methane. Biogas thus has chemical energy, and the electricity produced by biogas therefore comes from the conversion of this chemical energy into mechanical energy and ultimately into electricity. Feedback has shown that this conversion is done through the use of generators and turbines which convert energy from one form to another. This involves connecting the source of biogas such as the bottle containing pressurized gas or a digester to the inlet of the gas engine and then connecting the gas engine to the alternating current generator so that the shaft rotary feeds the generator with alternating current. The movement transferred to the generator produces electricity by magnetism. The generator is connected to cables that transfer electricity to a rechargeable battery for storage or directly to an electrical distribution network for consumption. Tests of co-digestion of faecal sludge with the fermentable fractions of solid waste from the city of Sokodé in Togo, showed a significant production of biogas with a proportion of more than 65 % of methane. This high proportion of methane is a source of energy that could be converted into electrical energy for lighting the Sokodé faecal sludge treatment plant. Thus, the objective of this work is to estimate the amount of energy available from the biogas produced by the co-digestion of faecal sludge and fermentable fractions of solid waste. Methane is the origin of the use of biogas as an energy source. Estimating the amount of energy produced from biogas requires prior knowledge of the Lower Calorific Value (LCV) of the methane contained in this biogas. In fact, the LCV corresponds to the combustion reaction with the formation of water in the gaseous state. The LCV of biogas is proportional to its methane content [7]. It is therefore between 10.74 MJ. Nm^{-3} and 25.06 MJ. Nm^{-3} for a methane content between 30 and 70 % [8].

Materials and methods

Amount of biogas and proportion of methane

The main purpose of anaerobic digestion is the production of biogas. In this study, biogas was produced by co-digestion of faecal sludge and fermentable fractions of solid waste. The tests were carried out in digesters. The pilot digesters were connected through gas supply pipes, to inverted test tubes immersed in a beaker containing a trap solution, consisting of water saturated with NaCl and acid (5 % hydrochloric acid, 20 % NaCl and pH = 2) in order to minimize the dissolution of CO_2 in the biogas [9, 10]. This aqueous trap solution makes it possible, by moving the liquid, to properly quantify the daily production of biogas. The volume of biogas is measured using a hydraulic system (liquid displacement). The gas produced at the exit of the digester passes into a graduated cylinder immersed in a liquid, which will displace the level of the liquid contained in the cylinder and thus indicate the volume of the gas produced (**figure 1**).

Figure 1. Biogas production device

The proportion of methane is obtained by formula 1.

$$\%\text{methane} = \frac{\text{Quantity of methane obtained}}{\text{Total amount of biogas}} \quad (1)$$

Energy that can be produced by biogas in one year

The energy produced by biogas is calculated from the Lower Calorific Value (LCV) of methane which is 9.94 kWh/m^3 under normal temperature and pressure conditions [6]. The total energy is obtained by the formula 2.

$$\text{TotE} = \text{LCV} \times \text{V}_{\text{CH4}} \quad (2)$$

Recoverable energy produced in one year

We allow 5 % energy loss in order to be sure that an engine is rather overfed than underfed. The energy recoverable by an engine is therefore obtained by formula 3.

$$\text{ER} = 0.95 \times \text{TotE} \quad (3)$$

Calculation of the energy supplied by the biogas in one hour

The energy supplied by biogas in one hour is obtained by formula 4.

$$\text{ES} = \frac{\text{ER}}{(365 \times 24)} \quad (4)$$

Results and discussion

Amount of biogas and proportion of methane

The results of the co-digestion show that from 1 L of co-substrate in 42 days of co-digestion, an average production of 4 L/g.DM is estimated, or a volume of approximately 3 L of CH_4. This quantity of methane corresponds to a proportion of 65.6 % CH_4. From these results, an extrapolation of the quantities of biogas and methane by 2035 was established (Table 1). This extrapolation is made from the equation of the curve obtained during the co-digestion tests. These tests consisted in establishing the production of biogas by varying the amount of co-substrates.

Table 1. Quantities of biogas and methane estimated by 2035

Year	Total amount of co-substrates (t.DM)	Volume of biogas (m^3)	Volume of CH_4 (m^3)
2018	1 853.22	36 508.00	23 949.25
2019	2 449.54	48 255.00	31 655.28
2020	2 470.34	48 665.00	31 924.24
2025	2 811.76	55 391.00	36 336.50
2030	3 435.08	67 671.00	44 392.18
2035	4 158.96	81 931.00	53 746.74

Table 1 shows that by 2025, the co-digestion of the fermentable fractions of solid waste and faecal sludge from the city of Sokodé would produce around 36,337 m^3 of methane. In 2030, production would be around 44,392 m^3 and in 2035 it would be 53,747 m^3. These quantities are quite large and could be used in households and solve the problem of gas stock in the city of Sokodé.

Quantity of energy produced, recoverable and supplied by biogas

The amount of energy produced by biogas is calculated from the LCV of methane. It is 9.94 kWh / m^3 under normal temperature and pressure conditions [11]. With regard to recoverable energy, it is calculated by admitting 5 % energy loss in order to be sure that the engine is rather overfed than underfed. The results obtained are presented in Table 2.

Table 2. Quantity of energy produced, recoverable and supplied

Year	Total energy produced (kWh)	Recoverable energy (kWh)	Energy supplied by the biogas in 1 h (kWh)
2025	361 190	343 131	40
2030	441 257	419 195	48
2035	534 246	507 534	58

Table 2 shows that by 2035, the co-digestion of fermentable solid waste and faecal sludge from the city of Sokodé, would produce 534,246 kWh. The recoverable part would be

507,534 kWh and the energy supplied is 58 kWh. This energy could be used to run an engine and supply the faecal sludge treatment plant in the city of Sokodé. The motor to be chosen must be able to operate between 50 % and 100 % of its nominal load, with an optimum efficiency of around 75 %.

Conclusion

The objective of this work was to assess the amount of energy produced from the biogas obtained from the co-digestion of the fermentable fractions of solid waste and faecal sludge in the town of Sokodé. The results obtained show that the quantity estimated at horizon 2035 is significant and could be used to run an engine and provide lighting for the faecal sludge treatment plant. The pilot tests were carried out on a laboratory scale and in future investigations, it will be a question of large-scale implementation of the technology for producing biogas and converting this biogas into energy. Moreover, this work is part of current research themes on renewable energies and for environmental protection. Thus, in the rest of the work, the assessment of the environmental impacts of this project will be addressed. In fact, it will be a question of making an assessment of the energy and emissions saved by the conversion of biogas into electrical energy, compared to the production of electricity using natural gas will be made. Knowledge of the CO_2 emissions saved would be an added value in terms of the project's contribution to reducing CO_2 emissions. With the saving of fossil resources, this project will also contribute to the energy independence objectives of the faecal sludge treatment plant in the city of Sokodé.

Acknowledgments

We are grateful for the Head of the Water and Environmental Sanitation Laboratory and Supervisor of this work, Professor Gnon BABA for funding.

REFERENCES

1. Samah H. Diagnosis of the energy situation in Togo. Togolese Republic: Ministry of the Environment, Department of Water and Forests; 2015.
2. Tcha-Thom M. Study of a sustainable way of methanization of fruit and slaughter wastes in Togo: Evaluation of the agronomic potential of digestate on the soil of Kara.. INIS; 2019 July, p. 205.
3. Sigot L. Fine purification of biogas for energy recovery in a SOFC-type fuel cell: Adsorption of octamethylcyclotetrasiloxane and hydrogen sulfide. Environment and Society. Lyon: INSA; 2014.
4. Lejeune P. Electrical and thermal recovery of methanization biogas. Paris: EFE training - Biomass for energy uses; 2008.
5. Haushalter J. Sizing of a biomass cogeneration. Mulhouse: Wärtsilä; 2007
6. Couturier C. Techniques for producing electricity from biogas and syngas. 2009.
7. Heduit. Methanization of animal droppings. Depollution and energy production. General review of thermics. 1987;26(3):228-235.
8. Ohannessian A. Volatile Organic Silicon Compounds: A brake on energy recovery from biogas. Genesis and Mechanisms of Formation. Lyon: National Institute of Applied Sciences; 2008..

9. Akpaki O. Physico-chemical characterization of Attidjin faecal sludge (prefecture of the gulf-togo). Chemistry of Water and the Environment, University of Lomé; 2015, p. 167.

10. Pouech, P. Interest of co-digestion for the recovery of slurry and the treatment of fermentable waste at the scale of a territory. 37th Swine days' Research; Paris. 2005, 39-44..

11. Couturier C, Berger S, Hérau I. Anaerobic digestion of urban sludge. Toulouse: Water Agency Adour-Garonne; 2001.

2nd German-West African Conference on Sustainable, Renewable Energy Systems SusRES – Kara 2021

Biomass Energy

https://doi.org/10.52825/thwildauensp.v1i.18

Published: 15 June 2021

Optimization of biogas production by co-digestion of organic waste (cow dung and water hyacinth)

Alfred D. DOHOU*[1,2,3], KOTO N'GOBI Gabin[1,2,3], Clément A.KOUCHADE[1,2,3], Basile B. KOUNOUHEWA[1,2,3]

[1]Laboratoire de Physique du Rayonnement (LPR), Bénin

[2]Département de Physique, Bénin

[3]Université d'Abomey-Calavi, Bénin

Abstract. The objective of this work is to determine the co-digestion ratio of water hyacinth and cow dung for the optimization of biogas production at Sô Ava, a lake city of Southern Benin. To achieve these ratios, we suppose that the water hyacinth has a high gas yield and cow dung ensures stability in the biodigester because it brings fresh bacteria and has a strong buffering capacity (maintenance of a stable pH). For 45 days, we have introduced a mixture of water hyacinth and cow dung in 5 mini-biodigesters of 10 liters each: digester n°1 (100% of cow dung); digester n°2 (100% of the water hyacinth); digester n° 3 (50% of the water hyacinth and 50% of the cow dung); digester n°4 (75% of cow dung and 25% of water hyacinth); digester n°5 (75% of the water hyacinth and 25% of the cow dung). The measurements of the pH, temperature and the proportion of gas (CH_4, CO_2, O_2 and H_2S) in the mini-biodigesters was done. The measurements show that the digester n° 5 produces the highest capacity of 15.24L of biogas with 70% of methane while the digester n °2 has the lowest capacity 5.47L of biogas with 58% methane. These results show that the yield of biogas produced is greater when using the mixture of the substrate with the ratio of 75% of water hyacinth and 25% of cow dung. This result encourages the energy recovery from water hyacinth, once considered as a seasonal plague which hinders navigation of local boat in the lake.

Keywords: co-digestion, cow dung, water hyacinth, optimization

Introduction

Anaerobic digestion is the biochemical process of producing biogas by transforming complex organic materials into a clean, renewable source of energy. The co-digestion process is a reliable alternative process which is used to solve the environmental drawbacks of the substrate management. The use of co-substrates generally improves biogas yields due to the positive synergies established during the digestion process and the supply of missing nutrients by the co-substrates [1]

Several studies have been carried out on the production of biogas using different biomasses as mono-substrates [2],[3]. However, the direct use of substrates is difficult due to their nutritional imbalance, which usually lack of microorganisms and the effect of operational factors. The process of co-digestion has been recommended to overcome these difficulties [4]. Anaerobic co-digestion has been widely used to improve biogas production. A number of published articles have investigated co-digestion in recent years. Astals et al [5] studied the co-digestion of livestock manure with other different biomasses to improve biogas production rates [6] reported that the combination of whey and poultry manure was found to be able to

maintain the correct C/N (Carbon to nitrogen ratio) ratio in the reactor. According to Murto et al (2004) [7], a highly buffered system was obtained by co-digestion of solid wastes, manure, fruit and vegetable waste. The process worked well with a gas yields reaching 0.8 m^3kg^{-1} of dry matter. Somayaji et al [8] conducted a study with digesters fed with cow manure and varying proportions of wheat straw and concluded that the highest specific methane yields were observed with 40% straw of wheat total solids in the raw material. Ghaly et al [9] studied a 155 L two-stage, two phases unmixed anaerobic reactor for treating whey with dairy manure and concluded that the pH should be controlled at the methanogenic phase; otherwise the production of biogas was not possible. The anaerobic co-digestion of grass silage, sugar beet tops and oat straw with cow manure was evaluated by Lehtomaki et al [10] in continuously stirred tank reactors. In the laboratory supplied semi-continuously.

Gelegenis et al [11] reviewed a series of laboratory experiments in continuously stirred tank reactors under mesophilic conditions, semi-continuously filled with various mixtures of diluted poultry manure and whey. Co-digestion of whey with manure has been shown to be possible up to a 50% participation of whey (by volume) in the daily feed mixture without any addition of chemicals. Anaerobic co-digestion of sludge from grease traps and sewage sludge has been successfully performed in both laboratory batch trials and pilot scale continuous digestion trials [12]. The possible use of the potato tuber and its industrial by-products (potato tubs and potato skins) for farm-scale co-digestion with pork manure was examined in laboratory by Kaparaju and Rintala [13]. The results showed that the potato tuber and its industrial by-products can be co-digested with pig manure at a loading rate of 2 kg VS m^{-3} day^{-1} in continuously stirred tank reactors at 35 ° C. The proportion of waste in the mixture appears to be large and the feed may contain at least 15-20% potato waste. Zupancic et al [14] carried out a large-scale experiment on the co-digestion of organic waste from household waste (swill) with municipal sludge. The results showed that anaerobic digestion is the solution to the handling of organic waste (swill) and above all it is very beneficial with little negative impact on the environment. An 80% increase in the amount of biogas was also observed. The potential of semi-continuous mesophilic anaerobic digestion for the treatment of solid waste, fruit-vegetable waste and manure in a co-digestion process has been experimentally evaluated and presented by Alvarez et al [15]. They found that a combined treatment of different types of waste such as manure (cattle and pigs), solid waste from slaughterhouses (rumen, rumen and blood of cattle and pigs) in a mesophilic co-direction process gives the possibility of treating waste, which cannot be treated separately. The feasibility of anaerobic co-digestion of mixed industrial sludge with municipal solid waste was investigated in three simulated anaerobic landfill bioreactors over a period of 150 days [16]. They concluded that the anaerobic co-digestion of industrial sludge with organic wastes is a feasible process in waste stabilization and in the treatment of leachate releases from simulated anaerobic reactors. Gomez et al [17] presented the results obtained for the digestion of primary sludge and the co-digestion of this sludge with the fruit and vegetable fraction of municipal solid waste under mesophilic conditions. The co-digestion of the fruit and vegetable fraction of municipal solid waste with the primary sludge produced more biogas than the digestion of the primary sludge, due to the higher concentration of volatile solids contained in this feed. The feasibility of anaerobic co-digestion of five coffee wastes from the production of coffee and sewage sludge was assessed by Neves et al [18]. Methane yields of between 0.24 and 0.28 m^3 / kg of VS were obtained with the exception of a barley-rich waste which only reached 0.02 m^3 of CH_4 / kg of VS. Fezzani et al [19] studied for the first time the thermophilic anaerobic (55°C) co-digestion of oil mill wastewater with solid waste from oil mills in semi-continuous tubular digesters at laboratory scale. They concluded that wastewater from oil mills could be successfully degraded by co-digestion with solid waste from oil mills under thermophilic conditions without prior dilution and without the addition of nitrogenous chemicals. The co-digestion of onion juice and aerobic wastewater sludge produced by an onion processor using an anaerobic mixed biofilm reactor was investigated by Romano et al [20] for the potential for biogas energy production and waste treatment.

Several articles have exposed the co-digestion of certain substrates, that of cow dung and water hyacinth is lacking to our knowledge. This is why the present work focuses on optimizing the production of biogas by co-digestion of organic waste (cow dung and water hyacinth).

Work hypothesis:

Co-digestion with a high percentage of water hyacinth in cow dung optimizes biogas production.

Material and methods

Material

Substrate

The substrate is made up of finely cut water hyacinth (grain size around 5cm), collected in the Nokoué Lake and cow dung collected in Agassa-Godomey. It was introduced into each mini-digester 6kg of the water hyacinth - cow dung mixture. Figure 1 and Figure 2 present the chopped water and cow dung used during the experiments.

Figure N°1: Chopped water hyacinth

Figure N°2: Cow dung in pretreatment

Experimental device

***The digester**

The five digesters are hermetically closed to ensure total anaerobiosis.

During the unfolding of the anaerobic digestion process, the air chamber collects the produced biogas.

*** Biogas volume measurement device**

The volume of biogas is measured every day using the displaced liquid method [21]

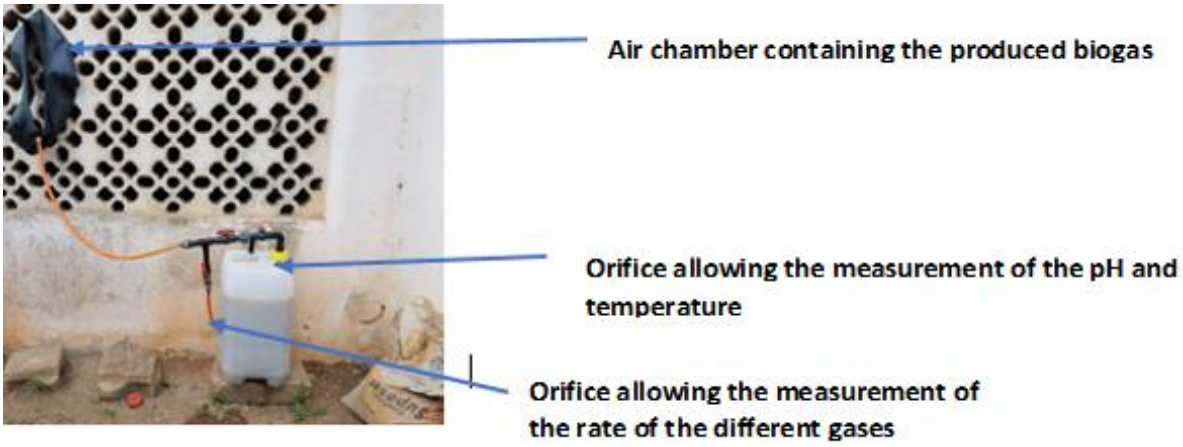

Figure N°3: Methanization device

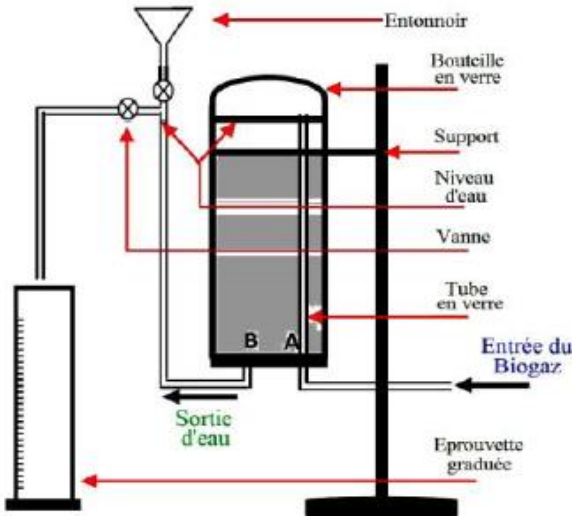

Figure N°4: Biogas volume measuring system [21]

*** The gas analyzer**

Figure N°5: Gas analyzer; IRCD4 model

Methods

We introduced into 5 cans with a capacity of 25 liters each, the mixtures of water hyacinth and cow dung in different proportions:

- digester n ° 1 (100% cow dung only);
- digester no. 2 (100% of the water hyacinth without inoculum);
- digester n ° 3 (50% of the water hyacinth and 50% of the cow dung);
- digester n ° 4 (75% of cow dung and 25% of water hyacinth);
- digester no.5 (75% of the water hyacinth and 25% of the cow dung).

These mixed remained for 45 days in the digesters.

The percentage of the 4 gases (CH_4, CO_2, O_2, H_2S) is measured daily from the 3rd day after putting the mixtures in the digester by molecular absorption spectrophotometry according to the protocols accompanying the equipment of the IRCD4 brand Biogas Analyzer Manual Instruction.

Results and analysis

pH variation

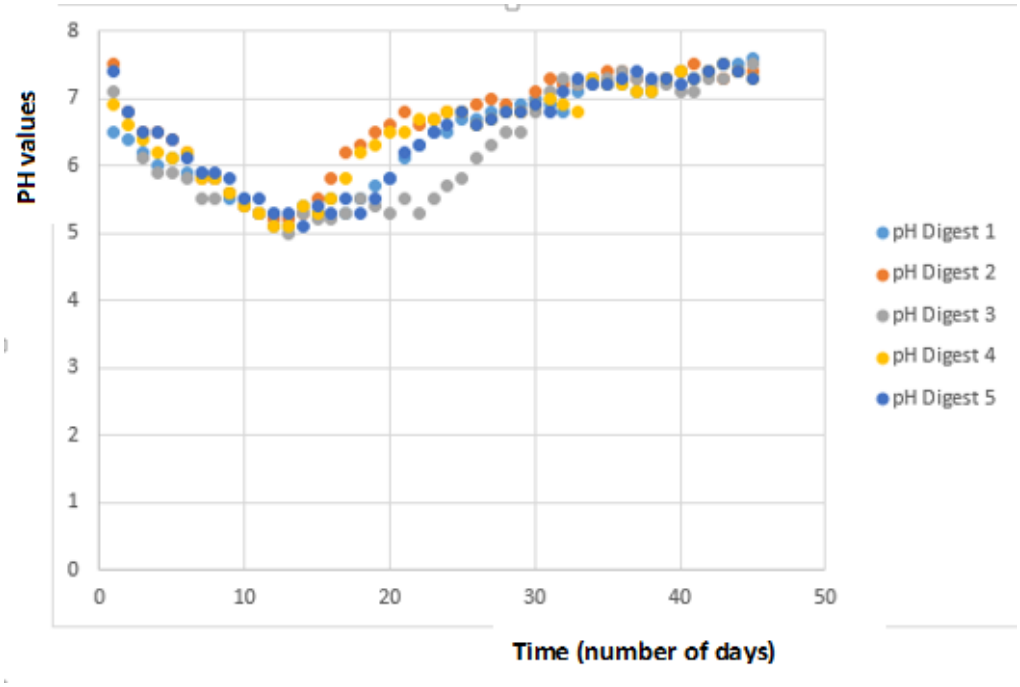

Figure N°6: pH variation in the 5 digesters

The figure 6 presents the change in pH during the experimental process. The pH values decrease from 5 to 7.5 during the first fifteen days of measurement in all the digesters it is the hydrolysis and acidogenesis phase. From the 16th day, the pH values begin to increase to reach a maximum value of around 7.5 on the 45th day for the majority of the digesters (acetogenesis and methanogenesis phase).

Adjusting the pH to around 7 promotes the development of methanogenic bacteria which are responsible for the formation of methane.

Temperature variation

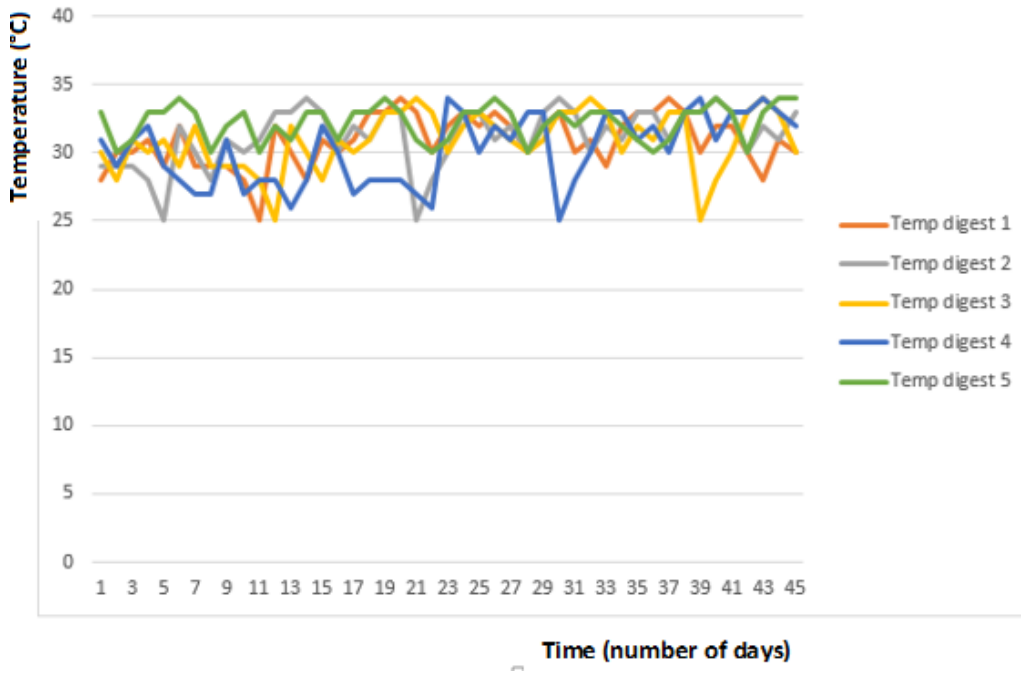

Figure N°7 : Temperature variation in the 5 digesters

The figure 7 shows the evolution of temperature during anaerobic digestion in the five digesters. From the measurement period,, the temperature fluctuated around 30°C (25°C à 35°C) Digestion is then carried out under mesophilic conditions which is one of the main conditions for optimizing anaerobic digestion.

Yield of CH_4, CO_2, O_2, H_2S in the biogas

The percentage of the different gases is read directly on the screen of the biogas analyzer. The Figure below illustrate the change in the level of CH_4, CO_2, O_2, H_2S in the biogas produced

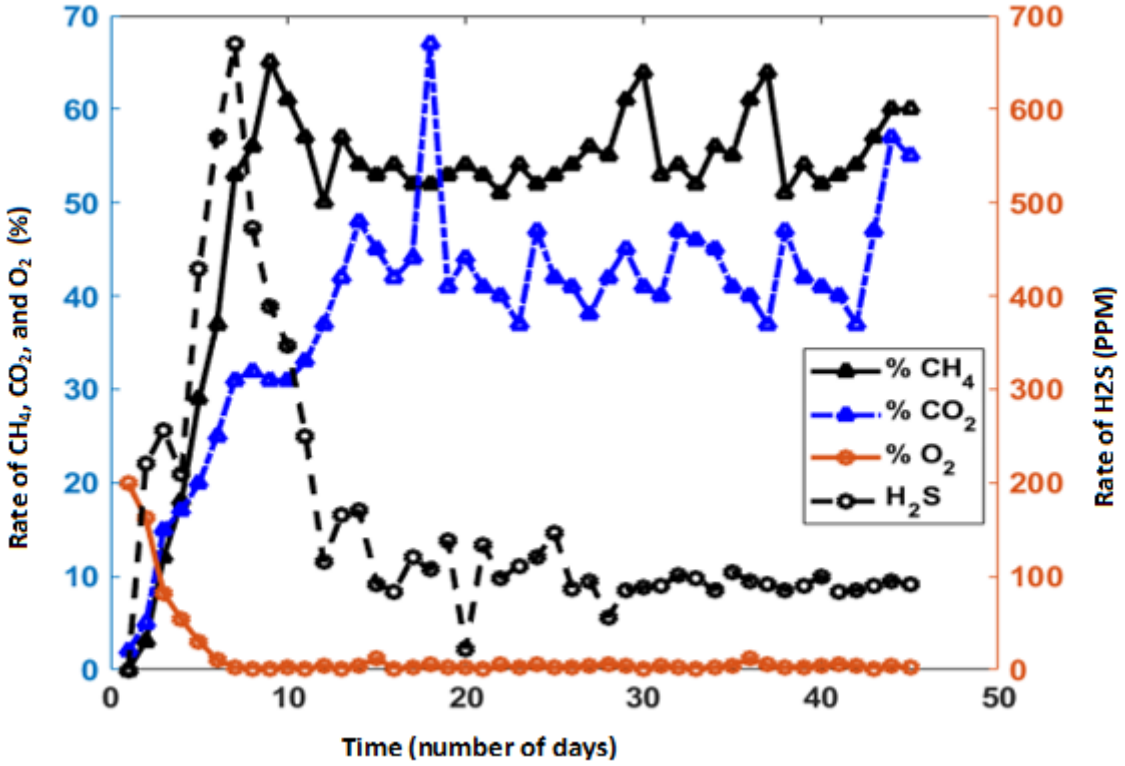

Figure N°8: Variation in the rate of CH_4, CO_2, O_2 and H_2S in the biogas produced in digesters N°1

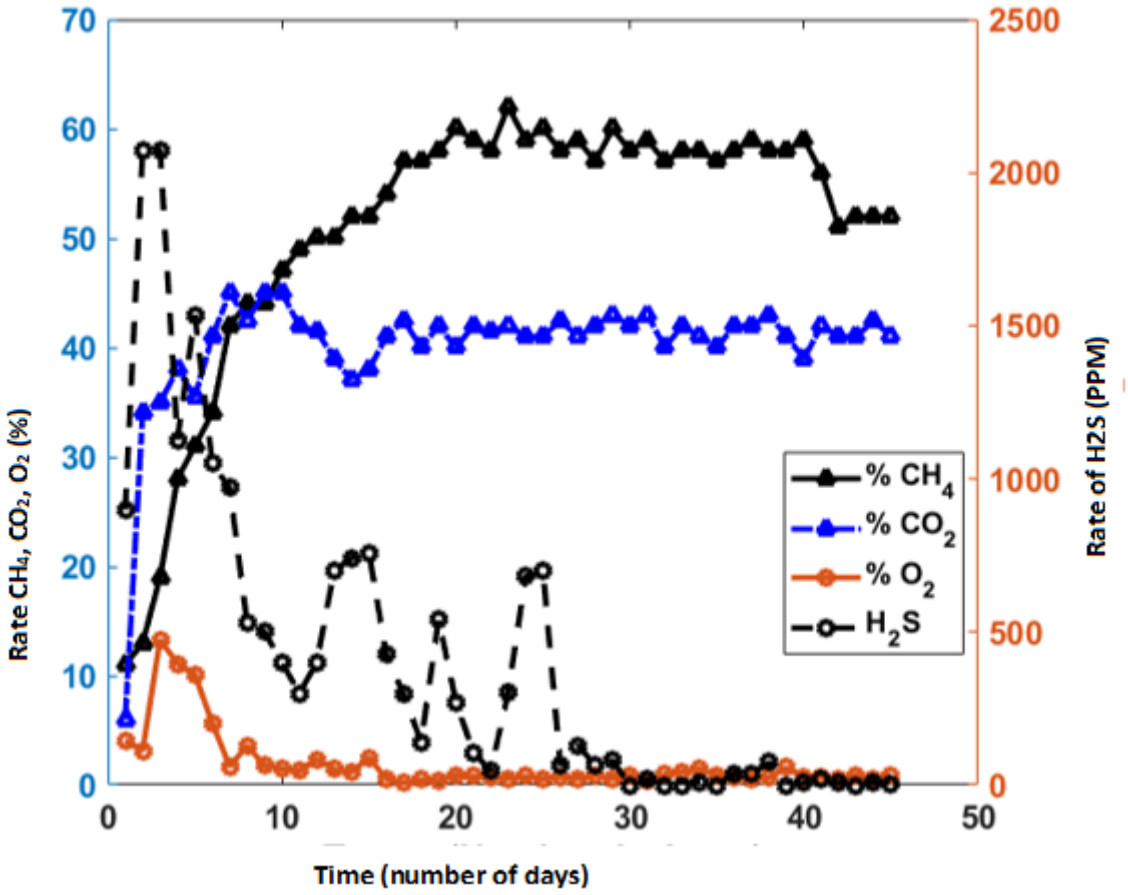

Figure N°9: Variation in the rate of CH_4, CO_2, O_2 and H_2S in the biogas produced in digesters

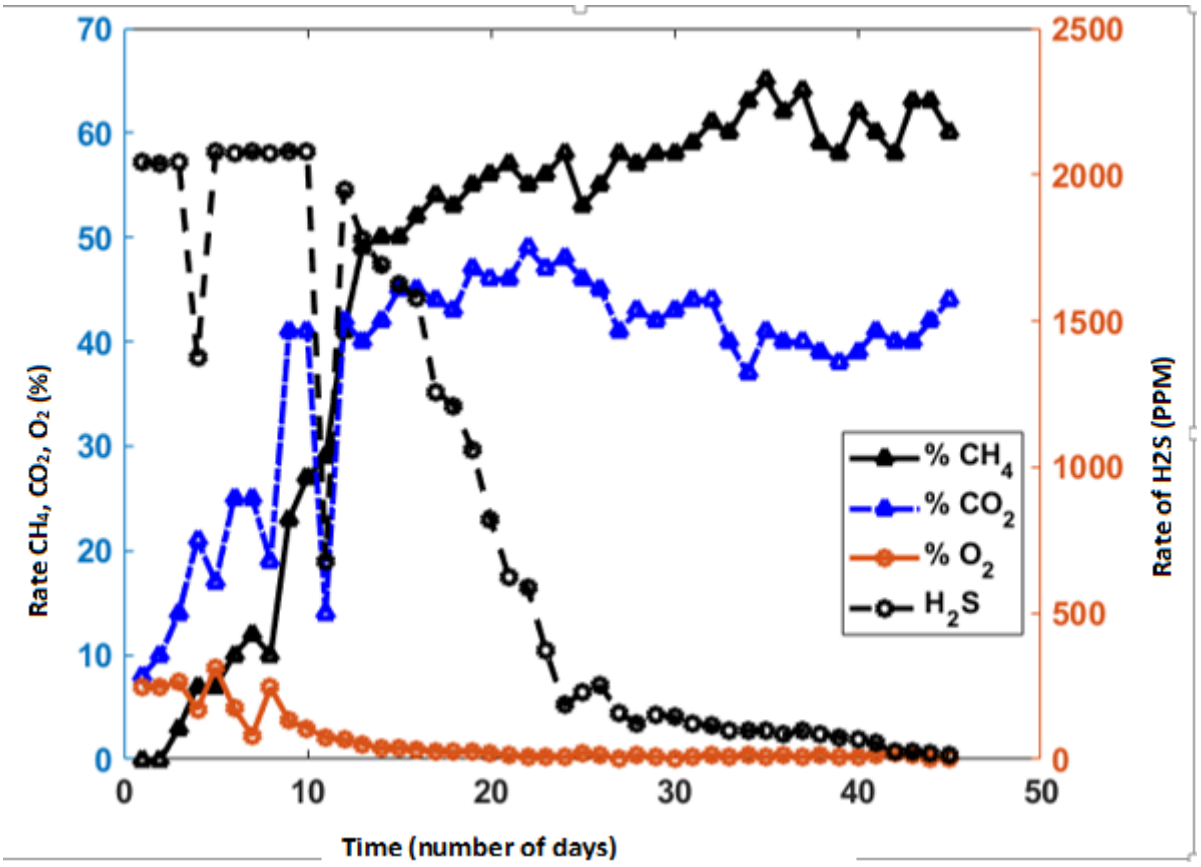

Figure N°10: Variation in the rate of CH_4, CO_2, O_2 and H_2S in the biogas produced in digesters N°3

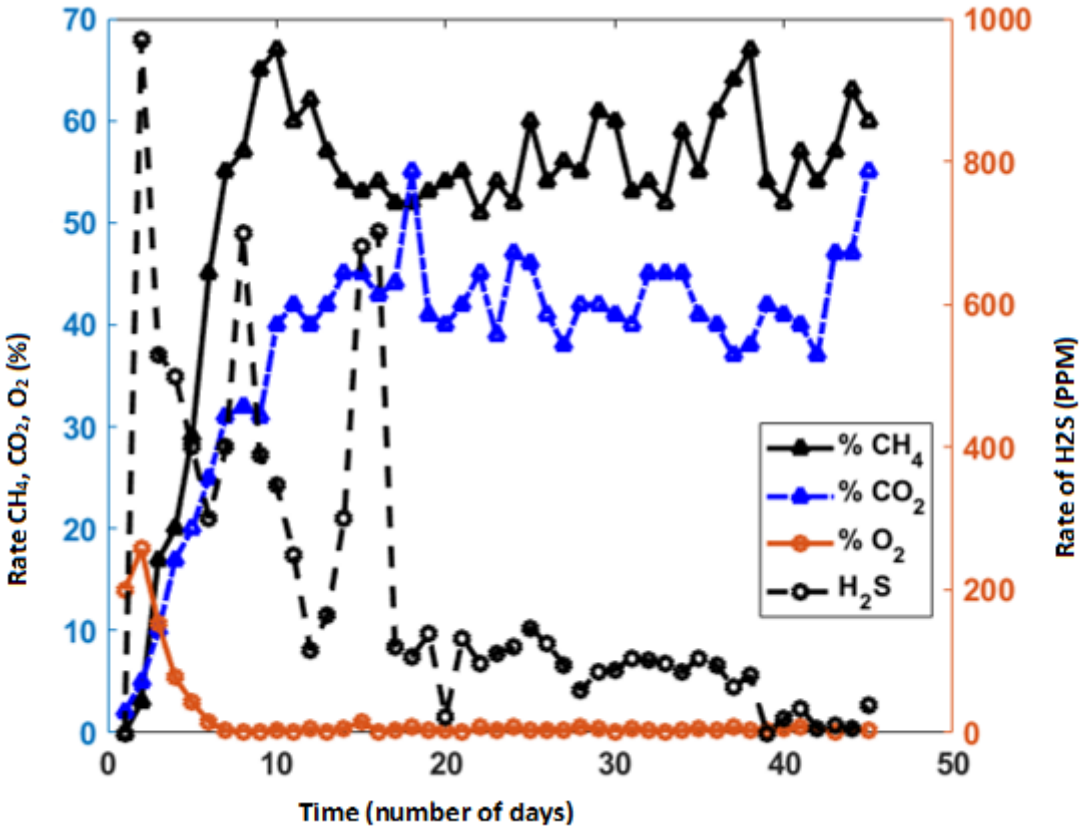

Figure N°11: Variation in the rate of CH_4, CO_2, O_2 and H_2S in the biogas produced in digesters N°4

In the first 10 days, the methane and carbon dioxide levels increased in all the five digesters showing the production of these gases. But, the O_2 level gradually decrease because of the anaerobic reactions in the biodigester. After the 10th day, the oxygen level fluctuated around 0.1% throughout the experiment. The level of H_2S has gradually decreased in all cases until it approaches 0 except in digester N°1 (Figure 8) where the cow dung is 100%. In the digester N1, after the 10th day, the CH_4 level increased before stabilizing around an average value of 60%. In digester N°2 (100% water hyacinth) we also notice a gradual increase in the CH_4 level till an average of 58%. In digester 3 (50% of the water hyacinth and 50% of the cow dung) the average level of CH_4 is 59%. Methane level also increased in Digester 4 (75% cow dung and 25% water hyacinth) and Digester 5 (75% water hyacinth and 25% cow dung). The average methane levels found are 60% and 70% respectively. We also notice that the concentration of CH_4 and CO_2 seems to mirror each other in any case as if the sum of the levels of these two gases were constant.

Variation in the volume of biogas produced

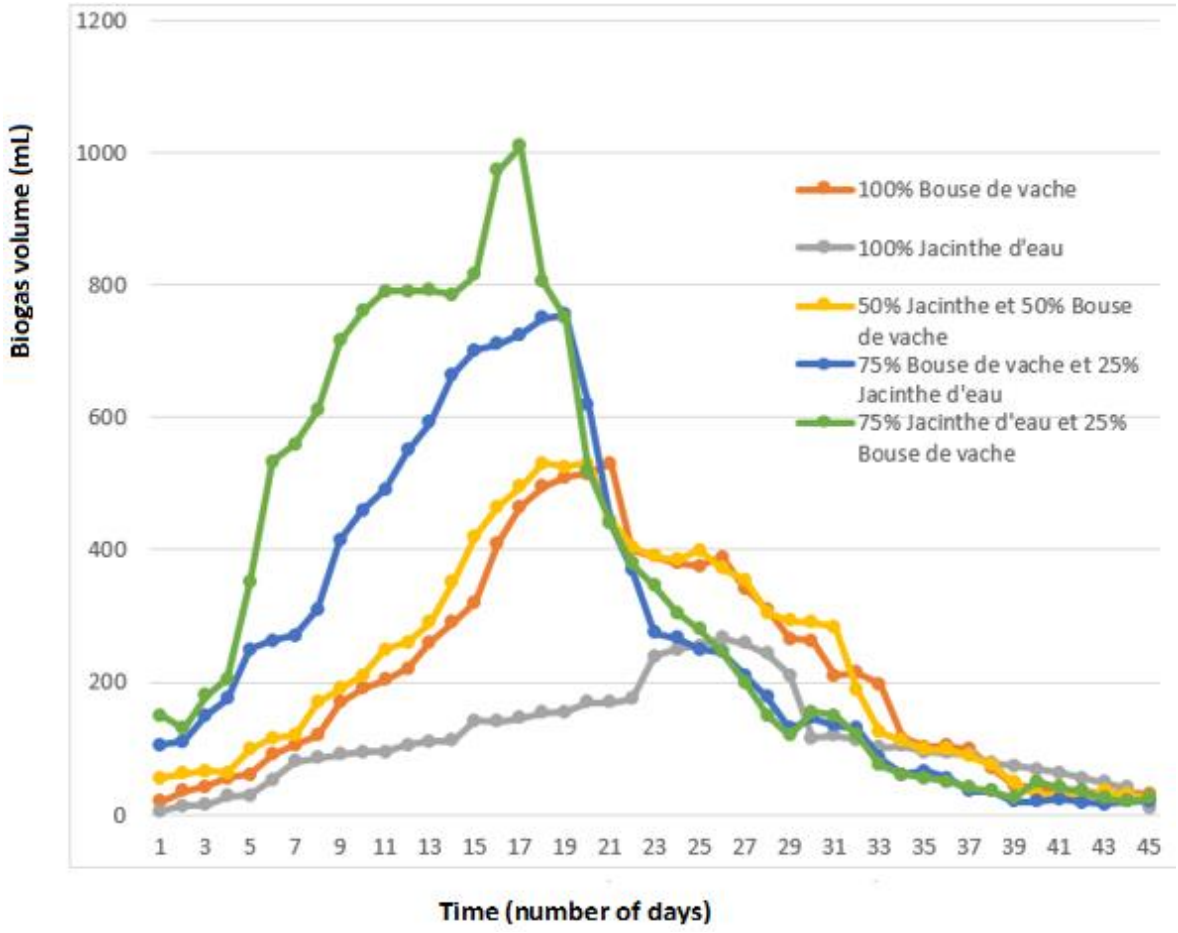

Figure N°13: Variation of the volume of biogas produced in each digester

Figure N°13 represents the change in the volume of biogas produced as a function of time. During the first ten days, the volume of biogas produced remains low and non-flammable (hydrolysis and acidogenesis phase). After the tenth day, the volume begins to increase variably for each digester. The best results are recorded at the level of digester 5 composed of 75% water hyacinth and 25% cow dung, with a maximum value of 1010 mL on the 20th day; while the low values are recorded at the level of digester 2 composed of 100% water hyacinth, the highest volume is 266 mL on the 27th day. Microorganisms have a hard time appearing in Digester 2 (100% water hyacinth) because there is no inoculum. The microorganisms promoting anaerobic digestion took a long time to appear in the environment. During this time, the other digesters produced biogas. This explains the yield

obtained at the level of digester No. 2. In digesters containing hyacinth, biogas was produced over a long period because the microorganisms had a large amount of organic matter.. In general, plant materials have a high gas yield because of the carbon inside it, as well as food waste rich in fats and proteins. Animal droppings have a lower energy power, but ensures stability in the culture medium because they provide fresh bacteria and have a strong buffering capacity (maintaining a stable pH). The results we have obtained show that in the case of semi-continuous digestion, substrate should be added already from the 15th day.

Total flammable volume produced by each digester

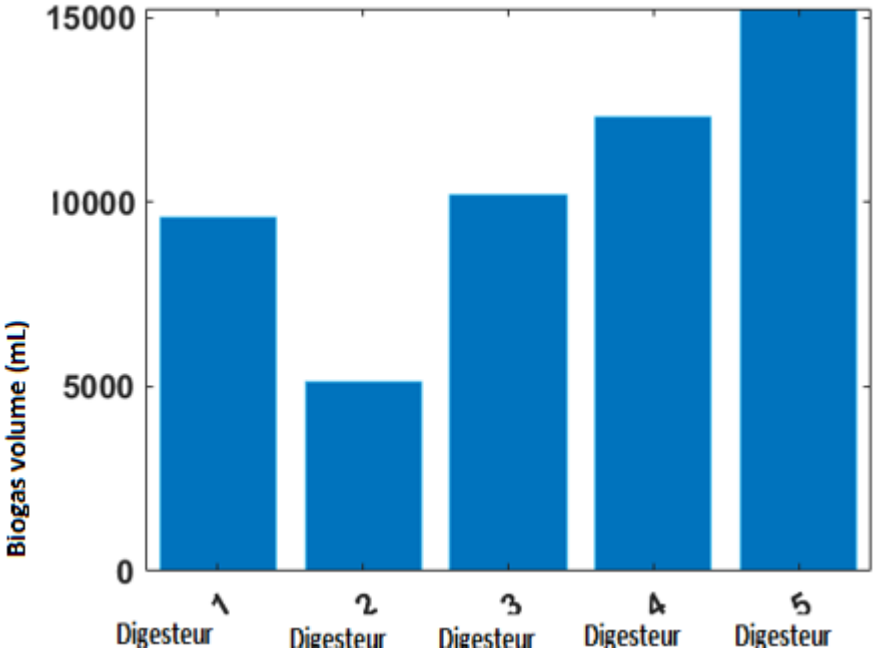

Figure N°14: Volume of biogas produced in each digester

Figure N°14 shows that the digester 5 has a higher value than the remains of the digesters (15249 mL), while the digester 2 gave the lowest value of the volume of biogas (5153mL). Digesters 2 and 3 have a similar gas production (9585 mL and 10189 mL).

Conclusion

The present study has shown that the biogas yield is greater for a substrate consisting of 75% water hyacinth and 25% cow dung with a rate of 70% methane, whereas for a substrate consisting of 100% of water hyacinth, biogas production is low with 58% methane. The initial hypothesis: Co-digestion with a high percentage of water hyacinth in cow dung optimizes biogas production is thus verified. On the other hand, we have found that in the case of semi-continuous digestion, substrate should be added already from the 15th day. The co-digestion of water hyacinth has been shown to be effective. It could no longer be considered as a constraint but as wealth. In the rest of our work, we will size the digester to estimate the amount of energy that could be produced using anaerobic digestion. We will thus estimate the number of households that could be supplied with energy, for example.

References

[1] Mata-Alvarez J, Macé S, Llabrés P. Anaerobic digestion of organic solid wastes. An overview of research achievements and perspectives. Bioresource Technology. 2000 08;74(1):3-16. https://doi.org/10.1016/s0960-8524(00)00023-7

[2] Khalid A, Arshad M, Anjum M, Mahmood T, Dawson L. The anaerobic digestion of solid organic waste. Waste Management. 2011 08;31(8):1737-1744. https://doi.org/10.1016/j.wasman.2011.03.021

[3] Salminen E, Rintala J. Anaerobic digestion of organic solid poultry slaughterhouse waste – a review. Bioresource Technology. 2002 05;83(1):13-26. https://doi.org/10.1016/s0960-8524(01)00199-7

[4] Astals S, Nolla-Ardèvol V, Mata-Alvarez J. Thermophilic co-digestion of pig manure and crude glycerol: Process performance and digestate stability. Journal of Biotechnology. 2013 07;166(3):97-104. https://doi.org/10.1016/j.jbiotec.2013.05.004

[5] Astals S, Ariso M, Galí A, Mata-Alvarez J. Co-digestion of pig manure and glycerine: Experimental and modelling study. Journal of Environmental Management. 2011 04;92(4):1091-1096. https://doi.org/10.1016/j.jenvman.2010.11.014

[6] Desai M, Patel V, Madamwar D. Effect of temperature and retention time on biomethanation of cheese whey-poultry waste-cattle dung. Environmental Pollution. 1994;83(3):311-315. https://doi.org/10.1016/0269-7491(94)90152-x

[7] Murto M, Björnsson L, Mattiasson B. Impact of food industrial waste on anaerobic co-digestion of sewage sludge and pig manure. Journal of Environmental Management. 2004 02;70(2):101-107. https://doi.org/10.1016/j.jenvman.2003.11.001

[8] Somayaji D, Khanna S. Biomethanation of rice and wheat straw. World Journal of Microbiology & Biotechnology. 1994 09;10(5):521-523. https://doi.org/10.1007/bf00367657

[9] Ghaly A. A comparative study of anaerobic digestion of acid cheese whey and dairy manure in a two-stage reactor. Bioresource Technology. 1996 Oct;58(1):61-72. https://doi.org/10.1016/s0960-8524(96)00105-8

[10] Lehtomäki A, Huttunen S, Rintala J. Laboratory investigations on co-digestion of energy crops and crop residues with cow manure for methane production: Effect of crop to manure ratio. Resources, Conservation and Recycling. 2007 09;51(3):591-609. https://doi.org/10.1016/j.resconrec.2006.11.004

[11] Gelegenis J, Georgakakis D, Angelidaki I, Mavris V. Optimization of biogas production by co-digesting whey with diluted poultry manure. Renewable Energy. 2007 Oct;32(13):2147-2160. https://doi.org/10.1016/j.renene.2006.11.015

[12] Davidsson Å, Lövstedt C, la Cour Jansen J, Gruvberger C, Aspegren H. Co-digestion of grease trap sludge and sewage sludge. Waste Management. 2008;28(6):986-992. https://doi.org/10.1016/j.wasman.2007.03.024

[13] KAPARAJU P, RINTALA J. Anaerobic co-digestion of potato tuber and its industrial by-products with pig manure. Resources, Conservation and Recycling. 2005 01;43(2):175-188. https://doi.org/10.1016/s0921-3449(04)00119-3

[14] Zupančič GD, Uranjek-Ževart N, Roš M. Full-scale anaerobic co-digestion of organic waste and municipal sludge. Biomass and Bioenergy. 2008 02;32(2):162-167. https://doi.org/10.1016/j.biombioe.2007.07.006

[15] Alvarez R, Lidén G. Semi-continuous co-digestion of solid slaughterhouse waste, manure, and fruit and vegetable waste. Renewable Energy. 2008 04;33(4):726-734. https://doi.org/10.1016/j.renene.2007.05.001

[16] Ağdağ ON, Sponza DT. Co-digestion of mixed industrial sludge with municipal solid wastes in anaerobic simulated landfilling bioreactors. Journal of Hazardous Materials. 2007 02;140(1-2):75-85. https://doi.org/10.1016/j.jhazmat.2006.06.059

[17] Gómez X, Cuetos M, Cara J, Morán A, García A. Anaerobic co-digestion of primary sludge and the fruit and vegetable fraction of the municipal solid wastes. Renewable Energy. 2006 Oct;31(12):2017-2024. https://doi.org/10.1016/j.renene.2005.09.029

[18] Neves L, Oliveira R, Alves M. Anaerobic co-digestion of coffee waste and sewage sludge. Waste Management. 2006 01;26(2):176-181. https://doi.org/10.1016/j.wasman.2004.12.022

[19] Fezzani B, Cheikh RB. Thermophilic anaerobic co-digestion of olive mill wastewater with olive mill solid wastes in a tubular digester. Chemical Engineering Journal. 2007 08;132(1-3):195-203. https://doi.org/10.1016/j.cej.2006.12.017

[20] Romano RT, Zhang R. Co-digestion of onion juice and wastewater sludge using an anaerobic mixed biofilm reactor. Bioresource Technology. 2008 02;99(3):631-637. https://doi.org/10.1016/j.biortech.2006.12.043

[21] Tahri A. Amélioration du rendement de la production de biogaz par co-digestion des déchets organiques (déchets d’abattoir et de volaille). Revue des Energies Renouvelables SIENR Ghardaïa. 2012 January;12:375-380.

2nd German-West African Conference on Sustainable, Renewable Energy Systems SusRES – Kara 2021

Hyrdrogen Energy

https://doi.org/10.52825/thwildauensp.v1i. 10

Published: 15 June 2021

Hydrogen and Usability of Hydrogen Storage Technologies

Liquid Organic Hydrogen Carriers (LOHC) versus other Physical and Chemical Storage Methods

Lutz B. Giese [1] and Jörg Reiff-Stephan [1[https://orcid.org/0000-0003-4176-6371]

[1] Technical University of Applied Sciences Wildau, Germany

Abstract: Science, technology and politics agree: hydrogen will be the energy carrier of the future. It will replace fossil fuels based on a sufficient supply from sustainable energy. Since the possibilities of storing and transporting hydrogen play a decisive role here, the so-called LOHC (Liquid Organic Hydrogen Carriers) can be used as carrier materials. LOHC carrier materials can reversibly absorb hydrogen, store it without loss and release it again when needed. Since little or no pressure is required, normal containers or tanks can be used. The volume or mass-related energy densities can reach around a quarter of liquid fossil fuels.

This paper is to give an introduction to the field of hydrogen storage and usage of those LOHC, in particular. The developments of the last ten years have been related to the storage and transport of hydrogen with LOHC. These are crucial to meet the future demand for energy carriers e.g. for mobile applications. For this purpose, all transport systems are under consideration as well as the decentralized supply of rural areas with low technological penetration, e.g. regions of Western Africa which are often characterized by a lack of energy supply. Hydrogen bound in LOHC can provide a hazard-free alternative for distribution. The paper provides an overview of the conversion forms as well as the chemical carrier materials. Dibenzyltoluene as well as N-ethylcarbazole - as examples for LOHC - are discussed as well as chemical hydrogen storage materials like ammonia boranes as alternatives to LOHC.

Keywords: hydrogen storage, LOHC, climate-neutral mobility

Introduction

Renewable energy sources are important sources of electricity, and the expansion of renewables is one of the central pillars in Germany's energy transition. The energy supply is to become more climate-friendly, and is also to make us less dependent on imports of fossil fuels. In this context, hydrogen is the renewable energy carrier of the future [1],[2]. If it is produced from renewable electricity, it is climate-friendly, storable and transportable over long distances. It thus contributes to sector coupling - a key concept of the energy transition - and becomes the basis for climate-neutral mobility, industry and heat supply. In addition, the development and marketing of hydrogen technology has the potential to become a driver of the German economy. However, there are currently only a few German hydrogen and fuel cell products on the market. One reason for this is the complexity of hydrogen value chains: This complexity means high risk, especially for first movers in the industry and for small and medium-sized enterprises (SMEs). For them, creating economies of scale is crucial to reduce manufacturing costs and develop an internationally competitive industry for green hydrogen applications in Germany [3].

Liquid organic hydrogen carriers (LOHC) technology turn hydrogen into a secure power storage technology. LOHC hydrogen storage systems use liquid hydrogen carrier media, which can be used to store and transport hydrogen at ambient temperature. The advantages of LOHC are that hydrogen is stored at high energy density and that the existing distribution infrastructure of liquid fuels can be used. As a result, LOHC represents another option for efficient hydrogen storage that reduces hydrogen volume and stores hydrogen safely. Figure 1 describes the broad applicability of LOHC, particularly in use for medium-term storage systems. It thus describes an excellent basis for use, especially for mobile applications.

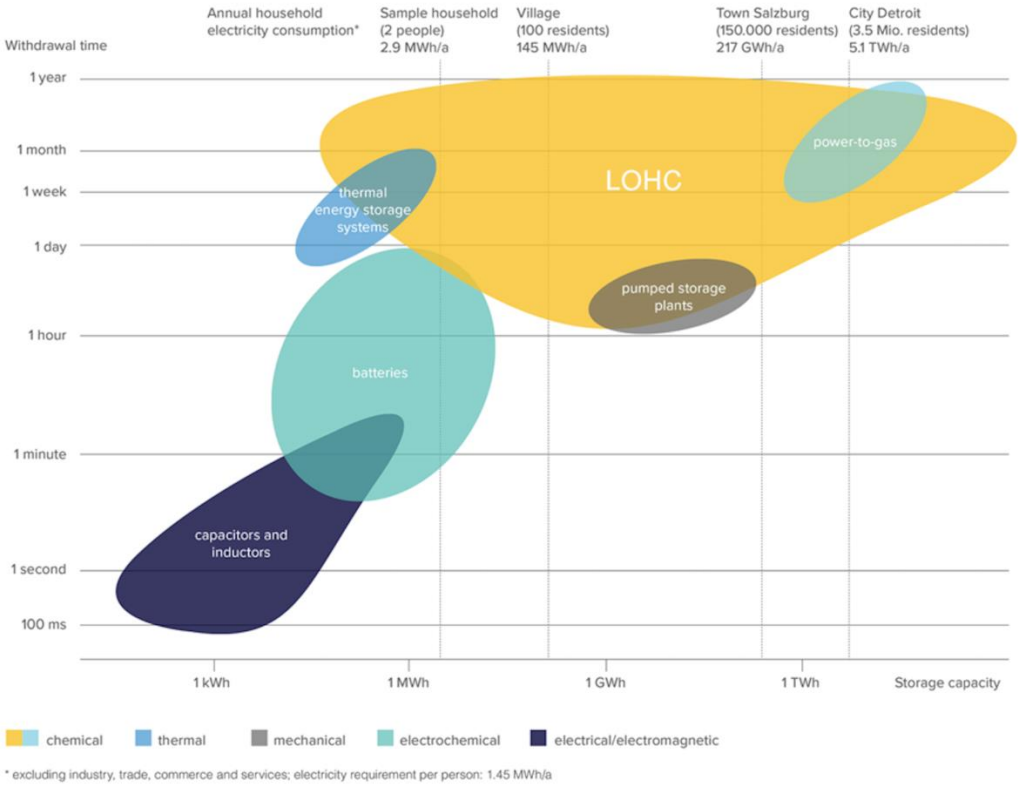

Figure 1. LOHC compared to other storage materials [4].

Fundamentals

According to the Federal Ministry for Economic Affairs and Energy, in 2019, Germany still used around 87 % of its primary energy based on conventional energy sources - e.g. fossil natural gas [5]: it mainly consists of methane (CH_4) - and thus - like all fossil energy sources - it releases climate-damaging carbon dioxide when burned (see equation 1):

$$CH_4\ (g) + 2\ O_2\ (g) \rightarrow CO_2\ (g)\uparrow + 2\ H_2O\ (g)\uparrow \quad (1)$$

One kilogram of methane - that is approximately 1.4 standard cubic meter CH_4 - has a sensible enthalpy of combustion (lower calorific value) of 50,140 kJ - this corresponds to 13.9 kWh [6]. Taking into account the primary energy rucksack, the emission factor of natural gas is 0.22 kg CO_2 per kWh of fuel energy (calorific value).

On the contrary, one kilogram of hydrogen - that is equivalent of 11 standard cubic meters H_2 - has a sensible enthalpy of combustion (lower calorific value) of 120,900 kJ - this corresponds to 33.6 kWh - and only releases water during combustion or an electrochemical conversion in a fuel cell (see equation 2; compare table 1 [7],[8]):

$$2\ H_2 + O_2 \rightarrow 2\ H_2O \quad (2)$$

Table 1. Properties of hydrogen [7],[8].

Property	**Value**	**Unit**
Density (as gas)	0.0899	kg/Nm^3 (per standard cubic meter)
Density (as liquid)	70.79	kg/m^3 (per cubic meter of liquid)
Lower calorific value	3.0	kWh/Nm^3 (per standard cubic meter)
	33.6	kWh/kg (by weight)
Upper calorific value	3.5	kWh/Nm^3 (per standard cubic meter)
	39.4	kWh/kg (by weight)

Hydrogen is seen today as an important energy carrier of the future. However, due to the energy source and the following process steps, there is CO_2 footprint, as well. The catalytic steam reforming of fossil fuels to hydrogen and other gases is still important today (see town gas, synthesis gas, Haber-Bosch process for ammonia synthesis, etc.; equations 3 and 4):

$$\text{I.} \quad CH_4\,(g) + H_2O\,(g) \rightarrow 3\,H_2\,(g) + CO\,(g) \tag{3}$$

$$\text{II.} \quad CO\,(g) + H_2O\,(g) \rightarrow H_2\,(g) + CO_2\,(g) \tag{4}$$

Also electrolysis methods, such as PEMEL, AEL, or SOEC, are traditional ways of producing hydrogen [8] (see equation 5):

$$2\,H_2O + W_{el} \rightarrow 2\,H_2\uparrow + O_2\uparrow \tag{5}$$

In 2019, renewable energies contributed around 14.9 % to primary energy consumption in Germany [5]. While the contribution to heat and, in particular, to mobility still was low, in 2017 nearly 33 % of gross electricity generation was provided from renewable sources (see figure 2). Wind energy, bioenergy and photovoltaics play an important and growing role, but because of fluctuations they temporarily and increasingly generate surpluses that have to be put to use. Under the term "Power-to-X", the generation of hydrogen via electrolysis is likely to play an important role in the future.

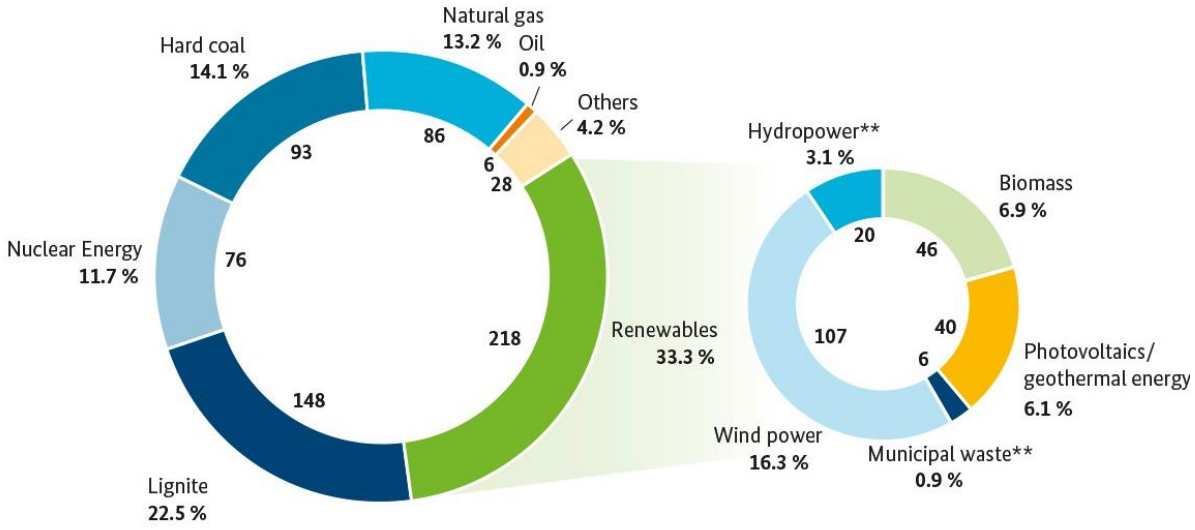

Figure 2. Energy data - gross electricity generation in Germany 2017 (total 654.8 TWh) [3].

In addition to the generation, the transport, possibly storage and use of the generated hydrogen are central issues [8]. In principle, the uptake of hydrogen or reform methane in the existing natural gas networks (natural gas H, limited admixture of H_2) is possible. Later, either the mixture can be used directly or the hydrogen is separated from the mixture again - using suitable methods.

A transfer of physically compressed hydrogen by means of transport is also possible, e.g.

- compressed,
- liquefied under pressure, or
- cryo-adsorptively bound.

However, the chemical compression of hydrogen is very interesting, because it enables high storage densities to be generated in a simple manner, both in terms of volume and weight [9]. The following ways are possible:

- Salt-like hydrides of the alkali or alkaline earth metals
- Other substances such as methanol or formic acid as products via synthesis gas
- Aromatics, boranes and the like as LOHC carrier materials by means of reversible hydrogenation

Principle of Energy Storage via Hydrogen with LOHC Materials

LOHC carrier materials can reversibly absorb hydrogen, store it without loss and release it again when needed. Since little or no pressure is required, normal containers or tanks can be used. The volume or mass-related energy densities are higher than with conventional electrochemical storage devices (accumulators) and can reach around a quarter of the energy densities of liquid fossil fuels [10].

The following is a brief explanation of the process sequence (see figure 3).

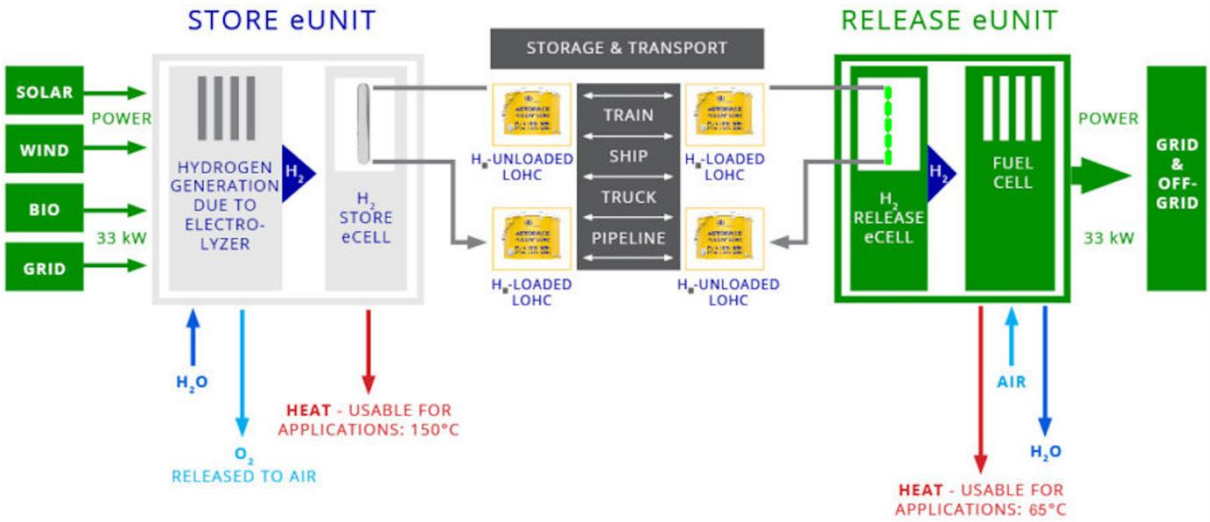

Figure 3. Scheme of the chemical storage of regenerative electricity via hydrogen with the aid of a reversible hydrogenation reaction of e.g. polyaromatics such as N-ethylcarbazole or hydrogen storage [4].

If fluctuating, electricity from RES is generated in excess at times of low load in the grid, this excess could endanger the stability of the grid frequency and thus the safe grid operation. As an alternative to activating generation systems for renewable electricity, in addition to conversion into useful heat (via power-to-heat, e.g. with heat pumps), generation of hydrogen via electrolysis can be useful. As shown in figure 3, the hydrogen for the hydrogenation of suitable LOHC carrier materials can in the meantime be chemically bound and thus stored without loss, in order then to be used again after dehydrogenation. Mobile as well as stationary applications, in particular in combined heat and power, are possible here.

The hydrogen can be converted into mechanical energy, electrical energy and/ or heat using internal combustion engines, gas turbines or fuel cells. The electrical energy generated can be used on site, be used to charge plug-in electric vehicles or to be fed into the grid.

Emerging heat can serve as space heat, hot water heat or process heat as well as for the hydrogenation/ dehydrogenation process of the LOHC itself.

Important Carrier Materials for Chemical Hydrogen Storage

The following carriers for reversible hydrogen storage should be briefly discussed:

- LOHC carrier materials
- Other materials

LOHC Carrier Materials for Chemical Hydrogen Storage

The abbreviation LOHC means "Liquid Organic Hydrogen Carrier". This is a liquid, organic carrier material based on fossil petroleum or natural gas today. LOHC compounds can also be sustainably generated in the future on the basis of renewable energies, e.g. biomass. The LOHC carrier material is not consumed or is only consumed to a small extent during application, but thus can be used over many cycles.

Disadvantages of hydrogen transport or hydrogen storage using LOHC materials compared to pipelines are the higher transport costs due to the additional mass of the carrier, larger storage volumes due to the energy density and, last but not least, often the need to store groundwater hazardous substances with all the associated expense. LOHC is a fossil-fuel-based carbon compound (e.g. dibenzyltoluene).

The following LOHC carriers should be discussed (for organic chemistry compare [11]):

- Dibenzyltoluene $C_{21}H_{20}$
- *N*-ethylcarbazole $C_{14}H_{13}N$
- Toluene C_7H_8

Dibenzyltoluene

Dibenzyltoluene $C_{21}H_{20}$ is a polyaromatic and is suitable for storing hydrogen via a hydrogenation and dehydrogenation reaction (see figure 4). There are several structural similar isomers of this compound. Around 50 kg of hydrogen can be stored per ton of carrier.

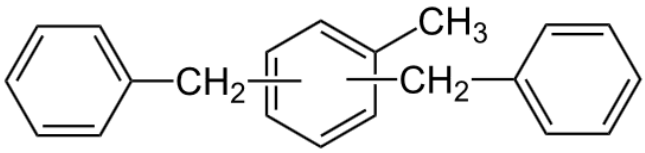

Figure 4. Dibenzyltoluene (polyaromatic) for hydrogen storage via a reversible hydrogenation reaction [12].

According the magazine HZwei from 2016, the carrier absorbs the hydrogen at 150° to 250°C in the reactor, while the catalyst here is ruthenium [13]. One litre of LOHC can store 600 l of gaseous hydrogen, which means the energy density is 1.9 MWh per cubic meter of LOHC. The reversible loading and unloading cycle can be carried out around 1,000 times. The density is 1,050 kg/ standard cubic meter, the LOHC can be stored indefinitely.

Using for simplification the *Ideal Gas Law* (see equation 6; [6]),

$$p * V = n * R * T \quad (6)$$

with

p: Pressure (Pa)
V: Volume (m^3)
n: Amount of substance (mole)
R: Universal gas constant (8,314 J/[mole*K])
T: Temperature (K)

the energy density can be roughly calculated for control purposes:

- 600 standard cubic meters hydrogen/ standard cubic meters LOHC (= 1.05 t LOHC)

According to the *Ideal Gas Law*, 600 standard cubic meters of hydrogen correspond to

- 600,000 l/ (22.4 l/ mole) = $26.79*10^3$ mole H_2 = 53.6 kg H_2

Thus, the specific hydrogen loading on the carrier is

- 53.6/ 1050 = 5.1 % by weight.

A complete hydrogenation of dibenzyltoluene according to the reaction (see equation 7)

$$C_{21}H_{20} + 9\ H_2 \rightarrow C_{21}H_{33} \quad (7)$$

would result in a maximum specific hydrogen loading on the carrier of

- 6.2 % by weight, that would be 65.1 kg H_2 per standard cubic meter LOHC (or per 1.05 ton LOHC).

However, with the specific sensible enthalpy of combustion (lower calorific value) of

- 120,900 kJ/kg H_2 = 33.6 kWh/kg H_2,

the energy density of the LOHC dibenzyltoluene at 600 standard cubic meters of hydrogen per standard cubic meter of LOHC is around

- 1,800 kWh per standard cubic meter LOHC (= 1.8 MWh without burning the carrier), or 1,715 kWh per ton LOHC

N-Ethylcarbazole

Another example of a suitable process is the catalytic hydrogenation and dehydrogenation of *N*-ethylcarbazole ($C_{14}H_{13}N$) or similar compounds (such as *N*-ethylcarbazole or phenylene carbazole; see figure 5).

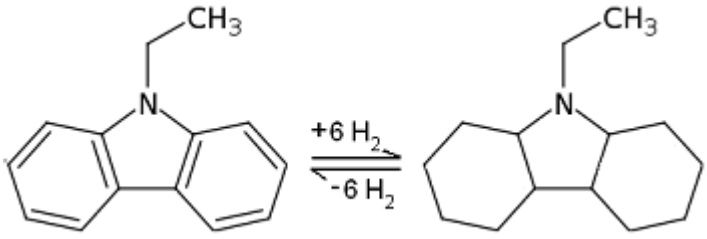

Figure 5. Principle of the chemical storage of hydrogen generated by renewable electricity with the help of a reversible hydrogenation reaction of polyaromatics such as *N*-ethylcarbazole [14].

In an exothermic chemical reaction under increased pressure and temperature, the compound is hydrogenated with hydrogen to form the perhydro compound catalytically at temperatures above 100°C (see equation 8):

$$C_{14}H_{13}N + 6\ H_2 \rightarrow C_{14}H_{25}N \quad (8)$$

The maximum specific hydrogen loading would be

- 12/207 = 5.8 % by weight

with a complete hydrogenation according to the above equation, that would be around 58 kg H_2 per ton of loaded LOHC. Information on measured values is not available, but it is estimated that similar, if somewhat lower, volume and mass-related energy densities than with dibenzyltoluene can be achieved with *N*-ethylcarbazole.

Toluene (to Methylcyclohexane)

Another possibility for reversible hydrogen storage is the hydrogenation/ dehydrogenation of toluene C_7H_8 to methylcylohexane. This process is known as methylcyclohexane-toluene-H_2 system (MTH). Toluene is a widely used solvent that is suspected of being carcinogenic. Because of the difficulty in dehydrogenation, research has shifted to other substances.

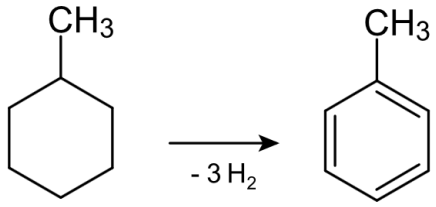

Figure 6. Dihydrogenation reaction from methylcyclohexane to the aromatic toluene (1-methyl-benzene) for the reversible storage of hydrogen with the aid of the hydrogenation reaction [15].

According to the reaction (see equation 9)

$$C_7H_8 + 3\ H_2 \rightarrow C_7H_{14} \qquad (9)$$

the maximum specific hydrogen loading would be

- 6.1 % by weight, so that would result in around 61 kg of hydrogen per ton of loaded LOHC.

Other Chemical Hydrogen Storage Materials

The following substances are also named as potential hydrogen carriers:

- Ammonia boranes
- Hydrocarbons
- Formic acid
- Methanol

While ammonia boranes starting from NBH_4 (or NBH_6 in the hydrogenated state) or C_4NBH_{12} sometimes achieve values of over 10 % by weight hydrogen loading, they are considered to be rather difficult to handle.

The reforming and re-reforming (= ADAM & EVA process, canned can process) from methane to hydrogen and vice versa takes place via synthesis gas (= CO/ H_2 mixture) according to the equations 3 and 4. In technology, this process is used for energy transport and can also be seen as a kind of chemical hydrogen carrier process. In addition, it is the first stage of the Fischer-Tropsch synthesis. On this basis, partially or completely sustainable methane can be made from hydrogen, which was obtained regeneratively via electrolysis, e.g. using (i) CO_2 from fossil waste/ flue gases after sequestration (CCS, CCU), or more sustainably (ii) after recovery of CO_2 from the air or (iii) after separation from biogas. Conversion into hydrogen is possible in the opposite direction.

The synthesis gas process, in conjunction with the methanol synthesis (III, see below) and the Fischer-Tropsch synthesis (I and II, see below), enables the production of (i)

alcohols such as methanol, (ii) dimethyl ether (DME, from methanol), (iii) light, medium and heavy hydrocarbons (e.g. petrol), as well as other energy carriers (e.g. formic acid) [9],[16]. The preferred carbon source (input) is sustainable CO_2 (e.g. from biogas) or other biomass.

The synthesis gas process initially generates CO/ H_2 mixtures, which can then be converted into gaseous and liquid hydrocarbons or C/H/O compounds. Catalysts made of cobalt or iron are used here, at around 160°-300°C and up to 25 bar. The following reaction schemes I to III can occur, among others (equations 10a to 15):

I. Alkanes - chains (e.g. n = 8: petrol [octane])

$$n\ CO + (2n+1)\ H_2 \rightarrow C_nH_{2n+2} + n\ H_2O \quad (10a)$$

$$8\ CO + 17\ H_2 \rightarrow C_8H_{18} + 8\ H_2O \quad (10b)$$

II. Alkenes - chains; alkanes - rings (e.g. n = 6: cyclohexane)

$$n\ CO + (2n)\ H_2 \rightarrow C_nH_{2n} + n\ H_2O \quad (11a)$$

$$CO + 12\ H_2 \rightarrow C_6H_{12} + 6\ H_2O \quad (11b)$$

III. Alcohols (e.g. n = 1: methanol)

$$n\ CO + (2n)\ H_2 \rightarrow C_nH_{2n+1}OH + (n–1)\ H_2O \quad (12a)$$

$$CO + 2\ H_2 \rightarrow CH_3OH \quad (12b)$$

Further specific reactions can be:

IV. Methane (compare equations 3, 4 and 10a)

$$CO + 3\ H_2 \rightarrow CH_4 + H_2O \quad (13)$$

V. Formic acid

$$CO + H_2O \rightarrow HCOOH \quad (14)$$

VI. Dimethyl ester (DME)

$$2\ CH_3OH \rightarrow CH_3OCH_3 + H_2O \quad (15)$$

Formic acid HCOOH (see equation 14) is a hazardous substance that can catalytically split off hydrogen, but is also rather difficult to handle. Methanol CH_3OH (see equation 12b) is widely used as a solvent in industry. It can be obtained via the so-called methanol synthesis using synthesis gas, which today mainly comes from the reforming of fossil natural gas according to equations 3 and 4. Methanol would rather be burned or can be used advantageously in fuel cells of the DMFC type (Direct Methanol Fuel Cell). In synthesis it can be used to produce DME (see equation 15) or for transesterification of rapeseed oil into biodiesel (FME, fatty acid methyl ester).

Conclusions

Science and technology as well as politics agree: Hydrogen is the energy carrier of the future, which can and will probably replace fossil energy carriers, especially natural gas, and will increasingly replace them by the middle of the century. A sufficient supply of sustainable energy from regenerative sources is of course decisive for climate protection. However, logistical steps are of crucial importance for this conversion of the energy supply. In addition to the production via e.g. electrolysis, the possibilities of storing and transporting hydrogen naturally play a decisive role. In the future, LOHC will be used as a carrier material for this purpose, e.g. in hydrogen storage systems to supply stationary, decentralized electricity storage systems with fuel. However, LOHC can also be used in the form of mobile hydrogen storage systems for hydrogen-based mobility. For example, hydrogen from electrolysis could

be stored in suitable locations and then be transported to the respective consumption points such as hydrogen filling stations or the chemical industry. This procedure can supplement and support the distribution of hydrogen via pipelines or pressurized gas containers. Because of the technical requirement to convert to hydrogen, the use of LOHC as a pressureless, transportable and storable carrier material is of great importance.

The aim of this work was therefore to give an overview of the possibilities of storing hydrogen in so-called LOHC systems. In fact, the analysis has shown that there are (i) a large number of different types of carriers and conversion methods, e.g. via the Fischer-Tropsch synthesis, but also that (ii) we already have flexible carrier materials with acceptable energy densities that can substitute liquid fossil fuels. Therefore, it will be important in the next few years to further investigate these possibilities, e.g. for mobility with hydrogen, and ultimately to make them usable.

References

[1] Teichmann D, Stark K, Müller K, Zöttl G, Wasserscheid P, Arlt W. Energy storage in residential and commercial buildings via Liquid Organic Hydrogen Carriers (LOHC). *Energy & Environmental Science*. 2012;5(10):9044. https://doi.org/10.1039/c2ee22070a

[2] Hodoshima S, Takaiwa S, Shono A, Satoh K, Saito Y. Hydrogen storage by decalin/naphthalene pair and hydrogen supply to fuel cells by use of superheated liquid-film-type catalysis. *Applied Catalysis A: General*. 2005 04;283(1-2):235-242. https://doi.org/10.1016/j.apcata.2005.01.010

[3] Renewable Energy. https://www.bmwi.de/Redaktion/EN/Dossier/renewable-energy.html. Accessed 2021 February 23.

[4] LOHC Technology Turns Hydrogen into a Secure Power Storage Technology. https://h2-industries.com/en/technology/. Accessed 2021 February 03.

[5] Energiedaten - nationale und internationale Entwicklung. www.bmwi.de. Accessed 2021 February 20.

[6] Brdička R. *Grundlagen der physikalischen Chemie*. Berlin: VEB Dt. Verl. d. Wiss.; 1985.

[7] Töpler J, Lehmann J, eds. *Hydrogen and Fuel Cell: Technologies and Market Perspectives*. Berlin, Heidelberg: Springer; 2017. https://doi.org/10.1007/978-3-662-44972-1

[8] Gribova M. Transition of the Fossil Energy Supply into the Hydrogen Based Economy of the Future. TH Wildau; 2020.

[9] Sterner M, Stadler I, eds. *Energiespeicher - Bedarf, Technologien, Integration*. 2 ed.. Springer; 2017.

[10] Sievi G, Geburtig D, Skeledzic T, Bösmann A, Preuster P, Brummel O, Waidhas F, Montero MA, Khanipour P, Katsounaros I, Libuda J, Mayrhofer KJJ, Wasserscheid P. Towards an efficient liquid organic hydrogen carrier fuel cell concept. *Energy & Environmental Science*. 2019;12(7):2305-2314. https://doi.org/10.1039/c9ee01324e

[11] Schirmeister T, Schmuck C, Wich P. *Beyer/Walter Organische Chemie* . 25. ed.. Hirzel; 2016.

[12] Mixture of Several Structural Isomers of Dibenzyltoluene. https://commons.wikimedia.org/wiki/User:J%C3%BC. Accessed 2021 February 21.

[13] Geitmann S. LOHC - Eine Pfandflasche für Wasserstoff. https://www.hzwei.info/blog/2016/05/11/lohc-eine-pfandflasche-fuer-wasserstoff. Accessed 2016 February 20.

[14] Cüppers P. Reaction N-Carbazol / Perhydro-N-Carbazol. https://commons.wikimedia.org/wiki/File:Perhydro-N-Carbazol.PNG. Accessed 2021 February 21.

[15] Mattern R. Synthese von Toluol mit Methylcyclohexan als Zwischenstufe. https://commons.wikimedia.org/wiki/File:Toluol-Synthese.svg. Accessed 2021 February 21.

[16] Kainer F. *Die Kohlenwasserstoff-Synthese nach Fischer-Tropsch*. 1. ed. . Springer (reprint 2014); 1950.

2nd German-West African Conference on Sustainable, Renewable Energy Systems SusRES – Kara 2021

Hyrdrogen Energy

https://doi.org/10.52825/thwildauensp.v1i.9

Published:15 June 2021

Sustainably Produced Hydrogen

Possible Variants and its Main Supply Paths

Maria Gribova[1], Lutz B. Giese[2]

[1] Technische Hochschule Wildau (Graduate), Germany

[2] Technische Hochschule Wildau, Germany

Abstract: The fossil fuels used to provide energy, such as coal, crude oil and natural gas, are largely responsible for carbon dioxide emissions and other so-called greenhouse gases. Hydrogen gas (H_2) can make a key contribution to decarbonization. It can be produced using various processes. Several processes are available to produce hydrogen, such as (i) steam reforming, (ii) cracking process or (iii) electrolysis. Depending on the source of origin, there is a distinction made between different “colours”. Gray, blue, turquoise, yellow and green hydrogen is available, the latter made using Renewable Energies. However, items such as (i) possible variants of hydrogen, (ii) leading export countries or (iii) provision paths to be preferred in the future will be discussed in this paper.

Keywords: Hydrogen, Green Gas Supply, Renewable Energy Sources

Introduction

According to the “Energy Data, Complete Edition” of the German Federal Ministry for Economic Affairs and Energy (BMWi), worldwide carbon dioxide emissions in 2018 were 34.0 billion tons per year [1]. With around 731 million tons, Germany had a share of around 2 % with a world population share of around 1 %. The total emissions of the European Union amounted to 3.47 billion t per year in 2018 (in comparison: Africa as a whole, on the other hand, had only 1.28 billion t per year with 1.3 billion inhabitants [2]). In spite of relevant agreements in 2015 via the Paris Agreement, these emissions are still on the rise. The fossil fuels used to provide energy, such as coal, crude oil and natural gas, are largely responsible for these carbon dioxide emissions and for a certain part of the so-called greenhouse gases, which, in addition to CO_2, combine methane (CH_4) and nitrous oxide (N_2O) to form relevant part of the CO_2-equivalents and thus contribute significantly to climate change. A German citizen still emits approximately 10 t CO_2 yearly, an average Europe has a per capita emission of approximately 8 t CO_2 yearly. Renewable energies and hydrogen as a gaseous energy carrier obtained from them are seen as essential means to change this situation in the near future and to avert harmful climate change as far as possible.

Thus, hydrogen gas (H_2) can make a key contribution to decarbonization. Its versatile use as (i) raw material and fuel in industry, as (ii) fuel in mobility, as (iii) energy storage and as (iv) energy source in the provision of heat enables sector coupling, which can take place on the basis of an energy source, whose combustion product is only water. In 1874, the French science-fiction author Jules Verne wrote, that *“Water Will Be the Coal of the Future”* [3]. But hydrogen can only make a contribution to decarbonization if it is produced with low emissions.

Hydrogen

Characteristics and Physicochemical Properties of Hydrogen

Hydrogen is the lightest element and is composed of a mixture of three isotopes, the main part is (i) ^{1}H, in addition there are traces of (ii) D (^{2}H, deuterium) and the radioactive T (^{3}H, tritium). Hydrogen is significantly lighter than air, the standard cubic meter (Nm^3, at 1.013 bar and 273.15 K) weighs only around 89.9 g. Hydrogen is flammable, can form explosive mixtures, is highly diffusive and has an embrittling effect on materials such as steal e.g. of system components or pipelines. Thus, dealing with hydrogen requires certain technical precautions.

For compression and storage, the high volatility, the very low boiling point and the low critical point must also be taken into account (Table 1).Please notice that there is no indent in the first paragraph of a section or subsection. There also no indent in the first paragraphs which follow a table, figure, equation, etc.

Table 1. Properties of hydrogen [4].

Property	Value	Unit
Density (as gas)	0.0899	kg/Nm^3 (per standard cubic meter)
Density (as liquid)	70.79	kg/m^3 (per cubic meter of liquid)
Melting temperature	14.01	K
Boiling temperature	21.15	K
Critical point	33.18	K (13.0 bar)
Lower calorific value	3.0	kWh/Nm^3 (per standard cubic meter)
	33.33	kWh/kg (by weight)
	2.79	kWh/l (per cubic meter of liquid)
Upper calorific value	3.5	kWh/Nm^3 (per standard cubic meter)
	39.41	kWh/kg (by weight)

Provision of Hydrogen

Elemental hydrogen does not exist naturally on earth, but in chemically bound form in water, organic compounds and rocks. However, it can be produced using various processes, e.g. by splitting water or hydrocarbons. Several processes are available, essentially (i) steam reforming, (ii) the cracking process and (iii) electrolysis. Depending on the source of origin, a distinction is made between different “colours” [5] [6]:

- Gray hydrogen
    - Manufactured from natural gas via steam reforming (SMR or ATR process) with full greenhouse gas emissions
- Blue hydrogen
    - Manufactured from natural gas via steam reforming with partial greenhouse gas reduction via CCS (carbon capture and storage; SMR: -60%; ATR: -90%)
- Turquoise hydrogen
    - Manufactured from natural gas via methane pyrolysis (cracking process) with low greenhouse gas emissions
- Yellow hydrogen
    - Manufactured using nuclear energy with lower greenhouse gas emissions, e.g. using electrolysis with nuclear power
- Green hydrogen
    - Manufactured using renewable energies with little to no greenhouse gas emissions, e.g. via electrolysis with solar or wind power

Nowadays, hydrogen is used in a variety of material and energetic ways, e.g. in the manufacture of fertilizers or to drive spacecraft (Figure 1). More than 90 % of hydrogen is currently generated from fossil fuels, often from natural gas (methane) by the catalytic steam reforming ($\Delta H_{R(I)}$ = +206.2 kJ/mole CH_4; $\Delta H_{R(II)}$ = -41.2 kJ/mole CO [7]; compare grey/ blue hydrogen):

$$(I) \quad CH_4\,(g) + H_2O\,(g) \rightarrow 3\,H_2\,(g) + CO\,(g) \qquad (1)$$

$$(II) \quad CO + H_2O\,(g) \rightarrow H_2\,(g) + CO_2\,(g) \qquad (2)$$

Available process variations are

- steam reforming (SMR = Steam Methane Reforming),
- partial oxidation (POX), and
- dry reforming or autothermal reforming (ATR).

Hereby, the SMR and ATR process allow parts of the carbon dioxide formed during steam reforming to be separated from the synthesis gas mixtures, e.g. to render it inert by underground storage. This sequestration of carbon dioxide is also known as carbon capture and storage (CCS). The CCS process is only popular to a limited extent among climate protectionists.

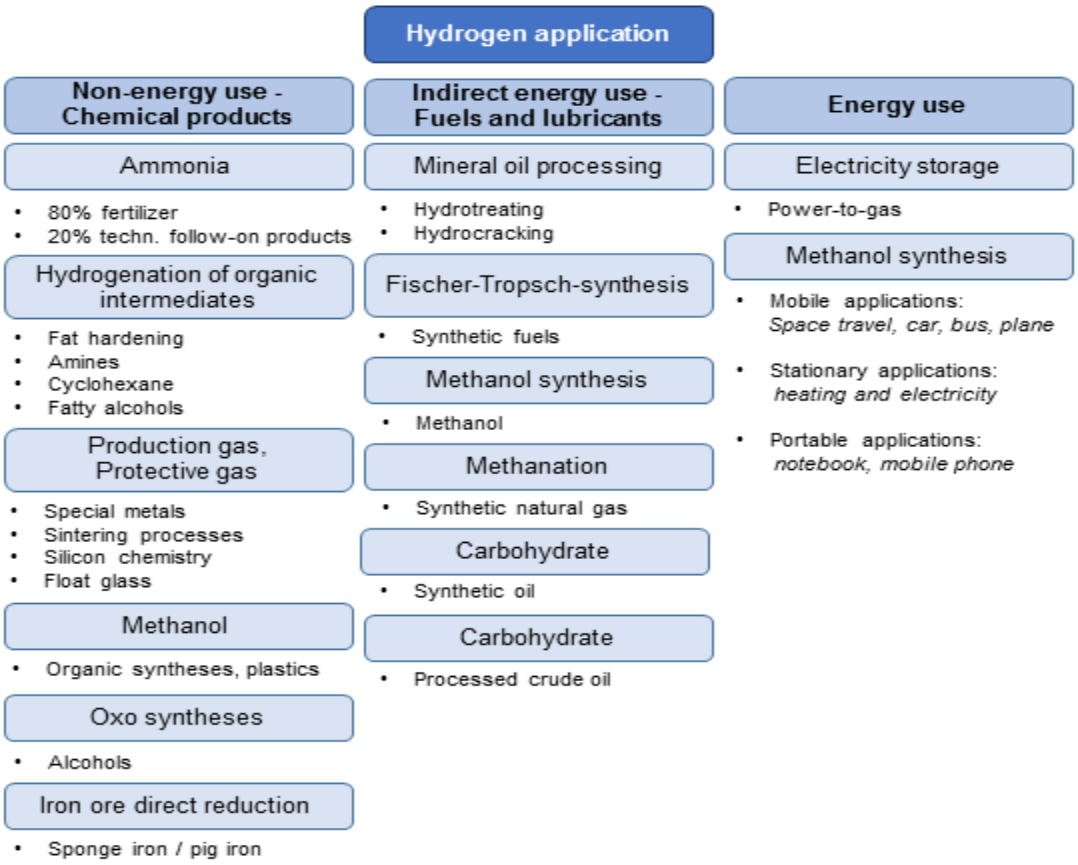

Figure 1. Today's material and energetic use of hydrogen [8] [9].

An alternative process is the methane cracking (methane pyrolysis), revised by the IASS Potsdam and KIT Karlsruhe for the environmentally friendly and efficient production of hydrogen from natural gas (methane) in addition to graphite powder (compare turquoise hydrogen; ΔH_R = +74.9 kJ/mole CH_4) [7]:

$$CH_4\,(g) \rightarrow 2\,H_2\,(g) + C\,(s)\downarrow \qquad (3)$$

In this case, small methane bubbles are placed from below into a column filled with molten tin. The cracking reaction takes place while they are rising in the liquid metal. The carbon is

deposited on the surface of the bubbles and, when the bubbles disintegrate, deposited as a powder at the top of the reactor. More than 75 % of the methane can be converted into hydrogen at 1200°C. The process could take on the role of a bridging technology. With it, the energy potential of natural gas could be used in a more climate-friendly way. Thus, the integration of the clean energy carrier hydrogen into the energy system could be made easier [10].

Renewable energies are of course the most environmentally friendly source of producing hydrogen (compare green hydrogen; see Figure 2). In addition to biogas fermentation, biomass gasification or its pyrolysis (partly with reforming), the use of renewable electricity for water electrolysis is certainly the best alternative. Electrolysis processes are therefore particularly suitable for the climate-friendly production of hydrogen. The ecological rucksack of the individual conversion methods is decisive for the greenhouse gas reduction, but this also means that the amount of green hydrogen available via electrolysis is directly dependent on the amount of renewable electricity provided or its primary energy resources. Today these are essentially wind power, biomass and photovoltaics, or possibly also hydropower, solar thermal power plants and geothermal energy. In general, however, the demand for renewable electricity will increase significantly by 2100, presumably for reasons of growth of population and standards, the introduction of e-mobility, but also the needs of ecological transformation of technologies.

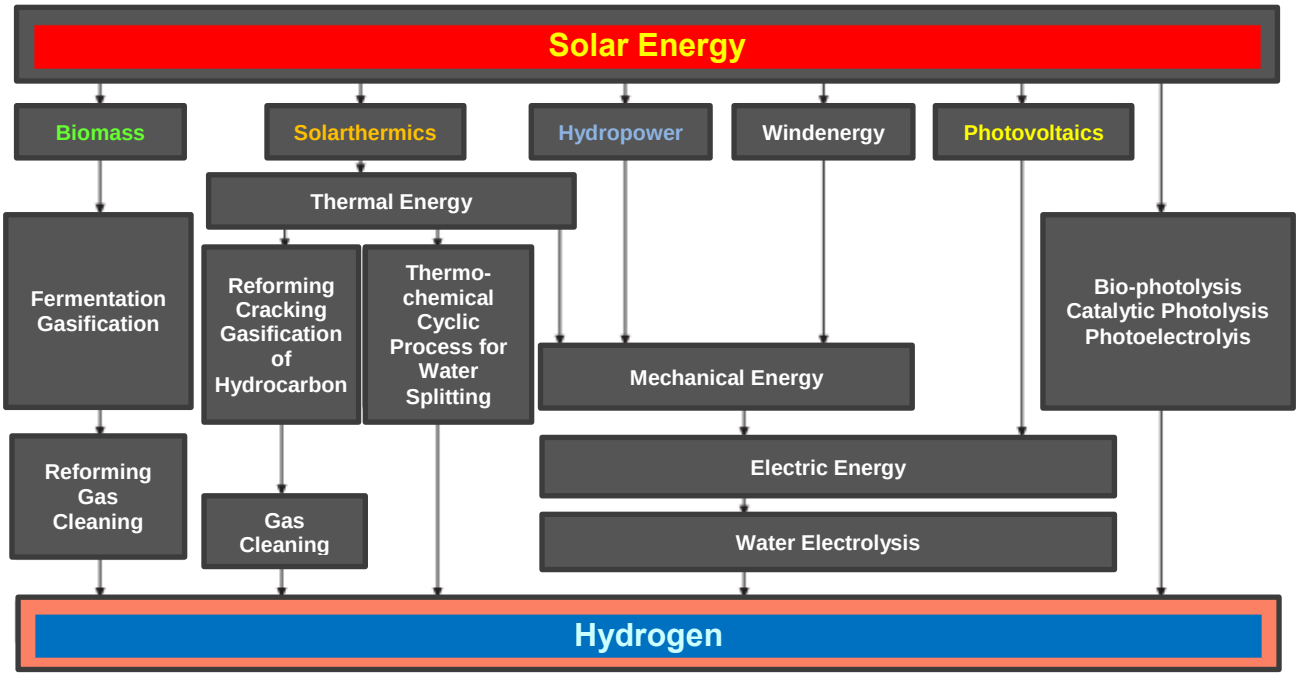

Figure 2. Energy conversion steps of non-fossil, renewable hydrogen production [11].

However, electrolysis processes achieve efficiencies in excess of 70 %. Here, water is split into its components hydrogen and oxygen (ΔH_R = +285.8 kJ / mole H_2O) [7]:

$$H_2O\ (l) \rightarrow 2\ H_2\ (g)\uparrow + O_2\ (g)\uparrow \qquad (4)$$

The process of producing hydrogen by electrolysis of water has been state of the art for over 100 years (chlorine-alkali electrolysis). Basically, three different types of electrolysis processes can be distinguished from one another according to the type of ion-conducting electrolyte, the operating temperature and the level of development:

- Alkaline electrolysis (AEL)
- Polymer electrolyte membrane electrolysis (PEMEL)
- High temperature electrolysis (SOEC)

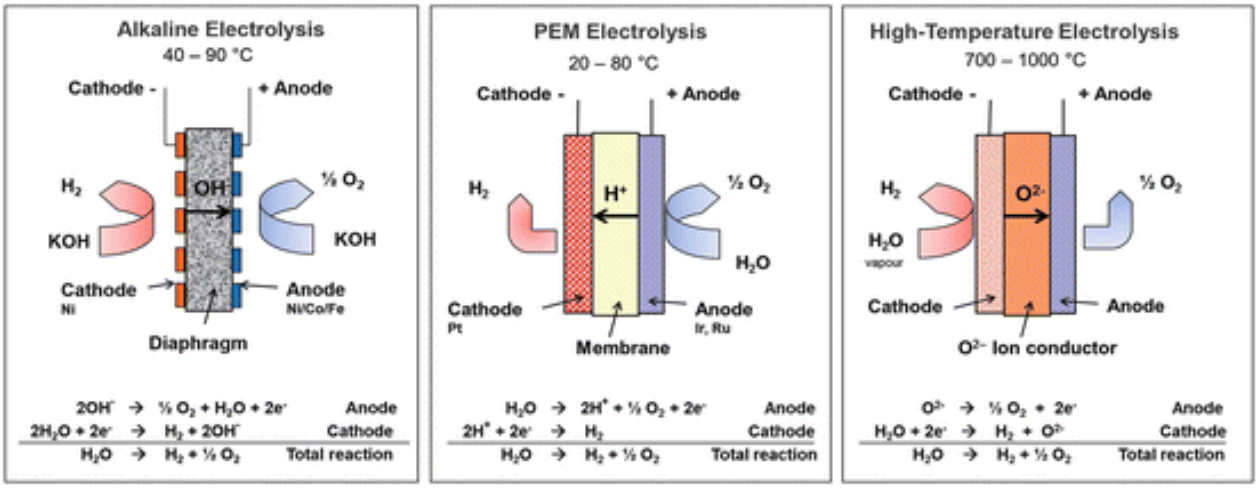

Figure 3. Functional principles of electrolysis cells and various electrolysis processes [4].

The functional principle of each individual electrolysis cell and the reaction equations are shown in Figure 3. A comprehensive technology comparison between alkaline and PEM electrolysis is shown in Table 2.

Table 2. Technology comparison between AEL and PEMEL electrolysis [12].

	AEL	**PEMEL**
Operating temperature	60° - 80°C	50° - 80°C
System pressure	< 30 bar	< 40 bar
Current density	0.2 - 0.4 A/cm^2	0.6 - 2.0 A/cm^2
Cell voltage	1.8 - 2.4 V	1.8 - 2.2 V
Specific energy consumption	press.less: 4,3 - 4,6 kWh/ Nm^3 H_2 pressure: 4.5 - 5.0 kWh/Nm^3 H_2	4.9 - 6.7 kWh/ Nm^3 H_2
Lower partial load range	20 - 40 %	0 - 10 %
Efficiency	62 - 82 %	67 - 82 %
H_2 production rate per stack/	< 760 Nm^3/h	per Stack < 10 Nm^3/h
Useful life	< 90,000 h	< 20,000 h

Every type of hydrogen has its potential leading export countries. Which provision path is preferred in the future from an ecological and economic point of view and which opportunities open up for Africa will be discussed in this publication.

Storage, Transport and Distribution of Hydrogen

Important further points in the logistics of the use of hydrogen should only be briefly addressed here. The storage of hydrogen, the transport and the distribution are often difficult due to the specific physical properties, e.g. with regard to compression, shelf life, corrosiveness, etc..

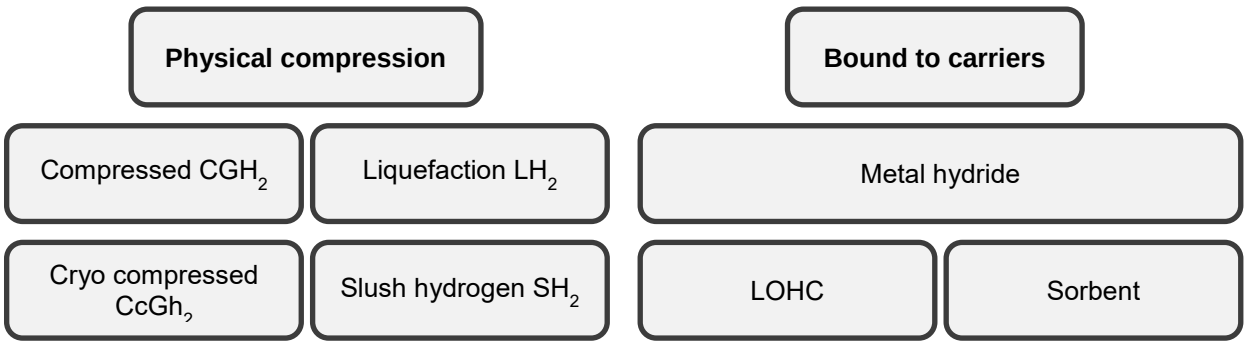

Figure 4. Types of hydrogen storage [13].

The storage concepts include the options to be seen in Figure 4. Some of those storage technologies are useful for transport of hydrogen, as well. So-called LOHC such as dibenzyltoluene are of special interest as pressure-less hydrogen carrier materials with high energy density. This technology can be applied as static storage or for transporting of hydrogen as well as after distribution as a mobile fuel.

Preliminary studies and initial field tests are being carried out currently in order to test the admixture of hydrogen in natural gas pipelines with the aim of long-distance transport.

Application Goals and Possible Supplier Countries

Power-to-Gas (PtG or P2G) is often referred to as the key technology of the energy transition, as it is the central coupling element between electricity and gas infrastructure, which enables the production of renewable gases and the storage of energy from RES resources on a large-scale volume realized over longer periods of time (Figure 5).

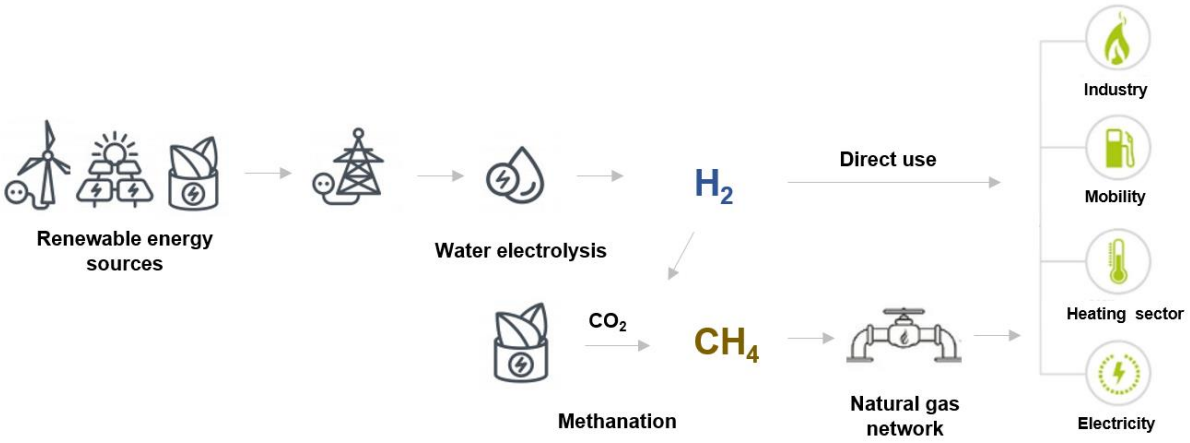

Figure 5. The Power-to-Gas concept [9] (adapted from [14]).

The hydrogen produced offers the possibility of storage in large quantities over longer periods of time (e.g. underground) and can later be converted back into electricity without CO_2 through cold (electrochemical) combustion using fuel cell technology. On the other hand, hydrogen can also be transported directly to the place of consumption or converted into methane beforehand by adding carbon monoxide or carbon dioxide. The process is known as methanation and is used, among other things, to store green methane in existing natural gas networks (compare Equation 1 and 2). In addition, the required CO_2 from biogas plants can be bound in the methanation process and thus does not get into the atmosphere.

Potential Hydrogen Suppliers

Each type of hydrogen has its potential supplier countries. Potential hydrogen suppliers differ according to the type of original energy source for hydrogen production. The transition from conventional energy sources to the hydrogen economy only makes sense if there are ecological relief effects. For this reason, the production of gray or yellow hydrogen on an industrial scale is not planned in the future. Table 3 shows the CO_2 emissions for each type of hydrogen production.

Table 3. Carbon dioxide emissions depending on the type of hydrogen production [15].

	GHG average		Thereof upstream emissions	
H_2-origin	**kg CO_2/ kg H_2**	**g CO_2/ kWh**	**kg CO_2/kg H_2**	**g CO_2/ kWh**
Gray	13.24	398	3.24	98
Blue	5.61	168	3.24	98
Green	0.88	26	-	-
Turquoise	6.1	183	3.24	98

The production of gray, blue and turquoise hydrogen is based on natural gas and is therefore not emission-free. This is due to the upstream emissions. Greenhouse gases are released into the atmosphere during the extraction, processing and transport of natural gas. Greenpeace Energy attributes 25 % of the total emissions (upstream chain and combustion/ use) of natural gas to the upstream chain emissions [15].

The production of green hydrogen is also not completely without a negative effect on the CO_2 footprint. This is due to the upstream chain emissions in the manufacture of wind or solar systems as well as electrolyzers. The electrolysis with wind power produces 26 g CO_2/ kWh H_2 [15].

Blue and Turquoise Hydrogen from Russia

The import of natural gas from Russia offers a possible supply path for blue hydrogen. The natural gas is converted into gray - and then blue - hydrogen using SMR or ATR processes, in that the carbon dioxide produced is "captured" and stored underground. The process is known as carbon capture and storage (CCS). Similar to this underground storage of carbon dioxide the sub-surface storage of hydrogen in exhausted natural gas and oil deposits or natural structures is planned. However, Figure 6 shows one of the possible deployment paths.

The use of blue hydrogen represents the bridge into the hydrogen age. Due to the limited storage capacity underground, a comprehensive CCS application can lead to storage problems.

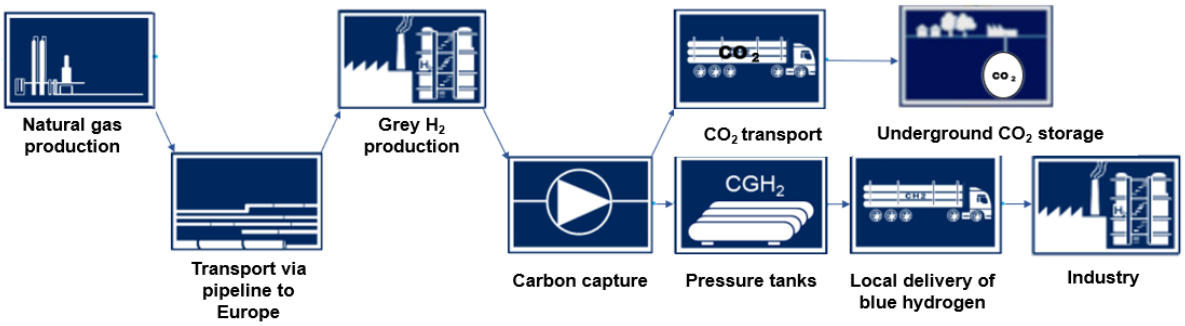

Figure 6. Delivery path - blue hydrogen from Eastern Europe (Russia) [9].

Another option for importing hydrogen is delivery by pipeline from Russia. This is CO_2-neutral turquoise hydrogen, which is created through the thermal splitting of methane (methane pyrolysis). Since no oxygen is involved in the fission process, only solid carbon is created as a by-product instead of the greenhouse gas CO_2. The largest natural gas supplier from Russia, Gazprom, is currently developing processes on an industrial scale. This means that the natural gas can be decarbonized in the immediate vicinity of the production source. The deployment path is shown schematically in Figure 7.

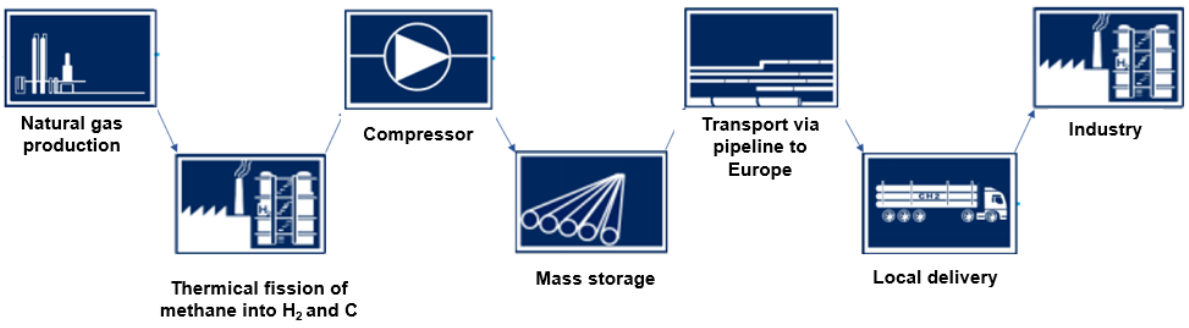

Figure 7. Delivery path - turquoise hydrogen from Russia [9].

Green Hydrogen from Africa

Due to the great potential for solar and wind energy as well as sufficient space for the development of RES, the German Federal Ministry of Education and Research BMBF relies primarily on cooperation with West and South Africa [16]. The Federal Ministry of Research has requested the “Hydrogen Potential Atlas”, which is to examine the areas of the African continent for the potential of production and export. Firstly, an interactive map is to be developed within the scope of this project, which has to show the most compatible locations for the construction of an infrastructure for the production of green hydrogen. Second, the project should then show through pilot projects how the export and sale of green-generated hydrogen can be organized most efficiently.

One of the possible hydrogen supply paths from Africa is shown in Figure 8. The idea is to produce hydrogen cost-effectively from wind and solar power in Africa, liquefy it for greater transport efficiency, store it in LH_2 tanks or LOHC, and ship it to Europe. Local deliveries can be made to the industrial sites in appropriate tanks by truck.

The solar and wind power plants as well as the electrolyzers are to be provided from Germany. The water required for electrolysis is to be obtained from the sea using renewable electricity by desalination. The plants for seawater desalination are also to be supplied from Germany.

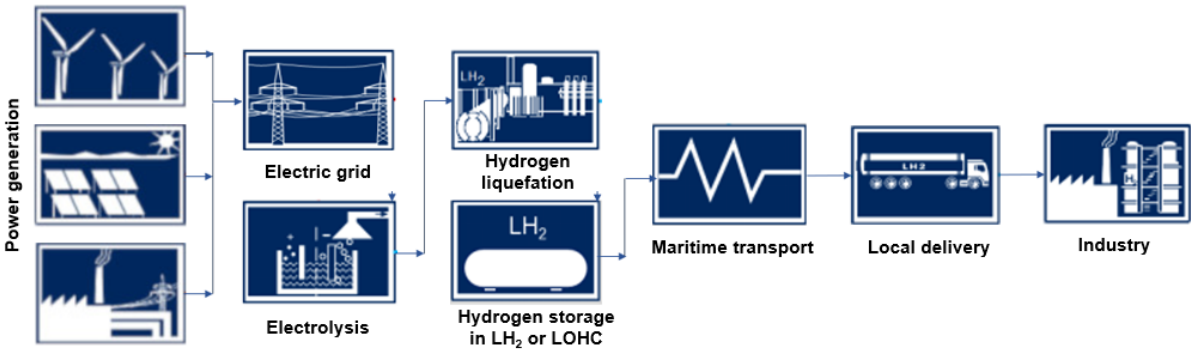

Figure 8. Delivery path - green hydrogen from Africa [9].

Green and Blue Hydrogen from the OPEC Countries

The OPEC states, especially the Gulf countries and North Africa are the other potential hydrogen suppliers. These countries have the unique opportunity to no longer (only) supply Europe and the world with crude oil and natural gas, ultimately hydrocarbon fuels, but with pure CO_2-free hydrogen. This is possible from North Africa via the existing natural gas pipelines or from the Gulf countries using liquid hydrogen by tanker.

The Gulf countries are the ideal future manufacturer and supplier of green hydrogen because of the very inexpensive production of electricity from solar power plants. The enormous demand for green hydrogen for the sectors transportation, industry, households etc. cannot be produced easily from the sources available in Germany and Europe. In this way, the Gulf countries can already counter a possible drop in prices and the loss of importance of crude oil and natural gas due to the steadily increasing e-mobility and (over)compensate for this by supplying hydrogen [17].

Conclusions

Hydrogen can make a key contribution to decarbonization - it is a sustainable energy carrier whose combustion product is only water.

By 2050, as part of the German energy transition (“Energiewende”), there will be a considerable need for hydrogen for the provision of non-fossil fuels. However, the ecological relief effects of hydrogen (i) depend on the degree of conversion, but a significant decarbonization is only possible through the use of hydrogen (ii) if it is produced with low emissions. The currently ready-to-use gray hydrogen produces approximately 13 kg CO_2/ kg H_2, while blue and turquoise hydrogen still produce approximately 6 kg CO_2/ kg H_2 - due to the upstream chain emissions of natural gas and methane leaks [15]. Even the procurement of green hydrogen is not entirely without CO_2 pollution. Its emission factor of 0.88 kg CO_2/ kg H_2 is due to the energy used in the upstream chain to produce its supply technology, e.g. wind power and PV systems plus electrolyzers [15]. A complete examination of the ecological relief effects through the use of renewable hydrogen must be considered separately for each consumer, industry or process.

Currently, around 96% of the world's hydrogen is produced using fossil energy sources [18]. The future need for green hydrogen poses major challenges for the RES and electrolysis markets. According to forecasts, the green hydrogen volumes ultimately required from renewable sources cannot be made available on an industrial scale until 2040. As an interim solution, fossil-based hydrogen could be used, such as blue or turquoise hydrogen. The use of blue hydrogen must, however, be questioned critically because it requires an available CCS infrastructure, but CCS is socially not accepted. The turquoise hydrogen is an attractive solution, as the natural gas could be decarbonized directly in the vicinity of its production source. The only by-product is graphite, which can be stored or used industrially - without CO_2 emissions.

The future German demand for renewable hydrogen cannot be met only by German domestic production. In addition to its own production volumes, Germany needs a powerful but sustainable external energy policy, because even in the age of renewable energies there will be limited energy imports. The following import options should be considered:

(i) green hydrogen from West and South Africa,

(ii) blue and turquoise hydrogen from Russia and

(iii) green, maybe blue/ turquoise hydrogen from the Middle East/ North Africa (MENA).

These partnerships can help the partner countries set up the relevant structures and ensure that the imported energy can be generated sustainably and under socially just conditions. However, the partner countries' own supply of renewable energies must always have priority over exporting to Europe.

References

[1] Energiedaten - nationale und internationale Entwicklung. www.bmwi.de. Accessed 2020 October 23.

[2] Prognose der Bevölkerung in den Kontinenten in den Jahren 2020 und 2100. https://de.statista.com/statistik/daten/studie/184686/umfrage/weltbevoel kerung-nach-kontinenten/. Accessed 2021.

[3] Verne J. *The Misterious Island” [Reprint of: L’Île mystérieuse, 1874]*. Ware (Hertfordshire): Wordsworth Editions Ltd; 2010.

[4] Töpler J, Lehmann J, eds. *Hydrogen and Fuel Cell: Technologies and Market Perspectives*. Berlin-Heidelberg: Springer; 2017. https://doi.org/10.1007/978-3-662-44972-1

[5] Eine kleine Wasserstoff-Farbenlehre. https://www.bmbf.de/de/eine-kleine-wasserstoff-farbenlehre-10879.html. Accessed 2021.

[6] *The National Hydrogen Strategy*. BMWi [German Federal Ministry for Economics and Technology]; 2020.

[7] Brdička R. *Grundlagen der physikalischen Chemie*. 15. ed. Berlin: VEB Dt. Verl. d. Wiss.; 1985.

[8] *Wasserstoff - Schlüssel zu weltweit nachhaltiger Energiewirtschaft - Beispiele aus Nordrhein-Westfalen von der Herstellung bis zur Nutzung*. EnergieAgentur.NRW; 2013.

[9] Gribova M. Transition of the Fossil Energy Supply into the Hydrogen Based Economy of the Future. UAS [TH] Wildau; 2020.

[10] Crack it: Fossile Energie ohne Klimagase. - IASS und KIT entwickeln Technologie zur Erzeugung von Wasserstoff aus Methan ohne Kohlendioxid-Emissionen. https://www.kit.edu/kit/pi_2015_139_crack-it-fossile-energie-ohne-klimagase.php. Accessed 2015.

[11] Schnurnberger W, Janßen H, Wittstadt U. Wasserspaltung mit Strom und Wärme. In: Stadermann G, ed. *Wasserstoff und Brennstoffzellen – Energieforschung im Verbund*. Themenheft 2004. Berlin: Forschungsverbund Sonnenenergie; 2005:51.

[12] Brinner S, Schmidt M, Wagener L, Zuberbühler U. *Technologiebericht 4.1 Power-to-gas (Wasserstoff) - Technologien für die Energiewende – Teilbericht 2 [to BMWI]*. Wuppertal/ Karlsruhe/ Saarbrücken: Wuppertal Institut; 2018.

[13] Zukunft Erdgas e.V.. Power-to-Gas Verfahren. https://www.energie-experten.org/erneuerbare-energien/oekostrom/sektorkopplung/power-to-gas. Accessed 2021.

[14] Bukold S. *Kurzstudie Blauer Wasserstoff – Perspektiven und Grenzen eines neuen Technologiepfades*. Hamburg: Greenpeace Energy; 2020.

[15] Potenzialatlas Wasserstoff: woher soll der Grüne Wasserstoff kommen?. https://www.bmbf.de/de/woher-soll-der-gruene-wasserstoff-kommen-11766.html. Accessed 2021.

[16] Sturm H. Grüner und blauer Wasserstoff aus den OPEC-Staaten. https://www.pv-magazine.de/2019/10/08/gruener-und-blauer-wasserstoff-aus-den-opec-staaten/. Accessed 2019.

[17] Weger L, Abánades A, Butler T. Methane cracking as a bridge technology to the hydrogen economy. *International Journal of Hydrogen Energy*. 2017 01;42(1):720-731. https://doi.org/10.1016/j.ijhydene.2016.11.029

2nd German-West African Conference on Sustainable, Renewable Energy Systems SusRES – Kara 2021 Energy Efficiency

https://doi.org/10.52825/thwildauensp.v1i.16

Published: 15 June 2021

Numerical study of heat and water vapour exchanges inside a green roof building in a high irradiation area for passive cooling purpose

Hodo-Abalo SAMAH[1,2][https://orcid.org/0000-0002-0698-4843], N'Detigma KATA[1], Kodjo KPODE[1,2], Magolmèèna BANNA[2], and Bekacem ZEGHMATI[3]

[1] Laboratoire Matériaux et Energie Renouvelable et Environnement (LaMERE), Université de Kara, Togo

[2] Laboratoire sur l'Energie solaire LES/GPTE, Université de Lomé, Togo

[3] Laboratoire de Mathématique et Physique des Systèmes, Université de Perpignan Via Domitia, France

Abstract. Vegetation cover provides shading and protects the soil beneath them from warming. Vegetation can be used as passive cooling technique that reduces the thermal load of a building. A numerical study has been carried out on laminar double-diffusive mixed convection in a green roof enclosure. The model is equipped with inlet and outlet openings for air removal while the left vertical wall is heated and partially saturated with water for indoor air humidification. The mathematical model is governed by the two-dimensional continuity, momentum, energy and concentration equations. Transfer equations are solved using a finite difference scheme and Thomas algorithm. The model was applied for the simulation of a building with green roof in Togolese climate conditions. Results showed that, the flow structure is a mixed convection type, but the isotherms et iso-concentration distributions reveal a vertical stratification of the temperatures and the relative humidity.To predict heat transfers inside the cavity, a correlation has been established for the estimation of the average Nusselt number as a function of the Leaf Area Index and Reynolds number under solar heat flux of 350 $W.m^{-2}$, the average in case of Togo. It was found that a larger Leaf Area Index reduces the solar flux penetration and therefore, reduces significantly heat transfer inside the enclosure and then stabilizes it temperature. For the LAI equal to 3, the indoor air fluctuates around 26°C and the relative humidity range is found to be 50% - 60% under solar heat flux of 350 $W.m^{-2}$.

Keywords: Leaf Area Index; Nusselt number; Sherwood number; passive cooling.

Introduction

Natural cooling techniques have been used over the centuries and their application has started to spread throughout the world, particularly in tropical regions where inside temperatures in buildings are far beyond the comfortable conditions. The introduction of mechanical air conditioning systems into the building, with their great energy expenditure, has become the standard alternative used to natural cooling. Many studies regarding this problematic are developed as ROOFSOL research project [1-4], which focused on the theoretical and experimental analysis of different roof solutions for cooling in arid region, mainly based on evaporative and radiative cooling principles. The green roof technique is also able to reduce the energy consumption and to improve the internal comfort in areas characterized by high temperature and irradiance values during the day [5-7]. With rapid urbanization, there has been high growth in population and building construction in cities. A high concentration of buildings actually raises many environmental issues, such as the Urban

Heat Island effect. The Urban Heat Island effect started mainly because of the loss of green areas in the urban environment. Plants when strategically placed around roofs can be considered a complement of urban greens. This natural solution also contributes to the thermal benefits in buildings and their surrounding environments. Greenery placed around buildings serves to reduce the surface temperature through direct shading of hard surfaces as well as cool the ambient air through absorbing solar heat for transpiration and photosynthesis. The shaded surfaces also emit less long-wave radiation due to lower surface temperature [8]. All these contribute to lowering energy consumption for cooling and mitigating Urban Heat Island effect in the urban environment. Many studies concerning the energy effectiveness of green roofs are based on the development of complex mathematical models [9-11] which involve an understanding of the characteristics of the vegetation and the substrate [12-14]. On the contrary, research which is based on the observation of monitoring data often refers to short periods of analysis and the results obtained, although of great interest for understanding the behaviour of the type of roof analysed, are difficult to extrapolate for other contexts and for other solutions. Furthermore, in most studies the green roof is considered as a single unit made up of plants and substrate and is always studied when there is the greatest density of vegetation, without bearing in mind that, unless it is a pre-vegetated green roof system, the vegetation takes time to develop after being installed and that the plants may die and the roof may have no vegetation for a certain period of time. In West Africa context, green roof is not investigated or poorly investigated. So modeling a vegetalised roof should be useful for engineer in optimization of such a passive system in practical buildings. Therefore, the aims of this work are to analyse the impact of vegetation density on the dynamic of heat and mass transfer inside a vegetalised building under Togolese climate conditions. The green roof potential was explored through the determination of its effect on the Nusselt number and the indoor temperature fluctuations.

Model description and assumptions

The domain under analysis is as sketched in Figure 1, a square two-dimensional cavity under the influence of a gravitational field. The heat flux imposed at the top wall is a fraction of solar heat transmitted into the cavity by the planted roof.

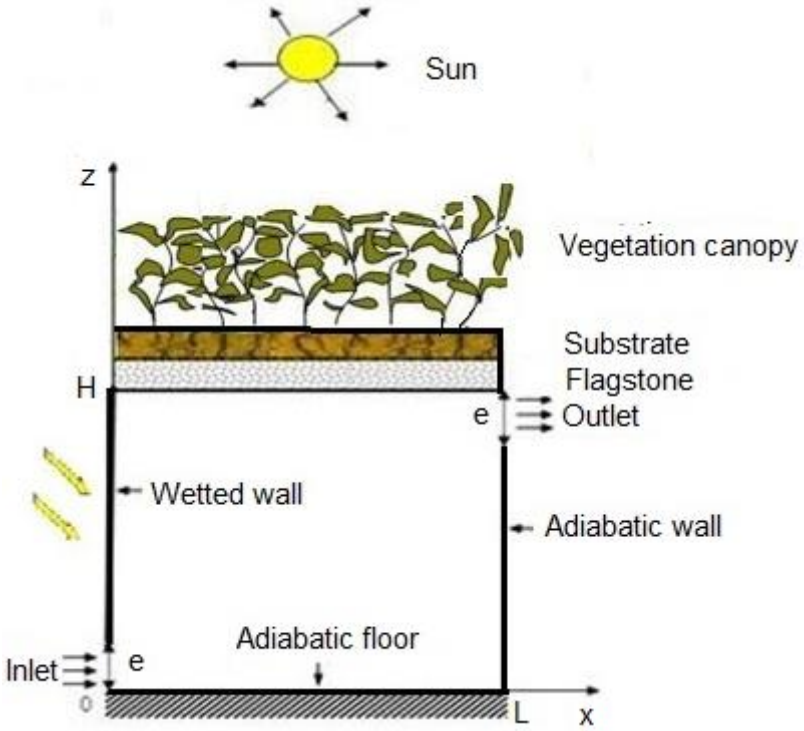

Figure 1. A schematic diagram for the problem.

The left vertical wall is partially heated and saturated with water. The bottom and the right vertical walls are assumed to be adiabatic. All side walls are impermeable. The inflow opening of size e is located on the lower left vertical wall while the location of the equal sized outflow opening is at the top of the right vertical wall as shown in Figure 1. Fresh air is injected at low speed through the inlet opening in horizontal direction and then the polluted hot air eliminated from the outlet opening at the right side wall. In this paper, the planted roof model is characterized by the Solar Heat gain Factor (SHF) defined as the ratio of the transmitted solar energy into the interior of the enclosure (through the complex roof including the vegetation canopy, the substrate and the flagstone support) to incident solar energy. The previous studies [15] proposed a correlation to calculate SHF as a function of Biot number (Bi) and the Leaf Area Index (LAI).

$$SHF = \sigma exp\left(-\frac{LAI}{\delta}\right) + \eta \quad (1)$$

Where:

$$\sigma = 97.48257 exp\left(-\frac{Bi}{3.27898}\right) + 8.07878$$

$$\delta = -0.19839 + 0.14606B_i - 0.00693B_i^2 + 0.00021B_i^3 - 2.916210^{-6}B_i^4$$

$$\eta = 1.98266$$

B_i is the Biot number

Inside the enclosure, the governing momentum, energy and water vapour conservation equations have been presented for double-diffusive mixed convective flows driven by the combined effect of the internal buoyancy induced by temperature and concentration differences and the external mechanically driven forced flow from the inlet opening.
The following assumptions are made in the analysis:

- The laminar airflow is two dimensional;
- Fluids are incompressible and isotropic;
- Thermo physical proprieties of the fluids are assumed to be constant except the density which obeys the Boussinesq approximation;
- Viscous heat dissipation is neglected.

Under these assumptions, the dimensionless governing equations are written in terms of vorticity and stream function formulation.
The heat and mass transfer rates on heat and mass source walls are described by the Nusselt and Sherwood average numbers, respectively as follows:

- on the top wall

$$Nu_{av} = \int_0^1 N_{u1}(X)dX \quad (2)$$

where local Nusselt is calculated as follow:

$$N_{u1}(X) = \frac{1}{\Theta}\Big|_{Z=1} \quad (3)$$

- on the left wall

Local Nusselt and Sherwood numbers are calculated as follows:

$$N_{u2}(Z) = \frac{1}{\Theta}\Big|_{X=0} \quad (4)$$

$$S_c(Z) = \frac{1}{C^*}\Big|_{X=0} \quad (5)$$

Reynolds number is defined as follow:

$$R_e = \frac{u_0 H}{\nu} \quad (6)$$

Numerical procedure and code validation

Transfer equations with appropriate boundary conditions are solved numerically by using an implicit finite difference method. The Thomas algorithm is employed to solve the algebraic equations. The diffusion terms are approximated by the central finite difference scheme and the implicit procedure to discretize the temporal derivatives is retained.

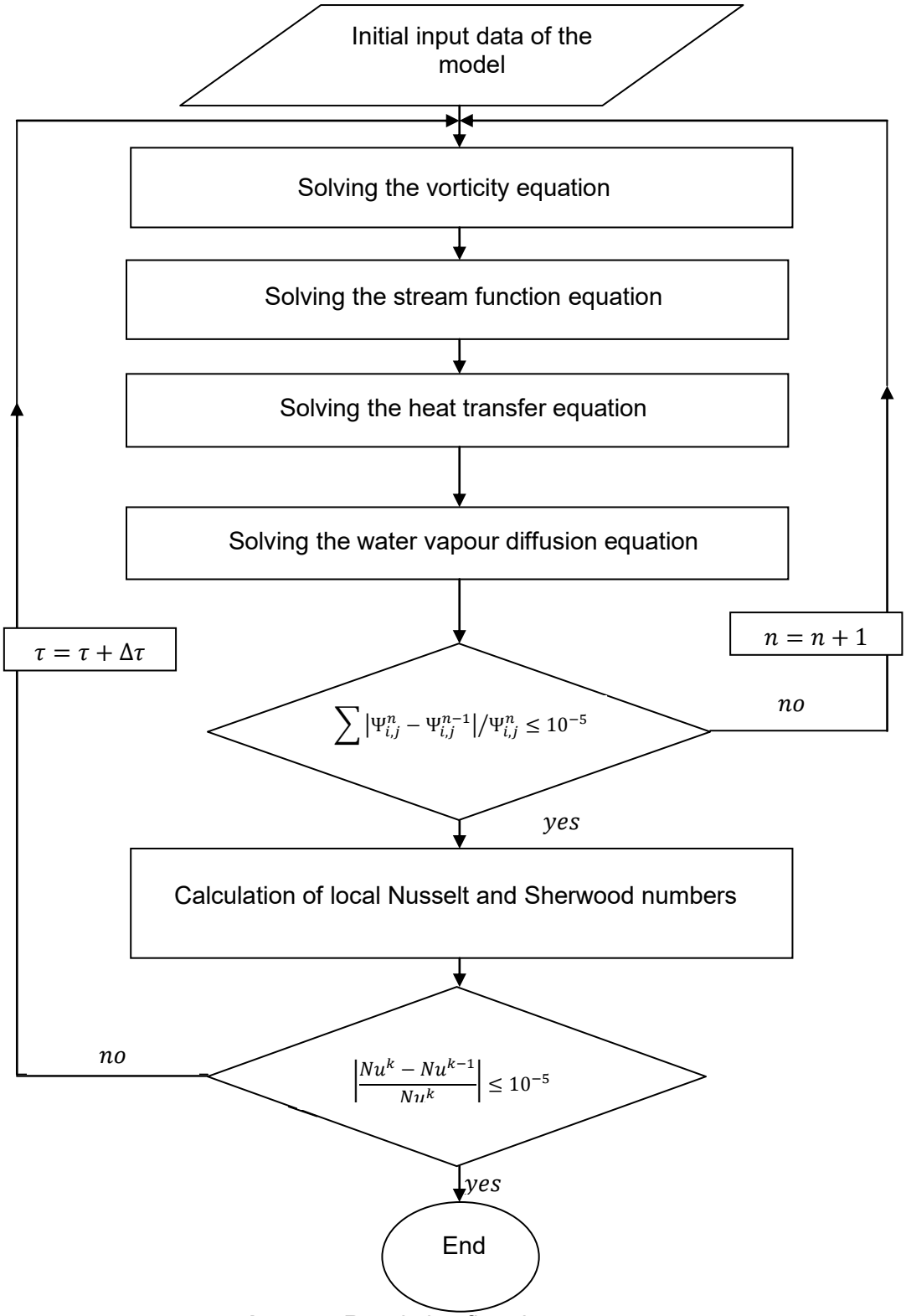

Figure 2. Resolution flowchart

The determination of the optimum mesh which represents a compromise between the criterion of stability Thomas algorithm and Gauss-Seidel method and an acceptable memory occupation was carried out by analyzing the influence of several steps of space and time on the mean Nusselt and Sherwood numbers. The following time and spatial steps Δt =0.0025 s and ΔX = 0.0025 m, ΔZ= 0.0025 m are respectively retained. Successive iterations were applied and the solution is considered satisfactory when the following convergence criterion is verified for each time:

$$\sum \left|\Psi_{i,j}^{n} - \Psi_{i,j}^{n-1}\right| / \Psi_{i,j}^{n} \leq 10^{-5} \quad (7)$$

where Ψ is a stream function

Figure 2 gives an overview of how the numerical resolution of the systems of algebrics equations associated with our problem is carried out.To ensure the convergence of the numerical solution to the exact solution, the grid size has been optimized, so results are independent of grid size. Furthermore, in order to verify the accuracy of our numerical procedure, we tested our algorithm based on the grid size 81x81 for a square enclosure with a discrete bottom wall heated and saturated with water. This computation of Sumon Saha [16] for mixed convection heat transfer inside a vented square cavity was validated and found to agree quite well. Similar distribution of streamlines is obtained as shown in figure 3.

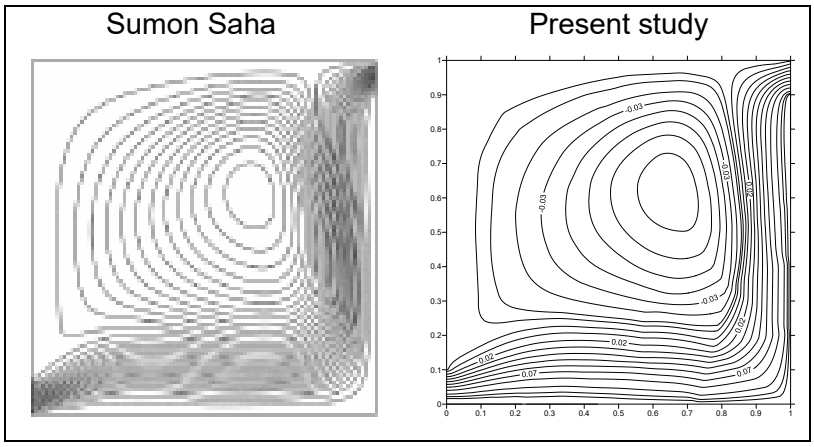

Figure 3. Comparison of streamlines with the results of Sumon Saha [16]

Results and discussion

Results were obtained for mixed convective flow and the Reynolds number is determined by the inlet wind speed. The Leaf Area Index (LAI) is chosen as the main parameter for the study. Then, particular attention is paid to the effects of this governing parameter LAI on the indoor air mixed convection. The range of LAI values used for the simulations is $1 \leq LAI \leq 6$. The objective of this study is to examine the heat transfer and the fluid flow characteristics due to mixed convection inside a square vented enclosure with a constant heat source on the top wall which represents the planted roof. The resulting flow structure is analyzed to provide a fundamental understanding of the effect of the Leaf Area Index and Reynolds number on the flow, thermal and water vapour concentration fields. Important dimensionless parameters for the present study are Nusselt and Sherwood numbers, on which the effect of the LAI and the Reynolds number is studied. The flow structure, the heat and mass transfers in the cavity are given in terms of streamline, isotherms and iso concentration lines. Figures 4 and 5 showed the effect of Leaf Area Index on *characteristics fields* for different solar heat flux amount reaching the planted roof. The airflow is characterized by open lines and pockets of fluid formed at the lower part of the right insulated wall.

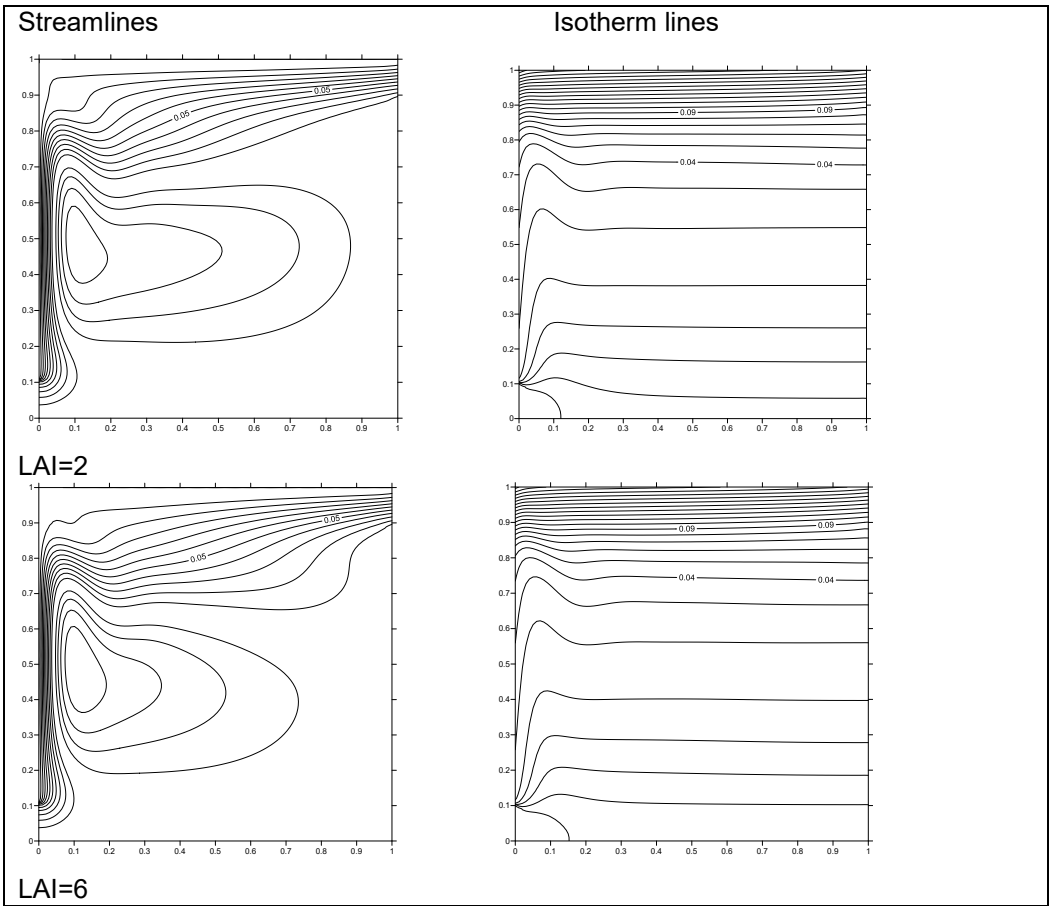

Figure 4. Streamlines and isotherm lines for $Rn(Z_R) = 200\ W/m^2$

It can be seen from figure 4 that the natural convection effect is present but remains relatively weak for higher values of the Leaf Area Index since open lines characterizing the imposed flow are still slightly dominant. The lower recirculation zone spreads and thereby squeezes the induced flow path resulting in almost the same kinetic energy in the bulk induced flow as that of the inlet section. Convection heat transfer induces the growth of the recirculation cell resulting in the faster removal of heat and mass from the heat and water sources. When the buoyancy force increases with the increase of heat flux and concentration gradients, the recirculation zone begins to develop by absorbing thermal energy through induced forced flow. Thereby the squeezed induced flow covers the whole of the heat and water source at low LAI. Similarly, the effect of natural convection on the temperature and water vapour concentration distribution is characterized by the displacement of the isotherm, isoconcentration and isohumidity fronts throughout the cavity. But, since the induced flow sweeps over the heat and water vapour concentration level to the left upper corner of the cavity decrease indicating a better heat and water vapour transfer. As transfer numbers increase nonlinearily, isotherm, isoconcentration and isohumidity lines become higher and plume formation is profound, indicating a well-established natural convection double diffusive flow. In this case, heat conduction in the fluid becomes more important than convection heat transfer (isotherm lines of figure 4). Furthermore, the distributions of isotherms and isoconcentrations describe a vertical stratification of air temperatures and humidity.

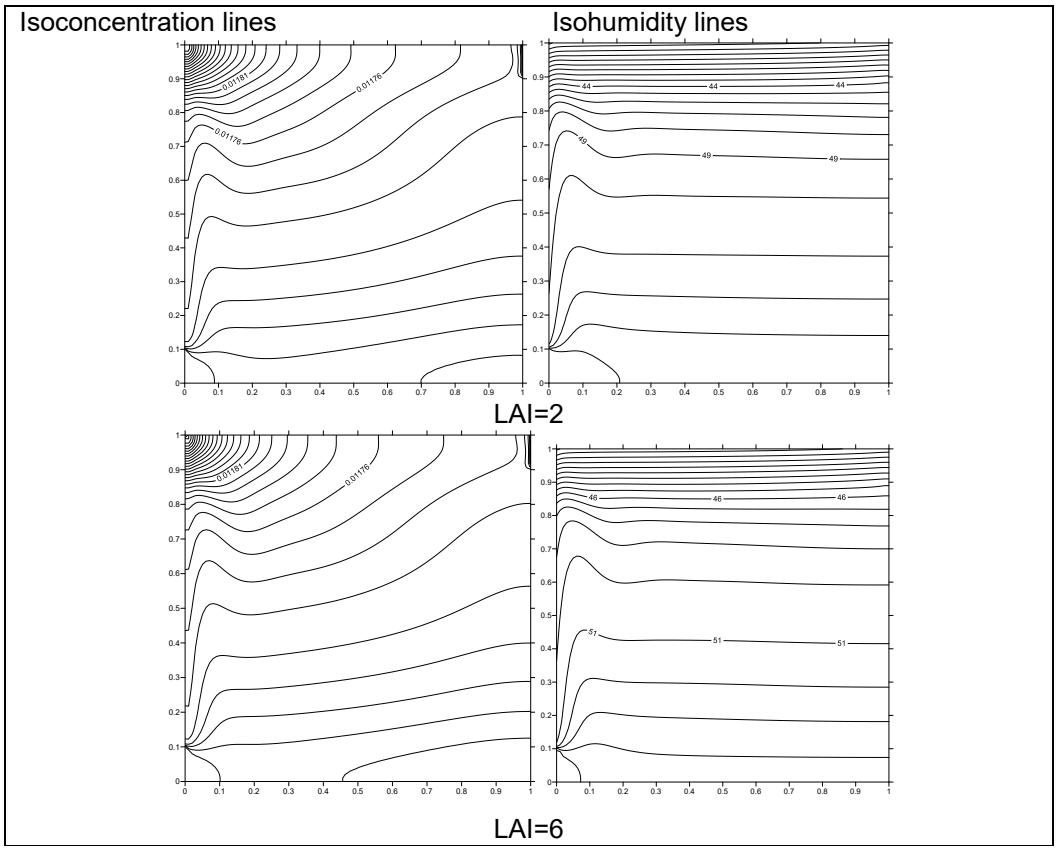

Figure 5. Isoconcentration lines and isohumidity lines for $Rn(Z_R) = 200\ W/m^2$

Increasing in solar heat flux reaching on a building leads to intensify simultaneously heat and mass transfers between the hot walls and the air in the cavity. Thus, the local Nusselt and Sherwood numbers increase nonlinearly when the solar flux on the walls increases as shown in figures 6 and 7.

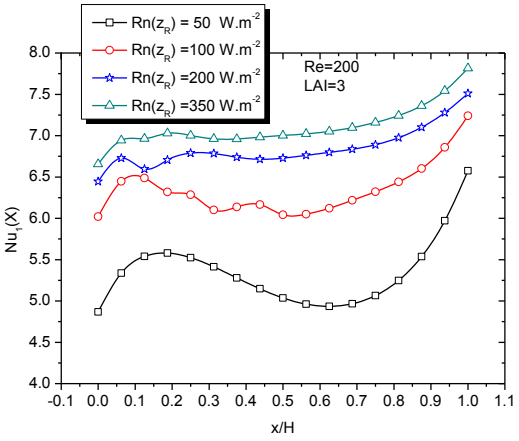

Figure 6. Effect of solar flux density on the variation of the local Nusselt number for upper wall of the cavity

For LAI equal to 3, figure 8 shows the variation in average temperature and relative humidity inside the cavity for different values of the solar flux density. This variation clearly indicates that the internal temperature undergoes very few fluctuations around 26 °C for solar flux of 350 W.m^{-2} while the relative humidity rate is between 50% and 60%.

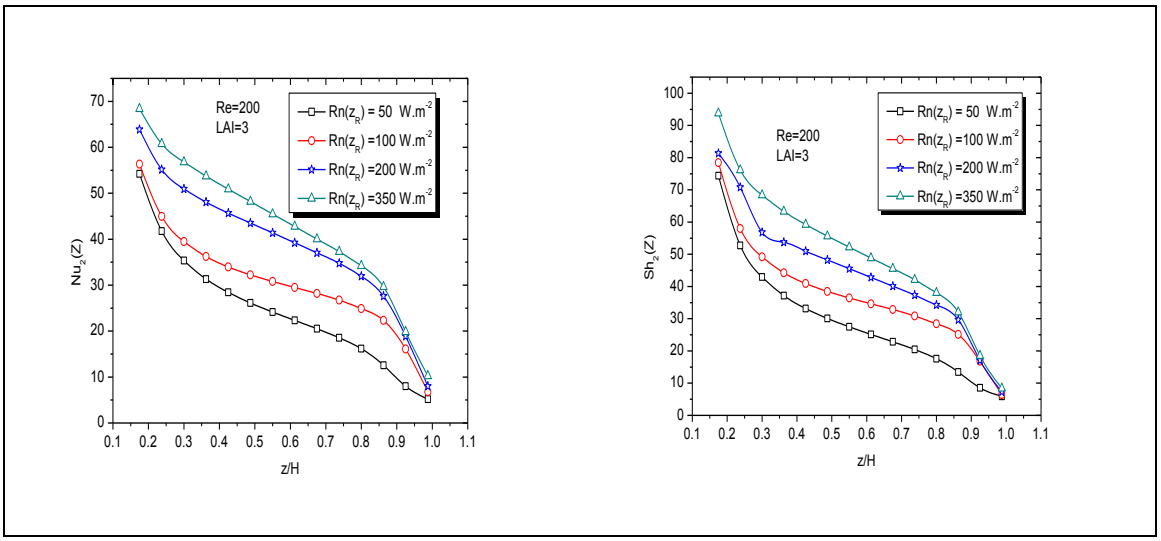

Figure 7. Influence of solar flux density on the variation of local Nusselt and Sherwood numbers for wetted wall

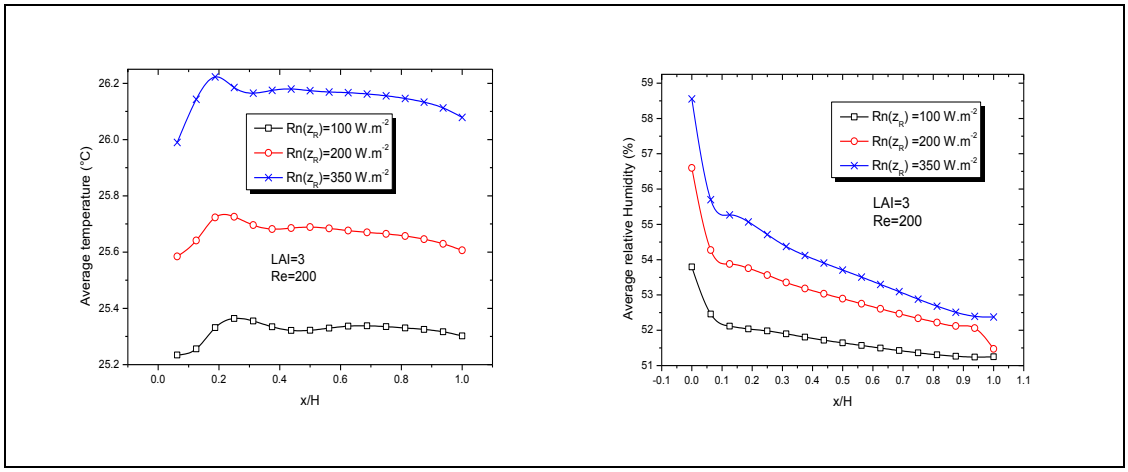

Figure 8. Variation in average temperature and relative humidity

To promote the technique of the vegetated roof, it seemed useful to establish a relation between the average Nusselt number, the Reynolds number and the Leaf Area Index. This relationship could contribute, during the architectural design, to facilitate the modeling and optimization of the characteristic quantities of this kind of building. The density of the solar flux being very variable during the day, heat exchanges between the vegetated slab and the indoor air has been expressed in the form of a heat transfer correlation as a fuction of the LAI and the Reynolds number for a solar flux density of 350 W.m^{-2} which represents an average value in Togolese climate conditions. According to profiles obtained, a polynomial expression has been proposed and tested.

$$Nu_{1mb} = Nu_{0b} + \beta_0(LAI) + \beta_1.\left(\beta_2^{\,LAI}\right) \tag{8}$$

Where:

$$Nu_{0b} = 4.32328 + 0.01435\ Re$$

$$\beta_0 = 0{,}01173 - 0.00008\ Re + 1{,}7041.10^{-10}Re^2 - 1{,}1285.10^{-10}Re^3$$

$$\beta_1 = -0{,}09443 + 0{,}00567\ Re - 3{,}5796.10^{-6}Re^2$$

$$\overline{\beta_2} = 0{,}3248$$

Table 1 presents the values of the coefficients Nu_{0b}, β_0 and β_1 for different values of Reynolds number. Values of the Reynolds number are calculated with increments in inlet air velocity to take into account natural and forced airflows in the cavity. The range of the Reynolds number Re and the LAI are respectively: $100 \leq R_e \leq 600$ and $0.5 \leq R_e \leq 7.5$.

Table 1. Values of coefficients as a function of the Reynolds number.

Re	**Nu_{0b}**	β_0	β_1	β_2
100	5,65929	0,00546	0,45319	0,32516
150	6,50321	0,00332	0,65562	0,32513
200	7,08072	0,00201	0,91765	0,32502
250	8,0435	8,5E-4	1,00832	0,32523
300	8,74486	4,1E-4	1,38658	0,32488
350	9,45462	2,2E-4	1,41504	0,32454
400	10,0606	2,9E-4	1,61724	0,32499
450	10,6813	5,3E-4	1,72380	0,32435
500	11,39398	9,6E-4	1,85128	0,32488
550	12,1831	0,00108	1,92126	0,32441
600	12,99244	0,00152	2,02727	0,32506

The coefficients Nu_{0b}, β_0 and β_1 given in the Table 1 are correlated as a function of the Reynolds number whereas, because of its weak variation, an average value is estimated for the coefficient $\overline{\beta_2}$. As shown in Figure 9, acceptable agreement is observed between the prediction using the correlation and numerical values.

Conclusion

This work has shown mixed convective heat and mass transfer inside a square ventilated enclosure. The momentum equation is solved in terms of vorticity and stream function formulation. A numerical model based on an implicit finite-difference method was developed for discretizing time average Navier-Stokes equations. The Thomas algorithm and the Gauss-Seidel iterative method were used to solve the algebraic equations. The model was applied in the simulation of a végetalised building in hot-humid climate. The numerical investigation was carried out under Togolese climate conditions. Analysis of the flow structure obtained showed a mixed convection type, but the isotherms et iso-concentration distributions reveal a vertical stratification of the temperatures and the relative humidity. To predict heat transfers inside the cavity, a correlation has been established for the estimation of the average Nusselt number as a function of the Leaf Area Index and the Reynolds number under solar heat flux of 350 W.m^{-2}, the average in case of Togo. It was found that a larger Leaf Area Index reduces the solar flux penetration and therefore, reduces significantly heat transfer inside the enclosure and then stabilizes it temperature. For the LAI equal to 3, the indoor air fluctuates around 26°C and the relative humidity range is found to be 50% -

60% under solar heat flux of 350 W.m^{-2}. It is clearly proved that the foliage density and hence the vegetable canopy type selection greatly influence heat transfer inside green roof building.

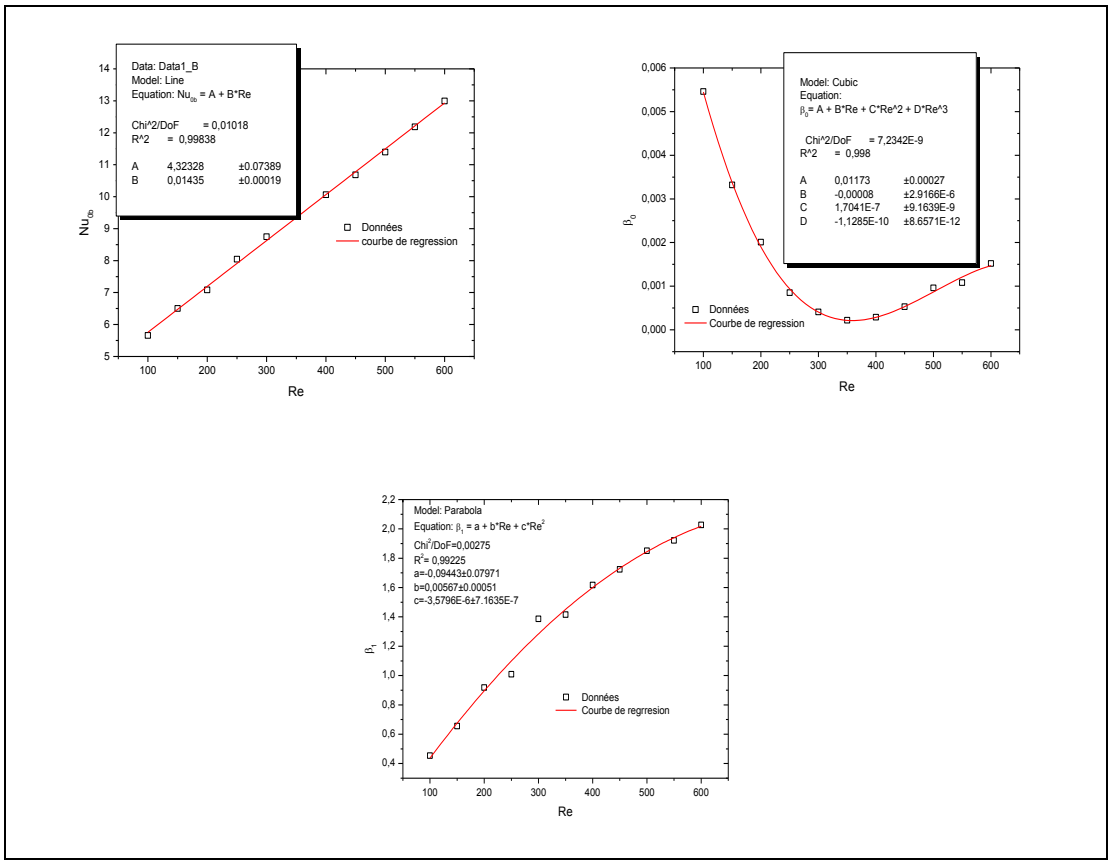

Figure 9. Regression curves of the coefficients as a function of the Reynolds number

Nomenclature

ν	Kinematic viscosity ($m^2.s^{-1}$)
Θ	Nondimensional temperature (-)
Ψ	Nondimensional stream function (-)
τ	Nondimensional time (-)
B_i	Biot number (-)
C^*	Nondimensional concentration (-)
e	size of inlet and outlet (m)
H	height of the cavity (m)
L	width of the cavity (m)
LAI	Leaf Area Index (-)
$N_u(X)$	Local Nusselt number (-)
$N_u(Z)$	Local Nusselt number (-)
Nu_{av}	average Nusselt number (-)
$Rn(Z_R)$	Solar heat flux $(W.m^{-2})$
R_e	Reynolds number (-)
$S_c(Y)$	Local Sherwood number (-)

SHF	Solar Heat gain Factor (-)
x, z	coordinates (m)
X, Z	Nondimensional coordinates (-)

References

[1] *ROOFSOL, Building in ROOFSOL, “Roof Solutions for natural cooling,”* . Commission of the European Communities. DG XII, Science, Research and Development; (Contract N° JOR3CT960074) 1998.

[2] Nahar N, Sharma P, Purohit M. Studies on solar passive cooling techniques for arid areas. *Energy Conversion and Management*. 1999 01;40(1):89-95. https://doi.org/10.1016/s0196-8904(98)00039-9

[3] Tang R, Etzion Y. On thermal performance of an improved roof pond for cooling buildings. *Building and Environment*. 2004 02;39(2):201-209. https://doi.org/10.1016/j.buildenv.2003.09.005

[4] Jain D. Modeling of solar passive techniques for roof cooling in arid regions. *Building and Environment*. 2006 03;41(3):277-287. https://doi.org/10.1016/j.buildenv.2005.01.023

[5] Fioretti R, Palla A, Lanza L, Principi P. Green roof energy and water related performance in the Mediterranean climate. *Building and Environment*. 2010 08;45(8):1890-1904. https://doi.org/10.1016/j.buildenv.2010.03.001

[6] Abalo Samah H, Banna M. Performance analysis of Thermal Insulation Screens used for Classic Roofs in hot-humid Tropics. *International Energy Journal*. 2009;10:255-266.

[7] Niachou A, Papakonstantinou K, Santamouris M, Tsangrassoulis A, Mihalakakou G. Analysis of the green roof thermal properties and investigation of its energy performance. *Energy and Buildings*. 2001 09;33(7):719-729. https://doi.org/10.1016/s0378-7788(01)00062-7

[8] Nyuk Hien W, Puay Yok T, Yu C. Study of thermal performance of extensive rooftop greenery systems in the tropical climate. *Building and Environment*. 2007 01;42(1):25-54. https://doi.org/10.1016/j.buildenv.2005.07.030

[9] Barrio EPD. Analysis of the green roofs cooling potential in buildings. *Energy and Buildings*. 1998 04;27(2):179-193. https://doi.org/10.1016/s0378-7788(97)00029-7

[10] Alexandri E, Jones P. Developing a one-dimensional heat and mass transfer algorithm for describing the effect of green roofs on the built environment: Comparison with experimental results. *Building and Environment*. 2007 08;42(8):2835-2849. https://doi.org/10.1016/j.buildenv.2006.07.004

[11] Tabares-Velasco PC, Srebric J. A heat transfer model for assessment of plant based roofing systems in summer conditions. *Building and Environment*. 2012 03;49:310-323. https://doi.org/10.1016/j.buildenv.2011.07.019

[12] Sailor D, Hutchinson D, Bokovoy L. Thermal property measurements for ecoroof soils common in the western U.S.. *Energy and Buildings*. 2008 01;40(7):1246-1251. https://doi.org/10.1016/j.enbuild.2007.11.004

[13] Ouldboukhitine S, Belarbi R, Djedjig R. Characterization of green roof components: Measurements of thermal and hydrological properties. *Building and Environment*. 2012 Oct;56:78-85. https://doi.org/10.1016/j.buildenv.2012.02.024

[14] Jim C, Tsang S. Biophysical properties and thermal performance of an intensive green roof. *Building and Environment*. 2011 06;46(6):1263-1274. https://doi.org/10.1016/j.buildenv.2010.12.013

[15] Hodo-Abalo S, Banna M, Zeghmati B. Performance analysis of a planted roof as a passive cooling technique in hot-humid tropics. *Renewable Energy*. 2012 03;39(1):140-148. https://doi.org/10.1016/j.renene.2011.07.029

[16] Saha S, Hasan MN, Khan IA. Double Diffusive Mixed Convection Heat Transfer inside a Vented Square Cavity. *Chemical Engineering Research Bulletin*. 2009 Oct 05;13(1). https://doi.org/10.3329/cerb.v13i1.2512

2nd German-West African Conference on Sustainable, Renewable Energy Systems SusRes – Kara 2021

Energy Efficiency

https://doi.or/10.52825/thwildauensp.v1i.15

Published: 15 June 2021

Minimization of the electric energy in systems using ultra-high density magnetic storage

PAKAM Tchilabalo[1], A. Adanlété Adjanoh[1]

[1]Laboratoire Matériaux et Energie Renouvelable et Environnement (LaMERE), University of Kara, Togo.

Abstract. We present an optimization of the thickness of the magnetic layers that serve to record the information of the daily need in order to minimize the useful electrical energy. The study provides details on the energy activation and distribution of the energy barriers in the samples of thickness $t_{C_o} = 0.7, 0.8\ and\ 1nm$. We find that distribution of the energy barriers $\mathrm{E_a}$, its distribution width σ_w, the real activation field $\mu_0 \mathrm{H_r}$ are lowest in the sample of thickness $t_{C_o} = 1nm$, hence this sample allows to use less electrical energy for information recording.

Keywords: Width of distribution of the energy barriers, information recorging, electrical energy minimization.

Introduction

The evolution of the digital economy and the use of ferromagnetic materials in ultra high density information storage has given rise to interest in these materials in recent decades for researchers. Research on these materials is oriented either towards the understanding of very fundamental mechanisms, or towards important perspectives for applications such as ultra high density storage [1,2]. In fact, the writing of elementary information is traditionally done by applying a magnetic field pulse [3]. The field and energy required to create a first magnetization reversal are called the activation field and activation energy, respectively. But the activation energy is not single in a real sample. In this case the simple activation energy is replaced by a distribution of energy barriers[10]. The lower the distribution of energy barriers, the less electrical energy is needed for the storage of information. Therefore, perfect control and optimization of these parameters controlling the distribution of energy barriers in order to reduce this energy as much as possible, is essential in order to minimize the electrical energy required for this effect. Some works has been devoted to the activation energy [3,4,5,6] but did not discuss the effect of the thickness on the distruibution and the width of the energy barriers in the samples. This paper has the particularity of showing that the thickness of the magnetic layers have an influence on the width of the distribution of energy barrier, hence on electrical energy.

Material and Method

Sample and Structural Characterizations

Si(100) substrate is beforehand cleaned by ultrasounds in an acetone bath. After the cleaning, this substrates is thermally oxidized in a furnace at 1200°C during 2 hours. This time is sufficient for the formation of an oxide layer on the silicon surface substrate.

Au/Co/Au films were prepared by electron beam evaporation in an ultrahigh vacuum chamber, with a base pressure about of $10^{-9}\ Torr$ and approximately $10^{-8} Torr$ during

deposition on SiO2, at room temperature. On Au film, cobalt layers with thicknesses (t_{C_o}) :1, 0.8 and 0.7 nm are then deposited [11]. At finally a second Au layer with a thickness about of 5nm is deposited on top of the cobalt layers. The (111) texture of the Au buffer layer suggests, in each case, a possible epitaxial growth of the cobalt layer with the Hexagonal Close-Packed (0001) structure [7,8,9].

Megnetic investigation

Magnetic hysteresis loops, at a field sweep rate of $\frac{d\mu_0 H}{dt} = 1.2\ mT$, were recorded at room temperature (RT) by polar magneto-optical Kerr effect magnetometry (PMOKE) using a He-Ne laser (λ= 633 nm). On the hysteresis loops we measured the coercive fields $\mu_0 H_c$ and the nucleation fields $\mu_0 H_n$. Table 1. shows magnetic quasi statistic parameters deduced from the hysteresis loops of the three samples [4].

Table 1. Data obtained from the quasi-static characterizations

t_{C_o}(nm)	0.7	0.8	1
$\mu_0 H_c$(mT)	31.60	29.20	26.50
$\mu_0 H_n$(mT)	27.4	24.9	23

Magnetization Reversal

- Average activation energy

The energy needed to reverse magnetization can be expressed in the following way [3,5] :

$$\mathrm{W(H)} = \bar{E}_a - \mathrm{M_s V_B}(\mu_0 \mathrm{H}) \quad (1),$$

and the time $t_{1/2}$ corresponding to the time at the end of which the sample is demagnetized, is expressed following Arrhenius law :

$$\mathrm{t_{1/2}} = \mathrm{t_0 exp}\left(\frac{\bar{E}_a - \mathrm{M_s V_B}(\mu_0 \mathrm{H})}{\mathrm{K_B T}}\right) \quad (2)$$

Where $\bar{E}_a$ is average activation energy at zero field, thermal energy required to initiate the magnetization reversal in the absence of the field, M_s is the saturation magnetization and V_B is the Barkhausen volume (the magnetization volume that reverses during a single activation event). The fitting of expérimental dots of $t_{1/2}$ vs $\mu_0 \mathrm{H}$ and their ajustement by eq (2) allows to have the values of $\mathrm{t_0}$, $\bar{E}_a$ and $\mathrm{M_s V_B}$ for differents samples represented on figure 1. And in table 2 [4].

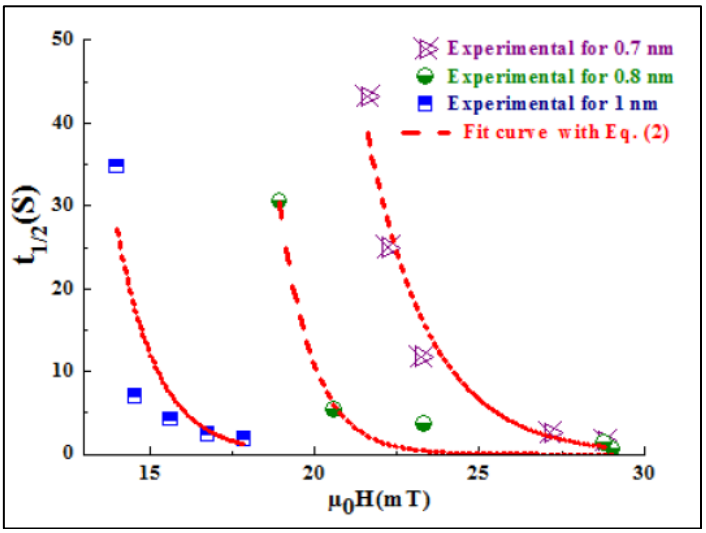

Figure 1. $t_{1/2}$depending on $\mu_0 H$ and it fitting by Arrhenius-Néel law Eq. (2), for the three samples

Table 2. Data from the fitting byArrhenius-Néel law

$\mathbf{t_{C0}(nm)}$	**0.7**	**0.8**	**1**
$\mathbf{t_0(s)}$	10^4	10^4	10^4
$\bar{E}_a$ (meV)	146.12	329.2	138.4
$\mathbf{M_s V_B(10^{-21} J/mT)}$	2.15	4.05	3.35

- Width of the distribution of the energy barriers

According to the work of A. Adanlété Adjanoh, R. Belhi [10,11], the weakness of $\bar{E}_a$ confirms the fact that the magnetization reversal in thises samples is mainly done by domain wall motion in the sample. In a real sample the magnetic domains have a dendritic structure as shown in image of fig. 3. This indicates that an activation energy would not be single in the sample. In this case the simple energy barrier is replaced by a distribution of energy barriers, characterized by a width σ_w . Bruno et al. [3] showed that if one assumes a square distribution of the energy barriers, the maximum slope of reduced magnetization m(t)=(M(t)+Ms)/2Ms represented as a function of $ln(t)$ is inversely proportional to the width σ_w of the distribution of the activation energy barriers:

$$m(t) = -\frac{K_B T * \ln t}{\sigma_w} \qquad (3)$$

The relaxation curves (t) vs (t) and their fittings using Eq.(3) for the layer of 1nm are presented on fig.2.

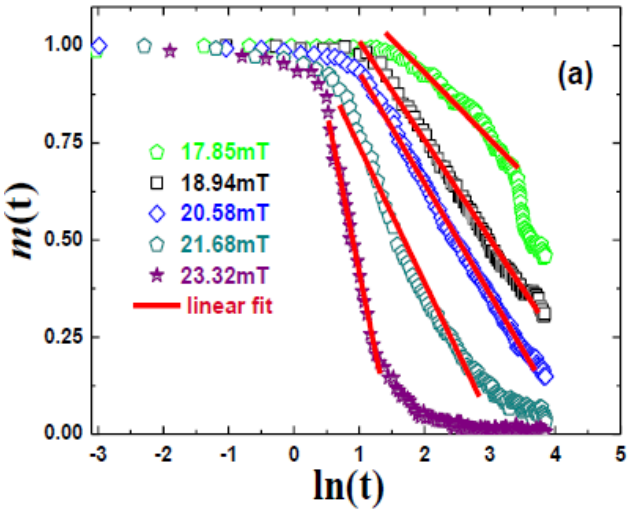

Results and discussions

Width of the distribution of the energy barriers

By analyzing the shapes of the curves and their fittings we can write this :

$$For \quad lnt \, \epsilon \,]-\infty, 0]; m(t) = cte = 1 \tag{4}$$

$$For \quad lnt \, \epsilon \, [0, b]; m(t) = \alpha lnt + \beta \tag{5}$$

With α and b values depending on the applied field and β a constant.

At the start of the reversal, the magnetization keeps its saturation value for a period of time (Eq.1), after this demagnetization is almost linear with a negative slope which depends on the field ($\mu_0 H$) applied.

Using the linear fittings and Eq.(5), We determine the value of $\beta = 1$. σ_w Depends on applied field [13]. Then α Inversely proportional to σ_w . Let’s take $\alpha = -\frac{K_B T}{\sigma_w}$, a negative slope due to decreases in the lines; we can then rewrite the eq. (5) as following:

$$m(t) = -\frac{K_B T lnt}{\sigma_w} + 1 \tag{6}$$

From this relation we can determine the demagnetization time $t_{1/2}$ such that

$$\frac{1}{2} = -\frac{K_B T ln(t_{1/2})}{\sigma_w} + 1$$

Which implies :

$$t_{1/2} = \exp\left(\frac{\frac{1}{2}\sigma_w}{K_B T}\right) \tag{7}$$

Now let us recall the expression of $t_{1/2}$ that follows Arrhenius' law in Eq. (1):

$$t_{1/2} = t_0 \exp\left(\frac{\bar{E}_a - M_s V_B(\mu_0 H)}{K_B T}\right)$$

Whith $\bar{E}_a$ the average of activation energy.

By equalizing the two relations (1) and (7) we end up with the expression for the width of the energy barrier:

$$\sigma_w = \sigma_{w_0} - 2\mu_0 M_S V_B H \tag{8}$$

With

$$\sigma_{w_0} = 2(\bar{E}_a + K_B T ln t_0)\,, \tag{9}$$

corresponding to the width of the distribution of the energy barriers at zero field.

This relation (Eq.(8)) shows that σ_w decreases as the applied field increases, which is in perfect agreement with the experimental measurement of σ_w in the sample of 1nm thick. With Eq. (7), we can calculate the value of σ_{w_0} for the three samples. We notice that by using $t_0 = 10^4$ we get high values of σ_{w_0} compared to those measured experimentally [10].

This leads us to think about the real value of t_0 in a real sample. Taking into account the dendritic form of the domains observed experimentally, the magnetization reversal curves for theses samples can be described by the compressed exponential form [11]:

$$m(t) = exp\left[-\left(\frac{Rt}{\tau(k)}\right)^{\beta}\right] \tag{10}$$

Where R is the nucleation rate and $\tau(k)$ a parameter inversely proportional to k which designates the competition between the nucleation and the propagation of magnetic domains and β a fractional exponent between 1 and 3.

From the relation (10) we deduce another expression of $t_{1/2}$:

$$t_{1/2} \approx \frac{\tau(k)(ln2)^{\frac{1}{\beta}}}{R_o} \exp\left(\frac{\overline{E_a} - M_s V_B(\mu_0 H)}{K_B T}\right) \tag{11}$$

Hence by identification of Eq.(11) with Eq.(1), we get the prefactor as $t_0 \cong \frac{\tau(k)(ln2)^{1/\beta}}{R_o}$. Using this expression of t_0 with the values of its parameters measured [11] and recorded in table.3:

Table 3. Data of the parameters of magnetization reversal compressed exponential form

$\mathbf{t_{C_o}(nm)}$	**0.7**	**0.8**	**1**
$\boldsymbol{\beta}$	1.41	1.73	1.49
$\mathbf{R_o(S^{-1})}$	$2\text{x}10^{-5}$	$3\text{x}10^{-5}$	$8.63\text{x}10^{-6}$
$\boldsymbol{\tau(k)}$	$5.5\text{x}10^{-4}$	$8.7\text{x}10^{-4}$	$2.4\text{x}10^{-4}$

We obtain the values of the width at zero field $\boldsymbol{\sigma_{w_0}}$ recorded in the table .4

Table 4. Values of the Width of the distribution of energy barriers in each

$\boldsymbol{t_{C_o}}$**(nm)**	**0.7nm**	**0.8nm**	**1nm**
$\boldsymbol{\sigma_{w_0}(meV)}$	435.01	799.84	420.63

We notice that these values are in perfect agreement with the values found by linear fitting in the 1nm thick layer and are low compared to that found for in multilayers $(PtCo)_3$ [6]. And that the value of the width of the distribution of the energy barrier, when no field is applied, is generally low in all thicknesses and the lowest value is obtained in this thickness of 1nm as shown fig.3. This means that it is easier to reverse the magnetization in the thickness of 1nm than 0.7nm and 0,8nm ; which makes it possible to save energy in the latter. The high value within 0.8nm can be explained by a high defect rate in this sample. These defects slow down the magnetization reversal process [10] ; hence this increases the width of the distribution of the energy barries in the sample.

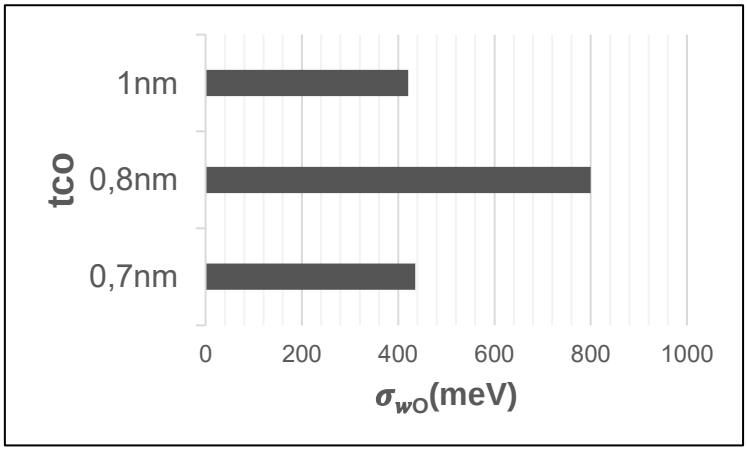

Figure 3. Width of the distributionof the energy barriers in each sample of thickness $\boldsymbol{t_{C_o}}$

Activation Energy barries in a real sample

Activation fields in a real sample is the field $\mu_0 H_r$ that must be applied to completely remove the width of the energy barrier distribution, i.e. to cancel the width of the barrier in a sample. From this definition we can then write :

$$\sigma_{w_0} - 2\mu_0 M_S V_B H_r = 0 \tag{12}$$

We find respectively $\mu_0 H_r = 16.19\text{mT}$, $\mu_0 H_r = 15.80\text{mT}$ and $\mu_0 H_r = 10.04\text{mT}$ for the thickness $t_{C_o} = 0.7\text{nm}, 0.8\text{nm}$ and 1nm. These values compared to those of the coersive field $\mu_0 H_c$ in table 1., are lower in the three cases, what shows that the magnetization reversal is well initiate in the real sample before it is demagnetized. The lowest value of $\mu_0 H_r$ is found in the sample thickness $t_{C_o} = 1\text{nm}$. It shows that magnetization reversal (the writing of elementary information) would not need enough electrical field ; therefore this sample will need less electrical energy.

Distribution of energy barries

The distribution of energy barries can be framed as follows [13]:

$$\bar{E}_a - \frac{\sigma_{w_0}}{2} \leq E_a \leq \bar{E}_a + \frac{\sigma_{w_0}}{2} \tag{13}$$

where $\bar{E}_a$ is the average activation energy in the sample, assumed to be equal to that found in table.2 . Using the Eq.(13) and Eq.(10), we get the following relation :

$$-K_B T \ln t_0 \leq E_a \leq 2x\bar{E}_a + K_B T \ln t_0 \tag{14}$$

On Fig 4. We show the distribution graph of the energy barrier in each sample.

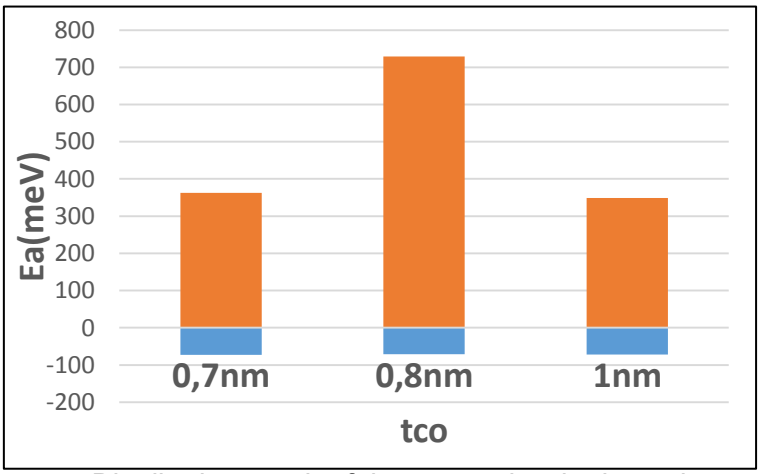

Figure 4. Distribution graph of the energy barrier in each sample

We find respectively the margins : $-72.38\, meV \leq E_a \leq 362{,}62\, meV$, $-70{,}72 \leq E_a \leq 729.12\, et - 71.91 \leq E_a \leq 348.71$ for thicknesses $t_{C_o} = 0.7\text{nm}, 0.8\text{nm}, 1\text{nm}$. It is clear here

too that the distribution margin of the energy barrier in the sample of thickness $t_{C_o} = 1\text{nm}$ is smaller. This shows that reversing the magnetization in the sample $t_{C_o} = 1\text{nm}$ will require less electrical energy ; so less electrical energy for information storage.

Conclusion

We have shown through this article the effect of the thickness of the magnetic layers of cobalt on the distribution of the energy barrier and therefore on the saving of electrical energy in the storage of information in these media. We theoretically calculated, the distribution of the energy barrier E_a, its distribution width σ_w and the real activation field $\mu_0 H_r$, and saw that all are different and weak in each thickness $t_{C_o} = 0.7\text{nm}, 0.8\text{nm and } 1\text{nm}$. Moreover, the smallest value of these parameters are found in the layer of thickness $t_{C_o} = 1\text{nm}$. Therefore, this state that the writing a bit of information in this thickness of 1nm would require less magnetic field. Hence the storage of information in cobalt thickness of 1nm would require less electrical energy.

References

[1] Pommier J, Meyer P, Pénissard G, Ferré J, Bruno P, Renard D. Magnetization reversal in ultrathin ferromagnetic films with perpendicular anistropy: Domain observations. Physical Review Letters. 1990 Oct 15;65(16):2054-2057. https://doi.org/10.1103/physrevlett.65.2054

[2] Shen JX, Kirby RD, Wierman K, Shan Z-, Sellmyer DJ, Suzuki T. Magnetization reversal and defects in Co/Pt multilayers. Journal of Applied Physics. 1993 05 15;73(10):6418-6420. https://doi.org/10.1063/1.352618

[3] Bruno P, Bayreuther G, Beauvillain P, Chappert C, Lugert G, Renard D, Renard JP, Seiden J. Hysteresis properties of ultrathin ferromagnetic films. Journal of Applied Physics. 1990 Dec;68(11):5759-5766. https://doi.org/10.1063/1.346944

[4] Adanlété Adjanoh A, Belhi R. Energy Depending on the Thickness of the Ferromagnetic Layer. J. Mat. Phys and Chem. 2018;.

[5] Czapkiewicz M, Stobiecki S, van Dijken. Thermally activated magnetization reversal in exchange-biased [Pt⁄Co]3/Pt/IrMn multilayers. Phys. Rev. B. 2008;77.

[6] Belhi R, Adanlété Adjanoh A, Vogel J. Influence of Pt thickness on magnetization reversal processes in (Pt/Co)3 multilayers with perpendicular anisotropy. Journal of Magnetism and Magnetic Materials. 2012 06;324(11):1869-1877. https://doi.org/10.1016/j.jmmm.2012.01.003

[7] Chappert C, Renard P, Beauvillain J. Ferromagnetism of very thin films of nickel and cobalt. J. Magn. Magn. Mater. 1986;54:795.

[8] Lee CH, He H, Lamelas F, Vavra W, Uher C, Clarke R. Epitaxial Co-Au Superlattices. Physical Review Letters. 1989 02 06;62(6):653-656. https://doi.org/10.1103/physrevlett.62.653

[9] Ohtake M, Futamoto M, Kirino F, Fujita N, Inaba N. Epitaxial growth of hcp/fcc Co bilayer films on Al2O3(0001) substrates. Journal of Applied Physics. 2008 04;103(7):07B522. https://doi.org/10.1063/1.2838848

[10] Adjanoh AA, Belhi R. Micro magnetic dendritic domain structure in the demagnetized state of perpendicular magnetic ultrathin film: The effect of the width of the distribution of the energy barriers. Journal of Magnetism and Magnetic Materials. 2019 03;473:12-15. https://doi.org/10.1016/j.jmmm.2018.10.025

[11] Adanlété Adjanoh A, Belhi R, Vogel J, Ayadi M, Abdelmoula K. Compressed exponential form for disordered domain wall motion in ultra-thin Au/Co/Au ferromagnetic films. Journal of

Magnetism and Magnetic Materials. 2011 03;323(5):504-508. https://doi.org/10.1016/j.jmmm.2010.10.002

2nd German-West African Conference on Sustainable, Renewable Energy Systems SusRES – Kara 2021

Smart Grids

https://doi.org/10.52825/thwildauensp.v1i.18

Published: 15 June 2021

Demand Response Model for optimized use of Renewable Energies in Production

Clemens Faller[1], Sonja Podjawerschek[1], Armin Co[1], Markus Dannehl[1], Moritz Paul Heimbach[1], Sory Ibrahima Nadiaye[1,]

[1] Bochum University of Applied Sciences, Germany

Abstract. A demand-response model was developed in the Automation Technology Laboratory at the Velbert/Heiligenhaus Campus (CVH) of Bochum University of Applied Sciences, in which energy users in the manufacturing sector are networked with a smart grid via a cloud platform in order to control production based on the supply of renewable energies.

Keywords: Demand-Response, Smart-Grid, Cloud-Platform, IOT, Industry 4.0

Introduction

Due to the increasing scarcity and thus price increase of energy, companies active in production are already under pressure to increase the resource efficiency of their production facilities. In the interaction between energy producers and users, data exchange enables optimized use of the available energy in order to minimize the reserve to be held from conventional energy sources [1]. As the specific energy consumption is constantly reduced, but at the same time the economy and thus also the manufacturing industry is growing, there is a need for further action with regard to the energy efficiency of production in order to counteract this rebound effect [2]. In order to provide manufacturing SMEs with a basis for analyzing their energy consumption in relation to the product produced and the operating resources from both an energy and productivity point of view, it is necessary to develop a manageable solution [3]. Such a manageable system for a demand response scenario, in which production and consumption of energy is balanced [4] was developed in the Automation Technology Laboratory at the Velbert/Heiligenhaus Campus (CVH) of Bochum University of Applied Sciences, in which energy users in the manufacturing sector are networked with a smart grid via a cloud platform in order to control production based on the supply of renewable energies.

Concept of the Demand-Response Architecture

The demand response model contains a smart grid model (SGM), a production facility and a cloud platform. The SGM illustrates an intelligent energy network with various electricity generators and consumers. This included both hardware and software components. The group of generators on the SGM is made up of one conventional component (a conventional power plant) and two renewable energy sources, a wind turbine and a photovoltaic farm. The group of consumers is represented by a cluster of houses. All these components are interconnected on the model. The connections are LED strips that can light up both green and red. Green stands for renewable energy and red for conventional energy. The wind turbine on the model has a motor, which can be used to illustrate the wind speed. The LED strips and the wind turbine are controlled by an Arduino, which adjusts the color and rotation speed via PWM.

The smart factory model is a system from Festo Didactic. This model consists of a conveyor belt and pneumatic actuators. A sorting task is carried out as an example application. The control system is a RevolutionPi (RaspberryPi in an industrial housing) with a CoDeSys PLC Runtime.

Both parts of the demand response model, i.e., the smart grid model and the production system, are connected via OPC-UA to an edge gateway, which sends the energy data to a cloud platform from the company EXOR. The demand-response application then runs on this cloud platform. The following scenarios were developed as part of the work: When a production order is to be started, it is calculated within the cloud platform whether sufficient renewable energies are available. If this is the case, the PLC receives the signal to start the sample application. If not enough renewable energy is produced in the smart grid model, the person responsible for production receives this information and can then decide, based on the importance of his order, to start production anyway or to wait for better availability of renewable energy sources.

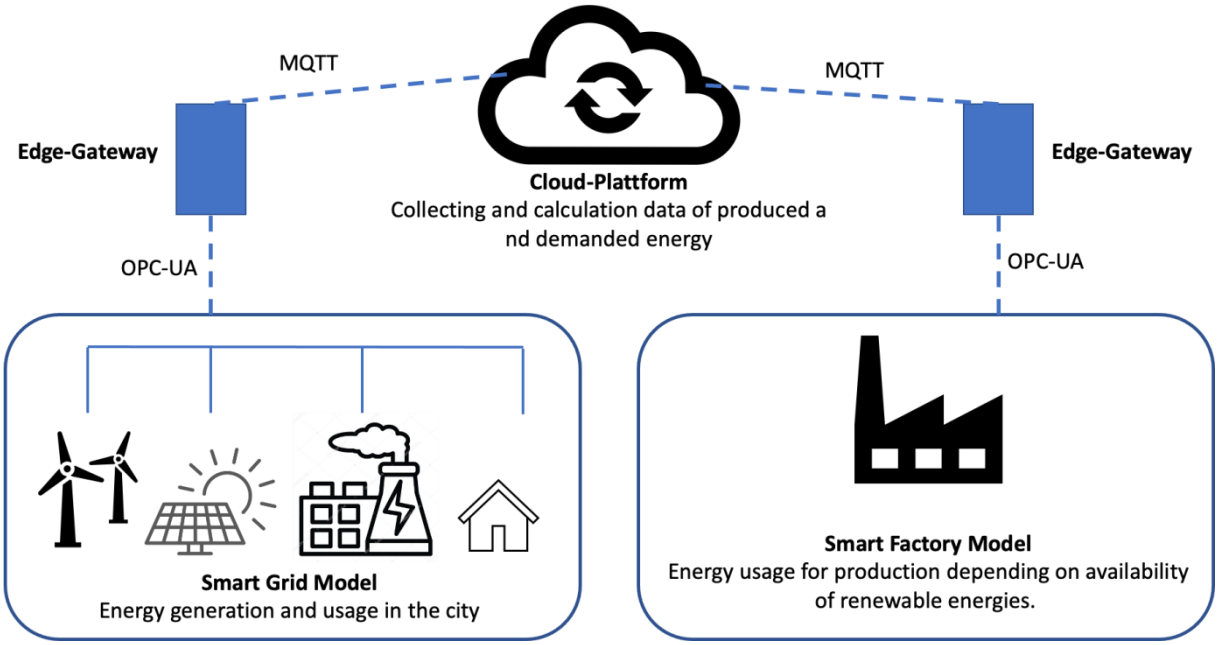

Figure 1. The demand response scenario.

Development of the Smart Grid Model

The SGM is a model of a city that uses electricity from conventional power plants when the electricity from renewable sources is not sufficient to supply the city. The wind turbine is not a real wind turbine in this sense, since it is driven by a motor and thus does not produce energy. It is only meant to serve as a visual object and simulate the energy generated from wind power. The model of the solar plant consists of models, which are supposed to represent solar panels. A brightness sensor is attached to one of these angles. This is connected to both the Arduino and the Raspberry Pi via its I²C interface and supplied with 3.3V voltage. Furthermore, a halogen lamp is mounted on SGM, which can be dimmed by minimizing the voltage supply. This allows to simulate the generation of photovoltaic energy.

On SGM the consumption distribution is displayed by means of LEDs. These LEDs are RGB LEDs, so that they can shine green as well as red. The red LEDs symbolize the coverage of consumers by conventional power generation, and the green LEDs symbolize the coverage by renewable energy sources.

For the representation of the energy production a simulation was developed, which represents a daily expiry, with time-of-day dependent consumption by dwellings and energy production by the renewable sources described above. Thus, at different times of the day there is sometimes a surplus of renewable energy and sometimes the supply is covered exclusively by conventional energy. Depending on the energy distribution within the grid, the LEDs are switched to visualize the status.

The OPC UA server should make it possible to simulate the simulation state and simultaneously switch consumers in the model on and off. For control purposes, the OPC UA Server therefore provides three control variables and also releases the state of the simulation to the outside:

- sim_mode_enabled This variable of type Boolean can be used to select between simulation and manual control modes.
- time This variable of type int can be used to set a time between 0 and 23 o'clock.
- producing This variable of type Boolean can be used to control whether an additional consumer (e.g., an industrial plant) is to be switched on or off in the model.
- excess_power (Surplus) renewable energy available in the grid.
- power_production Total energy provided, both renewable and conventionally.
- renewable_pwer Renewable energy produced.
- sun_power Energy produced by the photovoltaic park. used_power Commuted energy of all consumers. wind_power Energy produced by the wind turbine.

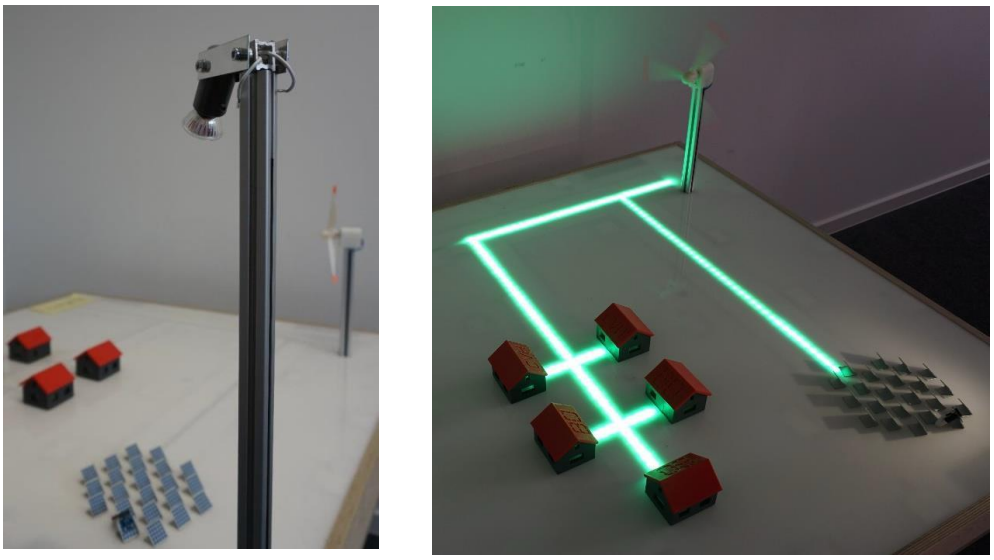

Figure 2. The smart grid model.

Development of the Production Model

The model of the smart factory to be controlled is an electropneumatic system with actuators and sensors from Festo. The core task of the system is the separation of workpieces with metal cores from workpieces without metal cores.

The core of the system is a conveyor belt that can be moved in both directions at two speeds and is equipped with a light barrier at both ends. At point 1, there is a magazine for workpieces, which is equipped with a light barrier and into which a pneumatic cylinder for pushing out is integrated. At station 2 there is a light barrier, an inductive sensor and a pneumatic cylinder that can pull workpieces down from the assembly line onto a ramp. There is also a light barrier in the ramp.

The process sequence for a workpiece is as follows: If there is at least one workpiece in the magazine, it is pushed onto the conveyor belt by the pneumatic cylinder. When the workpiece has been completely pushed out by the cylinder, the cylinder retracts, and the conveyor belt moves at the higher of the two speeds in the direction of station 2. If the light barrier is interrupted at station two, the conveyor belt speed is reduced so that the workpiece is moved slowly along under the inductive sensor. If a metal core is detected in the workpiece, it is pushed into the chute by the pneumatic cylinder and the conveyor belt is then stopped. If the light barrier is released again without a metal core being detected, the workpiece passes through the light barrier at the end of the conveyor, whereupon the conveyor stops.

The start button starts the production of one or more workpieces. If there is not enough renewable energy supplied by the smart grid model, the start button also confirms that you want to manufacture despite the lack of renewable energy. During production, the LED of the start button lights up. By pressing the Stop button, production in automatic mode ends after the current workpiece.

The left lamp Q1 lights up if there is not enough renewable energy. The right lamp Q2 lights up if a start of production has been requested despite insufficient renewable energy and this must be confirmed by a renewed start command.

For the control of the Festo plant a Revolution Pi Core 3 is used, which has a CoDeSys installation as PLC runtime.

The OPC server within the CoDeSys runtime delivers six variables to the edge gateway:

- StartSignalFromCloud has the same effect as pressing the start button on the line. If the variable is set to True while enough renewable energy is available, the production starts, if not enough renewable energy is available, the variable has to be set to False and then again to True to start the production process. (Data type Bool)
- StopSignalFromCloud has the same effect as pressing the stop button on the system. In automatic mode the production is set according to the current workpiece. (Data type Bool)
- NeededPowerInKW denotes the continuous power that the plant consumes in the production process. (Float data type, value 200)
- EnoughRenewableEnergy represents whether the currently available power from renewable energy is greater or less than the power required by the plant. (Data type Bool)
- NumToProduce is the number of parts to be produced in sequence by the plant in automatic mode. For each produced part this variable is reduced by 1. (Data type INT)

- IsProducing indicates whether the system is currently producing and thus consumes energy. (Data type Bool)

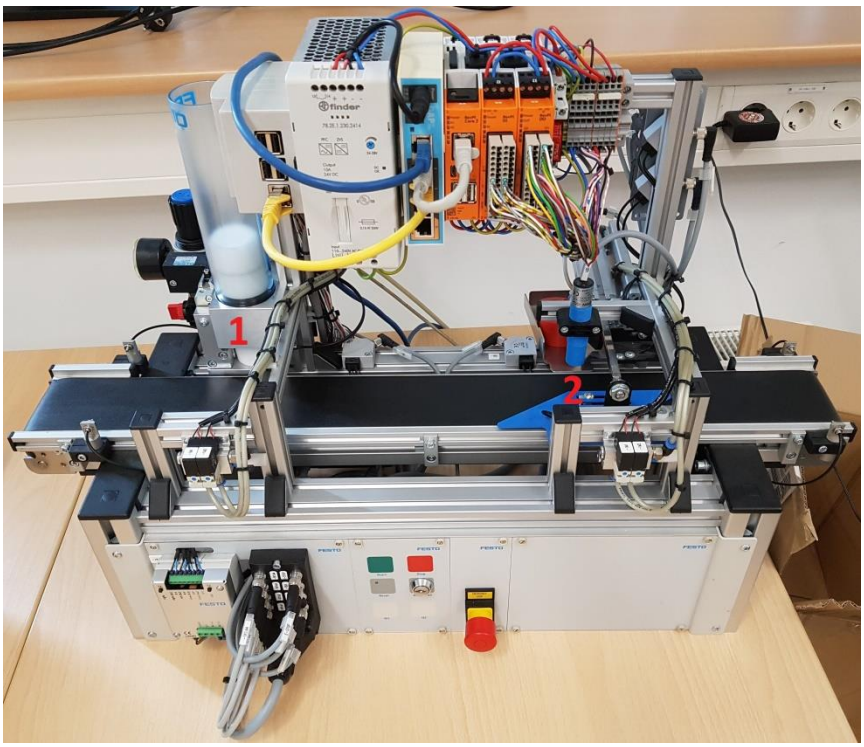

Figure 3. The smart factory model.

Implementation of the Cloud-Solution

The energy data from the smart grid and they will be connected via an OPC UA connection to an edge gateway, which will evaluate the relevant data and make it available on the cloud platform via MQTT. Within the cloud platform, the corresponding calculations for the demand response scenario must be performed. In the specific use case, the required power of the production plant should be compared with the given power of the smart grid plant for this purpose. As long as the smart grid provides enough power from renewable sources for production, the variable "EnoughRenewableEnergy" in the production plant should be set to "TRUE". For this purpose, a graphical view is created, and a number field is inserted in it via the "Widget Gallery". The number field is first connected to the variable "Excess_Power" To execute the calculation on every data change, an "OnDataUpdate" event is created, which triggers a JavaScript.

Now these variables can be assigned to the tags of the gateway by mapping. To do this, a tag list of the created device can be opened in the web interface. Then the tags can be assigned from the tag list to the variables in the mapping using drag-and-drop. Various settings can then be made, e.g. whether the variables are only available for read access or also for write access. Once all tags have been assigned, the mapping can be saved.

The variables loaded into the cloud and calculated there can be visualized under "Dashboards" within the cloud platform. Various layouts can be specified here via the "Gallery", which can then be filled with text and number fields, for example. Either fixed values can be assigned to the individual elements or a link can be created with the tags. A link can be created by dragging and dropping the tags from the "Devices" list into the "Value" field of the respective element. Once all settings are complete, the dashboard can be saved. It can then be found via the "Dashboard" menu item and viewed with live values at any time via the "Eyes" icon.

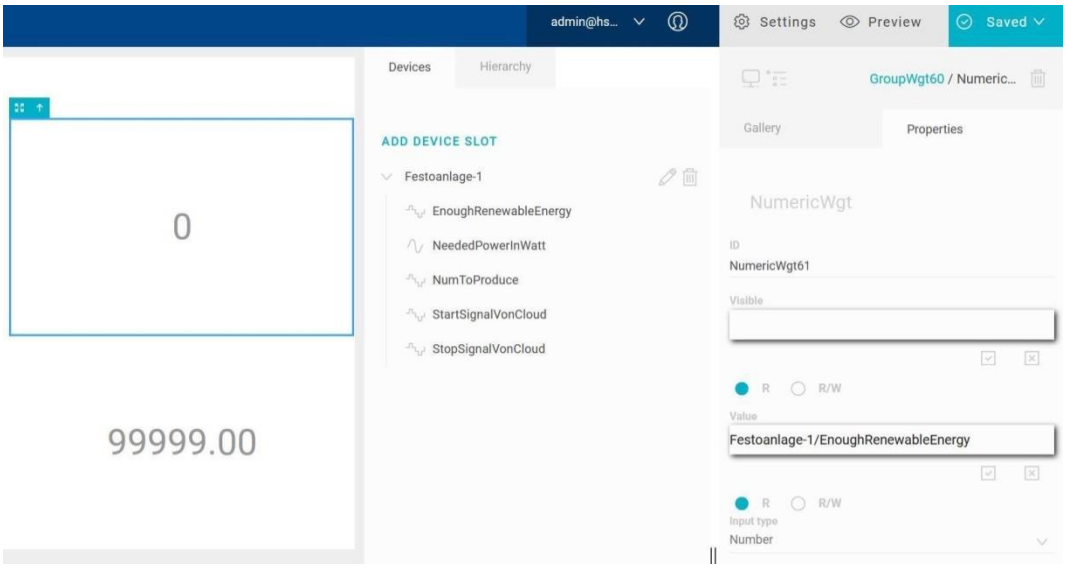

Figure 4. Web interface of the cloud platform.

Conclusion

The developed model shows a simple implementation of a demand response scenario to adapt the energy demand of a production to the availability of renewable energy. Standard technologies like CoDeSys PLC, OPC-UA and MQTT as cloud connection provide simple and manageable solutions to overcome the silo boundaries between energy production and consumption.

References

[1] Klima und Energie. http://www.hightech-strategie.de/de/83.php. Accessed 2018 December 18.

[2] Neugebauer R, Westkämper E, Klocke F, Kuhn A, Schenk M, Michaelis A, Spath D, Weidner E. *Energieeffizienz in der Produktion. Untersuchung zum Handlungs- und Forschungsbedarf*. München: Fraunhofer Gesellschaft; 2008.

[3] Industrie 4.0. http://www.hightech-strategie.de/de/59.php. Accessed 2018 December 6.

[4] Du P, Lu N, Zhong H. *Demand Response in Smart Grids*. 1. Springer International Publishing; 2019. https://doi.org/10.1007/978-3-030-19769-8

2nd German-West African Conference on Sustainable, Renewable Energy Systems SusRES – Kara 2021

Smart Grids

https://doi.org/10.52825/thwildauensp.v1i.18

Published: 15 June 2021

A Model-based Approach to Decarbonize an Island's Energy System

Case Study on the Island of Föhr, Germany

Clara Paetow[1], Mateusz Szymanski[1][https://orcid.org/0000-0002-5991-9906], Johannes Detje[1], Alexander Stolpmann[1][https://orcid.org/0000-0002-3021-2456]

[1] Technical University of Applied Sciences Wildau, Germany

Abstract. To achieve climate goals and contain further global warming, it is inevitable to reduce CO_2 emissions especially in energy consumption. A way to do so is by integrating renewable energy sources (RES) into an energy system's power generation. However, there is no standard procedure to decarbonise a locally restricted system. Therefore, the various local conditions have to be analysed and taken into consideration.

The authors propose a model-based approach to decarbonise the energy system of the island Föhr, Germany. This includes various collected data sets on local conditions such as climate data and heat and power demand. The data is used to represent the island's energy system and design a model-based solution in a simulation software.

The authors identify potentials by comparing costs and revenues by addressing the deployment of different RES technologies. One finding is that heat generation causes 91 % of CO_2 emissions making it the major producer. However, with the designed solution, emissions could be reduced to a third.

Keywords: decarbonisation, renewable energies, island

Introduction

The climate change becoming more and more perceptible, decarbonisation of energy systems is a topic of interdisciplinary interest. This paper approaches the complex problem as a case study by looking at the island Föhr, located in northern Germany in the North Sea.

Characterised by a strongly fluctuating population and therefore varying energy demand throughout the year, the island has lots of potential for efficiently harmonising power generation and consumption.

The island's municipal administration aims for a nearly CO_2-neutral energy cycle. Thus the extension of renewable energy sources and a more distributed generation are required. Föhr's municipal administration reached out to TH Wildau to conduct a holistic study on the topic of decarbonisation, especially focusing on reducing CO_2 emissions caused by electricity and heat sector. Previously, both sectors only have been considered individually. Results of this project are being presented and taken into account in this paper. Decentralizing an energy system accounts for major difficulties regarding system reliability and security due to fluctuations of the availability of renewable energy sources [1]. A solution for the decentralization and distributed generation of energy is the application of smart grids [2]. Hwang et al. [3] proposed a renewable-energy-based smart grid system on Gapa island, South Korea. However, with a maximum demand of 224 kWh and 281 residents, the island is 28-times smaller than Föhr, so results are not entirely transferable. For the utilization of the

renewable energy sources and the implementation of a smart grid system, local conditions have to be taken into account. Within the framework of the case-study, this paper presents a model-based decarbonized system for the island Föhr.

Related Works

For a model-based approach of decarbonizing an energy budget, islands or isolated regions are particular suited due to their clearly defined boundaries. Hence, they can often be found as case studies [4].

However, due to a wide variety in local conditions such as climate, energy demand or local policies, a standardized solution is not feasible. Tarasov [5] presents a methodological approach for decarbonizing isolated energy systems. These are characterized by extreme climate conditions which exclude the installation of wind and solar energy.

In contrast, Pascasio et al. [6] present a hybrid energy system for Philippine off-grid islands. Utilizing wind and solar energy, alongside with diesel generators and battery packs. The authors consider installation sites, costs and profits and show a reduction in emissions of 61.38%.

With the progress or further expansion of renewable energies, decentralized energy generation structures are emerging. However, there are some challenges such as uncertainty of generation output and unbalanced system conditions. A solution to that is implementing smart grids [7].

Case Study

Overview

With a surface area of about 82 km^2 and a longitudinal expansion of 12.5 km, the island Föhr is located in the far north of Germany close to the Danish-German border. It is surrounded by the Wadden Sea, part of the North Sea and UNESCO World Heritage. This results in roughly 200,000 tourists per year that visit the island. Figure 1 shows an aerial image of the island.

Figure 1. Aerial image of Föhr

The large number of tourists contrast strongly to Föhr’s population of 8,248 inhabitants (2018) [7]. Thus, the amount of people residing on the island varies strongly throughout the year. The peak of the population is reached during the summer in July and August with an additional percentage of inhabitants from 100 to 120 %.

Electrical energy is provided by the local distribution system operator, using a submarine cable as a connection to the mainland. In addition, a cable connection to the neighbouring island Amrum exists.

The initial data for that is the island’s resident population plus the number of overnight visitors, both in 2018. The numbers remained constant compared to the previous year’s record result [8]. Due to seasonal fluctuations, the number of tourists varies throughout the year with a peak in the summer months. Since tourists are having a significant impact on the island’s economy, they can be considered as additional inhabitants. These so called population equivalents are calculated from the tourist figures. However, only overnight stays were considered. It is assumed that one overnight stay is equivalent to one resident per day.

From 1.86 million overnight stays are resulting 5,095 population equivalents by tourists per year. These annual population equivalents are only of limited use, since the number of tourists fluctuates over the year. The overnight stays were distributed over the months of the year. As basis for the calculation the overnight stays in the whole of Schleswig-Holstein were used and thus a percentage share was obtained for each month. This was then applied to the total overnight stays on the island Föhr and from this the tourist population equivalents are calculated.

Data Acquisition

Electric Energy Demand

Since the island’s specific power consumption was unclear, numbers had to be calculated using national averages for electricity consumption in Germany in 2018. The main sectors are industry (43.9 %), residential (i.e. private households, 24.9 %), commercial (29 %) and transportation (2.2 %).

For private households, there is a per capita consumption of 1,550 kWh [9] which makes for Föhr’s 8,248 inhabitants a total residential/household demand of 12.78 GWh. For calculating the total demand, the national average from the gross electricity consumption per person was used, which is 7,274 kWh for all sectors. In figure 2, an overview of the calculated average electricity demand per month in kWh, with a maximum of 3,680 MWh in July, is given.

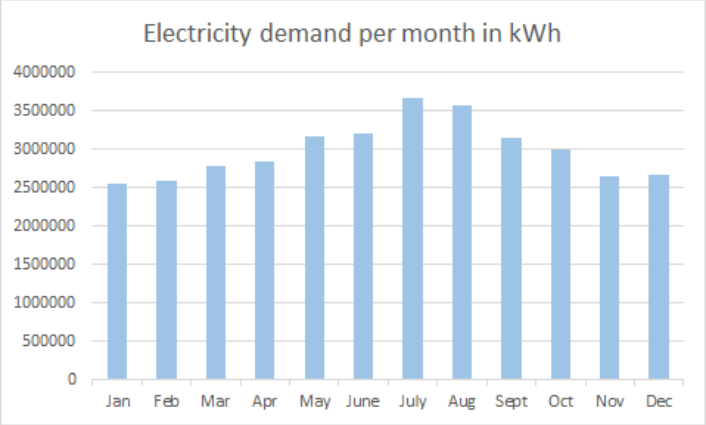

Figure 2. Total electricity demand per month

Heat demand

The term heat demand refers to the need for space heating and hot water. In 2018, the heat demand of an average household in Germany for hot water was 2608.38 kWh. Multiplied by the 3,916 households on Föhr this results in a demand of 10.21 GWh for hot water per year for the household sector. More differentiated statistics are available for the energy demand for space heating [10]. The number of different households on Föhr is derived from the absolute numbers of households on Föhr-Amrum, and was extrapolated down to the island of Föhr under the assumption that the distribution is the same. With the help of these figures, a space heating demand of 52.06 GWh per year for the household sector on Föhr could be determined.

The heat demand for the commercial sector could only be estimated by using the statistics from the Federal Environment Agency from the year 2017 [11]. Thereby, the total consumption figures of the sectors were put into relation as a percentage. This results in the commercial sector having about 41.47% of the space heating demand and 18.01% of the domestic hot water demand. Thus, the annual demand for the tertiary sector was calculated to be 21.59 GWh for space heating and 1.84 GWh for hot water.

To include tourists into the calculation, initially the heating degree days were analysed from the nearest weather station on the island of Sylt. The heating limit was set at 15 degrees Celsius, meaning when the outside temperature is lower, the day is considered a heating day.

In the heat sum, the respective difference between the outdoor temperature and the heating limit were added for each day [12]. In relation to the total heat sum, a percentage of the heating demand per month can be determined in relation to the year. These percentages are multiplied by the space heating demand of the households to obtain the monthly space heating demand. The number of inhabitants on Föhr was used to downscale this demand to one person. This was a step to determine the demand for tourists with the help of the population equivalents for the tourist’s sector.

To calculate the tourist’s energy demand for hot water, the demand for households was divided by the number of inhabitants, resulting in a demand per person per year. This value was multiplied by the monthly population equivalents of the tourists to establish their energy demand for hot water.

Figure 3 shows the calculated heat demand per month. There is a basic demand for hot water throughout the year which is increasing in summer due to the tourists. Additionally to the basic demand, the demand for space heating is added up, mostly in winter. The island’s total heat demand was calculated to be 109.67 GWh per year with the tourism sector making about a quarter of it.

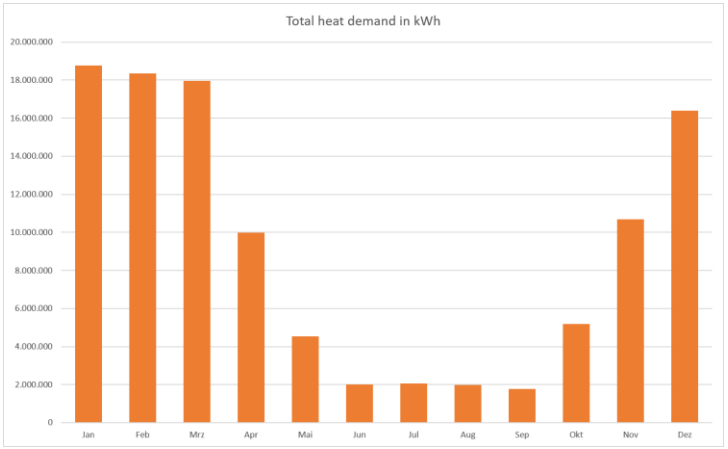

Figure 3. Total heat demand per month in kWh

Analysis of RES potential

On site available (renewable) energy sources are wind and biogas, and potentially solar and geothermal energy as a source for heat production. In a first analysis, potentials were examined and presented.

Concerning biogas, the town council of Wyk on Föhr did not favour the extension of existing biogas plants as corn cultivation would be needed. This would lead to high water consumption for the cultivation and negative impacts on landscape which was considered to be not beneficial for attracting tourists [13]. Hence, enlarging a potential biogas plant with corn silage as a substrate is not possible. In addition, the utilization of biowaste to biogas was assessed as unsuitable and therefore not considered any further.

Regarding Föhr’s local climate conditions, the installation of photovoltaic plants and solar collectors holds potential. One restricting point is that modules can only be placed in the free field due to the inappropriate building structures of the majority of houses on the island.

For geothermal energy, a potential for geothermal probes was discovered. Two design options were available, either with a large heat pump for district heating or decentralized heat pumps for local heating. Due to the undesired addition of further wind power stations, a simple expansion with more wind turbines is not possible. Nevertheless, a simulation of the existing power plants was made to estimate a possible optimization through the addition of power storage modules.

Data preparation and processing

For the simulation, usable time series from the collected data were created and additional data for further time series used. First of all, the actual state of the islands energy systems was modelled using a software called TopEnergy by GFaI. From the previously determined electricity demand, time series were created using standard load profiles [14]. Two different profiles were used for the calculation of the demand for households and tourists and for the commercial sector. All load profiles have a resolution of 15 minutes. Figure 4 shows the time series for the total electricity demand per sector.

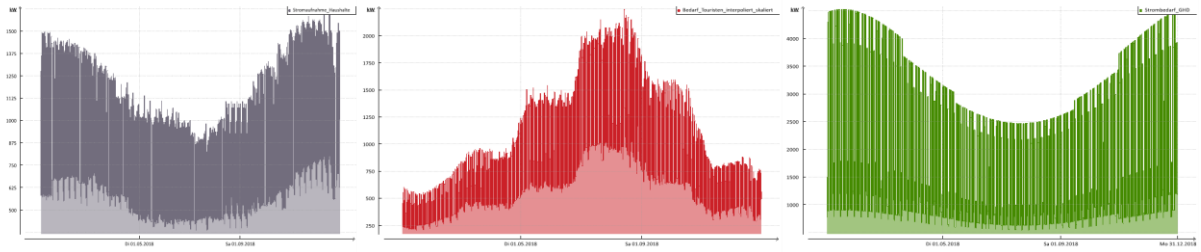

Figure 4. Time series for power demand per sector in TopEnergy software. Left: Private sector; middle: tourist’s sector; right: commercial sector

The input of weather data was indispensable for calculating the heat demand, but also the potential of renewable energies. The used parameters are the ambient temperature, global solar radiation and wind speed. Figure 5 shows the resulting time series for heat demand per sector.

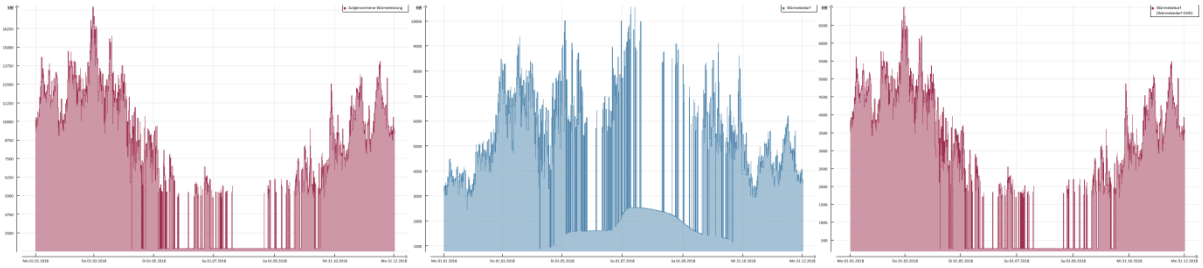

Figure 5. Time series for power demand per sector in TopEnergy software. Left: Private sector; middle: tourist’s sector; right: commercial sector

Simulation

Actual state

A model of the actual state represents the island’s current state of the energy supply in the form of electricity and heat in a simplified way. In the power grid, a distinction is made between the three sectors households, tourists and commercial. The demand is described by the already mentioned time series. The power grid is supplied by an electricity supplier that

bills the electricity via a local electricity tariff. Average local figures for CO_2 emissions in electricity generation were used and included in the simulation.

The simulation of the heat supply is based on the assumption of a district heating network that supplies all consumers, which is not exactly the case in reality. The consumers and their demands are connected to this heat network. Here, too, there is a breakdown into the household, tourist and commercial sectors based on the prepared time series. Figure 6 shows the model created in TopEnergy.

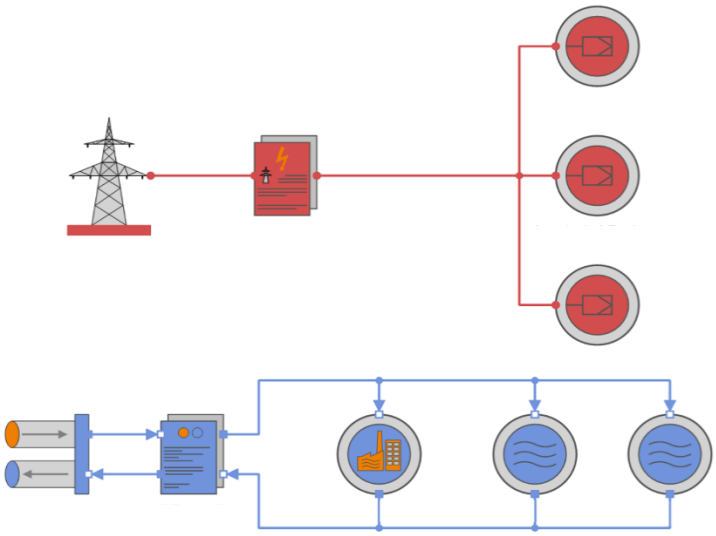

Figure 6. Model of the islands energy system’s actual state

Results

To obtain results for the energy system’s target state, the actual state was modified and supplemented. Figure 7 shows the much more complex model for the hypothetical target state.

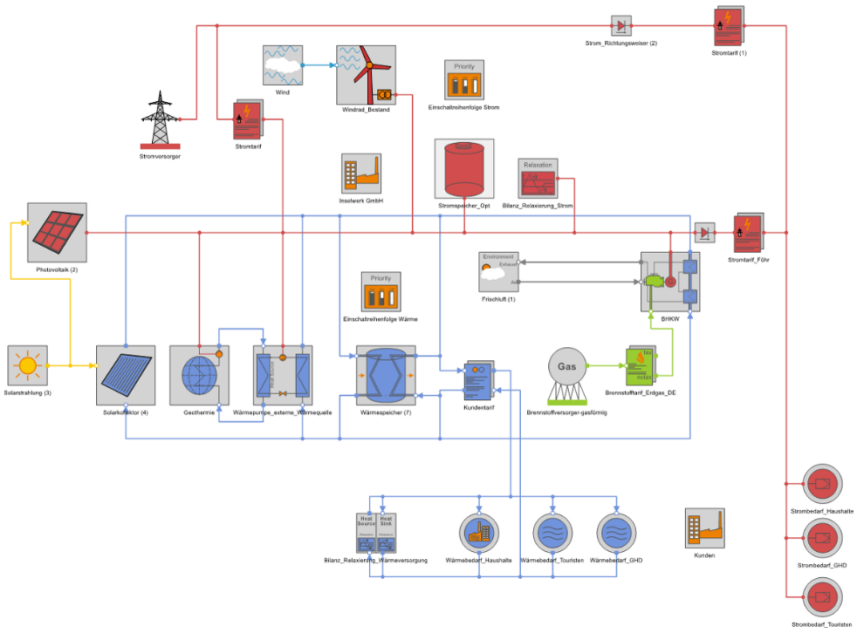

Figure 7. Model of the islands energy system’s target state involving RES technologies

In this combined model, components of wind power, solar energy, both solar collectors and photovoltaics and geothermal energy were implemented. In addition a cogeneration unit was operated, which emerged from the evaluation of the neighbourhood as well as island solution. For the control of the power flow, power direction indicators were used and switch-

on sequences for the cogeneration unit. A heat storage was used to mainly store surpluses from the solar collectors, thus reducing the load on the geothermal probes and reducing their size. The electricity storage was mostly used to store electricity from wind power and photovoltaics. The model contained eight time series with 35,040 time points each. To reduce optimization errors, relaxation modules were built in. Their function is to absorb surpluses and close shortages and show exact numbers of when and how much electricity or heat was spare or missing.

The simulation showed that the total electricity demand remained about constant throughout the year. In contrast, the demand for heat varies strongly throughout the year. Only the base load is constant and increases in summer due to the higher number of tourists. Especially in spring there is a high heat demand. This decreases in summer, when cold days, which cause a significant heat demand, are rare. In fall, the heat demand then increases again.

The CO_2 emissions of the actual state amount to a total of 31.4 kt/a. Of these, 9% are caused by electricity supply and 91% by heat. With its 28.5 kt/a of CO_2 emissions, the heat supply represents a very large factor in the total emissions. Accordingly, the highest savings potential was expected there.

As a result after comparing costs and revenues, the use of solar collectors for generating heat could not be recommended. Other mentioned technologies could be used to employ more electricity and heat produced by renewable energies. Figure 8 shows the comparison of costs and revenues.

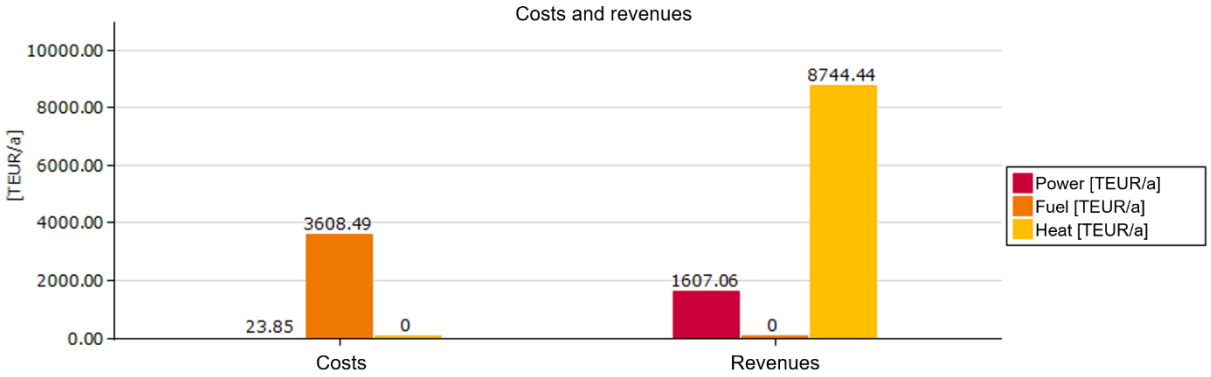

Figure 8. Comparison of costs and revenues per technology

In terms of reducing CO_2 emissions, applying a combination of the presented technologies would lead to a reduction of about a third compared to the actual state. Figure 9 shows the comparison regarding CO_2 emissions of the energy system’s actual state and the target state (in two variants).

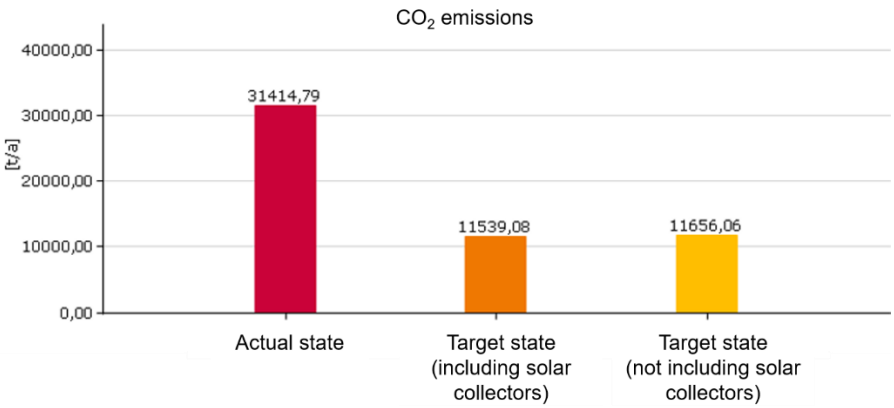

Figure 9. Comparison of CO_2 emissions

Conclusion

In this paper, a model-based approach for decarbonizing an island’s energy system is presented. First, the process of data acquisition for calculating a custom electricity and heat demand is presented. Further, the authors analyse the potential of on-site available renewable energy resources. Local climate data and calculated demands are processed into time series. A software model describing the island’s as-is state is explained and employed in the simulation to determine a baseline. Then the baseline model is expanded to integrate wind, solar and geothermal energy and a combined heat and power plant as well as storage technologies. As a result, solar collectors are not profitable within the local conditions. Nevertheless, the authors can show a significant decrease in CO_2 emissions by 63.27 %. A discussion of the applicability of a Smart Grid for the described energy system will be addressed by the authors in future work.

References

[1] Huang BB, Xie GH, Kong WZ, Li QH. Study on smart grid and key technology system to promote the development of distributed generation. IEEE PES Innovative Smart Grid Technologies. 2012 IEEE Innovative Smart Grid Technologies - Asia (ISGT Asia). 2012 05. https://doi.org/10.1109/isgt-asia.2012.6303265

[2] Brenna M, Foiadelli F, Petroni P, Sapienza G, Zaninelli D. Distributed generation regulation for intentional islanding in Smart Grids. 2012 IEEE PES Innovative Smart Grid Technologies (ISGT). 2012 IEEE PES Innovative Smart Grid Technologies (ISGT). 2012 01. https://doi.org/10.1109/isgt.2012.6175713

[3] Hwang W, Ingyu Choi, Ra D, Lee J, Kim SK, Zong Woo Geem. Case study of renewable-only smart grid system for a Korean island. ISGT 2014. 2014 IEEE Power & Energy Society Innovative Smart Grid Technologies Conference (ISGT). 2014 02. https://doi.org/10.1109/isgt.2014.6816394

[4] Calise F, Duic N, Pfeifer A, Vicidomini M, Orlando A. Moving the system boundaries in decarbonization of large islands. Energy Conversion and Management. 2021 04;234:113956. https://doi.org/10.1016/j.enconman.2021.113956

[5] Tarasov A. A Methodological Approach to the Decarbonization of an Isolated Energy System. 2020 International Multi-Conference on Industrial Engineering and Modern Technologies (FarEastCon). 2020 International Multi-Conference on Industrial Engineering and Modern Technologies (FarEastCon). 2020 Oct. https://doi.org/10.1109/fareastcon50210.2020.9271572

[6] D. Olivares, A. Mehrizi-Sani und A. Etemadi, „Trends in microgrid control,“ in *IEEE-PES Task Force on Microgrid Control*, 2014.

[7] Statistisches Amt für Hamburg und Schleswig-Holstein, „Bevölkerung der Gemeinden in Schleswig-Holstein 4. Quartal 2018,“ Statistisches Amt für Hamburg und Schleswig-Holstein, Hamburg, 2019.

[8] Föhr Tourismus GmbH, „Stabile Entwicklung der Übernachtungszahlen auf Föhr und Amrum,“ Föhr Tourismus GmbH, 2019.

[9] Bundesminiserium für Wirtschaft und Energie, „Kennziffern des Energieverbrauchs,“

BMWi, 2020.

[10] Statistisches Bundesamt, „Energieverbrauch der privaten Haushalte für Wohnen,“ 1 11 2019. [Online]. [Zugriff am 28 05 2020].

[11] Umweltbundesamt, „Energieverbrauch für fossile und erneuerbare Wärme,“ Umweltbundesamt, 2020.

[12] Institut Wohnen und Umelt, „Energiebilanzen für Gebäude,“ IWU, 2020.

[13] amtfa, „Resolution der Stadtvertretung der Stadt Wyk auf Föhr zu Biogasanlagen,“ 2011. [Online]. Available: https://info.amtfa.de/sessionnet/bi/vo0050.php?__kvonr=1435. [Zugriff am 9 9 2020].

[14] Stadtwerke Groß-Gerau Versorgungs GmbH, „Netzbilanzierung,“ 2020. [Online]. Available: https://www.ggv-energie.de/cms/netz/allgemeine-daten/netzbilanzierung-download-aller-profile.php. [Zugriff am 29 12 2020].

2nd German-West African Conference on Sustainable, Renewable Energy Systems SusRES – Kara 2021

Predictive Analytics

https://doi.org/10.52825/thwildauensp.v1i.32

Published: 15 June 2021

Positive-Unlabelled Learning-Based Novelty Detection for Industrial Chillers

A Data-Driven Approach to Avoid Energy Wastage

Ron van de Sand[1] [https://orcid.org/0000-0002-8975-4030],
Sandra Corasaniti[2] [https://orcid.org/0000-0002-0434-501X],
and Jörg Reiff-Stephan[1] [https://orcid.org/0000-0003-4176-6371]

[1] Technical University of Applied Sciences Wildau, Germany

[2] University of Rome "Tor Vergata", Italy

Abstract. Chiller systems are used in many different applications in both the industrial and the commercial sector. They are considered major energy consumers and thus contribute a non-negligible factor to environmental pollution as well as to the overall operating cost. In addition, chillers, especially in industrial applications, are often associated with high reliability requirements, as unplanned system downtimes are usually costly. As many studies over the past decades have shown, the presence of faults can lead to significant performance degradation and thus higher energy consumption of these systems. Thus, data-driven fault detection plays an ever-increasing role in terms of energy efficient control strategies. However, labelled data to train associated algorithms are often only available to a limited extent, which consequently inhibits the broad application of such technologies. Therefore, this paper presents an approach that exploits only a small amount of labelled and large amounts of unlabelled data in the training phase in order to detect fault related anomalies. For this, the model utilizes the residual space of the data transformed through principal component analyses in conjunction with a biased support vector machine, which can be ascribed to the concept of semi-supervised learning, or more specifically, positive-unlabelled learning.

Keywords: Chiller CBM, Machine Learning, Energy Efficiency

Introduction

Chillers are applied across many different fields of both industrial and commercial applications. As being large energy consumers with accounting up to 40% of a buildings total energy demand [1], these systems surely open up great potential for optimization. One promising approach to avoid energy losses while operating these systems is known to be condition based maintenance (CBM) [2] which constitutes several steps to asses a systems degradation state, of which fault detection (FD) [3] plays a key-role as it allows to detect novelties caused by one or multiple faults being present. This is particularly important as chillers can loose up to 30% of their coefficient of performance without any obvious sign of degradation being present to the operator [4]. Besides avoiding energy wastage, FD also contributes to saving operation as well as service costs. This can help to predict system malfunctions and therefore prevents unplanned downtimes, which is especially important for industrial applications as a chiller breakdown may cause an entire process line to stop [5].

This topic has attracted the attention of researchers for many decades and a great variety of models have been proposed to date. Generally, these approaches can be divided into model-based and data-driven [6]–[8], whereas the former utilizes a reference model to detect abnormal behaviour. The latter, however, relies on self-adapting algorithms that only require historical machine data [3] making it possible to develop FD models without any prior assumptions about the systems structure or the expected fault characteristics. Another limitation of model-based approaches is that finding a mathematical formulation to model a dynamical process can be difficult as well as time consuming due to changing operation conditions [9], and may sometimes even be infeasible when the system complexity is too high. Data-driven FD models can overcome these issues [3] and are, thus, considered to be more cost effective [10]. On the other hand, most existing data-driven models require labelled data of the dedicated system containing both positive (fault-free) and negative (fault) samples, which are often unavailable. The reason for this is twofold: first, as faults are rare events [11], certain faults may not have occurred in the past and therefore associated data cannot be obtained, and second, labelling is conducted by humans and consequently constitutes a high cost and time factor. However, in most application scenarios one comes across a situation where a few positive labelled samples and a lot of unlabelled data containing positive and negative patterns might be available. In this case, the unlabelled data can be exploited in the training phase in order to increase the model accuracy, which is commonly referred to as positive-unlabelled (PU) learning. Therefore, the work at hand proposes a PU learning based fault detection model which utilizes principal component analysis (PCA) in conjunction with the biased support vector machine (BSVM) [12]. Furthermore, we evaluate the model performance on two datasets stemming from the experimental investigation of different chiller types and demonstrate how the proposed model can be more effective compared to classical novelty detection approaches.

The paper is structured as follows: After this introduction, the related work in this field of research is briefly described. Then, the model principles and the description of the datasets used to train and validate the model are presented. In the following section, the model evaluation is then performed and discussed. Finally, the paper is summarized and an outlook is given.

Related Works

Data-driven novelty detection has been the subject of research for many years and a great variety of supervised machine learning were presented. For example, Han et al. [13] proposed to first reduce the dataset dimensionality using PCA and then train a support vector machine (SVM) classifier in a multi-class fashion to perform fault detection and fault diagnosis in a single task. This idea was later adopted by Beghi et al. [14] and Li et al. [15], who trained their model in the PCA residual space rather than the principal component space and showed that this approach could significantly improve the fault detection accuracy. Besides, both work considered the problem as a single-class learning task [16], where in [14] the one-class support vector machine (OCSVM) [17] and in [15] the support vector data description (SVDD) [18] is applied. The difference between the two is that the OCSVM classifier tries to solve for a hyperplane that best separates a positive labelled pattern from the rest of the space, whereas the SVDD classifier aims to find a hypersphere enclosing most of the data. It is worth noting that both algorithms yield equal results when used in conjunction with invariant kernels, such as the radial basis function (RBF) kernel [16]. Feature extraction has also been one of the major concerns of other papers such as, for example, in [19] and [20], where the authors applied genetic algorithms in different variations in order to select characteristic features (CF). In both cases, the SVM has been adapted for the final classification task. Other approaches considered the application of linear discriminant analysis [21], Bayesian networks [22] or statistical models [11]. Although many promising approaches were proposed, only few

contributions exist in this field of research considering the case when only a minor number of positive labelled and high number of unlabelled samples are available. Compared to labelled fault samples, labelled fault-free data is easier to obtain as, for instance, after commissioning the chiller or after performing maintainable actions. One example is given in [20], where the authors combined a Kalman filter with a recursive SVM to exploit unlabelled samples. Similarly, the model in [11] is developed in a semi-supervised fashion. Another approach is given by Fan et al. [9], who applied a transfer learning model to incoporate prior-knowledge from another chiller type. Even though some work in this field has already been conducted, a full understanding of PU learning for FD tasks as well as the effect of the number of available positive samples onto the model performance is still lacking. Therefore, this paper proposes a novel approach, namely the PCA-R-BSVM algorithm, for PU learning based novelty detection for industrial chillers and validates its performance based on two datasets. Furthermore, we compare our approach with the existing PCA-R-SVDD [15], or more specifically with the PCA-R-OCSVM [14] model, under the assumption that only a limited number of positive labelled samples is available.

Model

This section describes the model principles and describes PCA as well as the BSVM algorithm in more detail. Furthermore, a classification metric is introduced that can be employed for evaluating the classification performance based on positive and unlabelled data. This is especially crucial for optimizing the model’s parameter as most metrics require the presence of positive and negative labelled instances in the validation phase.

Principal Component Analysis

PCA is an unsupervised technique that has been widely applied for many dimensionality reduction tasks. In general, it is a linear transformation algorithm which aims to find a new data representation of uncorrelated features, namely the principal components (PC) [14], such that most of the data variance is represented by the first transformed features. Let $\mathcal{X} \in \mathbb{R}^{n \times k}$ be data sampled from the target chiller, with n being the number of observations and k the number of dimensions. The entire dataset can then be expressed as $\mathcal{D} = \{(x_1, y_1), \ldots, (x_n, y_n)\}$ with $y_i \in \{1, -1\}$ for positive and unlabelled instances respectively. After processing the data $\mathcal{X}$, one receives a transformed data representation that can be decomposed into the modelled PC space $\widehat{\mathcal{X}} \in \mathbb{R}^{n \times (k - k_R)}$ and the un-modelled residual subspace $\widetilde{\mathcal{X}} \in \mathbb{R}^{n \times k_R}$ to whose features we will refer to as the residual components (RC) throughout this paper (k_R is the number of RC). It is worth noting that while the PC space contains most of the data variance, the RC subspace contains noise as well as abnormal information [23]. As has been shown in previous studies [11], [14], [15], training a FD model in the RC space rather than the PC space can significantly improve its classification accuracy as the former is more sensitive to novelties.

Biased Support Vector Machine

The BSVM algorithm has been proposed by Liu et al. [12] and its working principle is similar to the idea of training the original SVM with imbalanced data, i.e. when instances from one class appear more frequently than from the other class. However, its motivation is slightly different as it assigns high weights to positive and low weights to unlabelled samples in order to bias the data to the favour of the known positive pattern. On the other hand, low weights are assigned to unlabelled patterns as these may also contain positive instances whose labels remain unknown during the training phase. As a consequence, this approach can be assigned to the field of semi-supervised machine learning. Following this idea, the primal form of the optimization problem can be formulated as

$$\begin{aligned} \min_{w,b,\xi} \quad & \frac{1}{2}\|w\|^2 + C^+ \sum_{i=1}^{n_p} \xi_i + C^- \sum_{i=n_p+1}^{n} \xi_i \\ \text{subject to} \quad & y_i\big(w^T \widetilde{x}_i + b\big) \geq 1 - \xi_i, \;\; \xi_i \geq 0 \end{aligned} \tag{1}$$

where w is a vector orthogonal to the hyperplane, C^+ and C^- the regularisation parameters assigned to positive and unlabelled samples accordingly, ξ_i a slack variable used to solve for a soft-margin decision boundary [16], and b the bias term. Furthermore, we denote $\widetilde{x}_i$ as any observation from the dataset using only its residual information after PCA transformation and n_p the number of positive labelled samples in the dataset. Substituting (1) into its Lagrangian dual form, one may use kernels in order to solve for a non-linear decision boundary in the input space. The decision function for an unknown observation $\widetilde{x}$ is defined as

$$h(\widetilde{x}) = \sum_{i=1}^{n} \alpha_i y_i k\left(\widetilde{x}, \widetilde{x}_i\right) + b \tag{2}$$

where α_i are the Lagrangian multiplies and $k(\cdot,\cdot)$ the kernel function. Similar to previous studies [14], [19], [20], [24], [25], we apply the RBF kernel function, which is given as

$$k(\widetilde{x}_i, \widetilde{x}_j) = \langle \varphi(\widetilde{x}_i), \varphi(\widetilde{x}_j) \rangle = exp(-\gamma \left\|\widetilde{x}_i - \widetilde{x}_j\right\|^2) \tag{3}$$

where $\varphi(\cdot)$ is a non-linear mapping function and γ the kernel width parameter that must be tuned.

Classification Metric

One major aspect of PU learning based classification approaches is how to evaluate the classification performance as most metrics require positive as well as negative samples to be available in the dataset. It goes without saying that this is particularly crucial for any parameter optimisation process, such as grid-search, because for any subset of chosen parameters, the algorithm’s performance must be evaluated on a given test dataset. Throughout this paper we apply a metric proposed by Lee and Liu [26] which was also applied in the original BSVM paper [12]. Similar to the well-known F-Score, the chosen accuracy metric is formulated as $r^2/Pr[h(\widetilde{X}) = 1]$, where r is the recall and $Pr[h(\widetilde{X}) = 1]$ is the probability that a pattern is classified as positive. As stated in [12], this metric behaves similar to the F-Score metric as it is low when either recall or precision is low and high when both values are high.

Overview

The model development can generally be distinguished in the preprocessing phase, PCA based feature extraction and parameter optimisation. In general, preprocessing combines three steps, namely: (a) steady-state detection, which is conducted to exclude transient system states from the dataset; (b) data-filtering to increase the signal-to-noise ratio; and (c) data scaling to exclude the negative influence of the different units on the classification result. It is worth noting that we applied the steady-state detector proposed by Beghi et al. [11] in this paper. In the following step, PCA is conducted on the available labelled fault-free samples, which represents the basis for mapping all further data samples into the PC and RC space. The reason for this is that with the PCA model trained on the fault-free data, the RC become more sensitive to faults as these features are subject to changes when novelties are present. As shown in Figure 1, grid-search is introduced for parameter optimisation. In particular, the model depends on the parameters γ, C^+ and C^-, which are determined through this searching strategy. In addition, the number of residual components k_R is adjusted in a similar way. Although solely positive labelled and unlabelled instances are utilized in the training

phase, a fully labelled dataset containing actual positive as well as negative samples is used for validation purposes.

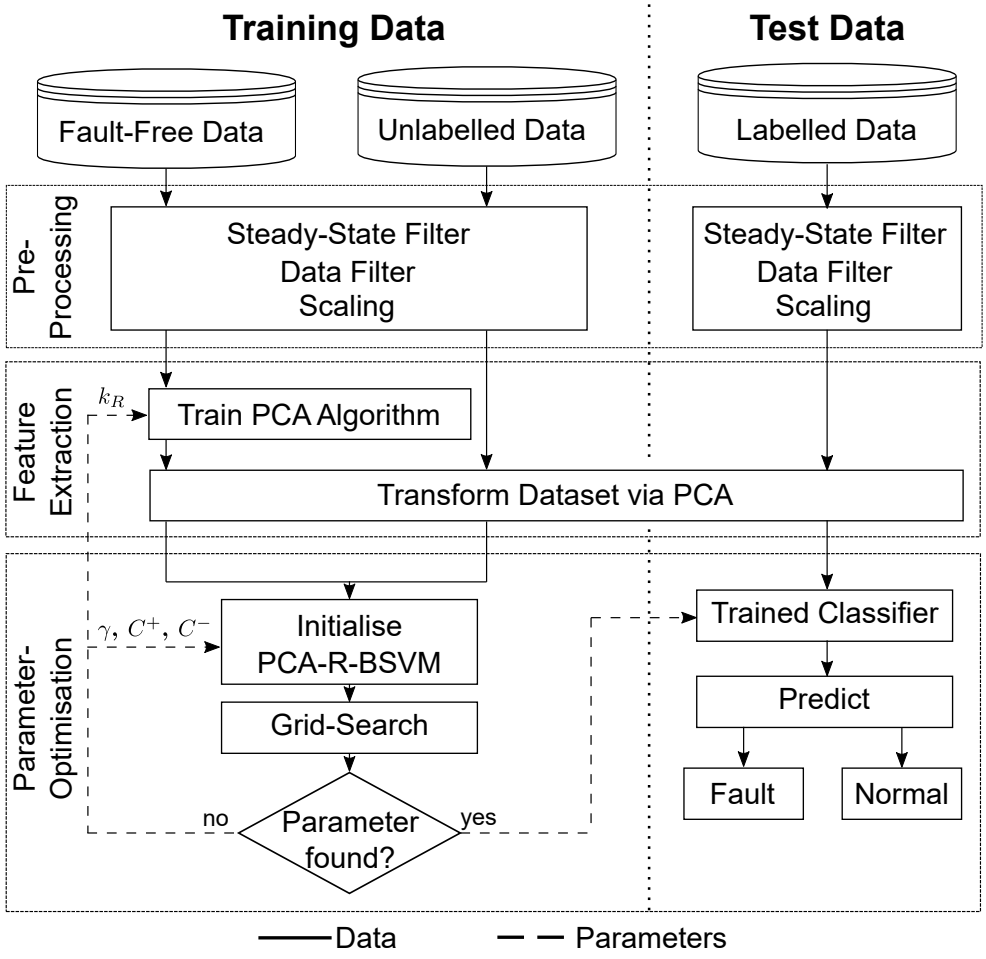

Figure 1. Training and testing procedure

Datasets

In this study, two datasets of two different chiller types is used for training and validating the model. The first datasets was collected during the experimental investigation of a 316kW water-cooled centrifugal chiller. In project ASHRAE RP-1043, carried out by Comstock et al. [27], seven typical chiller faults at four levels of severity were experimentally investigated. The other dataset has its roots in one of our previous works where various faults were investigated using a 100kW ammonia based screw compressor chiller [28], as shown in Figure 2. The data acquisition procedure was similar to that of the ASHRAE RP-1043 project, in which each fault was experimentally investigated at four levels of severity, starting from the lowest level and increasing to the highest. In both projects a test-sequence was defined consisting of several operating states, with each state meeting a steady-state criterion before moving to the next one. As listed in Table 1, 23 features were selected that are shared between both dataset. In the following, these datasets are utilized to train and validate the proposed model. Moreover, it is demonstrated how the model performs with only a minor number of positive samples being available in the training phase.

Table 1. Chosen features

Symbol	Description
f_1	Compressor pressure lift
f_2	Coefficient of performance
f_3	Isentropic compressor efficiency
f_4	Polytropic compressor efficiency
f_5	Instantaneous compressor power
f_6	Instantaneous compressor current
f_7	Evaporator cooling rate
f_8	Condenser heat rejection rate
f_9	Energy balance
f_{10}	Evaporator water inlet temperature
f_{11}	Evaporator water outlet temperature
f_{12}	Condenser water inlet temperature
f_{13}	Condenser water outlet temperature
f_{14}	Refrigerant temperature in Evaporator
f_{15}	Refrigerant discharge temperature
f_{16}	Refrigerant suction temperature
f_{17}	Refrigerant discharge superheat temperature
f_{18}	Refrigerant suction superheat temperature
f_{19}	Evaporator approach temperature
f_{20}	Evaporator water temperature difference
f_{21}	Condenser water temperature difference
f_{22}	Refrigerant pressure in evaporator
f_{23}	Refrigerant pressure in condenser

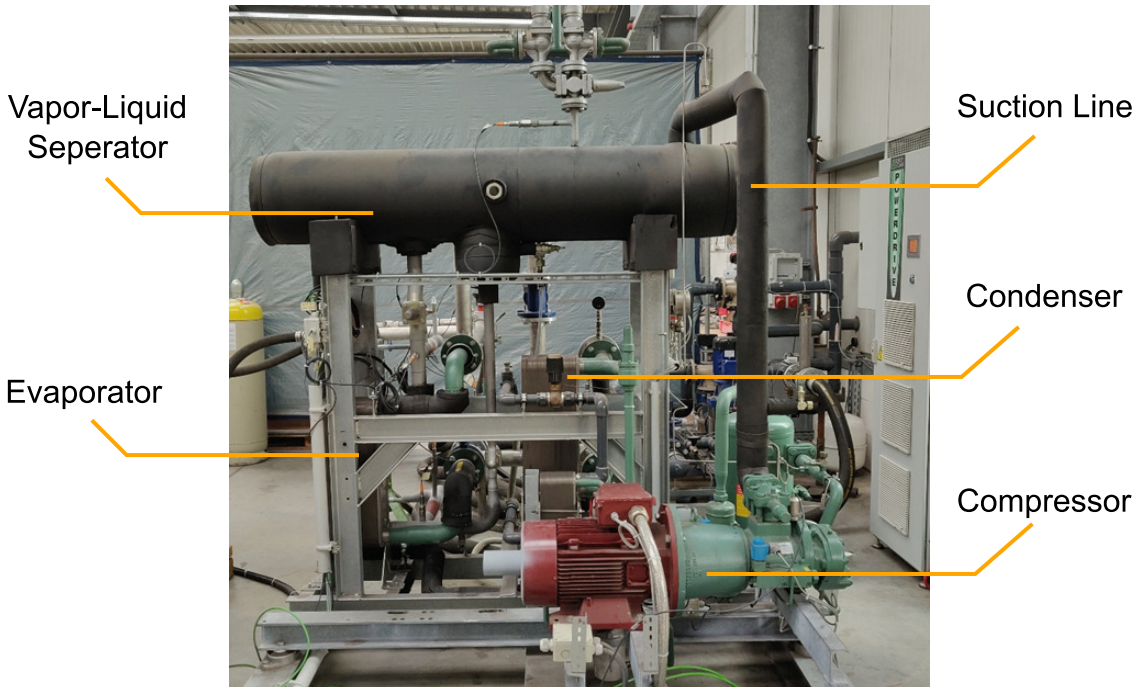

Figure 2. Test facility

Results

The model is characterized by two essential aspects; first, it is based on the RC space after processing the data using PCA, and second, it is trained in a semi-supervised fashion as unlabelled data is exploited in the training phase. As can be seen in Figure 3, the fault patterns become more distinct in the RC space. This is because most of the data variance is represented by the first principal components and is induced due to changing operating conditions rather than novelties. Therefore, by removing the PC from the dataset and exploiting the RC space instead, one may yield higher fault detection accuracy.

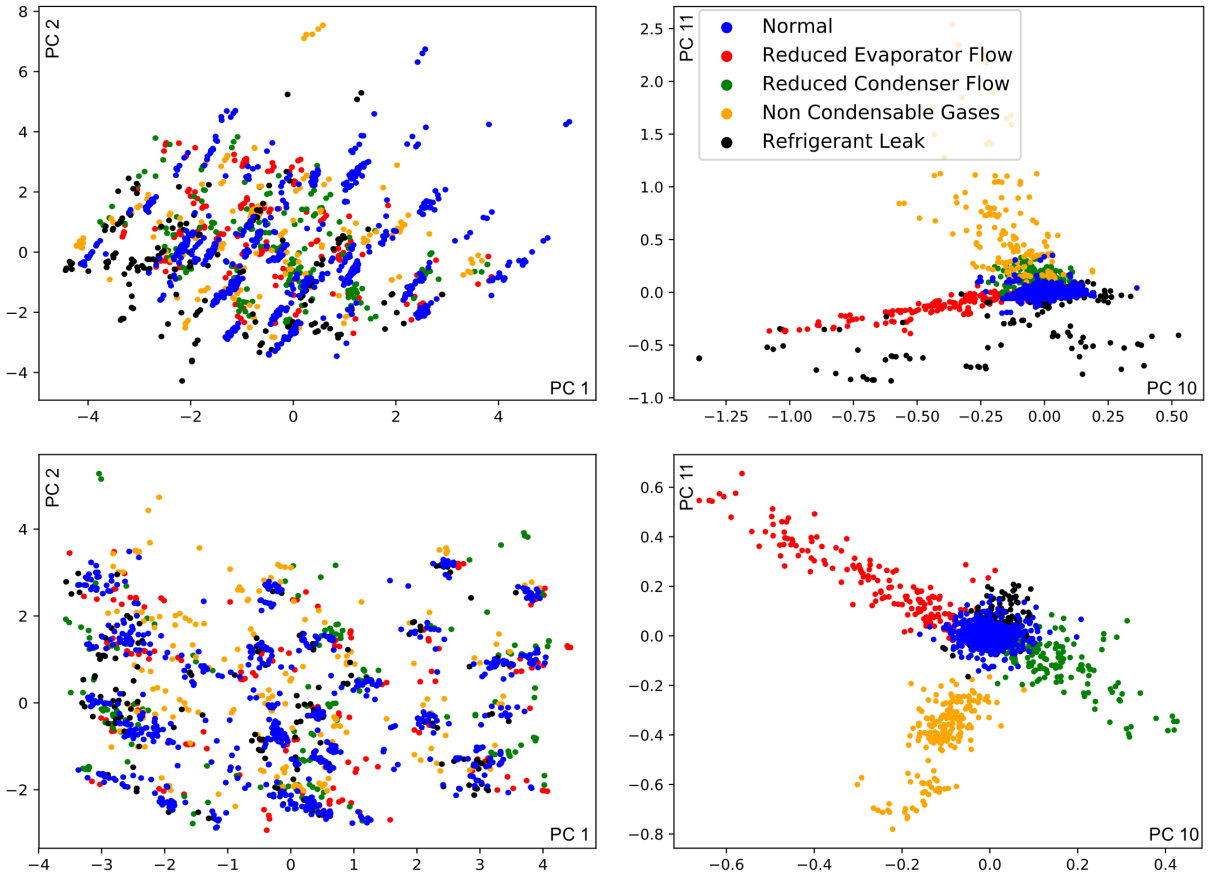

Figure 3. Scatter plot of the principal component and residual space after PCA transformation: upper left: the two first PC (screw compressor), upper right: residual subspace (screw compressor), lower left: the two first PC (centrifugal compressor), lower right: residual subspace (centrifugal compressor)

One crucial aspect of the proposed model is its performance in dependence on the available number of positive labelled instances in the training phase. To show how the model performs on real-world data, we select 1000 observations from the normal and 250 the fault dataset for each chiller type, of which 2/3 is used for training and parameter optimisation and 1/3 for testing. It should be noted that all faults are treated as one class as they represent novelties in this study. We then define a fraction of positive labelled samples θ and mark them as positive, whereas the rest, i.e. positive and negative patterns, are defined as unlabelled (-1). As shown in Figure 1, we repeat the model training process described previously for an increasing θ and compare the model's classification accuracy with the PCA-R-OCSVM baseline model. For comparison purposes, we train the baseline model in a similar fashion using the classification metric introduced previously. In general, the PCA-R-OCSVM algorithm requires three parameters to be optimized for of which the parameter ν replaces C^+ and C^-, whereas γ and k_R are equally utilized by both algorithms. Note that in the following, the test dataset is

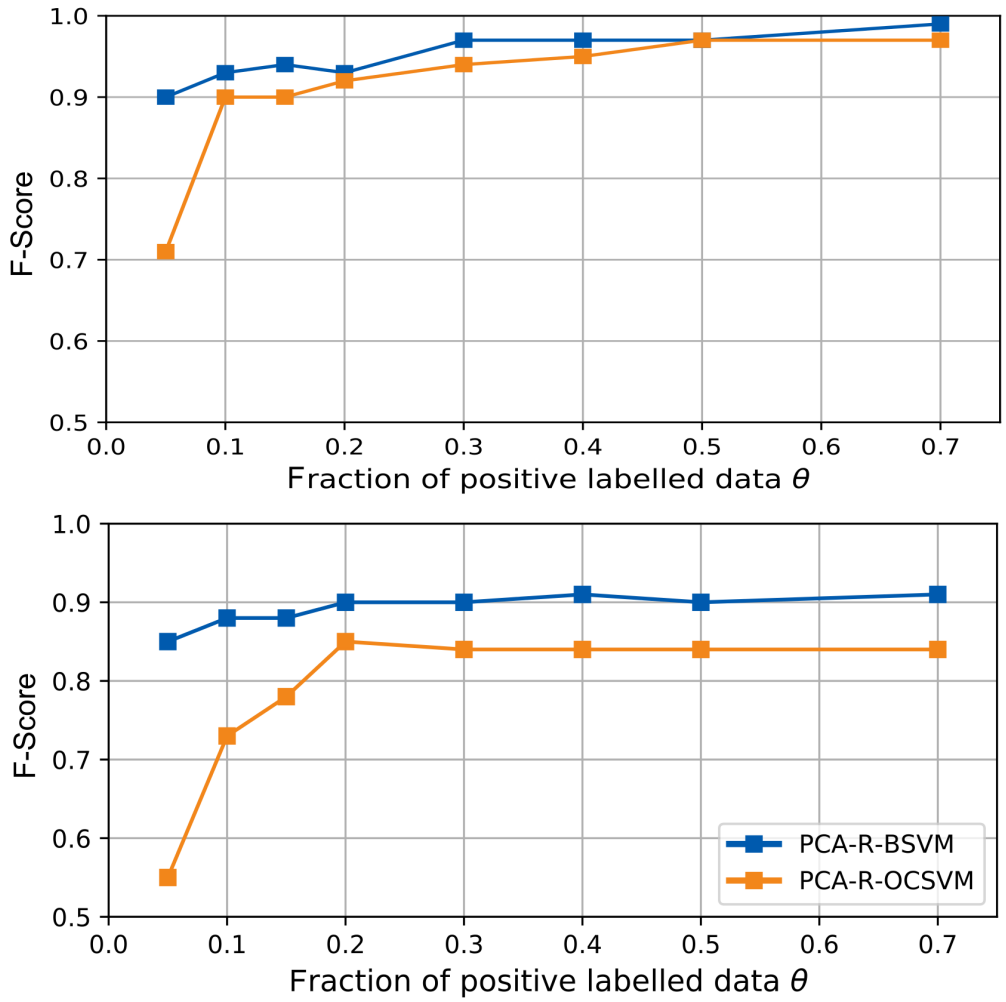

Figure 4. Accuracy plot over fraction of positive labelled samples: models trained on - upper: screw chiller dataset, lower: centrifugal chiller dataset

exploited for comparison purposes using the F-Score metric to evaluate the classification performance. As shown in Figure 4, one can see that the proposed model outperforms the baseline algorithm. This becomes even more distinct when θ is low, which certainly proofs that by incorporating unlabelled data in the training process, the model's classification accuracy can be significantly improved. The most significant difference between both models is at θ=0.05, where the baseline model deviates by 20% considering the screw-chiller dataset and more then 35% when applied on the centrifugal-chiller one. Throughout the experiments, the proposed PCA-R-BSVM model proofed to yield better classification results compared to the baseline algorithm by reaching scores as high as 0.97. Furthermore, its accuracy converges faster with increasing values of θ, which shows that it can be successfully applied for FD tasks, even when only a minor number of positive labelled samples is available.

Summary

In this paper a PU-Learning based novelty detection model was introduced for fault detection tasks. While relying on PCA or, more specifically, on the extracted residual components, it was shown that the model was highly sensitive to faults. Besides, it was shown how the model performs with only a limited number of positive samples being available in the training phase while the rest, including actual positive and negative observations, are treated as unlabelled data samples. The key-points of the proposed model can be summarized as follows:

1. Applying PCA onto the dataset can significantly improve the model performance when the first principal components, i.e. the ones associated with the largest values if eigenvalues, are removed from the dataset and the residual components are used for training the classifier
2. The proposed PCA-R-BSVM could outperform an existing novelty detection algorithm and performs well, even with only few labelled data being available
3. The model performance was validated on two datasets stemming from different chiller types

Acknowledgements

This research was partly supported by the German Federal Ministry for Economic Affairs and Energy (No: ZF4012225RE7) as well as the Ministry for Economic Affairs, Labour and Energy, State of Brandenburg (No: 80237615). Our special thanks go to our partner Potsdamer Anlagenbau und Kältetechnik GmbH for their great support in this research project.

References

[1] A. Afshari and L. Friedrich, “A proposal to introduce tradable energy savings certificates in the emirate of abu dhabi,” *Renewable and Sustainable Energy Reviews*, vol. 55, pp. 1342–1351, 2016.

[2] ISO, *Condition monitoring and diagnostics of machines–vocabulary*, 2012.

[3] G. J. Vachtsevanos, *Intelligent fault diagnosis and prognosis for engineering systems*. Wiley Hoboken, 2006, vol. 456.

[4] S. Wang, Q. Zhou, and F. Xiao, “A system-level fault detection and diagnosis strategy for HVAC systems involving sensor faults,” *Energy and Buildings*, vol. 42, no. 4, pp. 477–490, 2010.

[5] D.-W. Sun, *Handbook of frozen food processing and packaging*. CRC Press, 2016.

[6] V. Venkatasubramanian, R. Rengaswamy, and S. N. Kavuri, “A review of process fault detection and diagnosis: Part ii: Qualitative models and search strategies,” *Computers & chemical engineering*, vol. 27, no. 3, pp. 313–326, 2003.

[7] V. Venkatasubramanian, R. Rengaswamy, S. N. Kavuri, and K. Yin, “A review of process fault detection and diagnosis: Part iii: Process history based methods,” *Computers & chemical engineering*, vol. 27, no. 3, pp. 327–346, 2003.

[8] V. Venkatasubramanian, R. Rengaswamy, K. Yin, and S. N. Kavuri, “A review of process fault detection and diagnosis: Part i: Quantitative model-based methods,” *Computers & chemical engineering*, vol. 27, no. 3, pp. 293–311, 2003.

[9] Y. Fan, X. Cui, H. Han, and H. Lu, “Chiller fault diagnosis with field sensors using the technology of imbalanced data,” *Applied Thermal Engineering*, vol. 159, p. 113 933, 2019.

[10] C. Anger, “Hidden semi-markov models for predictive maintenance of rotating elements,” Ph.D. dissertation, Technische Universität, 2018.

[11] A. Beghi, R. Brignoli, L. Cecchinato, G. Menegazzo, M. Rampazzo, and F. Simmini, “Data-driven fault detection and diagnosis for HVAC water chillers,” *Control Engineering Practice*, vol. 53, pp. 79–91, 2016.

[12] B. Liu, Y. Dai, X. Li, W. S. Lee, and P. S. Yu, “Building text classifiers using positive and unlabeled examples,” in *Third IEEE International Conference on Data Mining*, 2003, pp. 179–186.

[13] H. Han, Z. Cao, B. Gu, and N. Ren, “PCA-SVM-based automated fault detection and diagnosis (AFDD) for vapor-compression refrigeration systems,” *HVAC&R Research*, vol. 16, no. 3, pp. 295–313, 2010.

[14] A. Beghi, L. Cecchinato, C. Corazzol, M. Rampazzo, F. Simmini, and G. A. Susto, “A One-Class SVM based tool for machine learning novelty detection in HVAC chiller systems,” *IFAC Proceedings Volumes*, vol. 47, no. 3, pp. 1953–1958, 2014.

[15] G. Li, Y. Hu, H. Chen, L. Shen, H. Li, M. Hu, J. Liu, and K. Sun, “An improved fault detection method for incipient centrifugal chiller faults using the PCA-R-SVDD algorithm,” *Energy and Buildings*, vol. 116, pp. 104–113, 2016.

[16] B. Schölkopf, A. J. Smola, F. Bach, *et al.*, *Learning with kernels: support vector machines, regularization, optimization, and beyond*. MIT press, 2002.

[17] B. Schölkopf, R. C. Williamson, A. Smola, J. Shawe-Taylor, and J. Platt, “Support vector method for novelty detection,” *Advances in neural information processing systems*, vol. 12, pp. 582–588, 1999.

[18] D. M. J. Tax and R. P. W. Duin, “Support vector data description,” *Machine learning*, vol. 54, no. 1, pp. 45–66, 2004.

[19] H. Han, B. Gu, J. Kang, and Z. R. Li, “Study on a hybrid SVM model for chiller FDD applications,” *Applied Thermal Engineering*, vol. 31, no. 4, pp. 582–592, 2011.

[20] K. Yan, Z. Ji, and W. Shen, “Online fault detection methods for chillers combining extended kalman filter and recursive One-Class SVM,” *Neurocomputing*, vol. 228, pp. 205–212, 2017.

[21] D. Li, G. Hu, and C. J. Spanos, “A data-driven strategy for detection and diagnosis of building chiller faults using linear discriminant analysis,” *Energy and Buildings*, vol. 128, pp. 519–529, 2016.

[22] Z. Wang, Z. Wang, S. He, X. Gu, and Z. F. Yan, “Fault detection and diagnosis of chillers using bayesian network merged distance rejection and multi-source non-sensor information,” *Applied Energy*, vol. 188, pp. 200–214, 2017.

[23] S. Wang and Y. Chen, “Sensor validation and reconstruction for building central chilling systems based on principal component analysis,” *Energy Conversion and management*, vol. 45, no. 5, pp. 673–695, 2004.

[24] H. Han, X. Cui, Y. Fan, and H. Qing, “Least squares support vector machine (LS-SVM)-based chiller fault diagnosis using fault indicative features,” *Applied Thermal Engineering*, vol. 154, pp. 540–547, 2019.

[25] Y. Zhao, S. Wang, and F. Xiao, “Pattern recognition-based chillers fault detection method using support vector data description (SVDD),” *Applied Energy*, vol. 112, pp. 1041–1048, 2013.

[26] W. S. Lee and B. Liu, “Learning with positive and unlabeled examples using weighted logistic regression,” in *ICML*, vol. 3, 2003, pp. 448–455.

[27] M. C. Comstock, J. E. Braun, and R. Bernhard, *Experimental data from fault detection and diagnostic studies on a centrifugal chiller*. Purdue University, 1999.

[28] R. van de Sand, C. Falk, S. Corasaniti, and J. Reiff-Stephan, “A data-driven fault diagnosis approach towards oil retention in vapour compression refrigeration systems,” in *2019 International IEEE Conference and Workshop in Óbuda on Electrical and Power Engineering (CANDO-EPE)*, 2019, pp. 197–202.

2nd German-West African Conference on Sustainable, Renewable Energy Systems SusRES – Kara 2021

Predictive Analytics

https://doi.or/10.52825/thwildauensp.v1i.33

Published: 15 June 2021

A comparison study of data-driven anomaly detection approaches for industrial chillers

Constantin Falk[1] [https://orcid.org/0000-0002-5406-4013],
Ron van de Sand[1] [https://orcid.org/0000-0002-8975-4030],
Sandra Corasaniti[2] [https://orcid.org/0000-0002-0434-501X] ,
and Jörg Reiff-Stephan[1] [https://orcid.org/0000-0003-4176-6371]

[1]University of Applied Sciences Wildau, Germany

[2]University of Rome “Tor Vergata” , Italy

Abstract. Faults in industrial chiller systems can lead to higher energy consumption, increasing wear of system components and shorten equipment life. While they gradually cause anomalous system operating conditions, modern automatic fault detection models aim to detect them at low severity by using real-time sensor data. Many scientific contributions addressed this topic in the past and presented data-driven approaches to detect faulty system states. Although many promising results were presented to date, there is lack of suitable comparison studies that show the effectiveness of the proposed models by use of data stemming from different chiller systems. Therefore this study aims at detecting a suitable data-driven approach to detect faults reliable in different domains of industrial chillers. Thus, a unified procedure is developed, to train all algorithms in an identical way with same data-basis. Since most of the reviewed papers used only one dataset for training and testing, the selected approaches are trained and validated on two different datasets from real refrigeration systems. The data-driven approaches are evaluated based on their accuracy and true negative rate, from which the most suitable approach is derived as a conclusion.

Keywords: Fault Detection, Refrigeration System, Data-Driven Machine-Learning

Introduction

Chiller systems are applied in many industries, while around 14% of the german electric power consumption are attributable to cooling processes [1]. Faulty system states in industrial refrigeration systems can lead to inefficient operating conditions, increased energy consumption or even wear and tear of system components. Since fault states usually occur sucsessively, plant monitoring systems are an important component to detect fault conditions on the basis of sensor data and to initiate appropriate corrective action as early as possible [2]. In this way, faults can be prevented before causing high energy wastage, damage or unscheduled downtimes, thus increasing the coefficient of performance (COP) of the plant and the deployment of maintenance workers [3]. In the future, machine-learned software is to be used to autonomously monitor real world systems and detect deviations at an early stage to initiate appropriate counter-measures, if necessary. To this end, the development sophisticated algorithms has been subject of research for decades and many solutions exist showing promising results [4]–[7]. To strengenth the performance of the resulting model in

detecting fault states, there is a preselection and comparison of these algorithms in terms of resource reqiurements and precision necessary.

The aim of this paper is the identification of a suitable data-driven machine-learning approach to be used in different domains of vapor-compression refrigeration systems. In the following, scientific publications in the field of autonomous fault detection at process plants, followed by a criterion-based pre-selection and short explanation of the selected approaches will be presented. To train those data-driven models appropiately a data-basis is necessary which will be shown subsequently. This is followed by a comparison of the approaches, while the conclusion draws results and summarizes the work.

Related works

In order to make a suitable selection of data-driven methods for chiller fault detection, this section aims at providing an overview of scientific contributions in recent years focusing on anomaly detection on chillers. As part of the data pre-processing, principal component analysis (PCA) has proven to be a very effective method for feature extraction and many athors demonstrated promising results in combination with a suitable classifier [4], [5], [8], [9]. Han et al. [8] used PCA in combination with a multiclass support vector machine (PCA-SVM), using a custom dataset containig both normal and faulty data instances and training with both types of data instances. It could be proven that the support vector machine (SVM) could yield higher classification accuracy through preprocessing the data trough PCA and could also be trained much faster due to the reduced dimensions [8]. However, this approach has limited applicability in practice, since datasets from possible fault cases of refrigeration plants are rarely available. For this reason, Zhao et al. [9] have chosen a similar approach, using a support vector data description (SVDD) classifier trained in the principal component space.

A similar approach in this regard is PCA in conjunction with a one-class support vector machine, which has been applied to chemical processes [10], [11] as well as in industrial refrigeration applications by Li et al. [5]. One important aspect of this is that the model was trained by exploiting only labelled data stemming from the chiller operating condition. For this purpose, the most relevant principal components are derived from the principal component subspace (PCS) and are used as input parameters for the OCSVM, to which we will refer as PCA-PC-OCSVM in the following. As shown by many studies, the RBF kernel showed decent results. Also, only data from normal states of the plant were used for training, after which the OCSVM can classify unknown observations as normal or abnormal. Furthermore, it has been shown that the SVDD and OCSVM are resulting in the exact same outcomes while using the RBF kernel for data transformation [12].

Beghi et al. [13] have implemented a similar approach by utilizing the same dataset, with the crucial difference of removing the most relevant principal components before training and fit the classifier using the residual component subspace (RCS) spanned by the residual components (PCA-R-OCSVM). They demonstrated that chiller faults can be reliably detected in the RS. A similar approach was also applied by Li et al. [5], where a SVDD classifier has been applied. Another approach relying on principal component analysis is the PCA-T^2-SPE according to Beghi et al. [4]. Thereby, Hotelling’s T^2 distribution of the PCS and the squared prediction error (SPE) of the residual space were used for fault detection and diagnosis. Both Li et al. [5] and Beghi et al. [13] conclude that indeed the models trained in the RCS may yield higher classification performance rather than in the PCS.

In general, SVMs are widely used in the field of fault detection as, for example, in [14], where an SVM classifier is used for fault detection to classify multiple fault cases. Thereby, a generic algorithm for detection of characteristic features (CF) was applied. CFs are features by which the occurence of fault cases can be characterized particulary well. Yan et al. [15] published an

approach whereby the dataset was mapped using an auto-regressive model with exogenoues inputs (ARX) after feature selection. The resulting AR-coefficients are used by a OCSVM for classification. Subsequently, the authors [7] published three years later another promising approach based on an extended kalman-filter and a recursive working OCSVM (EKF-ROSVM). The OCSVM is trained by AR-coefficients derived from an ARX-model, which was fitted with filtered data of the EKF and refines itself in testing phase by as normal classified observations. Furthermore, the authors propose to extract CF within a two step approach by exploiting Relief and generic algorithm. Other approaches also consider the application of artificial neural networks, such as in [16]. However, their model primarily focusses on the detection of sensor faults rather then anomalous system behaviour.

It should be noted that all PCA-based as well as the EKF-based approaches are based on the same dataset, which was collected by the American Society of Heating, Refrigerating and Air-Conditioning Engineers (ASHRAE) within the 1043-RP study, instead of the paper by Beghi et al. [4], where an own dataset was applied. This leads to the assumption of a general lag of appropiate datasets aswell as the evaluation of algorithms of data other than the ASHRAE dataset. Therefore this study compares a selection of models based on two datasets: on the one hand, the data from the ASHRAE study 1043-RP by Comstock et al. [17] and on the other hand with data from a previous project presented in [18]. In order to select some of the presented approaches, it is necessary to define selection criteria. Since chiller fault related data are rearely available from real refrigeration systems, the selected approaches should be trainable by only one class of data (data from the normal operating condition). In addition, the selected approaches should have been used in previous works on refrigeration systems. Thus, fault detection is considered in this study, while fault diagnosis is not specifically addressed. Although many approaches exist in the literature, only the most recent papers are considered throughout this study, i.e. the ones published within the last decade. Table 1 contains the most recent papers presented in this chapter, where the criteria-based selected approaches are highlighted in gray.

Table 1. Data-driven methods for fault detection on refrigeration systems

methods	author	year	one-class classifier
PCA-SVM	Han et al. [8]	2010	no
PCA-PC-OCSVM	Li et al. [5]	2016	yes
PCA-R-SVDD	Li et al. [5]	2016	yes
PCA-T^2-SPE	Beghi et al. [4]	2016	yes
EKF-R-OCSVM	Yan et al. [7]	2017	yes
CNN-CA	Du et al. [16]	2014	no

Model Training

Methodological approaches

The previously selected data-driven models will be presented further in this section. It should be noted that three of these models employ PCA for dimensionality reduction. PCA is an unsuperivsed feature reduction method that decomposes the given data into the model principal component space and the unmodelled residual component space, such that the first PCs represent most of the data variability. Feature extraction respective feature reduction is necessary scince utilizing high dimensional datasets to train data-driven models lead to high computational costs and memory requirements [13]. Moreover, high dimensional input data can lead to poor understanding of the resulting model [19, p. 32]. In order to reduce the

original number of dimensions, a defined amount of principal components can be selected, or a defined variance threshold that the selected principal components should represent determines the number to be selected. All of the selected PCA-based models split the resulting feature space into a PCS and RCS, where the PCA-PC-OCSVM utilizes the PCS for training and testing the OCSVM. Both remaining approaches use the RS for classifier fitting, while the PCA-T²-SPE only requires the SPE for fault detection while the T²-distribution is mainly necessary for fault diagnosis [4]. The subdivision of the principal component space is done accordingly to the comulative percentage variance (CPV) of the first k PCs, so that $CPV(k) \geq CPV_k$ applies. While Beghi et al. [4] proposes a $CPV_{k_1} = 95\%$, Li et al. [5] suggests to set this value to $CPV_{k_2} = 85\%$. The EKF-ROSVM is the only approach not utilizing the PCA as feature extraction method, while using ReliefF-algorithm in combination with an adaptive genetic algorithm (AGA) to select CFs [7].

Every approach uses a form of OCSVM for classification, except the PCA-T²-SPE. SVMs and different variations of it in general has been shown to be very popular in anomaly detection, since it is utilized in around 65% of all scientific contributions aiming for fault detection in refrigeration systems with data-driven methods [20]. The OCSVM is a subform of SVMs for novelty detection, whereby only one class is utilized for model training. The optimisation problem [12] is given as:

$$\min_{w,\xi,\rho} \frac{1}{2}||w||^2 + \frac{1}{\nu l}\sum_{i=0}^{l}\xi_i - \rho \tag{1}$$

$$\text{subject to } (w \cdot \Phi(x_i)) \leq \rho - \xi_i, \xi_i \leq 0 \tag{2}$$

where l is the number of observations, w a vector orthogonal to the separating hyperplane and ρ the offset of the hyperplane, while the slack variables ξ are margin errors. ν is a parameter bounded between 0 and 1 and represents the fraction of allowed outliers. Schölkopf et al. [12] showed the decision function for an OCSVM in (3). This decision function offers the advantage of an applicable kernel trick.

$$h(x) = sgn\left(\sum_i \alpha_i k(x_i, x) - \rho\right) \tag{3}$$

As shown in many previous papers [4]–[8], the RBF-kernel function shows superior results in chiller FDD application, which is given as: $k(x, x') = exp(-\gamma||x - x'||^2)$. In general, this leads to two parameters to be optimised during the training process, namely ν and γ, wheras the latter tunes the kernel band width while the former defines the fraction of outliers. In order to find the optimal decision boundary, an optimal combination of the parameters must be discovered, which will be discussed in the section parameter optimization.

The model proposed by Beghi et al. [4] detects faults calculating the SPE of the RS, whereby an observation is considered to be normal if $SPE(\boldsymbol{x}) \leq \delta^2$, where δ^2 is the control limit, the determination of which can be traced in [4]. While T² distribution serves the fault diagnosis, the SPE is fullfills the fault detection task considerd in this paper.

Procedure

To reach comparability between the results of different data-driven approaches, an abstract data-flow model has been developed so that all algorithms are trained using the same data and procedure, which can be seen in Figure 1.

Two datasets with balanced amount of normal and faulty observations are extracted from each dataset, to reach comparability between the results of the models. Accordingly all of the

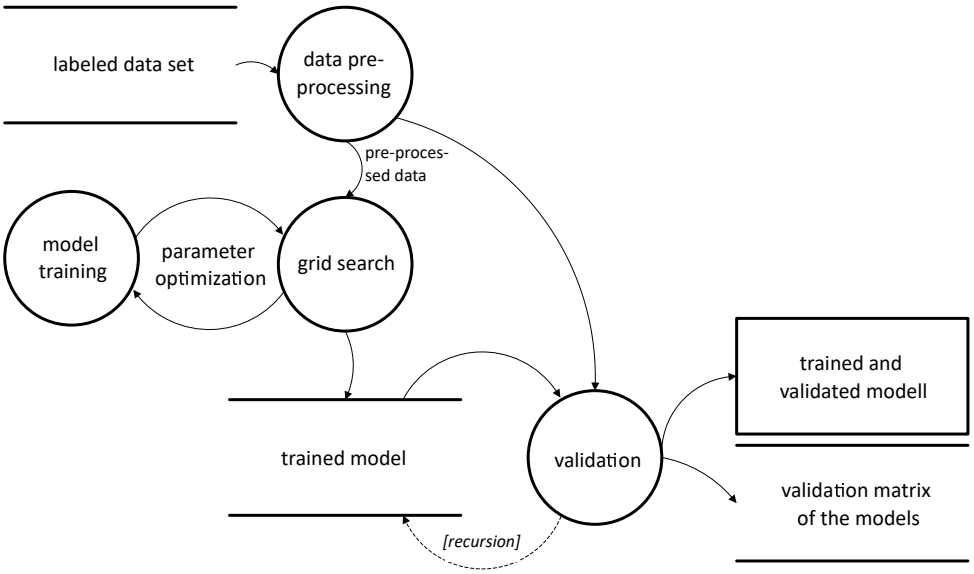

Figure 1. Data-flow diagram for machine-learning approach training

following steps are performed for each dataset. The function ’data pre-processing’ contains all approaches including pre-processing steps like filtering, normalizing, steady state finding, feature extraction or feature selection. Steady state detection is a pre-processing step to filter out transient operating conditions which can include overshoot and undershoot phenomena that may decrease the performance of the detection. Therefore, transient data is filtered out while the filtering process takes place according to Comstock et al. [17]. For validation purposes, the dataset is split into a train and test dataset. While the former is utilized for traning the repective model, the latter soely serves for validation purposes. In the semi-supervised setting, the model EKF-ROSVM [7] refines itself with self-labeled and as normal detected datapoints even after the model training, which is depicted in Figure 1 using a dashed line. This refinement is noted as *recursion* in Figure 1 with a dashed line, due not all approaches do recursion. The output of the data-flow diagram is the validation matrix of the models, containing the performance of each approach for every fault case as well as the trained and validated model, which can be used to classify unlabeled datapoints and to compare against other models.

Parameter Optimization

In the field of machine-learning, many applications require any type of (hyper-)parameter optimization for tuning the respective model parameters. Three of the selected data-driven approaches base on an OCSVM with the parameters γ and ν to optimize. In this paper a grid search in combination with 5-fold cross-validation is utilized, which has been proven as reliable optimizer with good generalization performance and prevention of overfitting the classifier [14]. In 5-fold cross-validation, the training set gets randomly split into five equal sized subsets, while each subset is used to validate the classifier trained on the conglomerate of the reamining four subsets. With the training and testing performed by cross-validation, the parameter combination gets rated with the mean performance out of the five different training sets. Every approach gets optimized twice (one model for each dataset) on the training dataset with selected features. The model with the best performing parameter set gets selected and will be validated afterwards. The resulting γ, ν and the corresponding $F1$-score for each OCSVM-based method on both datasets are shown in Table 3.

Table 2. Optimized parameter for every OCSVM-based approach with reached performance

	DS1			DS2		
method	γ_{DS1}	ν_{DS1}	$F1_{DS1}$	γ_{DS2}	ν_{DS2}	$F1_{DS2}$
PCA-T²-SPE	—	—	$89,43\%$	—	—	$69,10\%$
PCA-PC-OCSVM	$1,1$	$0,04$	$70,33\%$	$1,9$	$0,03$	$70,14\%$
PCA-R-OCSVM	$0,7$	$0,06$	$\mathbf{95,92}\%$	$3,3$	$0,01$	$82,58\%$
EKF-ROSVM	$7,0$	$0,01$	$89,14\%$	$3,4$	$0,02$	$\mathbf{88,50}\%$

Datasets

For appropriately training data-driven anomaly detection models, representative datasets are necessary. As data-basis serves the datasets from the ASHRAE study 1043-RP [21] and from a project of the Technical University of Applied Science Wildau [18]. Both datasets were arranged to study the impact of different fault types at multiple severity levels (SL). The ASHRAE project [21] is based on a centrifugal chiller system, with R134a as refrigerant, while the SmCoCo dataset is based on a screw compressor with ammonia (R717) as refrigerant. Besides the benchmark testruns, where the normal operating scenarios were investigated, both studies present gathered data from real fault states in the test chillers, including excessive Oil (exOil), reduced water flow in the evaporator (rVE) and condenser (rVC), non-condensables in the refrigerant circuit (NC) and a simulated refrigerant leak (RL). For simplicity, the ASHRAE dataset is abbreviated DS1 and the screw compressor dataset is abbreviated DS2 in the following.

Table 3. Feature selection by Relief and Relief+AGA

	Relief		Relief+AGA	
Feature	DS1	DS2	DS1	DS2
Overall evaporator heat loss coefficient	✓	✓		
Oil feed temperatur	✓		✓	
Refrigerant suction superheat temperature		✓		✓
Refrigerant suction temperature				
Refrigerant discharge temperature	✓		✓	
Refrigerant discharge superheat temperature	✓	✓		
Temperature difference of evaporator water		✓		✓
Temperature difference of condenser water	✓	✓	✓	✓
Evaporator approach temperature	✓	✓		✓
Temperature evaporator water out				
Temperature evaporator water in				
Temperature of evaporating refrigerant				
Condenser approach temperature	✓	✓	✓	✓
Temperature condenser water in				
Temperature condenser water out				
Pressure of evaporating refrigerant				
Pressure of condensing refrigerant	✓		✓	
Evaporator capacity				
Condenser capacity				
Current consumption				
Power consumption				
Coefficient of performance (COP)		✓		
Mass flow condenser water				
Volume flow condenser water				

Theoretically, the PCA-based approaches does not depend on prior feature selection, since PCA itself performs feature extraction, i.e. by deriving new features from the dataset. However, since all selected approaches could increase the performance of their classifier through feature selection, in this paper we perform a Relief-algorithm based feature selection [7] aswell. Therefore, a Relief-algorithm gets applied on some preselected CFs used in previous papers to identify the most significant ones, while the top third of the most influential features are selected. A more advanced approach is used by EKF-ROSVM and applies an AGA on the Relief-based feature selection in order to eliminate redundancies from the feature set [7]. The results of this analysis are listed in Table 3. As already mentioned, fault cases were simulated on both refrigeration systems. All fault cases were performed at different SLs ranging from SL1, with only slight impact on the overall chiller operating conditions, to SL4, representing serious fault effects.

Model-Evaluation

The evaluation of the data-driven approaches is performed on the test dataset extracted after the data pre-processing to examine the generalisation ability of the models for unseen obervations. The test data gets classified by trained models and the classification compared to the real class of the observations. Thus, the performance of the fault detection approaches can be evaluated divided by dataset, fault case and SL. Figure 2 shows the accuracy of all eight trained models, differenciated by the underlying dataset.

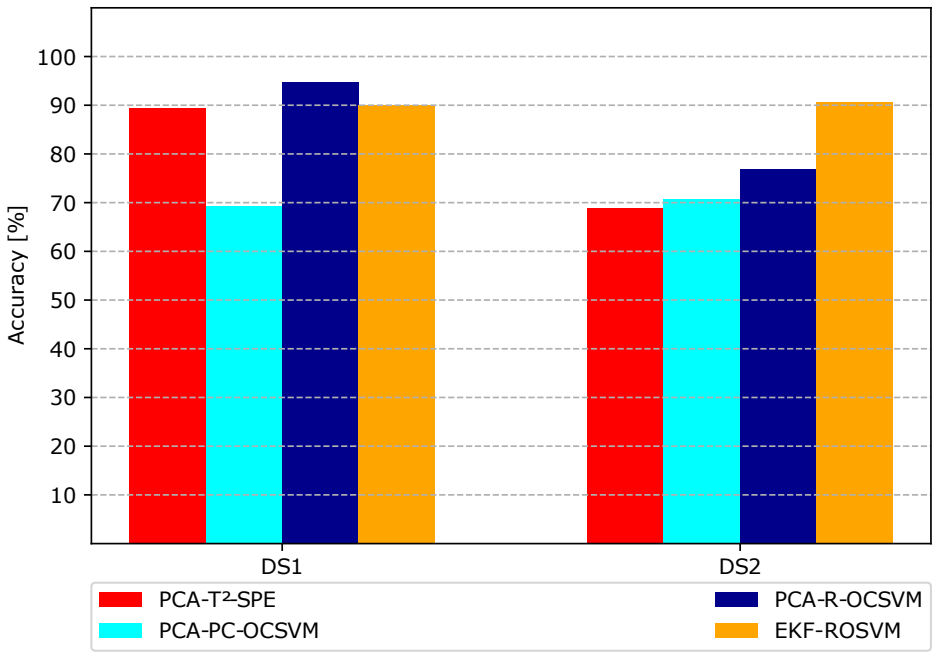

Figure 2. Accuracy of the approaches for DSs

It can be seen from the figure that the models vastly vary in their overall accuracy across the datasets. Especially, the PCA-based models perform better on DS1 than on DS2, with exception of the PCA-PC-OCSVM which performs slightly better on DS2 than on DS1. The EKF-ROSVM is the only approach showing promising performances on both datasets with accuracies higher than 90%, and give hope for good transferability to other refrigeration systems. PCA-T²-SPE's and PCA-R-OCSVM's performances seem to be very dataset

dependent, with the latter showing the highest accuracy of fault detection on DS1. However, in practice, one may be more interested in how reliable faults are correctly classified. Therefore, the true negative rate (TNR) of the models may be more meaningful and gets acquired in Figure 3.

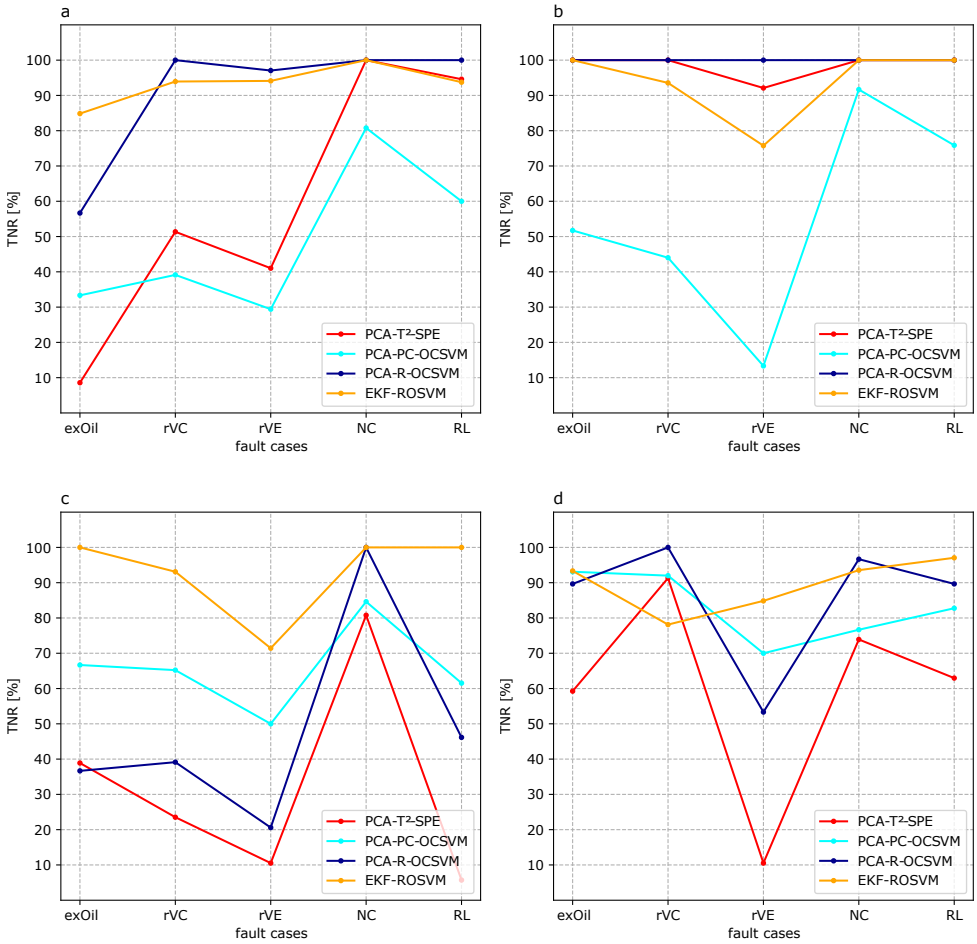

Figure 3. TNR of fault detection for DSs and SLs (a: DS1-SL1; b: DS1-SL4; c: DS2-SL1; d: DS2-SL4)

As shown in Figure 3, it gets clear that faults being present in lower SLs are less reliably detected compared to those in higher SLs. The reason for this might be explained throug the increasing faults characteristics with higher SL. Added to that, the faults appear to be detectable with varying degrees of reliability, which gets particularly evident in the case of the fault NC, which was dependably detected in both datasets across all degrees of hardness. The detection of other fault cases appear to be a challenging task for some approaches even in greater severity levels, like rVE. Interestingly, the PCA-T²-SPE model is the only approach that circumvents the mapping of data into a higher dimensional feature space, i.e. by applying kernels. Although this avoids the introduction of further parameters to be tuned by use of appropriate search methods, it becomes appearant that the model is outperformed by the other models. Nonethess, it might be highly favourable if no labelled fault samples are available from the target chiller, as it bypasses computational expensive parameter tuning induced by the other models. Thus, it appears that by introducing a non-linear mapping of the available observations into the higher dimensional feature space, faults can be detected more reliably. Nonetheless, this also introduces additional parameters to be optimized, which is somewhat disadvantageous in terms of computational complexity or the limited applicability of suitable search strategies. The EKF-ROSVM presents a remarkably high fault detection rate especially in lower SLs with a TNR always larger than 70% and accordingly stable behavior

over all fault cases. The PCA-PC-OCSVM shows a slightly reduced performance with TNRs between 12% and 92%, while it always gets outperformed in every fault case by any other approach.

Conclusion

The work at hand compared different data-driven approaches based on two different systems. Four models were derived from the literature, wherby all seem to to yield convinient classification perfomance. To ensure the comparability of different approaches, an abstract data-flow diagram were developed so that all models trained following the same procedure. Furthermore, the selected approaches were applied to two datasets of real refrigeration systems to evaluate the performances as well as the transferability of the selected approaches. Due to its high reliability, the EKF-ROSVM has proven to achieve the best classification performance in this study. The PCA-R-OCSVM showed promising results on the first dataset and outperformed even the EKF-ROSVM in most fault cases, but, however, showed vulnerabilities in transferability on the second dataset. The two remaining approaches showed promising results aswell, but were outperformed in each fault case by an other applied algorithm. In future works, the effect of recursive classifiers on the fault detection performance should be investigated more in detail. This study did not explicitly examines this influence, but only compared a recursive classifier with normal classifiers. On the other hand, a practical implementation of the identified fault detection approach could take place.

Acknowledgements

The research was partially supported by the european regional development fund (ERDF). We are particularly grateful to our industrial partner Potsdamer Anlagenbau und Kältetechnik GmbH for supporting this project through providing a test facility as well as during several troubleshooting phases.

References

[1] VDMA e.V. Allgemeine Lufttechnik, *Energiebedarf für kältetechnik in deutschland: Eine abschätzung des energiebedarfs von kältetechnik in deutschland nach einsatzgebieten 2017*, VDMA, Ed., Frankfurt (a.M.)

[2] Y.-h. Song, Y. Akashi, and J.-J. Yee, “A development of easy-to-use tool for fault detection and diagnosis in building air-conditioning systems,” *Energy and Buildings*, vol. 40, no. 2, pp. 71–82, 2008.

[3] M. A. Piette, S. K. Kinney, and P. Haves, “Analysis of an information monitoring and diagnostic system to improve building operations,” *Energy and Buildings*, vol. 33, no. 8, pp. 783–791, 2001.

[4] A. Beghi, R. Brignoli, L. Cecchinato, G. Menegazzo, M. Rampazzo, and F. Simmini, “Data-driven fault detection and diagnosis for hvac water chillers,” *Control Engineering Practice*, vol. 53, pp. 79–91, 2016.

[5] G. Li, Y. Hu, H. Chen, L. Shen, H. Li, M. Hu, J. Liu, and K. Sun, “An improved fault detection method for incipient centrifugal chiller faults using the pca-r-svdd algorithm,” *Energy and Buildings*, vol. 116, pp. 104–113, 2016.

[6] D. Li, G. Hu, and C. J. Spanos, “A data-driven strategy for detection and diagnosis of building chiller faults using linear discriminant analysis,” *Energy and Buildings*, vol. 128, pp. 519–529, 2016.

[7] K. Yan, Z. Ji, and W. Shen, “Online fault detection methods for chillers combining extended kalman filter and recursive one-class svm,” *Neurocomputing*, vol. 228, pp. 205–212, 2017.

[8] H. Han, Z. Cao, B. Gu, and N. Ren, “Pca-svm-based automated fault detection and diagnosis (afdd) for vapor-compression refrigeration systems,” *HVAC&R Research*, vol. 16, no. 3, pp. 295–313, 2010.

[9] Y. Zhao, S. Wang, and F. Xiao, “Pattern recognition-based chillers fault detection method using support vector data description (svdd),” *Applied Energy*, vol. 112, pp. 1041–1048, 2013.

[10] Q. Jiang and X. Yan, “Just-in-time reorganized pca integrated with svdd for chemical process monitoring,” *AIChE Journal*, vol. 60, no. 3, pp. 949–965, 2014.

[11] X. Liu, K. Li, M. McAfee, and G. W. Irwin, “Improved nonlinear pca for process monitoring using support vector data description,” *Journal of Process Control*, vol. 21, no. 9, pp. 1306–1317, 2011.

[12] B. Schölkopf, R. C. Williamson, A. J. Smola, J. Shawe-Taylor, J. C. Platt, *et al.*, “Support vector method for novelty detection,” in *NIPS*, vol. 12, 1999, pp. 582–588.

[13] A. Beghi, L. Cecchinato, C. Corazzol, M. Rampazzo, F. Simmini, and G. A. Susto, “A one-class svm based tool for machine learning novelty detection in hvac chiller systems,” *IFAC Proceedings Volumes*, vol. 47, no. 3, pp. 1953–1958, 2014.

[14] H. Han, B. Gu, J. Kang, and Z. R. Li, “Study on a hybrid svm model for chiller fdd applications,” *Applied Thermal Engineering*, vol. 31, no. 4, pp. 582–592, 2011.

[15] K. Yan, W. Shen, T. Mulumba, and A. Afshari, “Arx model based fault detection and diagnosis for chillers using support vector machines,” *Energy and Buildings*, vol. 81, pp. 287–295, 2014.

[16] Z. Du, B. Fan, X. Jin, and J. Chi, “Fault detection and diagnosis for buildings and hvac systems using combined neural networks and subtractive clustering analysis,” *Building and Environment*, vol. 73, pp. 1–11, 2014.

[17] M. C. Comstock, J. E. Braun, and R. Bernhard, *Development of analysis tools for the evaluation of fault detection and diagnostics in chillers: Sponsored by ASHRAE Deliverable for Research Projekt 1043-RP Fault Detection and Diagnostics (FDD) Requirements and Evaluation Tools for Chillers*. Purdue University, 1999.

[18] R. van de Sand, C. Falk, S. Corasaniti, and J. Reiff-Stephan, “A data-driven fault diagnosis approach towards oil retention in vapour compression refrigeration systems,” in *2019 International IEEE Conference and Workshop in Óbuda on Electrical and Power Engineering (CANDO-EPE)*, IEEE, 20.11.2019 - 21.11.2019, pp. 197–202.

[19] T. Hastie, R. Tibshirani, and J. H. Friedman, *The elements of statistical learning: Data mining, inference, and prediction*, Second edition, corrected at 12th printing 2017, ser. Springer series in statistics. New York, NY: Springer, 2017.

[20] R. van de Sand, S. Corasaniti, and J. Reiff-Stephan, *Review of condition based maintenance approaches for vapor compression refrigeration systems*, 2020.

[21] M.C. Comstock, J.E. Braun, and R. Bernhard, *Experimental data from fault detection and diagnostic studies on a centrifugal chiller*, 1999.

2nd German-West African Conference on Sustainable, Renewable Energy Systems SusRES – Kara 2021

Machine Learning

https://doi.org/10.52825/thwildauensp.v1i.27

Published: 15 June 2021

Design of an intelligent system for controlling and balancing renewable energy flows in an autonomous micro-grid

K. R. Assilevi[1], A.S. Ajavon[1], and K. H. Adjallah[2]

[1] CERME, Université de Lomé, 01 BP 1515 Lomé 1, Lomé, Togo

[2] LCOMS EA-7306, Université de Lorraine, 57078, Metz, France

Abstract. Pooling different renewable energy sources (hydrogen, solar, wind, geothermal, etc.) enables developing a standalone energy micro-grid. The energy flows from these various sources are neither constant nor equivalent. Therefore, control and balancing mechanisms should be established for optimal energy utilization through an intelligent system based on interconnected microcontrollers networked with sensors. Our contribution addresses this issue by proposing an original architecture of an intelligent and distributed control system based on a sensor network and a strategy to share the electric power through the micro-grid. In our work we consider a micro-grid powered by sources of wind turbine, pv panels and battery which energy flows are controlled and balanced through our system depending on power demand of the loads. Alternating Current (AC) bus and Direct Current (DC) bus are tied together by an inverter. A set of microcontroller-sensor-actuators (*which we named S.A.D for Sensor/Actuator Device*) are deployed at strategic points in the micro-grid providing constantly data from power generated and consumed, equipment health and status. A control algorithm developed in relation to a network control strategy is implemented by combining the performance different microcontroller boards. Relying on existing literature works, a review of solution approaches to the challenging problem, of the power flows balancing between the different energy sources and storage batteries embedding appropriate IoT technologies and exploiting energy big-data platforms, is presented.

Keywords: Micro-grid, sensor network, flow balancing, microcontroller, intelligent system, IoT, 5G

Introduction

Renewable energy micro-grids have proven to be an excellent alternative in terms of meeting energy needs around the world and especially in Africa where the traditional grid is showing its limits in providing electricity [1], especially in hard-to-reach areas [2],[3].

Depending of energy needs [4], different architectures are implemented [5] taking into account the available renewables energies.

Depending on the context, some micro-grids are deployed by pooling available energy sources. These micro-grids consisting of various types of the micro-generators as distributed generator [6] (wind turbine, photovoltaic (PV) array, fuel cells, diesel generator, and wave generator, CHP,…), [7] local storage elements (flywheel, energy capacitors and batteries) and loads. Storage devices play a key role in micro-grid control, reliability and stability.

So, with these different types of energy sources, the micro-grid architecture consists in an alternating current (hybrid AC) micro-grid with a direct current (DC) micro-grid, tied

together by a bidirectional AC/DC converter [8]. Distributed generators can be connected to the AC or to the DC feeder. This architecture combines the advantages of the AC and DC micro-grid.

Since, the energy flows from these various sources are neither constant nor equivalent. control and balancing mechanisms [9], [10], [11] should be established for optimal energy utilization through an intelligent system based on interconnected microcontrollers [12] networked with sensors [13].

Our work was carried out on a micro-grid installed in a peripheral area of Lomé in Togo (West Africa), in a district where wind and sun conditions favor the production of wind and solar energy.

The contributions in our work are as follows: (1) Design of an improved system architecture for controlling and balancing energy flows. (2) Development of a strategy for controlling and balancing energy flows. (3) Development and implementation of a responsive, intelligent algorithm embedded on microcontrollers installed at strategic locations in the micro-grid. (4) Connection of the system to an IoT platform via 5G network to monitor, analyze, and process new data resulting from the algorithm's implementation.

Related work

Recent work in micro-grid focused on the management of various renewable energies sources. Giorgio Graditi et al. [14] developed a heuristic-based formulation of shiftable loads; Amin et al. [15] formulated a model predictive control; Lei Zhang et al. [16] projected two-scale dynamic programming strategy and subsequently Ashabani et al. [17] proposed nonlinear control for energy management in micro-grid. In [18], Jinsung Byun et al. envisioned intelligent cloud home energy management system (iCHEMS), in which the appliances shedding is fared in accordance with the assigned priority considering the renewable energy capacity.

K. Venkatraman et al. [19] developed a micro-grid controller integrating the output from multiple types of renewable energy conversion systems, namely, wind and solar along with diesel generator as well as battery storage with source and load control features using Field Programmable Gate Arrays.

Another renewables energies sources system energy management is done by using PI controller in [20], [21],[22],[23]. Somnath Das et al. in [10], implemented a control strategy with fuzzy logic controller for smoothing of the power fluctuation and at the same time to maintain the battery state of charge with in allowable limits.

Betha et al. [24] combined an autonomous PV and a wind turbine using a DC bus, and the generated output power from the system is fed to all connected loads, while the extra power is injected into the electric grid.

Hajizadeh and Aliakbar Golkar [25] introduced an approach for active power sharing in a hybrid fuel cell/battery power source in order to improve the system’s efficiency and battery’s lifetime with an acceptable load.

Elmouatamind et al. [26] introduced a micro-grid system platform for efficient integration and management of renewable energy sources and storage devices.

Hangaragi [27] proposed a hybrid PV–wind system, which provides a sophisticated integration of the wind turbine and solar PV, in order to extract the optimum energy from the two sources, PV and wind.

In [28] a microcontroller network is implemented, interconnected to micro-grid sources. In this architecture, microcontrollers are connected to key elements of the micro-grid: collectors, energy storage devices and the energy management system among others.

These microcontrollers are the entry point to the sensor network. They are responsible for collecting the data and information produced at the level of the sensors, and for sending them via a VPN (Virtual Private Network) connection to the gateways. The latter proceed to transfer the data after the authentication and authorization procedures. These data, which are encrypted, are then conveyed to the heart of the sensor network for analysis and exploitation.

In our work, we used the performance of microcontroller boards, arduino and raspberry in order not only to make the system for controlling and balancing energy flows more efficient but also in case of addition of new components in the network and implementation of algorithms in arduino and python programming language for a dialogue between the platform and the cloud.

Micro-grid architecture

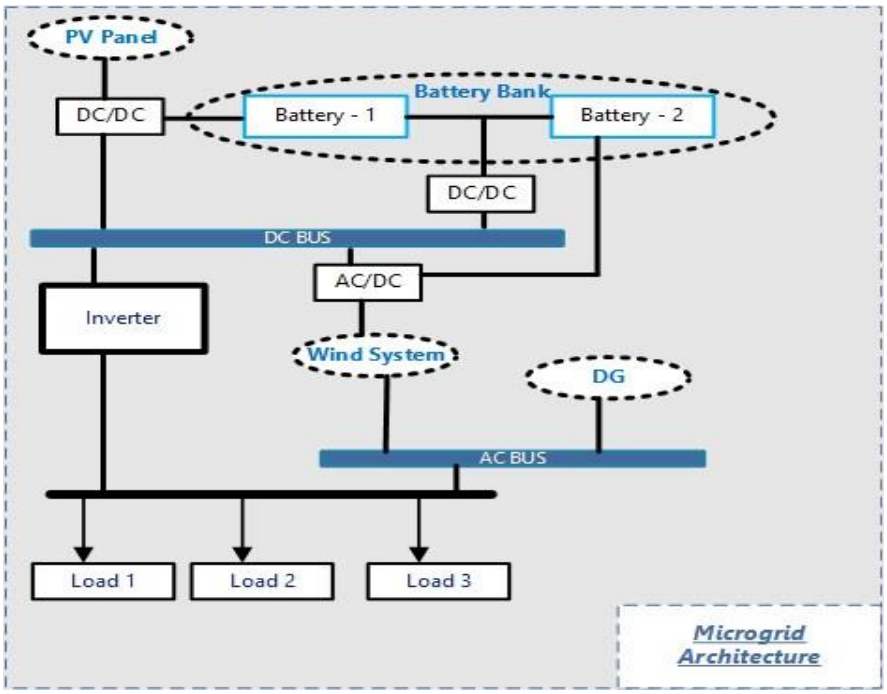

Figure 1. Micro-grid architecture

The micro-grid, subject of our study pools four energy sources. The priorities come from solar panels and wind turbines. The energy generated by these two sources is each stored in a specific battery. The two batteries, combined constitute a battery bank which is the third source of energy. This source is used in the event of a shortfall in solar and wind power generation. The fourth source of energy which is used upon in the ultimate event is the diesel generator. The architecture of the micro-grid is shown in Figure 1. The energy sources of this micro-grid are used to meet the needs of three different loads.

Proposed system and strategy

The proposed system interconnects with the existing micro-grid through specific nodes that we named S.A.D (for Sensor / Actuator Device). It is nothing more than a set of sensors and actuators linked to a microcontroller.

The S.A.D are placed in specific places depending on what we want to monitor and control. The S.A.D. are linked to a control and management center thus forming a network of

microcontrollers. This control center is connected to the cloud to which it sends data for monitoring needs and which is also stored in a database which is analyzed for future uses.

A. Proposed architecture

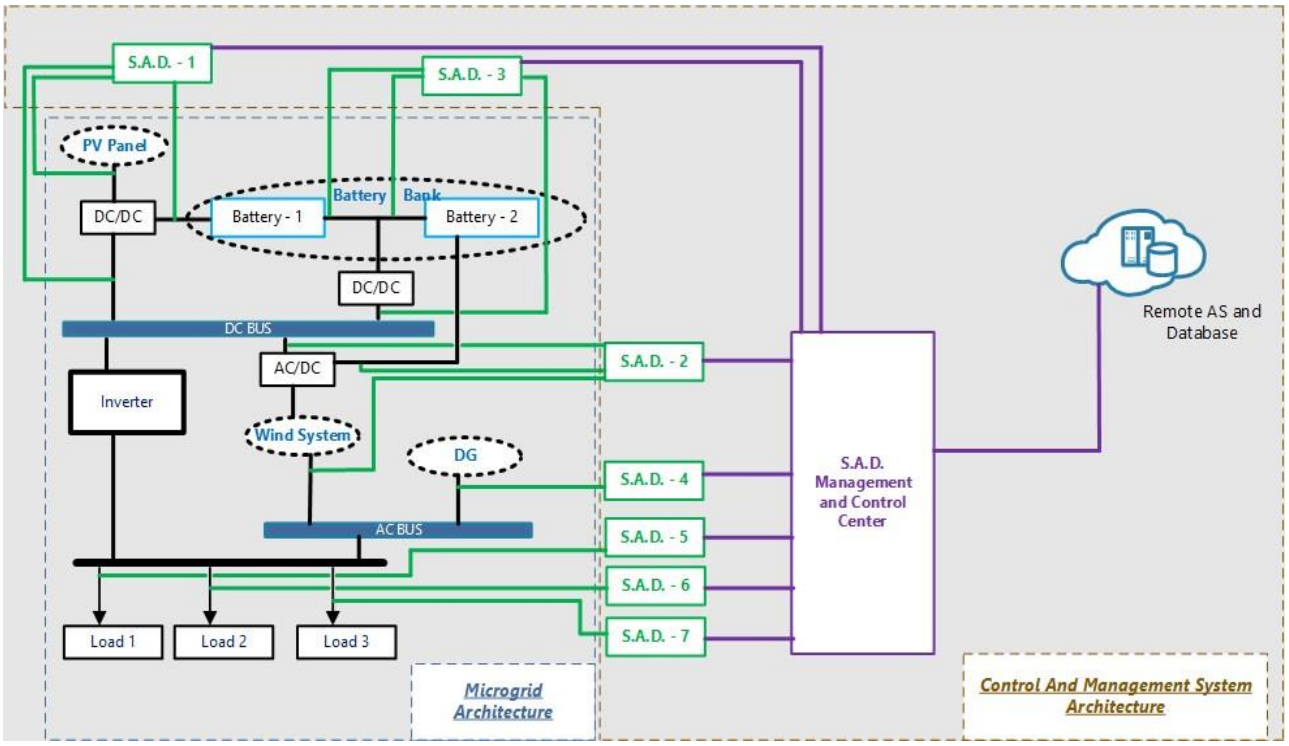

Figure 2. Control and management system architecture

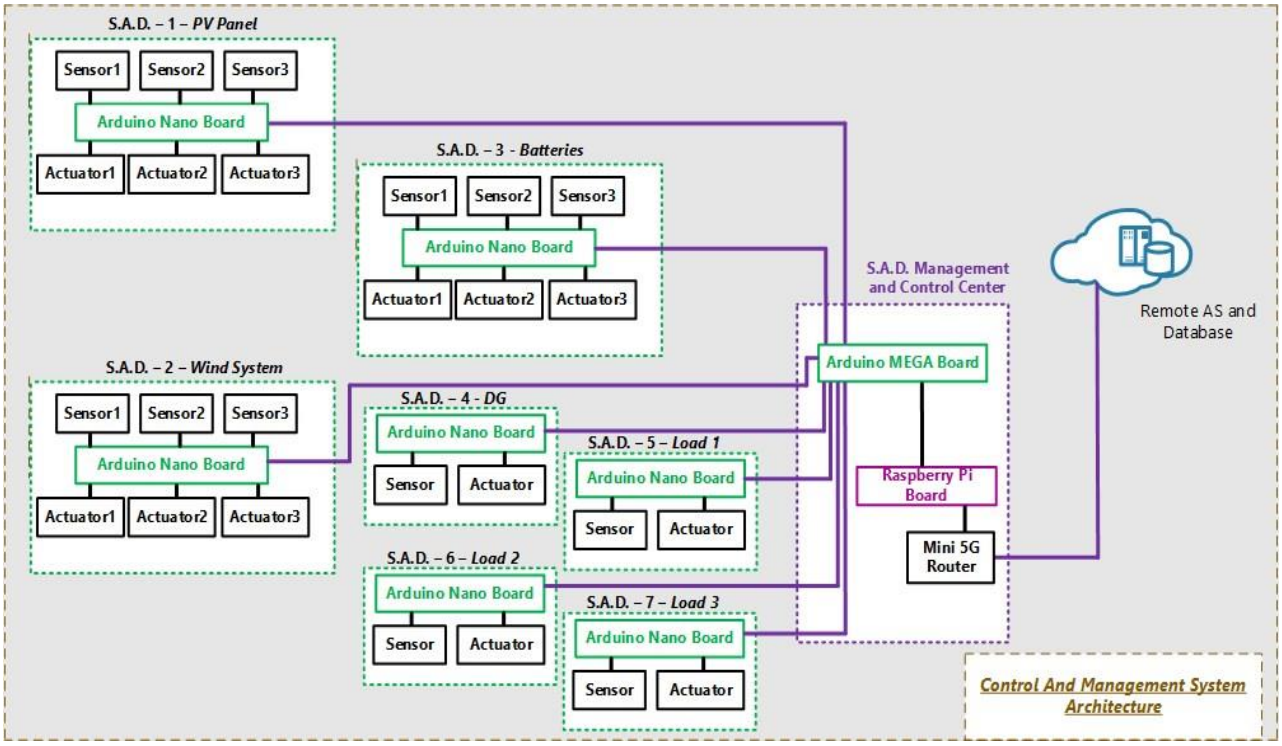

Figure 3. Control and management system architecture details

Figure 2. shows us the general architecture of the micro-grid connected to the network of microcontrollers formed by the S.A.D.. Thus presenting the architecture of the control and management system of energy flows.

The Sensor / Actuator association for each S.A.D depends on the source or the load to be controlled; therefore varying the number of elements to be connected to the microcontroller as shown in Figure 3.

The microcontroller network as well as the control strategy are shown in the following sections.

B. Microcontroller network

1. Sensor / Actuator Device (S.A.D.)

Figure 4 is an internal image of the S.A.D showing the connections of the microcontroller to the sensors on the one hand and to the actuators on the other hand.

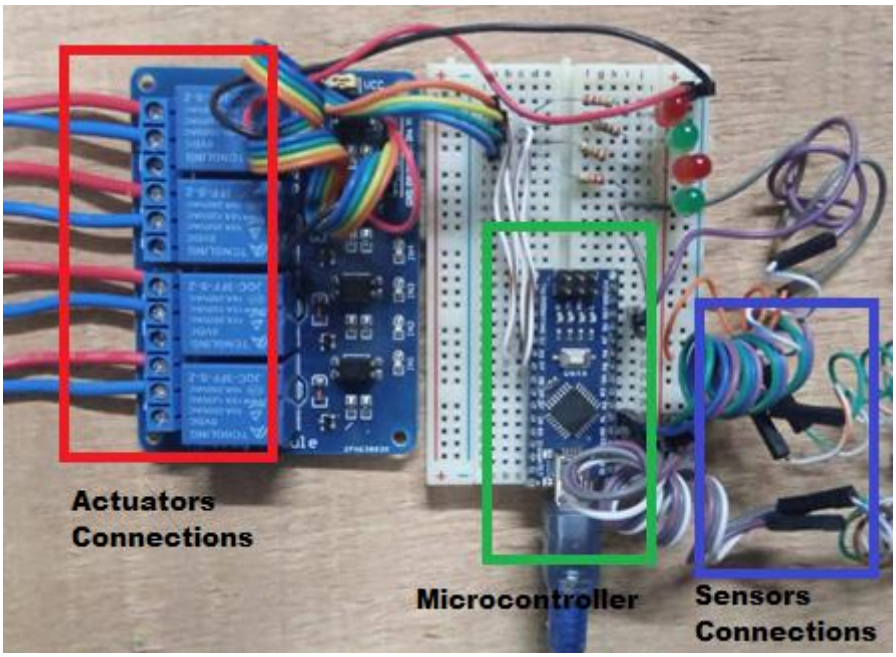

Figure 4. Sensor / Actuator Device

Each S.A.D in the network has a specific role to play depending on its location in the network. Table 1 summarizes the roles of each sensor and actuator of each S.A.D.

Table 1. S.A.D roles in the network

N° S.A.D	Source / Load	Sensor / Actuator	Roles
1	PV Pannel	Sensor 1	Sense power from PV pannel
		Sensor 2	Sense voltage and current between DC/DC converter and DC Bus
		Sensor 3	Sense voltage and current between DC/DC converter and Battery 1
		Actuator 1	Control link between PV panel and DC/DC converter
		Actuator 2	Control link between DC/DC converter and AC Bus

		Actuator 3	Control link between DC/DC converter and Battery 1
2	Wind Turbine	Sensor 1	Sense power from Wind turbine
		Sensor 2	Sense voltage and current between AC/DC converter and DC Bus
		Sensor 3	Sense voltage and current between AC/DC converter and Battery 2
		Actuator 1	Control link between Wind turbine and AC Bus
		Actuator 2	Control link between AC/DC converter and DC Bus
		Actuator 3	Control link between AC/DC converter and Battery 2
3	Battery	Sensor 1	Sense voltage and current from Battery 1
		Sensor 2	Sense voltage and current from Battery 2
		Sensor 3	Sense voltage and current between DC/DC converter and DC Bus
		Actuator 1	Control flow from Battery 1 to battery bank
		Actuator 2	Control flow from Battery 2 to battery bank
		Actuator 3	Control link between DC/DC converter and DC Bus
4	Diesel Generator	Sensor	Sense power from Diesel Generator
		Actuator	Control link between Diesel Generator and AC Bus
5	Load 1	Sensor	Sense Load 1 voltage and current
		Actuator	Switch ON/OFF Load 1
6	Load 2	Sensor	Sense Load 2 voltage and current
		Actuator	Switch ON/OFF Load 2
7	Load 3	Sensor	Sense Load 3 voltage and current
		Actuator	Switch ON/OFF Load 3

2. S.A.D. Management and Control Center

The S.A.D. Management and Control Center consists of an Arduino MEGA board to which all the S.A.D. of the network are connected. It exchanges data with the raspberry board which is connected to the cloud through a 5G mini router as shown in Figure 5.

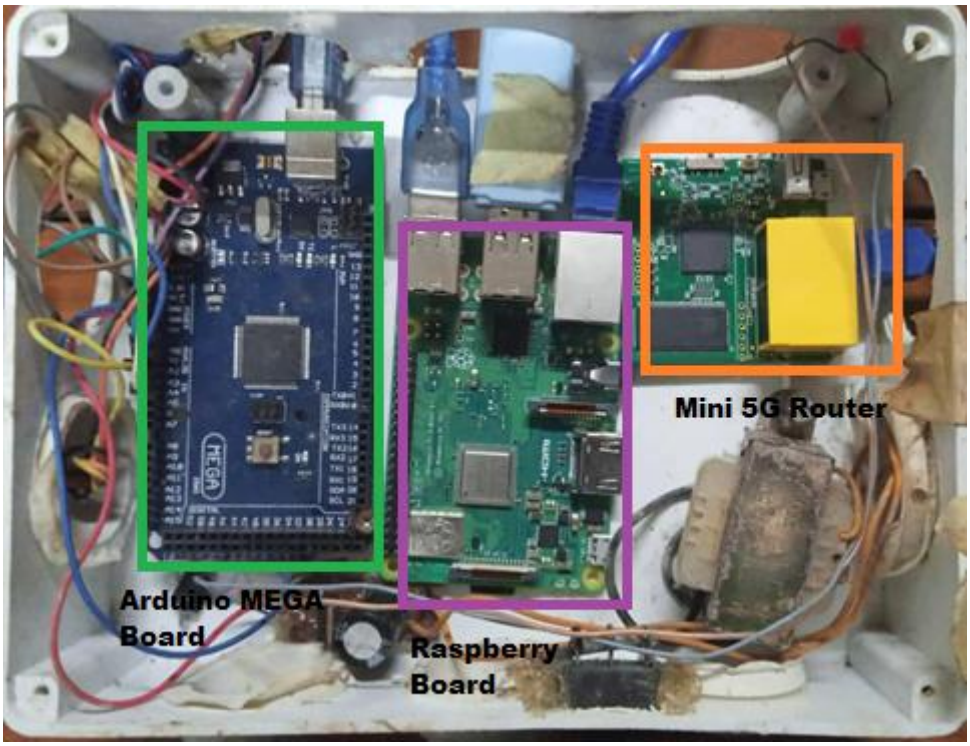

Figure 5. S.A.D. Management and Control Center

C. Flows control strategy

The S.A.D senses the flows generated and calculates the powers of energy supplied by the sources on the one hand, and the powers of energy required by the loads on the other hand.

These data are the inputs for the strategy of control and balancing of energy flows in the micro-grid.

The strategy is summarized as follows:

First, the powers generated by the sources and calculated are compared to the powers of the loads:

P_{solar} : PV pannel power

P_{wind} : Wind power

P_{DG} : Diesel Generator power

$P_{S\text{-}W}$: Solar and Wind total generated power

The voltage at the output of the battery bank is also taken into account.

V_{bat} : Battery Bank Voltage

$V_{bat\text{-}min}$: Minimum Battery Bank Voltage

$V_{bat\text{-}max}$: Maximum Battery Bank Voltage

In principle, the power of each load is taken into account the total power is then calculated.

P_{L1} : Load 1 power

P_{L2} : Load 2 power

P_{L3} : Load 3 power

P_L : Loads Total power

At the initial state, powers are computed as follows:

$$P_L = P_{L1} + P_{L2} + P_{L3}$$

$$P_{S\text{-}W} = P_{solar} + P_{wind}$$

For the control flow balancing:

If $P_L > P_{S\text{-}W}$ then Check V_{bat}

If $V_{bat} > V_{bat\text{-}min}$ then switch ON link between DC/DC converter and DC Bus

If still $P_L > P_{S\text{-}W}$ and $V_{bat} = V_{bat\text{-}min}$ then switch OFF link between DC/DC converter and DC Bus and switch ON DG

If $P_L \geq P_{DG}$ then switch OFF Load 3

If still $P_L \geq P_{DG}$ then switch OFF Load 2

If P_{solar} available and $V_{bat} \leq V_{bat\text{-}min}$ then swith ON link between DC/DC converter and Battery1

If still $V_{bat} \leq V_{bat\text{-}min}$ then check P_{wind}

If P_{wind} available and $V_{bat} \leq V_{bat\text{-}min}$ then swith ON link between AC/DC converter and Battery2

If $V_{bat} > V_{bat\text{-}min}$ and $V_{bat} \leq V_{bat\text{-}min}$ then swith OFF link between DC/DC converter and Battery1 and swith OFF link between AC/DC converter and Battery 2

If $P_L < P_{S\text{-}W}$ then switch OFF DG switch OFF Load 2 and OFF Load 3

This strategy is translated into an algorithm and implemented in a python script that runs on the raspberry board and arduino code on arduino board. The information is displayed on a monitoring interface accessible via the cloud.

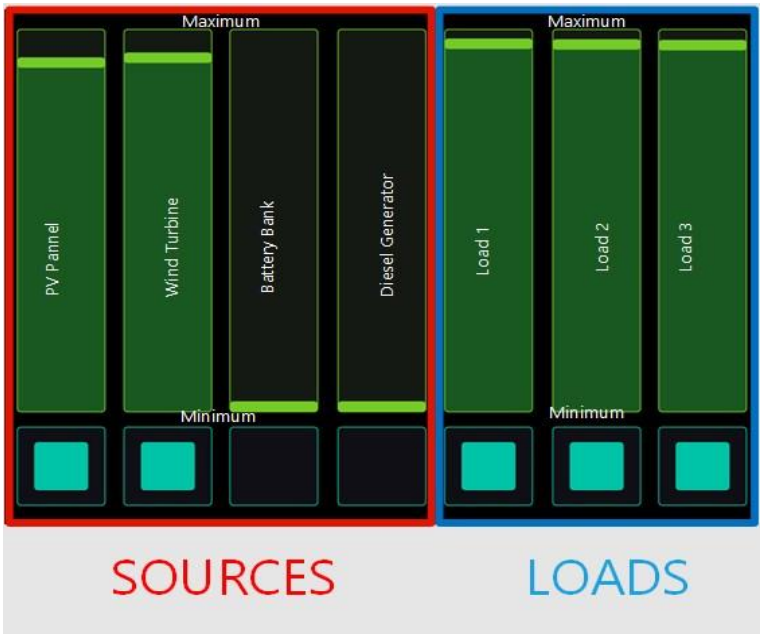

Figure 6. Monitoring Screen

On this screnn, P_{solar} and P_{wind} are at maximum of power. In this case, the generated power $P_{S\text{-}W}$ can easily supply all of loads (Load 1, Load 2 and Load 3). So, Battery bank and Diesel Generator are not used.

Simulations and results

Table 2. Sources informations

N°	Sources	Values (Voltage – Current – Power)
1	PV Pannel	137 V - 5 A - 685 W
2	Wind Turbine	126 V - 14.5 A -1827 W
3	Battery	124 V - 3 A
4	Diesel Generator	240 - 3.5 A - 840 W

A. Case 1: Wind Turbine OFF

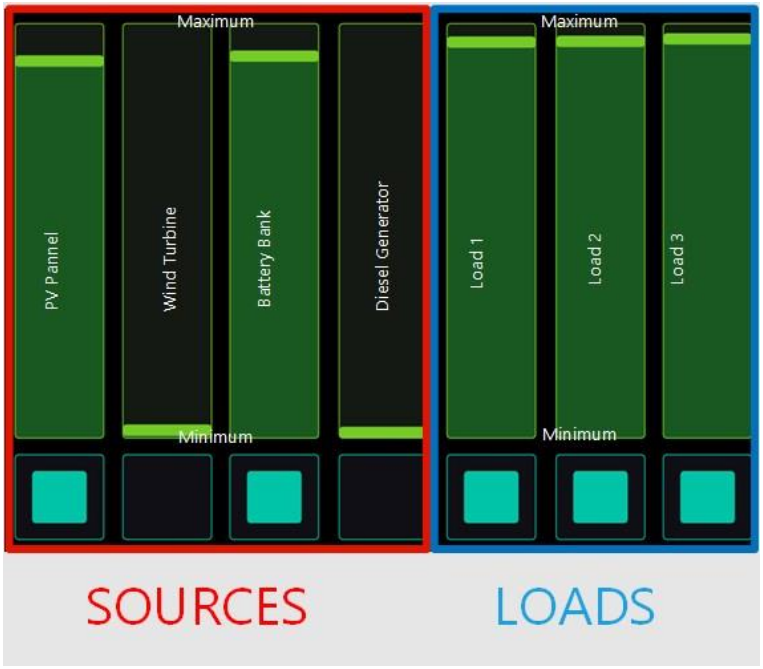

Figure 7. Monitoring Screen with PV panel Source and battery bank ON

The power generated is not sufficient to supply the loads, the battery bank is then used.

B. Case 2: PV pannel OFF

In this case, Wind turbine and PV panel are OFF and Battery voltage is not enough, so we swith ON Diesel Generator.

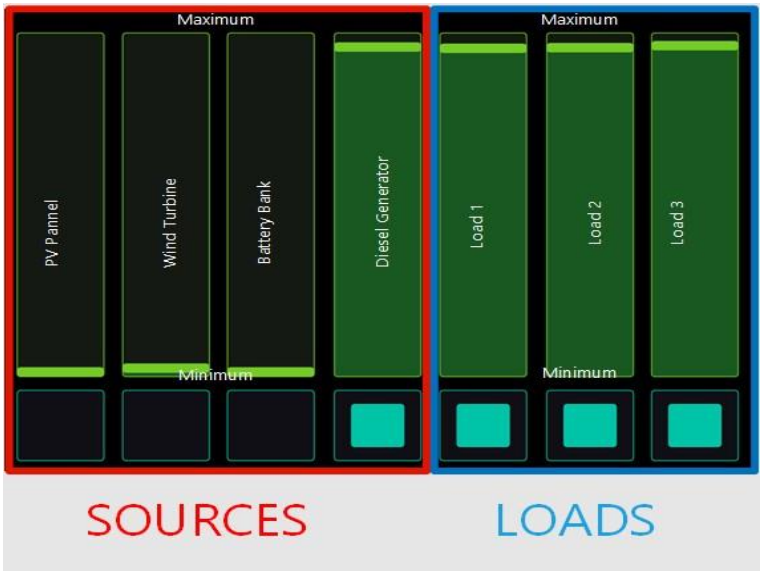

Figure 8. Monitoring Screen with DG ON and all loads ON

C. Case 3: Diesel Generator ON

With the DG being ON if the power generated does not cover the loads, we switch Load 3 OFF (Figure 9.) and if it is still not sufficient, we switch Load 2 off (Figure 10)

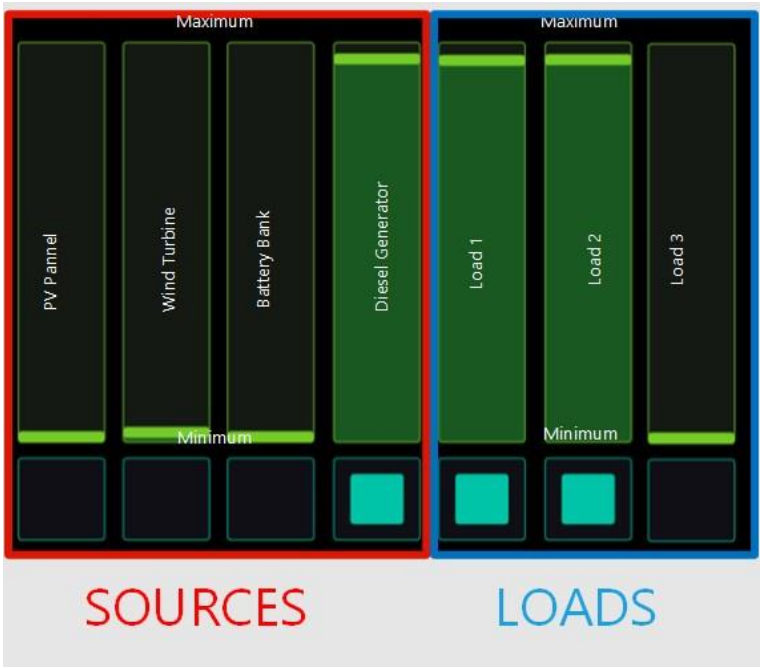

Figure 9. Monitoring Screen with DG ON and Load 3 OFF

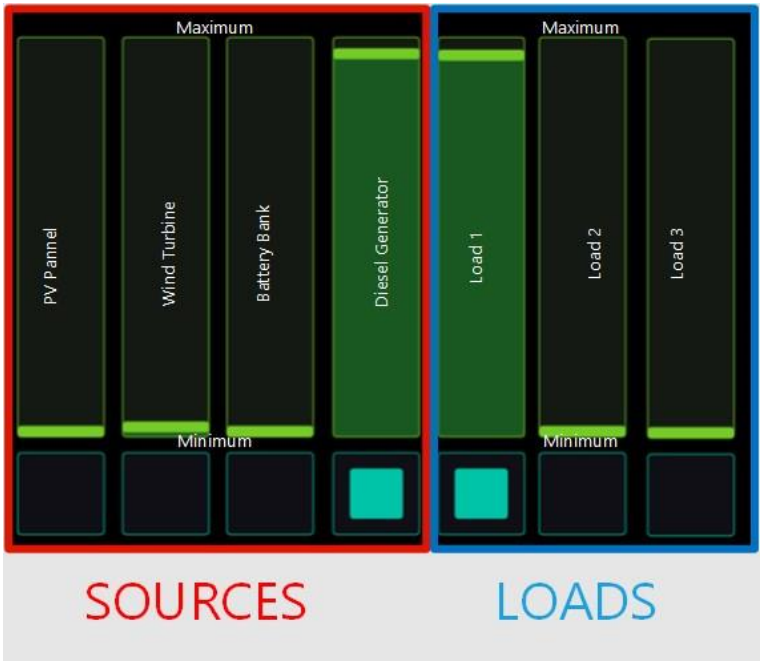

Figure 10. Monitoring Screen with DG ON and Load 2 and Load 3 OFF

Conclusion

In our work, we designed a microcontroller architecture interconnected to the renewable energy micro-grid.

A strategy is then implemented for the control and balancing of energy flows in the micro-grid.

The set of microcontroller-sensor-actuators (*S.A.D*) are deployed at strategic points in the micro-grid providing constantly data from power generated and consumed, equipment health and status.

The arduino and raspberry boards offer performance that collects data from the various equipment to which the sensors are connected. This data then travels to the cloud for analysis.

In the outlook, the power data will be analyzed and compared to the values collected over a given period, so as to detect the state of health of the equipment in order to take decisions in real time.

References

[1] Kpoda K, Ajavon A, Salami A, Kodjo K, Bedja K. Concise review of microgrid concepts and architecture. *Journal de la Recherche Scientifique de l’Université de Lomé*. 2018;4(4):613-631.

[2] Erbato TT, Hartkopf T. Smarter Micro Grid for energy solution to rural Ethiopia. *IEEE PES ISGT (Innovative Smart Grid Technologies)*. 2012;:1-7. https://doi.org/https://www.doi.org/10.1109/ISGT.2012.6175608

[3] Bekele G, Boneya G. Design of a Photovoltaic-Wind Hybrid Power Generation System for Ethiopian Remote Area. *Energy Procedia*. 2012;14:1760–1765. https://doi.org/https://doi.org/10.1016/j.egypro.2011.12.1164

[4] Dileep G. A survey on smart grid technologies and applications. *Renew. Energy*. 2020;. https://doi.org/https://doi.org/10.1016/j.renene.2019.08.092

[5] Ustun TS, Ozansoy C, Zayegh A. Recent developments in microgrids and example cases around the world - A review. *Energy Reviews*. 2011;. https://doi.org/https://doi.org/10.1016/j.rser.2011.07.033

[6] Patrao I, Figueres E, Garcerá G, González-Medina R. Microgrid architectures for low voltage distributed generation. *Renewable and Sustainable Energy Reviews*. 2015;. https://doi.org/https://doi.org/10.1016/j.rser.2014.11.054

[7] Hatziargyriou N. *Microgrids: Architectures and Control*. March 2014 Wiley-IEEE Press; 2014.

[8] Liu X, Wang P, Loh PC. A hybrid AC/DC microgrid and its coordination control. *IEEE Trans. Smart Grid*. 2011;. https://doi.org/https://www.doi.org/10.1109/TSG.2011.2116162

[9] Lo CH, Ansari N. Decentralized controls and communications for autonomous distribution networks in smart grid. *IEEE Transactions on Smart Grid*. 2013;4(1):66-77. https://doi.org/https://www.doi.org/10.1109/TSG.2012.2228282

[10] Das S, Akella AK. Power flow control of PV-wind-battery Hybrid Renewable Energy Systems for stand-alone application. *International Journal of Renewable Energy Research*. 2018;8(1):36-43.

[11] Zhang L, Gari N, Hmurcik L. Energy management in a microgrid with distributed energy resources. *Energy Convers. Manag*. 2014;. https://doi.org/https://doi.org/10.1016/j.enconman.2013.10.065

[12] Assilevi KR, Ajavon AS, Adjallah KH. Design of a virtual private network of intelligent microcontrollers for distributed control of an autonomous microgrid of renewable energy harvesters. *To appear in the ICEASSM'2019 Proc., the 2nd Int. Conf. on Engineering, Applied Sciences and System Modeling (),*. 2019.

[13] Majumder R, Bag G, Kim K. Power Sharing and Control in Distributed Generation with wireless sensor networks. *IEEE Power and Energy Society General Meeting*. 2012;. https://doi.org/https://www.doi.org/10.1109/PESGM.2012.6344966

[14] Graditi G, Di Silvestre ML, Gallea R, Riva Sanseverino E. Heuristic-Based Shiftable Loads Optimal Management in Smart Micro-Grids. *IEEE Trans. Ind. Inf.*. 2015;11((1)):271–280. https://doi.org/https://www.doi.org/10.1109/TII.2014.2331000

[15] Amin , Bambang R, Rohman A, Dronkers K, Ortega R, Sasongko A. Energy Management of Fuel Cell/Battery/Supercapacitor Hybrid Power Sources Using Model Predictive Control. *IEEE Trans. Ind. Inf.*. 2014;10((4)):1992-2002. https://doi.org/https://www.doi.org/10.1109/TII.2014.2333873

[16] Zhang L, Li Y. Optimal Energy Management of Wind-Battery Hybrid Power System With TwoScale Dynamic Programming. *IEEE Trans. Sustainable Energy*. 2013;4((3)):765-773. https://doi.org/https://www.doi.org/10.1109/TSTE.2013.2246875

[17] Ashabani, S, Mohamed Y. General Interface for Power Management of Micro- Grids Using Nonlinear Cooperative Droop Control. *IEEE Trans. Power Systems*. 2013;28((3)):2929-294. https://doi.org/https://www.doi.org/10.1109/TPWRS.2013.2254729

[18] Byun J, Hong I, Park S. Intelligent cloud home energy management system using household appliance priority based scheduling based on prediction of renewable energy capability. *IEEE Trans. Consumer Electronics*. 2012;58((4)):1194- 1201. https://doi.org/https://www.doi.org/10.1109/TCE.2012.6414985

[19] Venkatraman K, Reddy BD, Selvan MP, Moorthi S, Kumaresan N, Gounden NA. Online condition monitoring and power management system for standalone micro-grid using FPGAs. *IET Generation, Transmission and Distribution*. 2016;10(15):3875-3884. https://doi.org/https://doi.org/10.1049/iet-gtd.2016.0445

[20] Madaci B, Chenni R, Kurt E, Hemsas KE. Design and control of a stand-alone hybrid power system. *International Journal of Hydrogen Energy*. 2016;41(29):12485-12496. https://doi.org/https://doi.org/10.1049/iet-gtd.2016.0445

[21] Javad Mirazimi S, Fathi M. Analysis of hybrid wind/fuel cell/battery/diesel energy system under Alaska condition. *ECTI-CON 2011 - 8th Electrical Engineering/ Electronics, Computer, Telecommunications and Information Technology (ECTI) Association of Thailand - Conference 2011*. 2011;:917-920. https://doi.org/10.1109/ECTICON.2011.5947990

[22] Jayalakshmi N, Gaonkar D, Nempu PB. Power Control of PV/Fuel Cell/Super capacitor Hybrid System for Stand-Alone Applications. *International Journal of Renewable Energy Research*. 2016;6(2):672-679.

[23] Malla S, Bhende C. Voltage control of stand-alone wind and solar energy system. *Electrical Power and Energy Systems*. 2014;56:361–373. https://doi.org/https://doi.org/10.1016/j.ijepes.2013.11.030

[24] Betha D, Satish M, Sahu S. Design and control of grid connected PV/wind hybrid system using 3 level VSC. *IEEE 7th international advance computing conference*.. https://doi.org/https://doi.org/10.1109/IACC.2017.0102

[25]

Hajizadeh A, Aliakbar Golkar M. Intelligent power management strategy of hybrid distributed generation system. *Int J Elec Power*. 2007;29:783–795. https://doi.org/https://doi.org/10.1016/j.ijepes.2007.06.025

[26] Elmouatamid A, NaitMalek Y, Bakhouya M, Ouladsine R, Elkamoun N, Zine-Dine K, Khaidar M. An energy management platform for micro-grid systems using Internet of Things and Big-data technologies. *Proceedings of the Institution of Mechanical Engineers. Part I: Journal of Systems and Control Engineering*. 2019;233(7):904-917. https://doi.org/https://www.doi.org/10.1177/0959651819856251

[27] Hangaragi G. Recent Integration of a PV-wind energy system with enhanced efficiency. *Indian J Sci Res*. 2015;11((1)):72–78.

[28] Assilevi K, Ajavon A, Adjallah K. Design of a virtual private network of intelligent microcontrollers for distributed control of an autonomous micro-grid of renewable energy harvesters. *in the ICEASSM’2019 Proc., the 2nd Int. Conf. on Engineering, Applied Sciences and System Modeling (), 2019*.

2nd German-West African Conference on Sustainable, Renewable Energy Systems SusRES – Kara 2021

Machine Learning

https://doi.org/10.52825/thwildauensp.v1i.25

Published: 15 June 2021

Short-Term Electricity Generation Forecasting Using Machine Learning Algorithms: A Case Study of the Benin Electricity Community (C.E.B)

Agbassou Guenoupkati[1], Adekunlé Akim Salami[1], Mawugno Koffi Kodjo[1], and Kossi Napo[2]

[1]Department of Electrical Engineering, Ecole Nationale Supérieure d'Ingénieurs (ENSI), University of Lome, P.O. Box 1515 Lome Togo.

[2]Solar Energy Laboratory; L.E.S; Faculty of Sciences, University of Lomé, P.O. Box: 1515, Lomé, Togo

Abstract. Time series forecasting in the energy sector is important to power utilities for decision making to ensure the sustainability and quality of electricity supply, and the stability of the power grid. Unfortunately, the presence of certain exogenous factors such as weather conditions, electricity price complicate the task using linear regression models that are becoming unsuitable. The search for a robust predictor would be an invaluable asset for electricity companies. To overcome this difficulty, Artificial Intelligence differs from these prediction methods through the Machine Learning algorithms which have been performing over the last decades in predicting time series on several levels. This work proposes the deployment of three univariate Machine Learning models: Support Vector Regression, Multi-Layer Perceptron, and the Long Short-Term Memory Recurrent Neural Network to predict the electricity production of Benin Electricity Community. In order to validate the performance of these different methods, against the Autoregressive Integrated Mobile Average and Multiple Regression model, performance metrics were used. Overall, the results show that the Machine Learning models outperform the linear regression methods. Consequently, Machine Learning methods offer a perspective for short-term electric power generation forecasting of Benin Electricity Community sources.

Keywords: Linear regression models, Short-term forecasting, Electric power generation, Machine Learning Algorithms

Introduction

Nowadays, with the liberalization and technological advances in the energy sector, several electric companies are in perpetual competition in the energy market to satisfy customer demand. In addition to this, the evolution of demand has huge uncertainties and follows stochastic processes due to several complex factors such as the time, weather, seasonality, economic activity, days, preferential tariffs, occasional events, etc. which are all non-linear. At any given time, the energy supply must equal demand. unfortunately, the amount of electricity generated and the consumption of electricity should be balanced because there is no developed system that can store the electricity that should be generated in case of sudden demand.

Unbalanced demands for electricity generation lead to economic losses and user dissatisfaction. It is therefore important for electricity providers to maintain this balance. Overestimating future load can lead to unnecessary waste of resources, which in turn can lead to additional cost in capital expenditures. However, underestimation of future demand can also result in certain malfunctions or failures that may influence the long-term stability of the power system [1]. In this context, a robust forecasting tool remains essential for decision-

making on planning generation sources and improving the national economy. The electricity produced at each point in time is equal to the sum of demand and line losses. However, forecasting errors can, in fact, cause significant operational costs [2]. According to Hobbs et al. [3], a reduction in the average forecast error of 1% can save thousands or even millions of dollars in a power generation unit. Depending on the planning horizon, the different types of forecasts can be classified into four categories: ultra-short-term (less than 1 hour), very short-term (1 to 1 day, or 1 week), medium-term (1 week to 1 year) and long-term (1 year to 10 years).

Forecasting techniques can be classified into two groups, namely statistical models and artificial intelligence (AI) models. Traditional statistical models include regression analysis, moving average, exponential smoothing, stochastic time series models, etc. Machine learning, data mining, artificial neural networks, genetic algorithms, fuzzy time series and expert systems are based on AI techniques. Neural network algorithms are the most popular models for nonlinear time series problems compared to methods that have limitations when the aforementioned exogenous variables that influence power generation are considered. Several works have also focused on the development of ensemble methods in machine learning and hybrid models to improve the accuracy of electricity forecasting. Moreover, many recent studies have been conducted on load prediction using different deep learning techniques [4]. Deep Learning uses artificial neural networks that are inspired by the functioning of the human brain. These networks are composed of a multitude of hidden layers of neurons, each receiving and interpreting information from the previous layer.

The objective of this work is to develop Machine Learning models Support Vector Regression, Multi-Layer Perceptron, and the Long Short-Term Memory Recurrent Neural Network that have a strong generalization capability to predict the electric power production of the Electricity Community of Benin in order to minimize the Mean Absolute Percentage Error (MAPE) and improve the Coefficient of Determination (R^2) and other metrics are used as performance indicators. The CEB is an international organization co-owned by the governments of Benin and Togo. The contributions of this work are declined into five (05) points presented as follows:

- to develop an efficient one-step-ahead forecasting system for electricity generation companies and industries (CEB) for reducing the generating and operating cost;
- to investigate the application of appropriate techniques and tools of forecasting on electricity for Benin and Togo with minimum forecasting error;
- to investigate the application of the generated results as a guideline for the better performance of different Machine Learning models of Communauté Électrique du Bénin;
- to show the power and prospects of Machine Learning algorithms;
- identify the key parameters that influence the electricity generated by the electricity generation companies and industries (CEB).

Modeling

Suppose we have a training data set D containing T pairs of vector x and scalar y given by Eq. (1). Where y_t is a time series and x_t is a vector of dimension d $x_t = \left[x_1,...,x_d\right]^T$. All input vectors are often combined into a matrix X, and the output values into the output vector Y.

$$D = \left\{\left(x_t, y_t\right) \mid t = 1,...,T\right\} \tag{1}$$

The general model of a time series is given by Eq. (2):

$$y_t = f\left(x_t;\theta\right) + \varepsilon_t \tag{2}$$

Where f is a function that corresponds to the input, x_t the observation at time t, θ the parameter vector, ε_t is a random error term of zero mean that is assumed to have a Gaussian distribution unless otherwise specified by Eq. (3).

$$\varepsilon_t \sim \mathcal{N}(0, \sigma_N^2) \tag{3}$$

The forecast one at horizon h is done by evaluating the function f at the test point x_{T+h}.

$$y_{T+h} = f\left(x_{T+h}, \theta\right) \tag{4}$$

Where θ is the vector of parameters from the training on the training data set D [5]. With this general model, the following section offers a global view of all the prediction models developed in this study.

Multiple linear regression model

Multiple linear regression (MLR), also known simply as multiple regression, is a statistical technique that uses multiple explanatory variables to predict the outcome of a response variable. The objective of multiple linear regression (MLR) is to model the linear relationship between the explanatory (independent) variables and the response (dependent) variable. In case of multidimensional analysis. the MLR model is expressed by Eq. (5).

$$y = \beta_0 + \beta_1 \cdot x_1 + ... + \beta_n \cdot x_n + \varepsilon \tag{5}$$

Where y is the dependent variable, the x_i are the independent variable, the β_i are the parameters, and the ε are the error.

ARIMA model

There are three distinct integers (p, d, q) used to parameterize the ARIMA models. Hence the contracted notation ARIMA (p, d, q). Together, these three parameters account for seasonality, trend and noise in the data sets. ARIMA models are applied in some cases where the data show evidence of non-stationarity, where an initial differentiation step can be applied one or more times to eliminate non-stationarity [6]-[8]. The autoregressive part of the model (p) allows the effect of past values to be incorporated into the model. The integrated part of the model (d) includes the model terms that incorporate the amount of differentiation to be applied to the time series. The moving average part of the model (q). This allows us to define the error of our model as a linear combination of the error values observed at previous times in the past. An ARIMA (p, d, q) model using the lag polynomial L is expressed by Eq. (6).

$$\left(1-\sum_{i=1}^{p}\varphi_i L^i\right)(1-L)^d = \left(1+\sum_{j=1}^{q}\theta_j L^j\right)\varepsilon_t \tag{6}$$

Where L^i is the lag operator, the φ_i are the parameters of the autoregressive part of the model, the θ_j are the parameters of the moving average part and the ε_t are error terms.

Model selection can be performed based on the values of specific criteria such as the standard Akaike information criteria (AIC) [9]. The Akaike information criterion is written by Eq. (7).

$$AIC = 2k - 2\ln\left(L\right) \tag{7}$$

Where k is the number of parameters to be estimated for the model and L is the maximum of the likelihood function (a function of the parameters of a statistical model calculated from observed data) of the model. If we consider a set of candidate models, the model chosen is the one with the lowest AIC value. This criterion is therefore based on a trade-off between

the goodness of fit and the complexity of the model. We solved this problem by programmatically selecting the optimal parameter values for our ARIMA (p, d, q) time series model. We will use a "grid search" to iteratively explore different parameter combinations. Once we have explored the entire parameter landscape, our optimal set of parameters will be the one that gives the best performance for our criteria of interest. This process is called grid search (or hyper parameter optimization) [10] for model selection. Let us start by generating the different parameter combinations we want to evaluate. When evaluating and comparing statistical models with different parameters, each can be compared based on its fit to the data or its ability to accurately predict future data points. We will use the AIC (Akaike Information Criterion) value, which is returned with the ARIMA models. AIC is used to determine how well a model fits the data while taking into account the overall complexity of the model. A model that fits the data very well while using many features will be assigned a higher AIC score than a model that uses fewer features to achieve the same fit. Therefore, we are interested in finding the model that gives the lowest AIC value.

Multi-Layer Perceptron model (MLP)

Artificial neural networks are one of the approaches to artificial intelligence that are being developed through the methods by which humans are still trying to imitate nature and reproduce their own modes of reasoning and behavior. A neuron is essentially an integrator that performs a weighted sum of its inputs. The results of this sum are then transformed by a transfer function f which produces the output y of the neuron. Following the notations presented in the previous section, the n inputs of the neuron correspond to the vector X , while represents W the vector of weights of the neuron. The output s of the integrator is given by Eq. (8).

$$\mathrm{O}(\mathrm{t}) = \mathrm{W}^{\mathrm{T}} \cdot \mathrm{X}(\mathrm{t}) \pm \mathrm{b} \tag{8}$$

This output corresponds to a weighted sum of the weights and inputs plus what is called the bias b of the neuron. The result s of the weighted sum is called the activation level of the neuron. The bias b is also called the activation threshold of the neuron. When the activation level reaches or exceeds the threshold b, then the argument of becomes positive (or zero). Otherwise, it is negative. We will assume that all neurons are synchronous, i.e. that at each time t, they will simultaneously compute their weighted sum and produce an output given by Eq. (9).

$$\mathrm{y}(\mathrm{t}) = \mathrm{f}\left(\mathrm{O}(\mathrm{t})\right) = \mathrm{f}\left(\mathrm{W}^{\mathrm{T}} \cdot \mathrm{X}(\mathrm{t}) \pm \mathrm{b}\right) \tag{9}$$

The activation function f plays a very important role in the behavior of the neuron. It returns a value representative of the activation of the neuron, this function has as parameter the weighted sum of the inputs and the activation threshold. The nature of this function differs according to the network. There are various types of activation function presented in the literature. The ReLU (Linear Rectification Unit) function is a generalization function that solves the saturation problem of the Sigmoid and Hyperbolic Tangent functions. It is the most widely used function in deep network learning.

$$\mathrm{ReLu} = \begin{cases} \mathrm{y}(\mathrm{t}) = 0 \quad \mathrm{si} \quad \mathrm{O}(\mathrm{t}) < 0 \\ \\ \mathrm{y}(\mathrm{t}) = 1 \quad \mathrm{si} \quad \mathrm{O}(\mathrm{t}) \geq 0 \end{cases} \tag{10}$$

One of the most common algorithms used in this study is backpropagation. This algorithm changes the weights of a network whose architecture is fixed by the operator, each time an example $\mathrm{y_i} = \mathrm{f}(\mathrm{x_i})$ is presented. This change is done in such a way as to minimize the error between the desired output and the response of the network to an input $\mathrm{x_i}$. At each iteration

the input signal propagates in the network in the input-output direction, an output is thus obtained, the error between this output and the desired output is calculated and then by backpropagation intermediate errors, corresponding to the hidden layer are thus calculated and allow the adjustment of the weights $w_{ij}(t)$ of the hidden layer. The gradient backpropagation algorithm thus has 2 phases:

- propagation: at each step, an example is presented to the network as input. This input is propagated to the output layer.
- correction: For sure, the network will not provide exactly what was expected. We therefore calculate an error (usually the mean square sum of the errors for all the output neurons) which we back-propagate in the network. This process is interrupted as soon as the global error is estimated to be sufficient

Support Vector Regression (SVR)

Support Vector Regression (SVR) is an adaptation of Support Vector Machines (SVM) to the regression problem. SVMs and SVRs are a class of supervised learning algorithms, based on the same principles as neural networks. They are based on the search for the optimal hyperplane, which, when possible, correctly classifies or separates the data while being as far away as possible from all observations. The use of SVMs as much in classification optimization as in regression algorithms consists in determining the optimal Lagrange multipliers. The principle is therefore to find a classifier, or a discrimination function, whose generalization capacity is as large as possible. The model of the classifier is built from a training set de $\mathbb{N}$of examples labeled (x_i, y_i) with $x_i \in \mathbb{N}^p$ and $y_i \in \{-1; 1\}$ according to the class represents the dimension of the input vectors or the number of features in the input examples). The training allows, in the case where the examples are linearly separable, to build the decision function f also called separator hyperplane of the form defined by Eq. (11).

$$f(X) = \text{sign}(\langle W, X \rangle + b) \tag{11}$$

With $W \in \mathbb{N}^p$ and b the parameters to determine in which part of the hyperplane. The figure shows the linearly separable case, where the margin Δ is defined by the minimum distance between the two points of the different classes. The principle of SVMs is taken up and adapted by SVRs to model a regression problem. The goal is to approximate a set of data (x_i, y_i) by a function f in the form given by Eq. (12).

$$f(X) = \langle W, X \rangle + b \tag{12}$$

such that the error is expressed by Eq. (11).

$$|f(x_i) - y_i| \leq \gamma \tag{13}$$

With $i \in \{1,..., N\}$. The idea is to minimize the term w while being under the constraint of not exceeding an error rate γ. If we consider the minimization of $\|w\|^2$ we obtain the quadratic optimization problem. This description of the problem therefore assumes that a linear function f exists that approaches all examples with precision γ. In practice, this is not always the case. In the presence of outliers, it is also more important to allow some errors. In this case, the concept of flexible margin is used. It consists in introducing slack variables ξ_i and ξ_i^* to make the constraints of the optimization problem feasible in Eq. (14).

$$\begin{cases} \min : \frac{1}{2}\|w\|^2 + C\sum_{i=1}^{n}\left(\xi_i + \xi_i^*\right) \\ \text{subject to} \begin{cases} y_i - w^T x_i - b \le \varepsilon + \xi_i \\ w^T x_i + b - y_i \le \varepsilon + \xi_i^* \end{cases} \end{cases} \tag{14}$$

ξ_i and ξ_i^* representing respectively the positive and negative errors. The constant $C > 0$ is a hyper parameter to adjust the tradeoff between the allowed error and the flatness of the function f . Using the dual formulation and the Lagrange equation, the resulting function can be written by :

$$f(x) = \sum_{i=1}^{n}\left(\alpha_i + \alpha_i^*\right)\cdot K(x, x_i) + b \tag{15}$$

with α_i and α_i^* the Lagrange multipliers from the dual formulation. $K(\ )$ is a kernel function that induces a nonlinear transformation of the data to an intermediate space of higher dimension. Some commonly used kernel functions in the literature are Linear function, polynomial function, Radial basis function (RBF) and Sigmoid. This paper used the Gaussian radial basis function (RBF) as the kernel function, because RBF is the most effective for the nonlinear regression problems. The RBF can be expressed by Eq. (16).

$$K(x, x_i) = \exp\left(-\frac{\|x - x_i\|^2}{2\sigma^2}\right) \tag{16}$$

Where σ is the standard deviation. The selection of optimal hyperparameters was done by cross-validation.

Long Short-Term Memory Recurrent Neural Network (LSTM)

Long Short-Term Memory (LSTM) is an artificial recurrent neural network (RNN) architecture [1] used in the field of deep learning. Unlike neural networks. However, the hidden units are replaced by memory blocks. An LSTM unit consists of a cell (c), an input gate (i) , an output gate (o) and a forget gate (f). The output vector (h) represents the state of the LSTM hidden layers. The cell remembers values over arbitrary time intervals and the three gates regulate the flow of information into and out of the cell. The module has three gate activation functions σ_g (sigmoid function), σ_c (hyperbolic tangent), and σ_h (hyperbolic tangent) which is sometimes $\sigma_h(x) = x$. The operation performed by the LSTM layers is given by Eqs. (17).

$$f_t = \sigma_g\left(W_f \cdot x_t + U_f \cdot c_{t-1} + b_f\right) \tag{17}$$

$$i_t = \sigma_g\left(W_i \cdot x_t + U_i \cdot c_{t-1} + b_i\right) \tag{18}$$

$$o_t = \sigma_g\left(W_o \cdot x_t + U_o \cdot c_{t-1} + b_o\right) \tag{19}$$

$$c_t = f_t \odot c_{t-1} + i_t \odot \sigma_c(W_c \cdot x_t + b_c) \tag{20}$$

$$h_t = o_t \odot \sigma_h(c_t) \tag{21}$$

During model fitting, the mean square error is used as the loss function to optimize the LSTM model parameters and Adam is used as the optimization algorithm for the loss function.

Methodology

Historical power generation data is provided by CEB recorded every 1 hour collected from 1st January 2015 to 31st December 2019. This time series requires pre-processing, especially because there are many missing values and outliers in the original raw data. The presence of these outliers alters the accuracy of the predictions which could be lower. In this project, a filtering technique is used. Then the system is loaded with a dataset composed of 24 input variables using slide windows technique. The data is normalized using the min-max scaling method and then divided into training (1st January 2015 to 30th November 2019) and test sets (1st to 31st December 2019). Then, the SVR, MLP, LSTM, ARIMA and MLR models are built and trained. After that, the models are used to forecasting.

Result and Discussion

The objective of this project is to minimize the mean absolute percentage error (MAPE) which is used as a measure of accuracy. The results are presented in Table 1. According to the table, errors of ARIMA is the highest. Overall, the Machine Learning model performs better than the linear models. The ANN model can predict the electric power generation the minimum MAPE and maximum R^2. After examining the results, we realize that the best model is the Artificial Neutral Network (MLPRegressor) and it has the besSeveral statistical indicators including Mean Absolute Percentage Error (MAPE), Root Mean Square Error (RMSE), Normalized RMSE (NRMSE) and Correlation Coefficient (R^2) as well as other statistical tools can be used to provide a proper comparative evaluation of the forecasting models. Table 1 presents the different metrics used to test diffrent model permormance for the 1-hour-ahead forecast.

Table 1. Model performance evaluating using RMSE, nRMSE, MAPE and R^2

Model	RMSE	nRMSE	MAPE	R^2 value	Rank
ARIMA	17.9477	0.064058	14.3430	0.7629	5th
MLR	17.14236	0.061237	4.063912	0.7835406	4th
SVR**	16.6050	0.05931727	3.83646	0.796898	2nd
ANN*	16.2753	0.05825749	3.83245	0.80427	1st
LSTM	18.4812	0.06595	4.26894	0.749155	3rd

Conclusion

The objective of this project is to develop a system for forecasting the electricity balance between supply and demand using the Machine Learning technique and to evaluate its performance by comparing it to other linear regression techniques. Time series forecasting in the energy sector is important for utilities for decision making to ensure the sustainability and quality of electricity supply, and the stability of the power system. Unfortunately, the presence of some exogenous factors such as weather conditions, electricity prices, etc.… complicates the task with the use of linear regression models that become inadequate. Finding a robust predictor would be a valuable asset for utilities. To overcome this difficulty, Artificial Intelligence is distinguished from these prediction methods by Machine Learning algorithms that have been successful in the last decades in predicting multilevel time series. This work proposes the deployment of three univariate machine learning models: Support Vector Regression, Multilayer Perceptron, and Long Term Memory Recurrent Neural Network to predict the electricity production of the Benin Electricity Community. In order to validate the performance of these different methods, compared to the autoregressive integrated moving average model and the multiple linear regression model. Performance metrics were used. Overall, the results show that the machine learning models except LSTM perform better than

the linear regression methods. Therefore, machine learning methods offer a perspective for short-term forecasting of electric power generation.

Future Work

- Try on the new input structure more.
- Train the model using more datasets
- Apply another deep learning technique
- Adopted the K-Fold Cross-validation methodology when selecting the best parameter for a single model
- Extend the results of this paper
- Elaborate the work methodology
- Use Google Colab or Amazone Web Service for the study.

References

[1] Zjavka L, Snášel V. Short-term power load forecasting with ordinary differential equation substitutions of polynomial networks. Electric Power Systems Research. 2016 08;137:113-123. https://doi.org/10.1016/j.epsr.2016.04.003

[2] Haida T, Muto S. Regression based peak load forecasting using a transformation technique. IEEE Transactions on Power Systems. 1994;9(4):1788-1794. https://doi.org/10.1109/59.331433

[3] Hobbs B, Jitprapaikulsarn S, Konda S, Chankong V, Loparo K, Maratukulam D. Analysis of the value for unit commitment of improved load forecasts. IEEE Transactions on Power Systems. 1999;14(4):1342-1348. https://doi.org/10.1109/59.801894

[4] Hippert H, Pedreira C, Souza R. Neural networks for short-term load forecasting: a review and evaluation. IEEE Transactions on Power Systems. 2001;16(1):44-55. https://doi.org/10.1109/59.910780

[5] Swastanto B. Gaussian Process Regression for Long-Term Time Series Forecasting. Faculty of Electrical Engineering, Mathematics, and Computer Science, Delft University of Technology; 2016.

[6] Singh S, Parmar KS, Kumar J, Makkhan SJS. Development of new hybrid model of discrete wavelet decomposition and autoregressive integrated moving average (ARIMA) models in application to one month forecast the casualties cases of COVID-19. Chaos, Solitons & Fractals. 2020 06;135:109866. https://doi.org/10.1016/j.chaos.2020.109866

[7] Zhang L, Lin J, Qiu R, Hu X, Zhang H, Chen Q, Tan H, Lin D, Wang J. Trend analysis and forecast of PM2.5 in Fuzhou, China using the ARIMA model. Ecological Indicators. 2018 Dec;95:702-710. https://doi.org/10.1016/j.ecolind.2018.08.032

[8] Khan FM, Gupta R. ARIMA and NAR based prediction model for time series analysis of COVID-19 cases in India. Journal of Safety Science and Resilience. 2020 09;1(1):12-18. https://doi.org/10.1016/j.jnlssr.2020.06.007

[9] Ma T, Antoniou C, Toledo T. Hybrid machine learning algorithm and statistical time series model for network-wide traffic forecast. Transportation Research Part C: Emerging Technologies. 2020 02;111:352-372. https://doi.org/10.1016/j.trc.2019.12.022

[10] Mohamed H, Negm A, Mohamed Z, Oliver C. S. Assessment of artificial neural network for bathymetry estimation using high resolution satellite imagery in shallow lakes: case study el burullus lake. International Water Technology Journal. 2015 December;5:352-372.

2nd German-West African Conference on Sustainable, Renewable Energy Systems SusRES – Kara 2021

Machine Learning

https://doi.org/10.52825/thwildauensp.v1i.26

Published: 15 June 2021

Static and dynamic evaluation of wind potential in the Kara region of Togo using artificial neural networks

Arafat FOUSSENI[1], Mawugno Koffi KODJO[2], Assiongbon ADANLETE ADJANOH[1]

[1] University of Kara, Togo

[2] University of Lomé, Togo

Abstract. Togo's energy situation is characterized by a low rate of access to electricity (38.07 % in 2017). In the Kara region, there is certainly a wind potential whose study is necessary for the production of electricity. Thus, from the data recorded each day at intervals of one hour, we used Weibull distribution to evaluate the wind energy potential at 10m and then at 25m, 50m, 75m and 100m. However, the promotion of this source requires not only the knowledge of its potential but also the evolution of its quantity over time because in reality wind energy is confronted with the random nature of the wind. Thus, for the prediction of the wind potential in the region of Kara, we used artificial neural networks. The neural architecture used is a multilayer perceptron with a single neuron under the hidden layer whose activation function is a sigmoid function while the output layer uses a linear function. The prediction results obtained with an average squared error of 0.005 and a correlation of 0.96 show that the prediction results using this tool are acceptable and can be generalized under the same conditions on other sites. The evaluation of the wind potential in the region of Kara has enabled us to determine the amount of total energy available in the wind at different altitudes. Through the average values of wind speeds determined, we could make an optimal choice of wind turbine to convert this kinetic energy of the wind into electrical energy.

Keywords: Wind power, Weibull distribution, Artificial Neural Networks.

Introduction

Through improvement of technologies in recent years, wind power generation has reached a high level of technological maturity and industrial reliability [1]. However, the major problem with this energy is the high variability of its production due to the random nature of its source which is wind. The choice of wind turbines and the height of their mast therefore requires a prior determination of the wind potential. In this study, we will present the results and discuss the static assessment of wind potential in the Kara region after presenting the methodology and data used.

Methodology

Evaluating the wind potential of a site requires a rigorous scientific approach. This approach requires not only the meteorological data and the determination of the mathematical function used to approximate the histogram of wind speed frequencies.

Meteorological data collection

The Kara region is one of the five regions of Togo. It consists of seven prefectures: Assoli. Bassar, Binah, Dankpen, Doufelgou, Keran and Kozah. Wind characteristics must be known in order to assess the wind potential of a site. These characteristics are mainly wind speed and direction. To these two can be added ambient temperature, pressure, relative humidity.

Statical representation of the information

When wind data information is available, it can be represented in the form of a histogram. The histogram illustrates the variation in the relative frequency of wind speeds. If the wind speed intervals are decreasing, the limit of the histogram is a probability density function [2]. However, it is difficult to manipulate the data set for a wind speed frequency distribution. For theoretical considerations, it is more appropriate to approach the wind speed frequency histogram by a continuous mathematical function than by a discrete table of values. According to the literature, several models are available to model the wind speed distribution [3]. A Gaussian or Rayleigh distribution function is not always adequate in the case of wind speeds [4]. According to GUMBEL J.E [5], a better solution is to use the Weibull distribution [6]. Through In TROEN et al [7], the Weibull distribution is currently a standard for the representation of wind site climatology. The advantage of this representation is that the mean annual production of a given wind turbine can be quickly determined by knowing the Weibull characteristic of the site and the power curve of the wind turbine. as detailed in [7], [8].

Weibull distribution

The Weibull function can be described by two or three parameters. Due to its advantages highlighted by JUSTUS [9], [10] and to wind industry standards, we use the two-parameter Weibull function as described by TROEN et al [7]. Its mathematical expression is given by equation (1):

$$f(v) = \left(\frac{k}{A}\right)\left(\frac{v}{A}\right)^{k-1} \exp\left(\frac{v}{A}\right)^{k} \quad (1)$$

Where:

- $f(v)$ is the probability density and represents the frequency distribution of the velocities;
- A (m/s) is the Weibull scale parameter that provides information on the average wind speed characteristic of the site; it is the value of the speed for which the Weibull function admits a maximum;
- k (without unit) is the Weibull form factor. representative of the asymmetry of the function; it indicates the more or less pointed character of the distribution.

For k =1, we obtain an exponential law [4]. The Rayleigh distribution for k = 2 is only a special case of the Weibull distribution [12]. The approximation of a Gaussian distribution is obtained for k = 3.6.

Hybrid Weibull distribution

The Weibull hybrid distribution is used at sites where the frequency of calm winds is relatively high [9]. Indeed, this rather significant proportion of calm winds cannot be neglected, as the k factor is close to the value 1, thus representing an exponential distribution. Equation (2) gives us the expression of the Weibull hybrid distribution:

$$\mathrm{f(v)} = \begin{cases} \mathrm{F_0} \quad \text{pour} \quad \mathrm{v} < 1 \\ (1-\mathrm{F_0})\left(\frac{\mathrm{k}}{\mathrm{A}}\right)\left(\frac{\mathrm{v}}{\mathrm{A}}\right)^{\mathrm{k}-1} \exp\left(-\frac{\mathrm{v}}{\mathrm{A}}\right)^{\mathrm{k}} \text{ pour } \mathrm{v} \geq 1 \end{cases} \quad (2)$$

F_o represents the frequency of calm speeds. which is determined from wind data.

Available kinetic power

The available kinetic power in the wind is given by [2], [12], [13] through equation (3)

$$P_d = \frac{1}{2}\rho_a \, S \, v_m^3 \tag{3}$$

Where P_d is the available kinetic power in the wind, ρ_a is the air density. S is the area swept by the blades and v_m is the average wind speed upstream of the blades.

Recoverable power

It is impossible to transform all the kinetic power available in the wind into mechanical power by means of a wind turbine. That would have meant zero speed just behind the rotor. BETZ has shown [14-15] that there is an optimal wind speed behind the rotor so that there is maximum power extracted from the wind which then gives a maximum power coefficient C_p. The recoverable power is:

$$P_r = C_p \, P_d \tag{4}$$

$C_p = \frac{16}{27}$ for the maximum power coefficient according to Betz [14]. [15]. In practice, 0.35≤ C_p ≤0.45 according to A.W. Manyonge et al [16].

Vertical extrapolation

Wind speed can be extrapolated vertically by a logarithmic law [17].

$$v(z) = v_{10}\left(\frac{ln\left(\frac{z}{z_o}\right)}{ln\left(\frac{10}{z_o}\right)}\right) \tag{5}$$

where v(z) is the wind speed at altitude z. V_{10} is the wind speed at 10m. Z_o is the site roughness.

Wind speed forecasting techniques and extension to power forecasting

There are two main approaches to simulating the behaviour of the wind field at a site. These are the physical and statistical approaches. So-called "physical" models are based on considerations of the physics of the atmosphere and lead to a Numerical Weather Prediction (NWP). NWP models [18] (for an introduction to NWP models) are suitable for forecasts ranging from several hours to several days. The HIRLAM (Hight Resolution Local Area Modelling). [19] and the CFD (Computational Wind Dynamics) model are the main examples. When dealing with short forecast horizons (minutes to hours), the use of statistical methods is more advisable [20]. Models using these approaches are usually based on time series analysis. The simplest of these is the autoregressive (AR) model: an nth-order AR is a model in which the future value is obtained to within one noise (error) as a linear combination of the last n measured values. To model different weather series [21] such as monthly precipitation [22], annual flow [23] and many other applications [24]; their generalization ARMA (or ARIMA). [25-26] has been used. Kalman filter methods [27]. Markov chain tools [28] and wavelets [29] are also time series based approaches applied to wind speed data. However all approaches that directly describe the stochastic dynamics of the amplitude face problems related to the non-Gaussian nature of its statistics and the presence of seasonal effects [20]. Other more recent techniques, based on artificial intelligence have been considered in the context of wind resource forecasting. Black-box models would also allow non-linear processes to be modelled, unlike classical linear methods. Following the studies of Cadenas et al [30], who focused their comparison on the structure of the network, they concluded that a 2-layer network with 2 neurons on the input layer and 1 on the output layer is better. The squared error obtained for this architecture is indeed 0.16%. In our work. we used a two-layer perceptron and varied the number of neurons under the hidden layer. The activation function of the latter is sigmoid. At the output, the activation function is kept always linear.

Wind speed (v(t-1)), temperature (T(t-1)), pressure (P(t-1)), relative humidity (RH(t-1)) all at time t-1, velocity (v(t-2)) at time t-2 are the input variables of the model. The output is of course the wind speed (v(t)) at time t. The different configurations are presented in the table below.

Table 1. Presentation of the different configurations of the prediction models

Configurations	Input	Output
1	T(t-1). P(t-1), RH(t-1), v(t-1)	V(t)
2	T(t-2), P(t-2), RH(t-2), v(t-2)	V(t)
3	T(t-1), P(t-1), RH(t-1), v(t-2)	V(t)

Results. analysis and discussion

Choosing which Weibull distribution to use

The analysis of the wind frequency histogram (Figure 1) reveals that cool and moderate winds are quite frequent (98.70%). Calm winds, on the other hand are less frequent (1.30%). It is therefore more practical to use the classical Weibull distribution to assess the wind potential in the Kara region as it would better reflect the wind statistics in the Kara region.

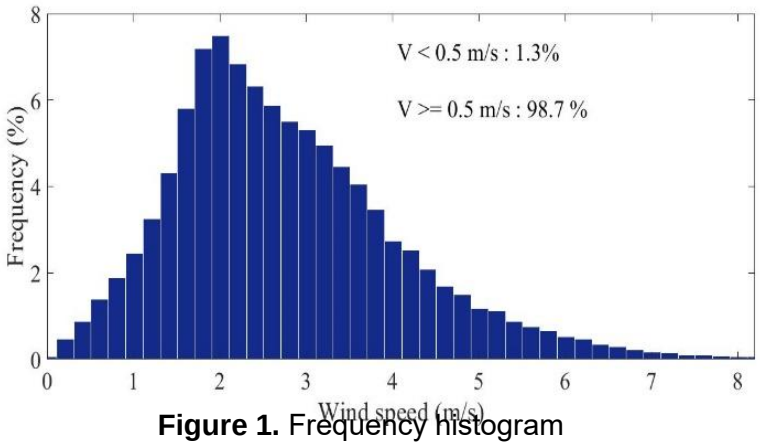

Figure 1. Frequency histogram

Frequency distribution of wind speeds

Figure 2 is a frequency distribution. As the velocity classes are sufficiently narrow, we had represented in red through equation 1 the Weibull probability density function which is a probability law in the form of an integral. The coefficients 3.15 and 2.16 are respectively the scale parameter and the Weibull form factor. The median of 2.58m/s reflects that the wind thus blows at less than 2.58m/s half the speed of the wind of the time and at more than 2.58m/s during the other half.

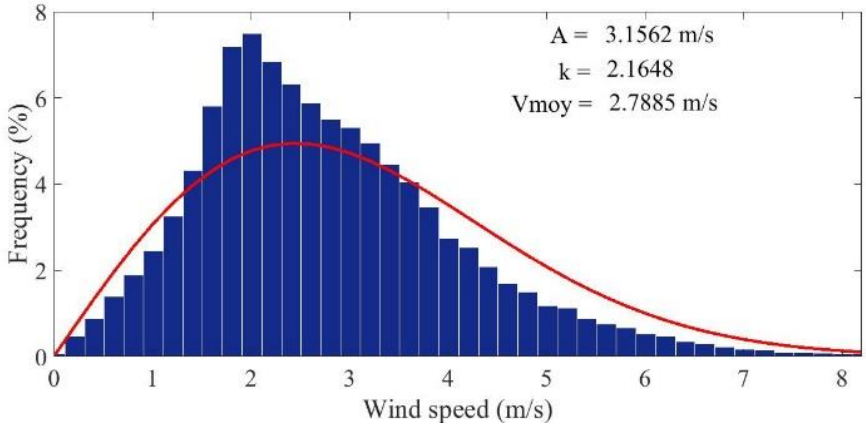

Figure 2. Weibul probability density

Static evaluation of wind potential using the conventional Weibull distribution at 10metres

The curve in Figure 3 represents the variation of the total energy available in the wind and the maximum recoverable energy at 10m as a function of wind speed. These curves were obtained using equations (3) and (4).

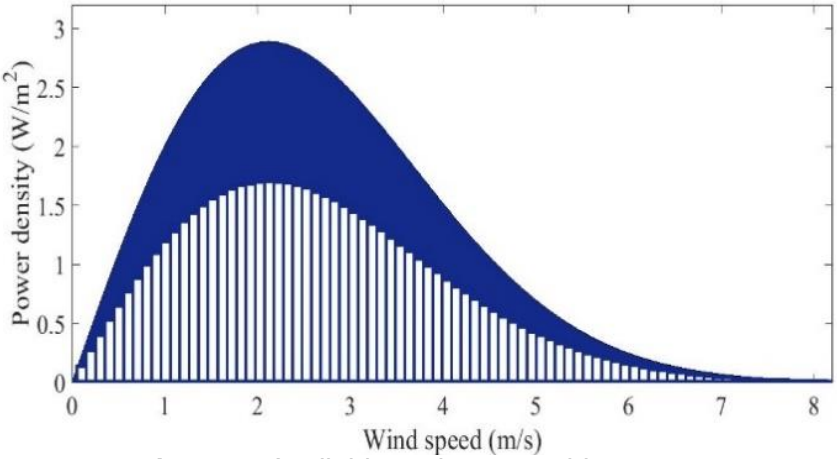

Figure 3. Available and recoverable power

On Figure 3. two main parts can be distinguished. Firstly, the extremities for which the power is almost zero. In reality, for speeds below 1m/s this is due not only to the scarcity of calm winds but also to the fact that their energy content is very low; on the other hand, for speeds above 5m/s the cause is solely due to the low frequency of strong winds. Secondly, for moderate winds with speeds between 1m/s and 5m/s, the value of the total power available is not negligible. However, at an altitude of 10m, the total energy available in the wind is low. Moreover, at this height, the wind is often slowed down by obstacles. In order to make optimal use of wind energy in the Kara region, we therefore need to get more wind at higher altitudes.

Extrapolation of results to different altitudes

Using equation (5). the wind speed data were then extrapolated to other heights.

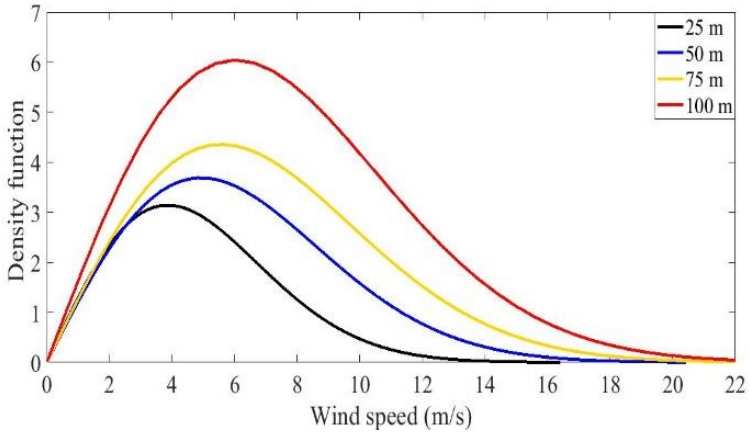

Figure 4. Wind speed distribution function at different altitudes

Analysis of Figure 4 reveals that as one moves upwards. the amplitude of the density curve increases and is shifted to the right. This phenomenon is due to an increase in the number of high wind speeds and a decrease in the number of low wind speeds resulting in an increase in the average speed. Table 2 summarizes the different average values of speed, total available and recoverable power, scaling parameter and form factor at different altitudes.

Table 2. Average values of speeds and energies at different altitudes

Height (m)	Average speed (m/s)	Total power (W/m²)	Recoverable power (W/m²)	Scale parameter A (m/s)	Form factor k
10	2.79	27.67	15.21	3.16	2.16
25	4.2	86.64	51.34	4.74	2.18
50	5.25	170.09	100.79	5.94	2.18
75	5.87	237.56	140.78	6.63	2.18
100	6.3	294.92	174.77	7.13	2.18

Dynamic evaluation of wind speed

Features of the best models in each configuration

The characteristics of the best model in each configuration are shown in the table below. For these 3 configurations. we note that the best results are obtained with a neuron under the hidden layer.

Table 3. Characteristics of the best architecture

Configurations	Number of neurons	MSE	RMSE	MAE	R^2	ρ
1	1	0.00538	0.07341	0.02630	0.90877	0.95851
2	1	0.01036	0.10179	0.04474	0.75627	0.88440

Configurations	Number of neurons	MSE	RMSE	MAE	R^2	ρ
3	1	0.01064	0.10317	0.04506	0.7489	0.88123

Prediction of available and recoverable energy with the chosen model

The best architecture is the configuration 1 with one neuron under the hidden layer. The input variables of the neural network model are wind speed (v(t-1)), temperature (T(t-1)), pressure (P(t-1)), relative humidity (RH(t-1)) all at time t-1. The output of the model is of course the wind speed (v(t)) at time t. The prediction results are shown in the table below in which we can distinguish the square error (MSE) and its square root (RMSE), the absolute error (MAE), the coefficient of determination (R^2) and the correlation coefficient (ρ). The figures below show the superimposed curves of target (red curve) and predicted (blue curve) energies at 10m, 25m, 50m, 75m and 100m respectively as a function of wind speed.

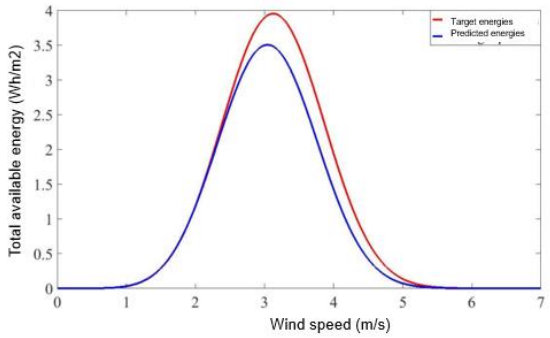

Figure 5. Target and predicted energy curves at 10m

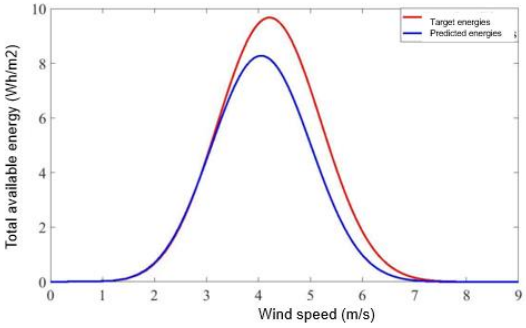

Figure 6. Target and predicted energy curves at 25m

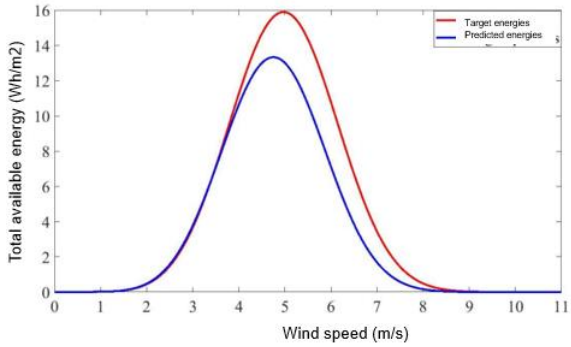

Figure 7. Target and predicted energy curves at 50m

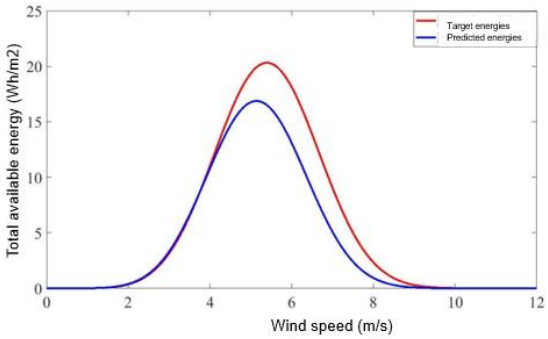

Figure 8. Target and predicted energy curves at 75m

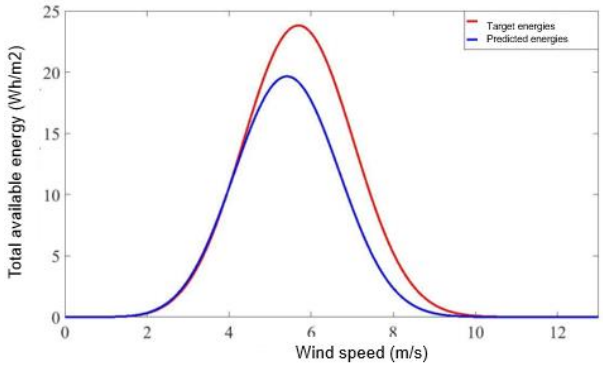

Figure 9. Target and predicted energy curves at 10m

The observation of the above figures reveals that each curve obtained by our neural network architecture model coincides with the energy curve available on the site. Nevertheless. a small shift between these curves is observed from 2.5m/s, 3.5m/s, 4m/s, 4.2m/s and 4.5m/s respectively at altitudes of 10m, 25m, 50m, 75m and 100m respectively. The maximum deviation is obtained when the curves reach their maximum and begins to narrow beyond the nominal speed until a new coincidence is reached when the energy is cancelled out. The results obtained for the estimation of available and recoverable energy at 10m. 25m. 50m. 75m and 100m are given in Table below.

Table 4. Predicted energies at different altitudes

	Available energy (Wh/m²)		**Recoverable energy (Wh/m²)**	
Height (m	**Target**	**Prediction**	**Target**	**Prediction**
10m	29.4362	27.9153	17.4437	16.5424
25m	99.3230	94.2226	58.8581	55.8415
50m	194.9986	185.0032	115.5547	109.6315
75m	272.3616	258.3854	161.9994	153.1172
100m	338.1195	320.7831	200.3671	190.0936

Pitch orientation

The compass rose allows us to better appreciate the dominant wind directions. Analysis of Figure 10 reveals that there are two dominant wind directions, northeast and southwest. However, southwest, and more precisely a southward tilt of a geometric angle varying between the first and second sector (between 0° and 60° to the South) remains the best option for the orientation of the pales as 32% of the winds blow in this direction. This figure also supports the thesis of KODJO et al. that winds tend to generally have one or two dominant directions for which most of the energy is produced [31].

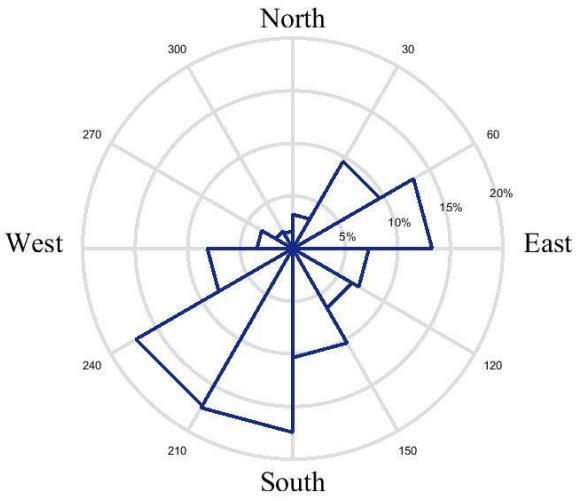

Figure 10. Compass rose

Conclusion

Prior knowledge of the wind characteristics of a site allows a better appreciation of its wind potential. In the Kara region, 20 years of data at an altitude of 10 m from the meteorological database of the website 'www.soda-pro.com/web-service/meteo-data/merra' were used. The wind speed data obey the Weibull distribution law with a scale parameter A = 3.16m/s and a form factor k = 2.18. The study shows that the mean wind speed varies from 2.79m/s at 10m to 6.3m/s at 100m. The average energy content of these speeds is higher at an altitude of 100m (294.92Wh/m^2). The wind rose indicates that more than 30% of the winds come from the southwest. In order to develop a much broader expertise, it would be interesting to make measurements in each prefecture of the Kara region. In this way, an atlas of the region could be established. In addition, other sites in Togo could also be studied in order to get an overview of the wind potential of the whole country. The choice of turbines should therefore be based on the characteristics of the site to better convert a large amount of the kinetic energy of the wind into electrical energy.

References

[1] de HERDE JFL, de HERDE H, GERIN A. Wind Energy: What Hybrid Energy to Fill its Defects. 2006;:pp.16.

[2] FICHAUX N. Évaluation du potentiel éolien offshore et imagerie satellitale. École des Mines de Paris, France; 2003.

[3] PHILIPPOPOULOS K, DELIGIORGI D, KARVOUNIS G. Wind Speed Distribution Modeling In The Greater Area Of Chania, Greece. International Journal of Green Energy. 2012;:9 : 174–193. https://doi.org/https://doi.org/10.1080/15435075.2011.622020

[4] PAVIA GE, O'BRIEN JJ. Weibull statistics of wind speed over the ocean. Journal of Climate and Applied Meteorology. 1986;vol. 25:pp. 1324-1332. https://doi.org/https://doi.org/10.1175/1520-0450(1986)025<1324:WSOWSO>2.0.CO;2

[5] GUMBEL JE. Statistics of extremes. Columbia University Press. 1958;:pp. 375.. https://doi.org/https://doi.org/10.7312/gumb92958

[6] Weibull W. A statistical distribution function of wide applicability. Journal of Applied Mechanics. 1951;:n°18, pp. 293-297.

[7] TROEN I, PETERSEN E. European wind atlas. Roskilde. Risoe National Laboratory, I. 1989;.

[8] JENSEN ON, PETERSEN E, TROEN I. World climate applications programme : extrapolation of mean wind statistics with special regard to wind energy applications. World meteorological organization. 1984;WMO/TD-No..

[9] JUSTUS C, HARGRAVES W, YALCIN A. Nationwide assessment of potential ouput from wind-powered generators. Journal of Applied Meteorology. 1976;n°15:pp. 673-678. https://doi.org/https://doi.org/10.1175/1520-0450(1976)015<0673:NAOPOF>2.0.CO;2

[10] JUSTUS C, HARGRAVES W, MIKHAIL A, GRABER D. Methods for estimating wind speed frequency distribution. Journal of Applied Meteorology. 1978;n°17:pp. 350-353. https://doi.org/https://doi.org/10.1175/1520-0450(1978)017<0350:MFEWSF>2.0.CO;2

[11] HENNESSEY J. A comparison of the Weibull and Rayleigh distributions for estimating wind power potential. Wind Engin. 1978;2:156–164.

[12] Merzouk N, Merzouk M. Estimation du Potentiel Energétique Eolien Utilisable-Application au Pompage dans les Hauts Plateaux. Revue des Energies Renouvelables. 2006;Vol. 9, N°:pp. 155 – 163.

[13] Sen Z, Altunkaynak A, Erdik T. Wind Velocity Vertical Extrapolation by Extended Power Law’, Hindawi Publishing Corporation. Advances in Meteorology. 2012;:pp. 6. https://doi.org/https://doi.org/10.1155/2012/178623

[14] HLADIK J. Energétique Eolienne, « Chauffage éolien, Production d’électricité, Pompage. (MASSON, ed). 1984.

[15] LEGOURIERES D. Energie éolienne, théorie, conception et calcul pratique des installations. 2è Edition. (Eyrolles, ed). 1982.

[16] Manyonge A, Ochieng R, Onyango F, Shichikha J. Mathematical Modeling of Wind Turbine in a Wind Energy Conversion System: Power Coefficient Analysis. Applied Mathematical Sciences. 2012;Vol. 6, :pp. 4527 – 4536.

[17] MOLIN B. Hydrodynamique des structures offshore. 2002;:pp. 440.

[18] Kalnay E, Lord SJ, McPherson RD. Maturity of Operational Numerical Weather Prediction: Medium Range. Bulletin of the American Meteorological Society. 1998 Dec;79(12):2753-2769. https://doi.org/10.1175/1520-0477(1998)079<2753:moonwp>2.0.co;2

[19] MACHENHAUER B, HIRLAM. Technical Report 5. Copenhagen: Danish Meteorological Institute; 1988.

[20] METATLA S. Optimisation et régulation des puissances d’une éolienne à base d’une MADA. École nationale supérieure polytechnique d’Alger; 2009.

[21] Katz RW, Skaggs RH. On the Use of Autoregressive-Moving Average Processes to Model Meteorological Time Series. Monthly Weather Review. 1981 03;109(3):479-484. https://doi.org/10.1175/1520-0493(1981)109<0479:otuoam>2.0.co;2

[22] Delleur JW, Kavvas ML. Stochastic Models for Monthly Rainfall Forecasting and Synthetic Generation. Journal of Applied Meteorology. 1978 Oct;17(10):1528-1536. https://doi.org/10.1175/1520-0450(1978)017<1528:smfmrf>2.0.co;2

[23] Carlson RF, MacCormick AJA, Watts DG. Application of Linear Random Models to Four Annual Streamflow Series. Water Resources Research. 1970 08;6(4):1070-1078. https://doi.org/10.1029/wr006i004p01070

[24] Makridakis S, Wheelwright SC, McGee VE. Forecasting: Methods and Applications. 2nd. JohnWiley & Sons; 1983.

[25] BOX P, JENKINS M. Times series analysis: forecasting and control. 1976.

[26] Corotis RB, Sigl AB, Cohen MP. Variance Analysis of Wind Characteristics for Energy Conversion. Journal of Applied Meteorology. 1977 Nov;16(11):1149-1157. https://doi.org/10.1175/1520-0450(1977)016<1149:vaowcf>2.0.co;2

[27] BOSSANYI E. Short-term wind prediction using Kalman filters. Wind Energy.9:1-8.

[28] Poggi P, Muselli M, Notton G, Cristofari C, Louche A. Forecasting and simulating wind speed in Corsica by using an autoregressive model. Energy Conversion and Management. 2003 Dec;44(20):3177-3196. https://doi.org/10.1016/s0196-8904(03)00108-0

[29] Kitagawa T, Nomura T. A wavelet-based method to generate artificial wind fluctuation data. Journal of Wind Engineering and Industrial Aerodynamics. 2003 06;91(7):943-964. https://doi.org/10.1016/s0167-6105(03)00037-0

[30] Cadenas E, Rivera W. Short term wind speed forecasting in La Venta, Oaxaca, México, using artificial neural networks. Renewable Energy. 2009 01;34(1):274-278. https://doi.org

[31] Kodjo M, Bédja K, Ajavon A, Lishou C. Neural networks for predictive control of the mechanism of orientation of a wind turbine. Journal des Sciences Pour l'Ingénieur . 2008;9.

2nd German-West African Conference on Sustainable, Renewable Energy Systems SusRES – Kara 2021

Intelligent Automation & Robotics

https://doi.or/10.52825/thwildauensp.v1i.11

Published: 15 June 2021

Development and Manufacturing of a controlled 3D printed bionic hand

H. Smajic [1][https://orcid.org/0000-0002-0669-1979], T. Duspara [1][https://orcid.org/0000-0002-6985-5950]

[1] Technische Hochschule Köln

Abstract. During a current project, a fully functioning prototype of a 3D printed bionic hand was developed. This paper explains principles such as: bionic hand movement, working rules of sensors and actuators etc. Design of all parts are performed, including the wiring of control system. The project includes two types of sensor control systems for bionic hand. One is with stretch sensors that replicates movement of human hand onto the bionic model. Other type is using machine learning (AI) and a camera. The average amputee cost is $30.000,00 for a new custom-built arm/hand. With the advancement of technology through time, manufacturing processes became cheaper and more accessible. Technical innovation of this project was the fact, that a functional prosthetic hand prototype was built for price lower than $50,00. The prototype does not have all the functions and capabilities as the full priced custom prosthetic hand, but it can replicate altogether the movements as the real device. All the fingers are capable of moving individually, sideways and with the work on the new version, gripping function could be perfected. Further work on materials, could help find the adequate material to increase friction and thusly enhance the grasp strength. The new challenge would involve testing with different kinds of materials to improve the working stability. As it was already unfavorable, this project was mostly based onto the actuation part, or rather the hand itself. Second part of research would involve exploring of different sensor systems. Two control solutions were designed and tested. Next steps would involve neurotransmission sensors, where arm would be controlled using brainwaves as signals that are transformed in movement.

Keywords: bionic hand, AI, 3D printing, low-budget

Introduction

Main goal while building a prosthetic hand is to replicate all the movements as a human hand has. To achieve desired movement, all bones of a human hand must be replicated and designed. 3D printed prosthetic hands are well known in 21st century but unfortunately, they are not widely used because of durability of the 3D printed material. With further advancement of technology, improvements of composite materials are inevitable.

Mechanical parts

A human hand consists of three basic bone groups. Those are phalanges, metacarpals and carpals. To design a 3D model of a hand, same bone parts should be engineered. Those are distal phalanx, middle phalanx and proximal phalanx. The main function of hand can be recreated and engineered using only phalanges, so metacarpal and carpal bones will be merged into a one piece.

Fingers (Phalanges) - Distal phalanx is the tip of the finger. On a 3D model of this part, a pre designed holes can be found. These include holes for the shaft, and grooves for the strings. Going from up to down, next part is the middle phalanx which is placed into the distal phalanx and secured with said shaft. On the top and the bottom of middle phalanx there are enter and exit holes for the string. Proximal phalanx represents the lowest phalanx bone. This is the last moving part of the bionic hand. It is the largest phalanx bone with the maximum length of approximately 60mm. It is connected to the rest of the hand using a connector and two shafts. The upper shaft is the same as with the two earlier mentioned bones. Lower shaft connects it to the central part of the hand which represents the merged metacarpal and carpal bones. The difference between two shafts is the freedom of movement. Upper shaft allows the piece to move towards and away from the palm. Lower shaft allows the movement of whole finger in a sideways direction. Because phalanges are connected to each other, movement of proximal phalanx sideways results in the movement of whole finger. Unlike the other fingers thumb consists of only two parts but it has the ability to move into two different directions. Bottom part of the thumb is actually a holder for a servo motor that rotates the thumb around its nominal axis. As well as with other fingers, string is placed through the thumb thus achieving the regular movement towards the palm, or in other

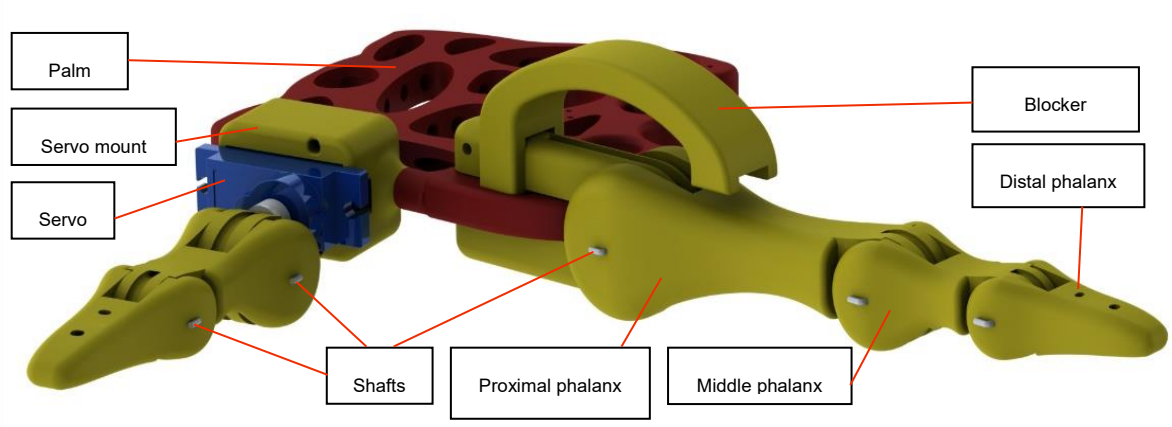

Figure 1. Phalanges Assembly.

words, the „grip“ itself.

Palm - As the movement of metacarpal and carpal bones is minimal, they will be replaced with a single piece that represents the palm of a bionic hand. Each finger has one string with two endpoints. Pulling one endpoint moves the finger towards the palmand other endpoint moves that guide the strings. It is crucial to design the blockers for each individual finger. These blockers are placed on the back side of the finger-palm connectors. When the finger goes from fully the finger back into the first position. To avoid confusion and mess, the palm has holes closed to fully open position, the proximal phalanx hits the blocker and stays in place.

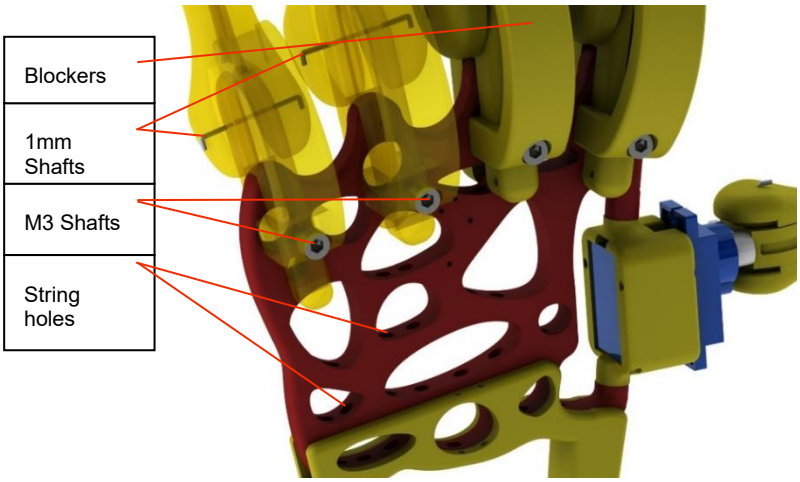

Figure 2. Palm Assembly.

Arm and stand design - While designing the arm the crucial thing to do is to provide slots for the servo motors. Arm model is compact and has slots for six servo motors. To avoid the collision between levers of servo motors, half of the servos are facing the front side and the other half are facing the back side. The stand is placed at the bottom of the hand. To lower the center of mass, and prevent falling of the hand due to movement inertia, a 0,5kg weight is added to the stand. The lower part of the arm fits snuggly into the stand. Stand is the last part of the mechanical assembly. In order to test the prototype, a housing was designed, which fits all the electronical components.

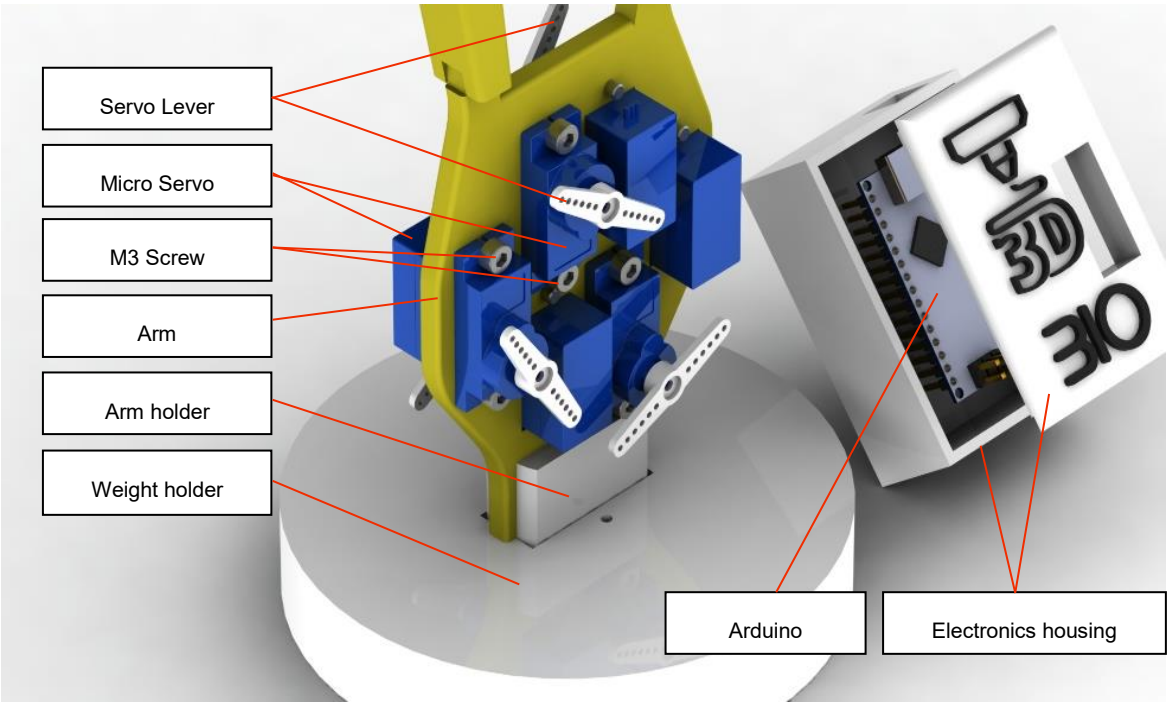

Figure 3. Arm assembly.

Strings - For the movement of fingers or in other word the connection between phalanges and servo motor, a fishing nylon is used. The one used for prototype is 0.2mm thick and it has the load strength of 20[N] which is more than enough to support the force required to achieve movement of the hand. Each piece of nylon string is cut to the size of approximately 600mm. This string is pulled through all of the phalanges in a way that the two endpoints beneath the arm are equally long. The center of string is glued on top of the distal phalanx of each finger. Later on the string goes through the holes inside the palm and finally through the arm-palm connector and to the servo motors placed on the arm. The string is pulled through holes on servo levers and secured with adhesive. Before securing the string itself, a proper movement should be checked. If everything is moving according to the plan, the strings can be attached onto the lever. For entire assembly, less than 3m of nylon are needed. Nylon is very cheap so material cost does not affect overall price.

Actuators

Actuators are devices that provide movement for the assembly. Micro servomotors are chosen because of their compact design and easy control. A servomotor is a rotary or linear actuator that allows for precise control of angular or linear position, velocity and acceleration. They can easily be mounted onto the arm part. For the full movement of the hand, seven servomotors are required. Five motors enable the movement of five fingers where the sixth motor enables the rotational movement of the thumb. The seventh motor is used for sideways movement of fingers. Servomotors can rotate their shaft for 180 degrees. The servo lever should be around 35mm long. If the lever is shorter, the finger doesn’t reach the end positions. There are two positions of the motors that are used for the movement. The 180-degree position places the finger fully open and 0 degree moves the finger back into its

first point. Servomotors used for prototype have metal gears inside them which makes them more durable. Another benefit from these motors is their price. For achieving the basic movements, seven servo motors are needed which in the end, adds up to the price of 19,99€.

Production process

Process of building a hand can be classified in five phases:

1. CAD/CAM Design
2. Manufacturing
3. Quality control
4. Assembly
5. Automation

CAD/CAM Design

Phase one includes scaling of the parts, so they can perfectly fit individual person. Each part needs to be scaled by certain percentage depending on the size of the hand. Scaling is done using a CAD software (SolidWorks, NX, etc.). After the scaling is done, an animation must be ran. Animation shows potential problems and irregularities without the necessity for a prototype. When animation shows solid work and movement of all the parts, each part needs

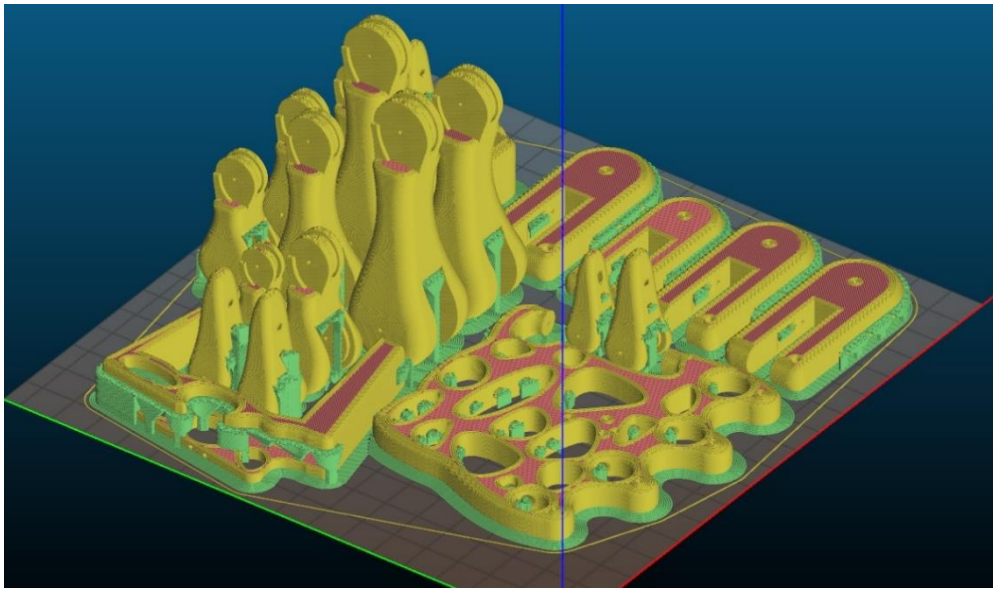

Figure 4. CAM Preparation.

to be converted into triangulated surface-s commonly known as STL files. Converted files are then imported into a CAM software. Software used is called “Slic3r” and it is utilized for 3D printer CAM preparation. CAM software takes the STL files, and later on computes the coordinates used for the printer movement, based on selected parameters. Parameters include: print, printer and material specifications. Most important are the print specifications, whereas other two depend on the specific machines that are used. Parts need to be manipulated and positioned on the print bed in a way that conserves the space on the printing surface. After thorough calibration and testing, the ideal parameters can be chosen. The ones chosen for this particular print and printer are shown in table below.

Table 1. Printing parameters.

	Parameter		Value	Unit
Printing settings	Layer height		0.16	mm
	Fill density		50%	
	Fill pattern		Triangle	
	Printing speed	Outer perimeters	20	mm/s
		Other perimeters	25	mm/s
			30	mm/s
	Skirt		1	loops
	Brim		5	mm
	Generate support material:		YES	
	Overhang threshold:		65%	

Manufacturing

When the parameters are all set, CAM software generates G-code used for the print. Parts are made out of ABS filament with 50% infill. Filament has 1.75mm diameter, so it is easy to calculate its mass. One spool of ABS material contains 290,7 meters of filament (1kg spool). Printers surface has printable area of 20x20cm. In regard to that, two separate G-Code files must be created to fit all the parts of a bionic hand. Printing process for entire hand uses 89,5m of ABS filament which weighs 308g. The main benefit behind this project is its “Low-cost factor”. ABS filament spool costs around 20,00€, so mechanical parts can be manufactured with this technology for only 4,52€. This means, that you can create all the mechanical moving parts of a bionic hand for under 5,00€ thanks to the advancement of manufacturing processes and technologies.

Print No.	Pieces	Filament length [m]	Fillament mass [g]	Layer count	Print time	Cost [€]
Print 1	22	59,242	203,78	1107	22:24:33	2,99
Print 2	13	30,271	104,12	312	07:59:01	1,53
Altogether	**35**	**89,513**	**307,91**	**1419**	**30:23:34**	**4,52**

Table 2. Material expenses.

According to the table above and earlier mentioned price of servomotors, overall assembly worth does not exceed 25,00€. In abstract there was a 50,00€ price mentioned for the assembly. This price consists of labor (staff), disposable material, screws etc.

Quality control

After the manufacturing process, which takes a little more than 30 hours, it is time to clean the parts and check dimensions. Support material must be removed from surfaces, and surfaces should be grinded. In order to achieve perfect clearance in between parts, all the dimensions must be checked and compared to the dimensions in CAD drawing. If some of the dimensions are unequal to the ones in the drawing, they must be corrected. Perfect gap between two parts can be tested after adding a shaft between them. If the parts move one around another smoothly and without any problems collide with their limit stops (blockers), then the clearance is fine and shaft can be fixed in place. If the movement seems too rough, then contact surfaces need to be grinded 0,2 ~ 0,4mm. This process is repeated for each connecting part until the clearance is satisfactory.

Assembly

Assembly phase starts after acquisition of all parts and components. Micro servomotors are placed into slots on the arm and secured in place with M3 screws. To extend servo levers, new longer levers were made and placed onto the existing ones. When all the mechanical parts are printed and dimensions are checked, all the parts should be lined up one next to another. Next phase is pushing the string through predesigned grooves on the phalanx’s parts. This process requires a lot of patience.

Figure 5. Full assembly of a bionic hand.

The grooves are very narrow and due to the imperfections of printing material, it is common for the strings to stick. After all the strings have been pulled through phalanges and palm, the shafts are mounted. At this point, string ends are equal length and they are secured at the top of distal phalanx with glue. Pulling the two endpoints will result in opening or closing fingers. If the movement is as desired, endpoints must be linked with servo levers. Before firmly securing string to servo levers, movement is checked by carefully rotating the axis of servomotor. Zero-degree position results in fully open finger whereas 180-degree position results in fully closed finger. When all the movements are examined and approved, strings are secured to servo levers with adhesive and leftover can be cut off.

Automation

With fully assembled hand, the means of control must be constructed. Control system requires a microcontroller that moves servomotors. Microcontroller used in this project is an Arduino Nano microcontroller. Arduino nano has 13 digital I/O pins. For control of the actuators, each servo requires one PWM output pin. That means that seven output pins are used for the servo movement. Generally Arduino can supply voltage to actuate these servos, but because there are seven servos attached to this assembly, Arduino voltage output cannot provide enough current to move all of them simultaneously. Additional power source is added to raise the current in servos. For this project a 20W power source is used. This provides servos with 5V of voltage and 4 Ampers of current. To connect all the servos to Arduino, a custom PCB bord was designed. On one end of the board there is a standard

voltage connector. The plus pin of voltage connector is soldered to the VIN pin of Arduino. This provides the power that Arduino needs to operate without additional power source (USB). The same pin is connected to all of the middle pins of servo connector. Other pin is soldered to the Arduino GND pin. With this, all the devices including servos and Arduino are powered with the same power source. The USB connector on the Arduino is only used to transfer the code from the computer to the microcontroller.

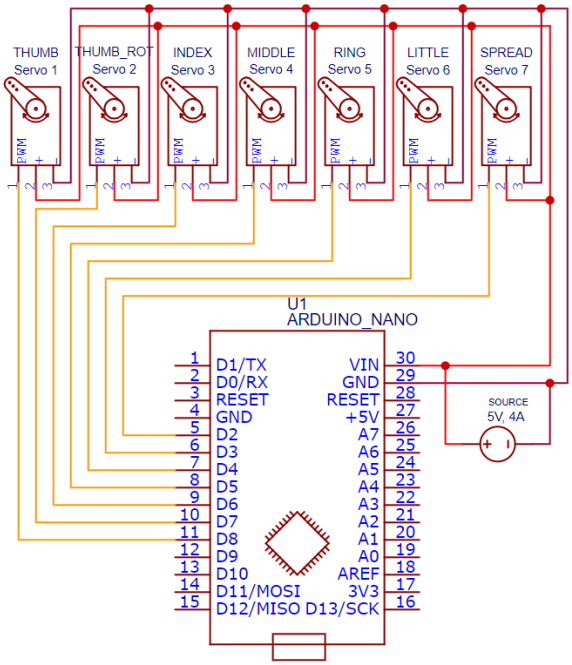

Figure 7. Wiring schematic.

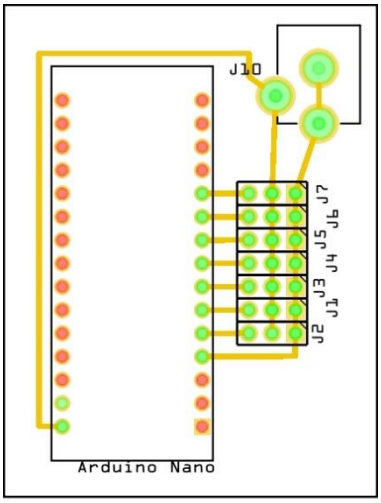

Figure 6. PCB Design.

Conclusion

During the work on this project, a final prototype was built. The average amputee pays tenths of thousands of Euros for a new custom-built arm/hand. With the advancement of technology through time, manufacturing processes became cheaper and more reachable. Technical innovation of this project was the fact, that a functional prosthetic hand prototype was built for under 30,00€. This prototype does not have all the functions and proficiency as the full priced prosthetic hand, but it can replicate all the movements as the real device. All the fingers are capable of moving individually, sideways and with the work on the new version, gripping function could be perfected. Further work on materials, could help find the adequate material to increase friction and thusly enhance the grasp strength. Further work on this project would involve experimentation with different kinds of materials to improve the operational stability. As it was already said, this project was mostly based onto the actuation part, or rather the hand itself. Second part of research would involve exploring of different sensor systems. Interesting potential was noticed in works with neurotransmission sensors. Next phase could involve synthesis of a low budget 3D printed bionic hand with said sensors.

References

1 Taylor C, Scwarz R. The Anatomy and Mechanics of the Human Hand. Artificial Limbs . 1955;2(2):22-35.

2 Shi W, Lyu Z, Tang S, Chia T, Yang C. A bionic hand controlled by hand gesture recognition based on surface EMG signals: A preliminary study. Biocybernetics and Biomedical Engineering. 2018;38(1):126-135. https://doi.org/10.1016/j.bbe.2017.11.001

3 Bronzino J, Peterson D. Biomedical engineering fundamentals. 2nd Edition. CRC Press; 2014. https://doi.org/https://doi.org/10.1201/b15482

4 Clement R, Bugler K, Oliver C. Bionic prosthetic hands: A review of present technology and future aspirations. The Surgeon. 2011 Dec;9(6):336-340. https://doi.org/10.1016/j.surge.2011.06.001

5 Aman M, Sporer ME, Gstoettner C, Prahm C, Hofer C, Mayr W, Farina D, Aszmann OC. Bionic hand as artificial organ: Current status and future perspectives. Artificial Organs. 2019 02;43(2):109-118. https://doi.org/10.1111/aor.13422

6 Syed A, Agasbal ZTH, Melligeri T, Gudur B. Flex Sensor Based Robotic Arm Controller Using Micro Controller. Journal of Software Engineering and Applications. 2012;05(05):364-366. https://doi.org/10.4236/jsea.2012.55042

2nd German-West African Conference on Sustainable, Renewable Energy Systems SusRES – Kara 2021
Intelligent Automation & Robotic
https://doi.org/10.52825/thwildauensp.v1i.34

Published: 15 June 2021

Concept towards Segmenting Arm Areas for Robot-Based Dermatological In Vivo Measurements

Mateusz Szymanski[1] [https://orcid.org/0000-0002-5991-9906],
Ron van de Sand[1] [https://orcid.org/0000-0002-8975-4030], Esther Tauscher[1], Olaf Rieckmann[2], and Alexander Stolpmann[1][https://orcid.org/0000-0002-3021-2456]

[1]Technical University of Applied Sciences Wildau, Germany

[2]Beiersdorf AG, Germany

Abstract. Dermatological in vivo measurements are used for various purposes, e.g. health care, development and testing of skin care products or claim support in marketing. Especially for the last two purposes, in vivo measurements are extensive due to the quantity and repeatability of the measurement series. Furthermore, they are performed manually and therefore represent a nonnegligible time and cost factor. A solution to this is the implementation of collaborative robotics for the measurement execution. Due to various body shapes and surface conditions, common static control procedures are not applicable. To solve this problem, spatial information obtained from a stereoscopic camera can be integrated into the robot control process. However, the designated measurement area has to be detected and the spatial information processed. Therefore the authors propose a concept towards segmenting arm areas through a CNN-based object detector and their further processing to perform robot-based in vivo measurements. The paper gives an overview of the utilization of RGB-D images in 2D object detectors and describes the selection of a suitable model for the application. Furthermore the creation, annotation and augmentation of a custom dataset is presented.

Keywords: Object Detection, Convolutional Neural Networks, RGB-D images

Introduction

Efficacy and safety studies play a key-role for the development of skin care products. Their core concept is based on performing dermatological laboratory tests on predefined skin areas that are reclusively conducted by specifically trained lab personal. However, the quantity and repeatability of these series of measurements constitutes a major challenge, as they are mostly carried out manually and therefore represent a nonnegligible cost and time factor. A solution to this is the implementation of collaborative robotics for the measurement execution. It goes without saying that common control procedures based on statically programmed software modules cannot be used, since robot-controlled skin measurements must contain additional information on the various body shapes and surface conditions. Furthermore, the position and orientation of the measurement area must be taken into account, which have to be dynamically updated during the measurement process. To solve this problem, information obtained from an image processing system can be integrated into the robot control process. In our previous work, the application of collaborative robotics for the execution of in vivo measurements was proposed [1] by identifying the measurement areas through markers (as

shown in Figure 1). Furthermore, by using a stereoscopic camera spatial coordinates could be determined by performing multiple linear regression. With the information provided, the target coordinates for the robot movement path could be computed as waypoints. However, this approach requires the manual marking of the measurement areas, which seems infeasible in practice. Therefore, the automatic definition of measurement areas can be of high value, as it reduces time and associated costs and may contribute to a higher repeatability. One solution is to use deep learning object detection for image processing with the aim of detecting certain body parts within the image such as upper arm, forearm or hands. More specifically image segmentation methods to retrieve body shapes and contours from the image, which can be further used to identify the respective measurement area. For this, stereoscopic camera depth information being obtained next to RGB (red-green-blue colour image) for each pixel can be used to extract useful features for the subsequent object detection tasks. Zhou et al. [2] and Xing et al. [3] have already shown that the use of RGB-D images (RGB with depth information) can outperform the RGB baseline models. With two types of state-of-the-art object detectors namely, two-/multi-stage or single-stage detector, there is a trade-off between the faster single-stage and the more accurate multi-stage detector [4]. For the online application in a robot control sequence, both speed and accuracy are critical. More recent developments show that this compromise is no longer valid. For example, Wang et al. [5] presented a single-stage focal loss based RetinaNet detector that outperformed the multi-stage detectors in accuracy. Li et al. [6] presented a multi-stage light-head Region-based Convolutional Neural Network, which outperformed the single-stage detectors You Only Look Once (YOLO) and Single Shot Multibox Detector (SSD) in speed and accuracy. Although many researchers dedicated their work to the field of image object detection and many approaches exists throughout the literature [7–11], the combination with robot based in vivo measurements is rarely considered in the past and remains a challenge to date. Therefore, this paper proposes a concept for segmenting arm areas into upper arm, forearm and hand, with the focus on in vivo dermatological measurements performed on the forearm. After this introduction, related works is followed by a concept. Furthermore, this work delivers an overview of state-of-the-art models in terms of applicability to the given application. After selecting a suitable model, it is presented in more detail and the creation of a dataset is described and discussed. Finally, a conclusion is given.

Related Works

Object recognition is one of the most important application fields of image processing [12] and can be used for different objects and tasks, e.g. faces [13], cars [14] or cats and dogs [15]. Histograms of oriented Gradients (HOG) [16], Scale Invariant Feature Transform (SIFT) [17] or Haar-like cascade filters [18] are used for feature extraction and Support Vector Machines (SVM) [19] or Deformable Part-based Models (DPM) [20] are used for classifying based on recognized features. For the detection of more than one object in an image or even objects of different classes it is necessary not only to classify but also to localize the object, this process is called object detection [21]. Most modern object detectors are based on convolutional neural networks (CNN), and although CNNs were proposed by LeCun as early as the 1980s [22] and used for character recognition [23], development stagnated in the early 2000s [21]. With the advancements in GPU computing [24, 25], larger annotated datasets [21] and deeper networks [26], CNNs, like other neural networks, become more advanced and receive more attention in recent years [21].

As mentioned in the previous section, the image identification and segmentation of arm areas is of significant interest to extract the shape and surface of the forearm. A similar problem was coped with in [27] or [28] where body parts for pose estimation where detected. Another model has been proposed in [29] for hand gesture recognition. Other application additionally considered the use of RGB-D data and showed that it can improve the model performance

[30],[31]. Chandra et al. [32] use RGB-D data to segment the limbs, torso and head of a person through a fully convolutional network for the use of a mobility assistance robot. Other works addressed the use of RGB-D images to train CNNs, for example in [33] proposed an R-CNN based model in this context. The depth information was primarily utilized for extracting significant features from the provided image. Another approach is proposed in [34] who implemented a YOLO based approach for detecting objects by using RGB-D images. The authors extended the structure of YOLOv3 by adding another channel in the input layer for the depth information. In addition to the 2D object detection approach, there are 3D object detectors [35, 36] for three-dimensional bounding box estimation. These utilize point clouds and are applied for pose estimation and scene understanding.

Concept

As mentioned in the introduction, the authors presented in their previous work an image processing system for performing robot-assisted dermatological in vivo measurements. As shown in Figure 1, measurement areas were defined using markings on a forearm, which were then used to transform the relevant depth information with the intrinsic and extrinsic parameters into the coordinate system of the camera. With this spatial information and the pixel coordinates of the target positions from the RGB image, target coordinates were computed and passed to the robot control system as waypoints.

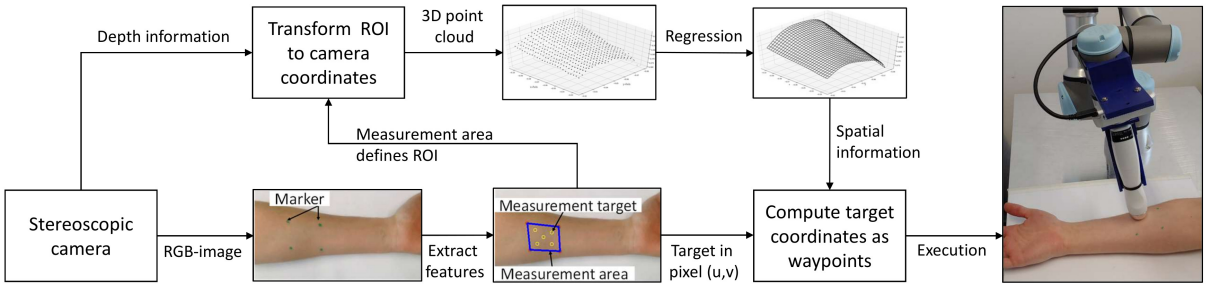

Figure 1. Marker based approach for defining the measurement area [1].

However, placing new markers on the forearm for each measurement seems to be impractical and may not be user-friendly. Therefore, in this work, a concept is presented to replace the markers with an CNN object detector for recognition and localization of the forearm. As input, the object detector receives the depth information in addition to the RGB values for each pixel. The output is expected to be the localization as well as the correct classification of the object contained in the respective picture. For this purpose a bounding box is output for each object, consisting of an anchor point in pixel coordinates and the height and width of the box. Although the authors focus on measurements on the forearm, the neighbouring body parts, hand and upper arm, are detected as well in order to identify the measurement area enclosed by. Due to the functionality of the bounding box determination via the parameters of the Intersection over Union (IoU) [37], the authors expect a higher robustness and better accuracy of the assignment, in particular of the transition areas between hand and forearm as well as forearm and upper arm. Subsequently, the bounding box of the forearm is used as Region of Interest (ROI) to perform an instance segmentation. This is described as determination of the affiliation of pixels to a certain object. For this purpose, the depth information is used to perform a background subtraction as described for different methods in [38] or [39]. Due to the setup and positioning of the camera, the authors are confident that the background is well described in both, the RGB image and especially in the depth information and that the subtraction can be performed reliably. The concept is shown in Figure 2 and the area relevant for this work is highlighted. To give further context on how the segmented information is used in the system, the next steps are also shown.

The pixels segmented to the forearm are used as ROI to transform them into camera coordinates. Unlike the marker based approach, the spatial information of the whole forearm is extracted by a multiple linear regression. With this information and a determined pose, measurement area(s) of a fixed size are fitted on the forearm. From here, the target coordinates are computed and passed to the robot as already shown in Figure 1.

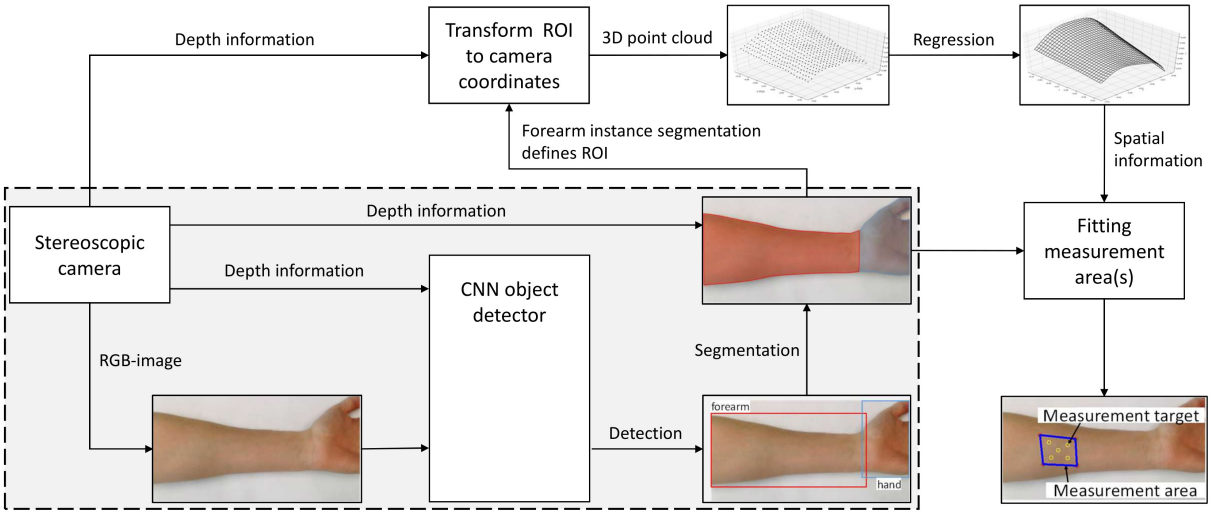

Figure 2. Proposed concept for segmenting arm areas and its further context in the image processing system.

Model Comparison and Selection

For the CNN object detector in the proposed concept, a suitable model must be selected. For this purpose, first an overview of the underlying models and their further developments for the utilization of depth information is given. Afterwards the models are compared and one is selected, which is then described in more detail.

A Brief Overview of Object Detection

In this section, pre-selected object detectors are described and the deployment of depth information based on the RGB models is presented. Selected are Region-based CNN, Fast Region-based CNN, Faster Region-based CNN, You Only Look Once and Single Shot MultiBox Detector.

Region-Based Convolutional Neural Network

Girshick et al. [7] propose a region-based CNN (R-CNN) for object detection. The localization problem is solved by proposing regions for an input image. At test time, about 2000 regions are proposed and each of them is scaled to a defined size. For the region proposal the selective search algorithm [40] is used. The size of the warped region represents the size of the input layer of the CNN. For each region, a feature vector is extracted and classified by a class-specific linear SVM. Gupta et al. [33] use depth images to encode geometric features, namely, horizontal disparity, height above ground and angle (HHA), and generate colour images from them. The authors used two CNNs to extract the features from the RGB images and the HHA features.

Fast Region-Based Convolutional Neural Network

Girshick et al. [8] propose a further development of R-CNN, the Fast R-CNN. The authors address the long training and test time and achieve a higher accuracy compared to R-CNN. First, a feature map is created for a whole image by several convolutional and pooling layers. Then, a ROI is generated for each proposed object and a feature vector is extracted through a

pooling and two fully-connected layers. Via further fully-connected layer the architecture ends in two different output layers. On the one hand a softmax layer for classification of the object and on the other hand an output layer for the bounding box regression. Yuanzhouhan et al. [41] propose RGB-D Fast R-CNN, the network inputs the entire RGB and depth image in two parallel Fast R-CNNs. Two convolutional feature maps are output, which are then concatenated for classification and bounding box regression.

Faster Region-Based Convolutional Neural Network

With the improvements of Fast R-CNN or SPP-net [42], the limitations of modern object detectors are in the region proposal methods. Ren et al. [9] propose Faster R-CNN with a Region Proposal Network (RPN) to address this problem. RPNs basically consist of multiple convolutional layers. Regions are proposed from the convolutional feature maps while simultaneously determining the region boundaries of the object. In principle, Faster R-CNN consists of an RPN for region proposal and Fast R-CNN for object detection. By proposing to share the convolutional features between the RPN and the object detection network, the computational cost is compensated. Ren et al. [43] propose Parallel RCNN for human detection. Parallel RCNN enhances the performance of simultaneously extracting features in RGB and depth images from two CNNs. Further the authors are experimenting with different methods of encoding depth images, e.g. HHA [33].

You Only Look Once

Redmon et al. [10] propose You Only Look Once (YOLO), a new method for object detection. Unlike other object detectors, YOLO views detection not as a region proposal problem but instead as a single regression problem. It processes entire images as input, dividing them into grid cells for this purpose. Each of these cells or cell combinations predicts a certain number of bounding boxes with confidence score. This score indicates how securely an object is located in the box and how well this box fits the contained object. Furthermore, for each box a probability of association with a specific class is predicted. These two are then combined to a final detection. Takahashi et al. [34] propose Expandable YOLO (E-YOLO), in which another channel is added in the input layer for depth information. Further, the authors introduce the 3D IoU with Volume of Overlap and Volume of Union for a better 3D bounding box proposal. Ophoff et al. [44] propose a different approach. They use a separate network stream for the RGB and depth information each and fuse them by a concatenation layer. For the fusion, the authors experiment with different positions of the fusion layer in the network. The authors refer to the proposed model as RGB-D Fusion YOLO.

Single Shot MultiBox Detector

Liu et al. [11] propose with Single Shot MultiBox Detector (SSD) a similar single-stage approach to [10]. SSD takes a whole image as input with ground truth boxes for training. With an input size of 300 x 300 pixel, SSD is faster and more accurate than YOLO with 448 x 448 pixel. The authors use VGG-16 as the base network and then add multiple feature layers. By using multi-scale convolutional bounding boxes that are output to these added feature layers, the bounding box regression problem is solved more efficiently. Further, the authors experiment with different datasets and larger input sizes of images. Sharma and Valles [45] present a base network for processing RGB-D images with SSD. The authors use two parallel streams with convolutional layers for the RGB and depth image. These are then fused using fully connected layers and additional feature layers are added for the detection. This is referred to as RGB-D Fusion SSD.

Model selection

In this work, the model selection is divided in two consecutive steps. First, the RGB baseline is compared in its performance and then the RGB-D models are compared in relation to the baseline, while at the same time evaluating whether the model is suitable for the application

presented. Some researchers may argue that the ranking assignment is not of high scientific value, which is indeed the case, but the wide variety of hardware and architectures and datasets makes it difficult to compare objectively. This applies in particular to the assessment of suitability, which is why it has to be regarded as subjective and will subsequently be addressed in the conclusion.

For the comparison of baseline performance, the metrics of mean Average Precision (mAP) and test time are used. In addition, the used architecture and dataset is given. The mAP gives the average over the precision over all classes of a dataset. The test time indicates how long the model needs to process one image during runtime. The comparison is given in Table 1.

Table 1. Comparison of different object detector models.

Model	**Architecture**	**Dataset**	**mAP**	**Test time [s]**
R-CNN [7]	AlexNet	VOC07	58.5	9.8
	VGG16	VOC07	66.0	47.0
Fast R-CNN [8]	VGG16	VOC07	66.9	0.32
Faster R-CNN [9]	VGG16	VOC07+12	73.2	0.2
YOLO [10]	VGG16	VOV07+12	66.4	0.048
	GoogLeNet	VOC07+12	63.4	0.022
SSD [11]	VGG16	VOC07	74.3	0.017

Table 1 shows that single-stage detectors such as YOLO or SSD can achieve the accuracy of Faster RCNN and are thereby significantly faster in test time. The next step is to compare the RGB-D models from the previous section. The models are benchmarked against their own, if known, RGB baseline to show the effect of using additional depth information. Since test time is often not specified, the effect on it is further estimated with Δ for better, $\circ$ for neutral and ∇ for worse compared to the baseline. The same metric is finally used to assess whether the model could be used for use case presented in this paper. The results are shown in Table 2.

Table 2. Comparison and rating of different RGB-D models.

Model	**Dataset**	**mAP**	**Test time [s]**	**Suitable?**
R-CNN	NYUD2	19.7	-*	
R-CNN + HHA [33]	NYUD2	32.5	-* ∇	∇
Fast R-CNN	B3DO	39.9	-*	
RGB-D Fast R-CNN [41]	B3DO	41.9	-* ∇	∇
Faster R-CNN	custom	90.0	-*	
Parallel R-CNN [43]	custom	91.5	-* ∇	$\circ$
E-YOLO [34]	custom	-*	0.023	Δ
YOLOv2	KITTI	39.87	-*	
RGB-D Fusion YOLOv2 [44]	KITTI	48.16	-* ∇	Δ
RGB-D Fusion SSD [45]	Princeton + Washington RGB-D	99.43	-*	Δ

* not available

The additional processing of depth information can basically be divided into three methods. First method, the encoding of the depth information into a three-channel colour image and processing in a parallel CNN. Similarly, in the second method the depth information is processed in a parallel CNN stream as a single channel input and then fused, with different approaches to when the fusion takes place in the network. And finally for the third method adding another input channel for the depth information. In general, the processing of additional depth information is considered to have a negative impact on the test time, since it requires

additional computations. The authors consider a test time of about 0.033 to 0.05 seconds per image, which corresponds to 20 to 30 frames per second, to be suitable. Therefore, the models based on the R-CNN family must be classified as not suitable for our application. Choosing between E-YOLO, RGB-D Fusion on YOLO or SSD, the authors opt for the latter. The decision is based on four considerations:

- First, SSD performs better in terms of accuracy and test time on the baseline (as shown in Table 1).
- Second, starting from the baseline, there are opportunities to sacrifice speed for accuracy.
- Third, the method of using a separate CNN stream for depth information is well known, as shown by other methods compared here.
- And fourth, the application for which the model is proposed, the grasping of different objects with a mobile robot arm, has certain similarity to our intention.

Model Description

With the selection of the RGB-D Fusion SSD model, it is described in more detail. The RGB and depth image are scaled to 200 x 200 pixel images and processed in two parallel CNN streams for convolution and feature extraction. These consist of five convolutional layers with maxPooling after the second, fourth and fifth layer. In addition, batch normalization is performed in the depth CNN stream after each convolutional layer. After feature extraction, the two CNN streams are merged via a concatenation through three fully connected layers [45]. From here on, the original SSD architecture [11] is used with four additional convolutional layers ending in a softmax layer for classification followed by a non-maximum suppression layer for fitting the bounding box. The whole architecture is shown in Figure 3.

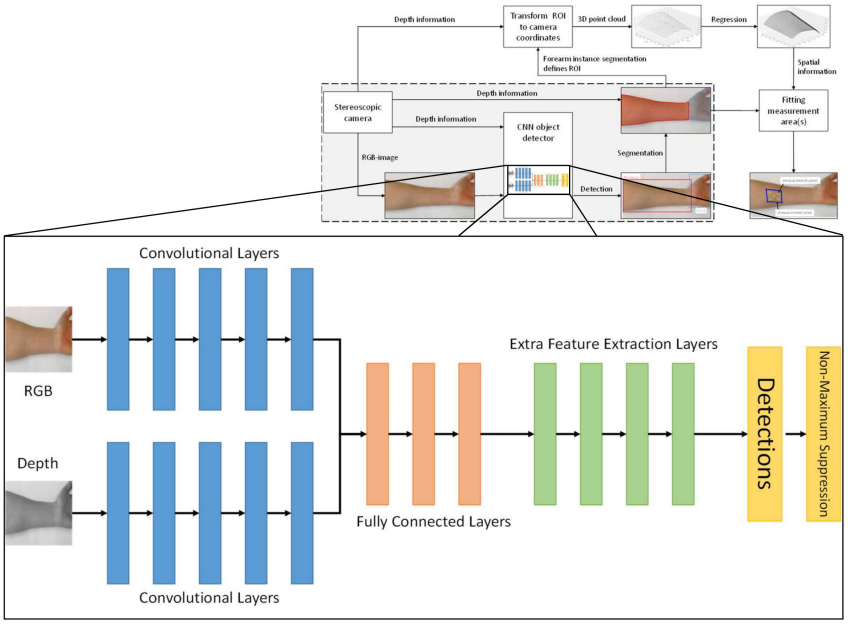

Figure 3. Network Overview of SSD with RGB-D Architecture derived from [45].

With the presentation of a concept and selection of a model, the following section deals with the creation of a dataset.

Dataset

For the very specific use case of detecting forearms, a custom dataset is created. The creation consists of three steps, data acquisition, annotation, and augmentation of the data.

For the data acquisition the setup from previous work is used, consisting of the collaborative robot UR3e from Universal Robots and an Intel RealSense D435i stereoscopic camera, which is attached on top of the robot's arm. The robot moves to five different positions in one pass. Each of these positions is randomized, within certain limits, to allow variation in depth and viewing angle. At each position, an RGB and depth image is captured. For each forearm, 2 to 3 passes are made in different poses. A total of 750 images are taken from 35 people. Further on, the images have to be labelled manually with the areas corresponding to the forearm, hand and upper arm. Each of them represents an individual label which consists of selected pixel coordinates. Due to the setup described above, there are three different possible combinations. Figure 4 shows an example of the annotation process for three images, with forearm and upper arm in row (a), forearm and hand in row (b) and all three labels in row (c).

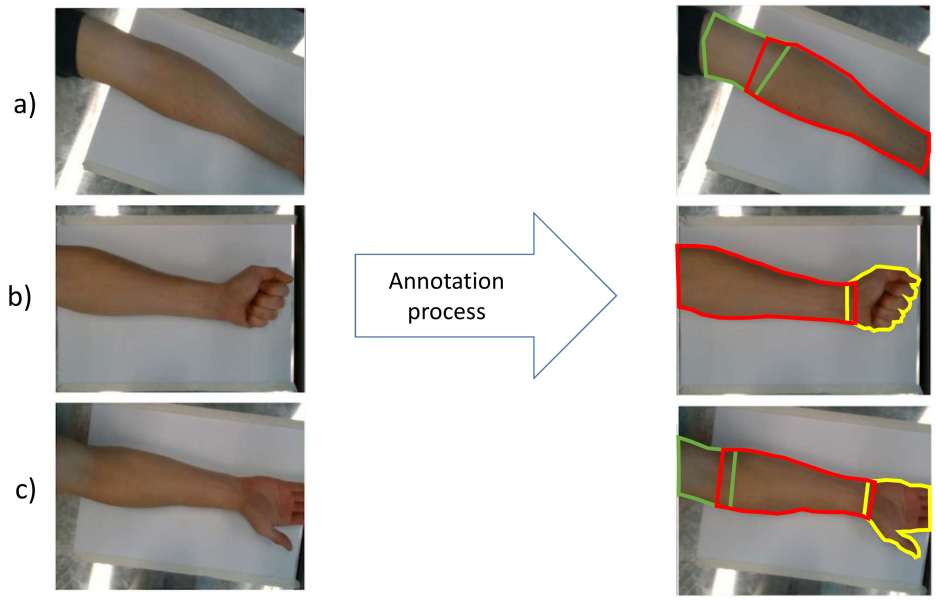

Figure 4. Annotation process for (a) forearm and hand, (b) forearm and upper arm and (c) all three labels.

In the final step, the raw images are augmented to a larger database. In order to achieve a certain robustness against changes in brightness and illumination, the image is converted to the HSV colour space and augmented in the H-S, H-V, S-V and HSV channels. The change in the corresponding channels is randomized within certain limits. Afterwards it is transferred back to the RGB colour space. To provide greater variation, rotations of 90°, 180° or 270° are applied. This results in seven different modes of augmentation. Attention must be given during rotation in regard to the annotated coordinates; they must also be rotated accordingly. Figure 5 shows an example of the augmentation for three images. In total the dataset consists of 6000 annotated images.

Discussion

It should be noted that model selection is not a trivial task and developers may draw different conclusions, as quantitative comparison of all models is only possible to a limited extend. Therefore, future work will address this issue in more detail by comparison multiple architectures in terms of accuracy and computational resources. Further, other methods to use depth information in 2D object detectors will be considered. Especially E-YOLO is interesting because of its simplicity and lightweight implementation. Moreover, the single channel input of the depth stream can be replaced by a three channel one, which allows the use of encoded depth images. Another field of research intersecting with this application are 3D object detectors. As aforementioned, in this work, the transformation of the camera depth

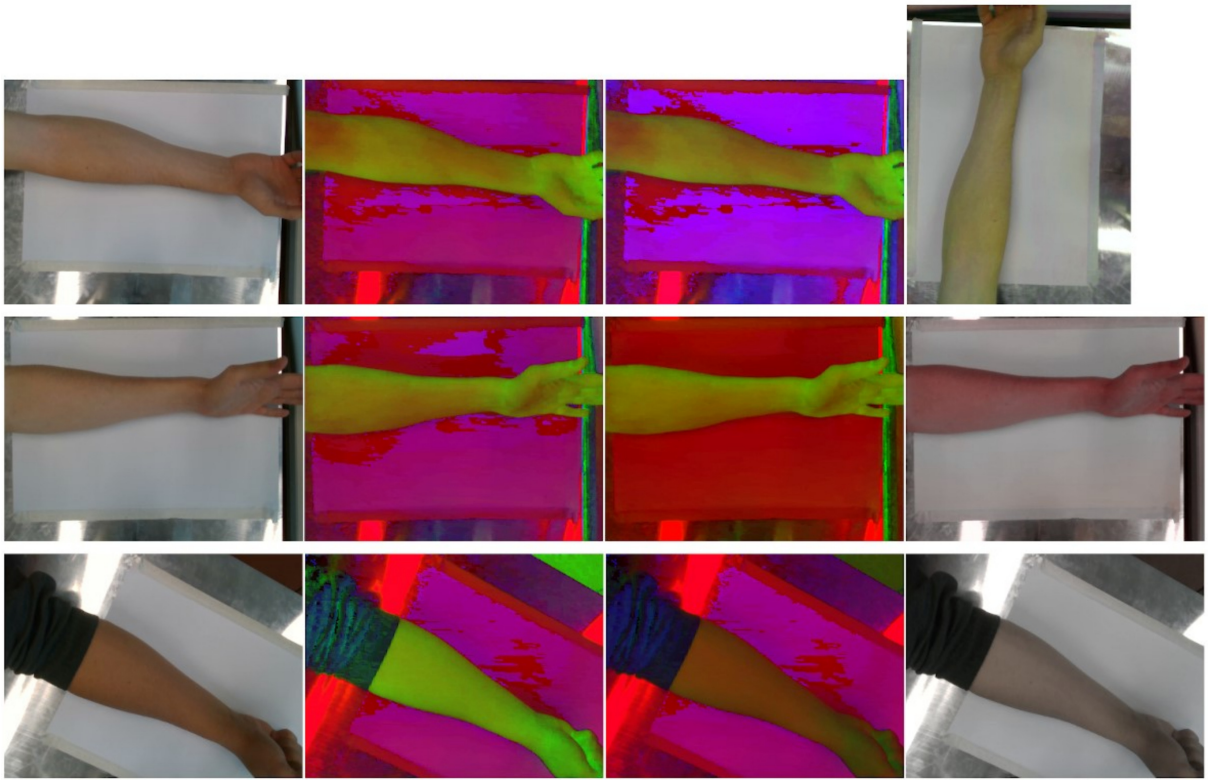

Figure 5. Image in RGB, image in HSV, augmented image in HSV, augmented image in RGB (from left to right), first row: H-V modified and rotated by 270°, second row: S-V modified, third row: H-S modified.

data into the 3D space is conducted after detecting the object of interest. Thus, only the area of interest is transformed while comparatively few computational resources are occupied. Despite that, the application of 3D object detectors could also be favourable. However, this may include the transformation of all depth points instead of a designated area only, which can be computationally expensive. Finally, further research projects will also focus on the generalisation ability of the model to generalise well by enhancing the dataset with, for example, different genders and skin colours.

Conclusion

In this paper, a concept for the detection and segmentation of arm areas using CNN-based object detectors with the context of automated execution of robot-based dermatological in vivo measurements is presented. The concept is based on previous work and gives further details on the use of the segmented arm areas in the image processing system. By deploying a stereoscopic camera both RGB images as well as associated depth information becomes available, which is considered in the derived concept. Furthermore, this paper gives an overview about methodologies to apply depth information in 2D object detectors and points out challenges within the described application framework. Besides, the creation, annotation and augmentation of a custom dataset is presented.

References

[1] M. Szymanski, R. van de Sand, O. Rieckmann, and A. Stolpmann, “Robotergestützte dermatologische in-vivo-Messungen,” *atp magazin*, vol. 62, no. 11-12, pp. 78–85, 2020.

[2] K. Zhou, A. Paiement, and M. Mirmehdi, “Detecting humans in RGB-D data with CNNs,” in *Proceedings of the fifteenth IAPR International Conference on Machine Vision Applications*, Piscataway, NJ: IEEE, 2017, pp. 306–309.

[3] Y. Xing, J. Wang, X. Chen, and G. Zeng, “2.5D convolution for RGB-D semantic segmentation,” in *2019 IEEE International Conference on Image Processing*, Piscataway, NJ: IEEE, 2019, pp. 1410–1414.

[4] P. Soviany and R. T. Ionescu, “Optimizing the trade-off between single-stage and two-stage deep object detectors using image difficulty prediction,” in *SYNASC 2018*, [Los Alamitos, Calif.]: IEEE Computer Society, 2018? Pp. 209–214.

[5] X. Wang, P. Cheng, X. Liu, and B. Uzochukwu, “Focal loss dense detector for vehicle surveillance,” in *2018 International Conference on Intelligent Systems and Computer Vision (ISCV2018)*, Piscataway, NJ: IEEE, 2018, pp. 1–5.

[6] Z. Li, C. Peng, G. Yu, X. Zhang, Y. Deng, and J. Sun, *Light-head R-CNN: In defense of two-stage object detector*.

[7] R. Girshick, J. Donahue, T. Darrell, and J. Malik, “Rich feature hierarchies for accurate object detection and semantic segmentation,” in *Computer Vision and Pattern Recognition (CVPR), 2014 IEEE Conference on*, 2014, pp. 580–587.

[8] R. Girshick, “Fast R-CNN,” in *2015 IEEE International Conference on Computer Vision*, Piscataway, NJ: IEEE, 2015, pp. 1440–1448.

[9] S. Ren, K. He, R. Girshick, and J. Sun, “Faster R-CNN: Towards real-time object detection with region proposal networks,” *IEEE transactions on pattern analysis and machine intelligence*, vol. 39, no. 6, pp. 1137–1149, 2017.

[10] J. Redmon, S. Divvala, R. Girshick, and A. Farhadi, “You only look once: Unified, real-time object detection,” in *29th IEEE Conference on Computer Vision and Pattern Recognition*, Piscataway, NJ: IEEE, 2016, pp. 779–788.

[11] W. Liu, D. Anguelov, D. Erhan, C. Szegedy, S. Reed, C.-Y. Fu, and A. C. Berg, “SSD: Single shot multibox detector,” in *Computer Vision – ECCV 2016*, ser. Lecture Notes in Computer Science, B. Leibe, J. Matas, N. Sebe, and M. Welling, Eds., vol. 9905, Cham: Springer International Publishing, 2016, pp. 21–37.

[12] P. F. Felzenszwalb, R. B. Girshick, D. McAllester, and D. Ramanan, “Object detection with discriminatively trained part-based models,” *IEEE transactions on pattern analysis and machine intelligence*, vol. 32, no. 9, pp. 1627–1645, 2010.

[13] J. Meng, Y. Gao, X. Wang, T. Lin, and J. Zhang, “Face recognition based on local binary patterns with threshold,” in *IEEE International Conference on Granular Computing (GrC), 2010*, X. Hu, Ed., Piscataway, NJ: IEEE, 2010, pp. 352–356.

[14] T. Moranduzzo and F. Melgani, “Detecting cars in UAV images with a catalog-based approach,” *IEEE Transactions on Geoscience and Remote Sensing*, vol. 52, no. 10, pp. 6356–6367, 2014.

[15] O. M. Parkhi, A. Vedaldi, A. Zisserman, and C. V. Jawahar, “Cats and dogs,” in *IEEE Conference on Computer Vision and Pattern Recognition (CVPR), 2012*, Piscataway, NJ: IEEE, 2012, pp. 3498–3505.

[16] N. Dalal and B. Triggs, “Histograms of oriented gradients for human detection,” in *CVPR 2005*, C. Schmid, C. Tomasi, and S. Soatto, Eds., Los Alamitos, Calif: IEEE Computer Society, 2005, pp. 886–893.

[17] D. G. Lowe, “Distinctive image features from scale-invariant keypoints,” *International Journal of Computer Vision*, vol. 60, no. 2, pp. 91–110, 2004.

[18] P. Viola and M. Jones, “Rapid object detection using a boosted cascade of simple features,” in *CVPR 2001*, Los Alamitos, Calif: IEEE Computer Society, 2001, pp. I-511-I–518.

[19] O. Chapelle, P. Haffner, and V. N. Vapnik, “Support vector machines for histogram-based image classification,” *IEEE transactions on neural networks*, vol. 10, no. 5, pp. 1055–1064, 1999.

[20] R. Girshick, F. Iandola, T. Darrell, and J. Malik, “Deformable part models are convolutional neural networks,” in *2015 IEEE Conference on Computer Vision and Pattern Recognition (CVPR)*, Piscataway, NJ: IEEE, 2015, pp. 437–446.

[21] Z.-Q. Zhao, P. Zheng, S.-t. Xu, and X. Wu, *Object detection with deep learning: A review*.

[22] A. Khan, A. Sohail, U. Zahoora, and A. S. Qureshi, *A survey of the recent architectures of deep convolutional neural networks*, 2020.

[23] Y. Lecun, L. Bottou, Y. Bengio, and P. Haffner, “Gradient-based learning applied to document recognition,” *Proceedings of the IEEE*, vol. 86, no. 11, pp. 2278–2324, 1998.

[24] D. Steinkraus, I. Buck, and P. Y. Simard, “Using GPUs for machine learning algorithms,” in *Proceedings / Eighth International Conference on Document Analysis and Recognition, 2005*, Los Alamitos, Calif.: IEEE Computer Society, 2005, 1115–1120 Vol. 2.

[25] K.-S. Oh and K. Jung, “GPU implementation of neural networks,” *Pattern Recognition*, vol. 37, no. 6, pp. 1311–1314, 2004.

[26] K. Simonyan and A. Zisserman, *Very deep convolutional networks for large-scale image recognition*.

[27] Q. Dai, J. Qiao, F. Liu, X. Shi, and H. Yang, “A human body part segmentation method based on markov random field,” in *International Conference on Control Engineering and Communication Technology (ICCECT), 2012*, Piscataway, NJ: IEEE, 2012, pp. 149–152.

[28] A. Jalal, A. Nadeem, and S. Bobasu, “Human body parts estimation and detection for physical sports movements,” in *2019 2nd International Conference on Communication, Computing and Digital Systems (C-CODE)*, Piscataway, NJ: IEEE, 2019, pp. 104–109.

[29] Z. Ren, J. Yuan, J. Meng, and Z. Zhang, “Robust part-based hand gesture recognition using kinect sensor,” *IEEE Transactions on Multimedia*, vol. 15, no. 5, pp. 1110–1120, 2013.

[30] C. Plagemann, V. Ganapathi, D. Koller, and S. Thrun, “Real-time identification and localization of body parts from depth images,” in *IEEE International Conference on Robotics and Automation (ICRA), 2010*, Piscataway, NJ: IEEE, 2010, pp. 3108–3113.

[31] N. Mohsin and S. Payandeh, “Localization and identification of body extremities based on data from multiple depth sensors,” in *2017 IEEE International Conference on Systems, Man, and Cybernetics (SMC)*, Piscataway, NJ: IEEE, 2017, pp. 2736–2741.

[32] S. Chandra, S. Tsogkas, and I. Kokkinos, “Accurate human-limb segmentation in RGB-D images for intelligent mobility assistance robots,” in *2015 IEEE International Conference on Computer Vision Workshop (ICCVW)*, IEEE, 7.12.2015 - 13.12.2015, pp. 436–442.

[33] S. Gupta, R. Girshick, P. Arbeláez, and J. Malik, “Learning rich features from RGB-D images for object detection and segmentation,” in *Computer vision - ECCV 2014*, ser. Lecture Notes in Computer Science, D. Fleet, Ed., vol. 8695, Cham: Springer, 2014, pp. 345–360.

[34] M. Takahashi, Y. Ji, K. Umeda, and A. Moro, “Expandable YOLO: 3D object detection from RGB-D images,” in *”2020 21st International Conference on Research and Education in Mechatronics (REM)”*, IEEE, 2021-01-12, pp. 1–5.

[35] S. Song and J. Xiao, “Deep sliding shapes for amodal 3D object detection in RGB-D images,” in *29th IEEE Conference on Computer Vision and Pattern Recognition*, Piscataway, NJ: IEEE, 2016, pp. 808–816.

[36] D. Xu, D. Anguelov, and A. Jain, “Pointfusion: Deep sensor fusion for 3D bounding box estimation,” in *2018 IEEE/CVF Conference on Computer Vision and Pattern Recognition*, Piscataway, NJ: IEEE, 2018, pp. 244–253.

[37] H. Rezatofighi, N. Tsoi, J. Gwak, A. Sadeghian, I. Reid, and S. Savarese, “Generalized intersection over union: A metric and a loss for bounding box regression,” in *2019 IEEE/CVF Conference on Computer Vision and Pattern Recognition*, Piscataway, NJ: IEEE, 2019, pp. 658–666.

[38] K. Greff, A. Brandão, S. Krauß, D. Stricker, and E. Clua, “A comparison between background subtraction algorithms using a consumer depth camera,” in *Proceedings of the International Conference on Computer Vision Theory and Applications*, SciTePress - Science and and Technology Publications, 24.02.2012 - 26.02.2012, pp. 431–436.

[39] E. J. Fernandez-Sanchez, J. Diaz, and E. Ros, “Background subtraction based on color and depth using active sensors,” *Sensors (Basel, Switzerland)*, vol. 13, no. 7, pp. 8895–8915, 2013.

[40] J. R. R. Uijlings, K. E. A. van de Sande, T. Gevers, and A. W. M. Smeulders, “Selective search for object recognition,” *International Journal of Computer Vision*, vol. 104, no. 2, pp. 154–171, 2013.

[41] C. Yuanzhouhan, S. Chunhua, and T. S. Heng, “Exploiting depth from single monocular images for object detection and semantic segmentation,” *IEEE transactions on image processing : a publication of the IEEE Signal Processing Society*, vol. 26, no. 2, pp. 836–846, 2017.

[42] K. He, X. Zhang, S. Ren, and J. Sun, “Spatial pyramid pooling in deep convolutional networks for visual recognition,” *IEEE transactions on pattern analysis and machine intelligence*, vol. 37, no. 9, pp. 1904–1916, 2015.

[43] X. Ren, S. Du, and Y. Zheng, “Parallel RCNN: A deep learning method for people detection using RGB-D images,” in *CISP-BMEI 2017*, Q. Li, Ed., Piscataway, NJ: IEEE, 2017, pp. 1–6.

[44] T. Ophoff, K. van Beeck, and T. Goedemé, “Exploring RGB+depth fusion for real-time object detection,” *Sensors (Basel, Switzerland)*, vol. 19, no. 4, 2019.

[45] P. Sharma and D. Valles, “Backbone neural network design of single shot detector from RGB-D images for object detection,” in *2020 11th IEEE Annual Ubiquitous Computing, Electronics & Mobile Communication Conference (UEMCON)*, IEEE, 10/28/2020 - 10/31/2020, pp. 0112–0117.

2nd German-West African Conference on Sustainable, Renewable Energy Systems SusRES – Kara 2021

CPS & IOT(IIOT)

https://doi.org/10.52825/thwildauensp.v1i.6

Published: 15 June 2021

Cyber-Physical Production Systems in Settings with Limited Infrastructure

Blind Spots and Implications

Bastian Prell[1], Norman Günther[1] and Jörg Reiff-Stephan[1] [https://orcid.org/0000-0003-4176-6371]

[1]Technical University of Applied Science Wildau, Germany

Abstract. During the last decade production innovation was mainly focused on connectivity aspects. The vision of smart factories running on software, that uses collected machine data, has become true but foremost for leading industrial companies in highly developed countries. Apart from these, production can also be found in non-industrialized craft professions as well as in less developed countries. As digitalization does not necessarily require an industrial or developed setting the latter could possibly benefit from it as well. Socio-cyber-physical production systems have been used to describe the interdependencies of linked production systems but usually focus on highly developed regions as well as for industrial applications. This paper lines out similarities and differences for each case, introduces the concept of cyber-physical production systems (CPPS) and its extension to socio-CPPS (SCPPS), which emphasizes the role of human workers in the production environment. The relation between industrial, non-industrial production and innovations is examined. Furthermore, the widening of SCCPS concepts for non-industrial production is discussed.

Keywords: Socio-Cyber-Physical Production Systems, Limited Infrastructure, Developing Countries, Craft, non-industrialized, Digitalization

Introduction of Terms and Concepts

The collective state of the art in production technology defines the market price for each good. The respective technology used by the individual company defines their costs, thus it directly affects their profits: This is why innovation itself is regarded as competitive advantage. Thus, producing companies are constantly on the lookout for innovations that can be used beneficial in a manufacturing context. Cyber-physical production systems (CPPS) are the application of cyber-physical systems (CPS) in production context. That is why the advancements of the last decade regarding information and communication technology (ICT) may revolutionize value creation. Especially availability of sensory equipment and smart software, made it possible to process large quantity of data and support or even make decisions and affect the physical world through actuators [1]. Production processes usually take place in a production system consisting of various machines that can carry out process steps. The digitalization of single machines is wide spread. Whatsoever, relevant benefits can usually only be unlocked, when regarding at least the complete production system or even the whole value creation process [2], [3]. These considerations have led to the concept of CPPS, which this work reviews from a non-industrial perspective.

CPPS have been widely discussed in literature. But even though it is often used as a homogenous concept a unique definition does not exist. Exemplarily the following citations show why the authors found it helpful to formulate a working definition of (Socio-)CPPS while taking existing ones into account but showing deviations explicitly.

Monostorie [4] (depicted in Figure 1 as a)) formulates CPPS as the combination of manufacturing science and ICT, and therefore as “systems of collaborating computational entities which are in intensive connection with the surrounding physical world and its on-going processes, providing and using, at the same time, data accessing and data-processing services available on the internet.” Meanwhile, Niggemann and Lohweg [5] (b)) state: “A CPPS is a holistic conception of modern, often distributed, production systems: It treats mechanical, computational and external aspects [, that] can only be handled if [it] comes with a set of intrinsic cognitive capabilities such as self-diagnoses, self-configuration, self-optimization and intelligent user interaction.” Thiede et al. [6] (c)) emphase the valid aspect, that CPPS “consisting of a physical component, as well as a virtual component, [… are] connected to the employee. A technology containing computational and physical capabilities combined with the possibility of human machine interaction.” Similarly, Rudtsch et al. [7] included prediction and almost real-time aspects (e)).

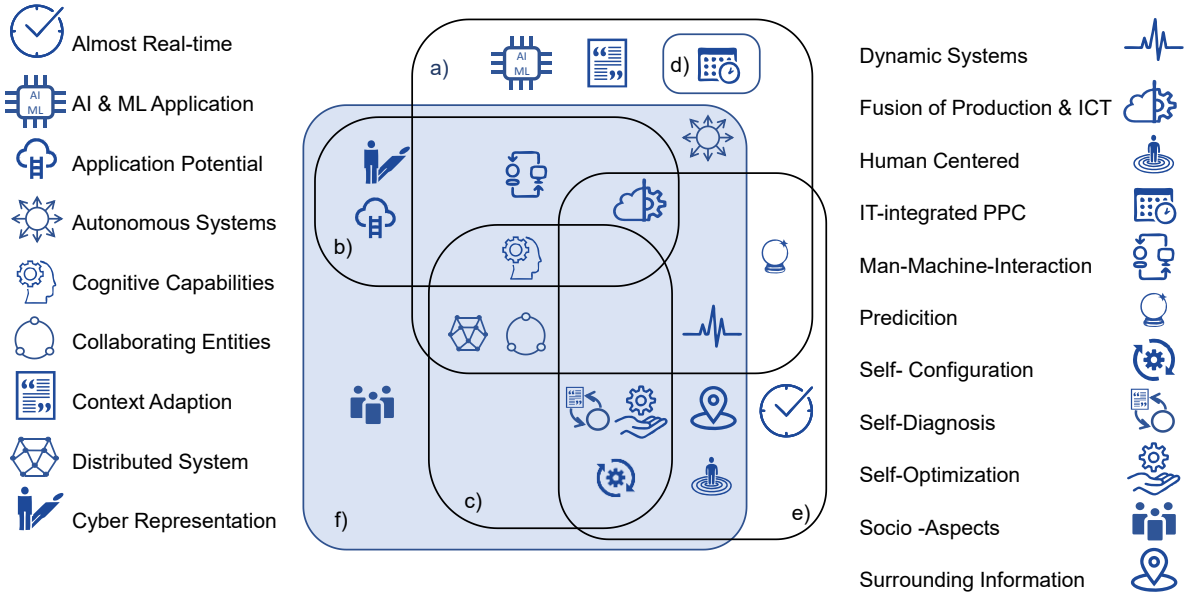

Figure 1. Defining Aspects of CPPS – usually related but not identical.

The working definition can be observed in the box f), and can be formulated as follows:

A CPPS is characterized by a virtual representation of the physical production means, which replicates the distributed entities and is enriched by surrounding information in order to unlock manifold application potential (e.g., self-configuration, self-diagnosis, self-optimization). Those systems are usually dynamic and therefore complex, the system itself needs to provide cognitive capabilities to achieve the goal of collaborating, autonomous entities. When several of those entities are human workers served by the technology, who then can rather be described as the user, one can speak of a socio-cyber-physical production system (SCPPS).

Thus, each SCPPS is a CPPS but not vice versa.

Motivation

The history of modern society has been closely linked to successful usage of innovations in production. Every time technology had advanced production potency, it was accompanied with major cultural changes, that in retrospective formed industrial revolutions, as they are depicted in Figure 2. Initiated by steam engines, heavy tasks could be performed by mechanical equipment, enabling the mechanical loom and thus the blossom of textile industries in Europe, making railway commuting necessary as well as available and also laying the foundations of the suburban housing system, e.g., in London. Soon steam engines were replaced by electric motors, that eased the constriction of central drives and allowing

the first value stream-oriented production lines, like the Ford Model T production. Dominating conveyor belts thus paved the way for the automotive society we take for granted nowadays. Automation then took over more complex motion sequences, enabling mass production for more and more product types, announcing the era of consumption (e.g., household appliances penetration rising esp. from the 1970s on [8]). These developments finally lead to the current informational interlinking of production means, for smoother transfer and creation of required data, information or even knowledge. Each of the industrial revolutions of the past had brought social change by the newly required work, qualifications and education but also by serving unmet demands [9].

Digitalization and *Industrial Internet of Things* are trending terms within the scientific but also practical production research community. Even first applications of artificial intelligence have proven to work beneficial. A more recent spin of this research area has proclaimed the human centered production system and thereby forecasting the upcoming change of paradigm [10], [11]. The change of mass production can be observed: Individualization, human-robot collaboration, sustainability, robotics and bionics are already found in some factories. SCPPS can be used to conceptually merge the paradigm shift with these nowadays linked production facilities [12].

Figure 2. Industrial Revolutions – so far.

As the digitalization of production means can be viewed as ongoing, its foreseeable implications as well as the blind spots regarding non-industrialized production shall be addressed by examining the research question, presented in the following section. The investigation will be structured by sections, each addressing one of those research questions. Hereafter, the findings are illustrated exemplarily for three scenarios. The paper concludes with a summary and outlook on further research.

Research Questions

The observed mega trend of individualization and flexibility in production has brought up the idea of an ideal industrial process with a batch size of one. CPPS are often seen as the technological base to achieve these goals. Batch sizes of one whatsoever have been a characteristic of non-industrial production. The first research question of this paper is therefore:

A) What are the implications of industrial and non-industrial production, both converging to a batch size of one?

CPPS have usually been viewed as a concept applying for industrial production, while focusing on developed (usually also industrialized) countries. The concepts implications shall be examined for non-industrial branches or regions by investigating the second research question:

B) Is the implicit focus of CPPS on industrial production justified?

Addressing Batch Size Convergence

When considering differences, similarities and convergences between producing structures in industrial and non-industrial context their origins as well the context of the corresponding demands needs to be reviewed.

Bulk production had been made feasible by industrialization from the 18th century on. Nonetheless, the population’s demand for consumption consists of both, products well suited for mass production and those that are less suitable. Therefore, non-industrial production remained predominant kind of manufacturing for certain produce, that proved not suitable for mass production for the respective state of the art. Whatsoever, innovations have widened the capabilities of mass production (as illustrated in Figure 3), but also enabled extended overall consumption. Therefore, a distinctiveness of production volume – both per capita as well as generally - between mass production and non-industrial production can be assumed.

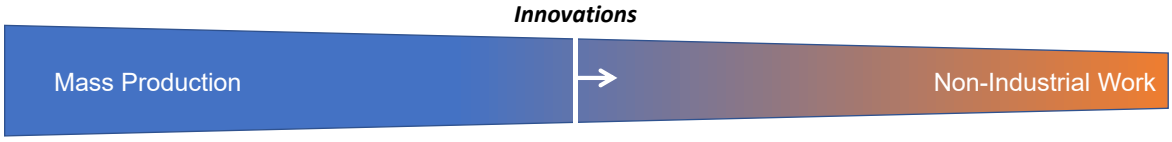

Figure 3. Relation between Mass Production, Innovation and Non-Industrial Work.

Craft Production

Generally, craft production is associated with craftspeople producing:

- artisan unicums (e.g. goldsmiths making jewelry),
- individualized utility produce (tailors, cabinet makers)
- construction site dependent / shifting serial work (tilers, carpenters)
- on-site/ off-site services (car / service mechanics)
- etc.

A similarity of these examples can be seen in the usually high degree of individual requirements that need to be met: Whether it’s the fitted measurements of a cabinet, the specific state of a building site or the error search at a particular car. Also, the ambivalence of assigning such jobs either to the manufacturing or the service sector becomes apparent. According to Hipp, unambiguous definitions seem hard to formulate [13]. Nonetheless, for the sake of this paper all produce generating activities shall be included when speaking of production.

In certain craft branches, especially in metal fabrication, shop floor layouts resemble those found in factories. The same holds true for the division of work. Therefore, such crafts, e.g., metal workers or welders, shall be excluded from the crafts definition for this paper, even though these professions are listed by the German chamber of crafts.

Industrial Production

Formed by the mentioned four industrial revolutions (Figure 2), industrial production came a long way from mass production, coping with serial production and is currently advancing towards individualization.

Traditionally, car manufacturers are leading innovators in Germany. Cars are usually produced in series, but different configurations that the customer can choose from can easily build up to more than 1000 variants for each manufacturer. Many of those individual configurations whatsoever only differ in non-essential qualities such as color mix or rim style, while major differences are grouped by modular platform strategies. Apart from these few different models, the observed individualization can be grouped as pseudo-individualization. More recently soft-individualization has been emerged, which describes that the functionality is built in every product but only activated when the customer choses so by buying it. Another example can be found with sneakers that can be configured by the customer regarding their color mix and stitching [14]. These mass customization branded approaches have in common, that individualized products shall be offered at costs, usually related with mass production [15].

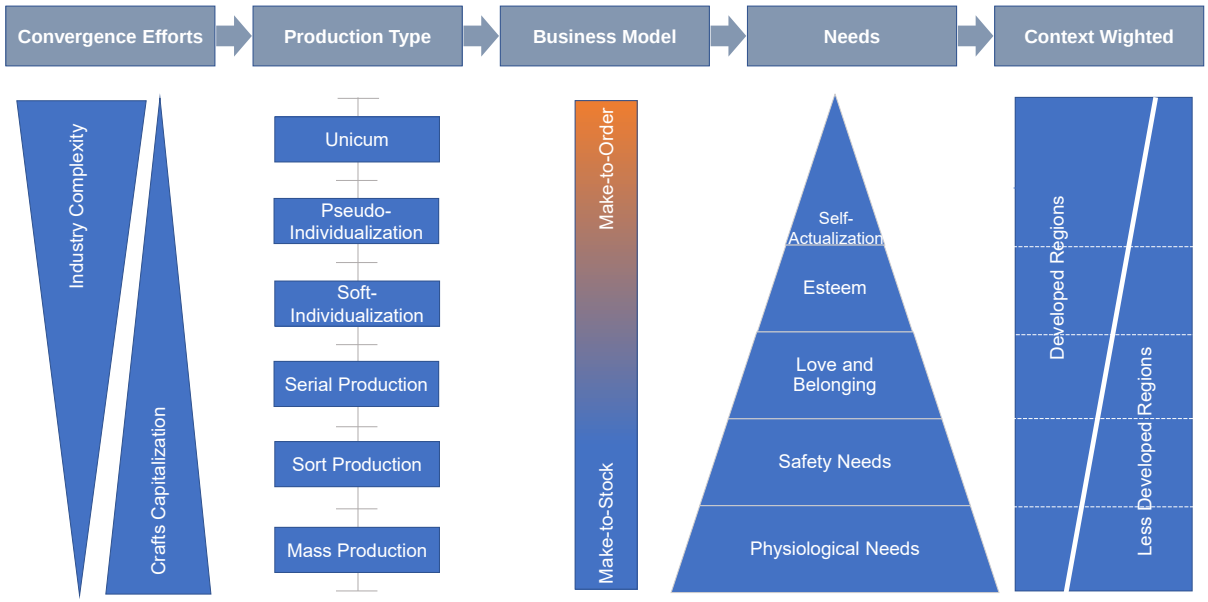

Figure 4. Convergence Aspects from Production and Demand Perspective.

Business Model, Needs and Demand

Figure 4 depicts the relation between the capability in industrial production to allow individualized production and the corresponding complexity. Vice Versa craft branches need to be capitalized, following industrial examples, if they were to target series or mass product markets. Inherently differences can be – generally speaking – observed for business models: While individualized products are self-evidently only manufactured for the respective order, mass products are usually constantly produced, without being directly linked to particular orders. Fluent transitions can be observed, for example when certain semi-finished products are pre-fabricated and stored until they are assembled according to a certain order.

Production should target demands. Demands are market manifested needs that can be structured accordingly to what is known as Maslow’s pyramid of needs scheme [16], [17]. This pyramid scheme by its form and arrangement displays, that the needs on top build up on those below. Those lower needs are also wider and translate more directly into materialistic wants. Therefore, industrial production, with its high output rates seems a reasonable production structure to meet these, so called deficiency needs. Higher needs like esteem or self-actualization are usually seen to be incompatible with the value adding work in the industrial sector [18]. This might be untrue for some industrial jobs and employed individuals, partially due to union backed attempts of purpose loading, but holds true in general [19].

The purchase of individualized goods cannot sustainably compensate for an alienated work environment. SCPPS therefore could approach this by empowering people within the industrial sector to find meaning and purpose in their work. This could be reached by supporting technology that takes over repetitive tasks and supplies information needed to understand the necessity of tasks to allow the worker to mentally participate in the value creation process. The approach of considering the human as a social entity with respective needs may be the next challenge for production technology. On the contrary, technology had been used to some extend to restrict workers alternatives of actions in order to enforce industrial motives and coordination [20]. Furthermore, the implementation of such SCPPS will be confronted with the common obstacles of reorganizations, as it affects not only production but potentially complete business models [20], [3].

Craft professions offer better possibilities of identification and self-actualization [21]. Unicums or small series as well as individualized produce had been their retreat, where cost cutting industrial production was not possible (not economically or technologically feasible).

Even though, complete redundancy of craft professions won’t be likely, a gradual shift, abstractly displayed in Figure 3, can already be experienced. Given the advantages of productive crafts for meeting higher needs for customers by individualized goods, as well as for workers by higher degrees of self-actualization and the social commitment to preserve such traditions [22], [23], it seems worth to look for fields of application for novel technologies such as SCPPS, also in craft professions.

Another perspective can be gained by putting these opposed advantages and disadvantages in the context of industrialized (what is usually meant by the term developed countries) and less developed regions, in that manner. On the one hand the population in industrialized societies can be assumed to have less urgent needs from the bottom categories of the needs pyramid, because most physiological needs and also those for materialistic safety have been met by industrial (over-) production. Populations of non-industrial countries on the other hand have not been confronted with extensive alienation from work, and therefore their self-actualization is not affected by these structures but more so by less than sufficiently met needs, from the need pyramids bottom [24].

Not without wit, this can be expressed in short by an African proverb, stating:

“You have the watches; but we have the time.”

Addressing SCPPS Focus on Industrial Production

This section will unfold, why CPPS have been focused on industrial application for the most part. Here after, the validity of the antithesis, that a non-industrial focus is I) possible, II) relevant, and III) reasonable, is shown.

Digitalization in production foremost has been regarded from the driving forces point of view: Mainly large companies, that can build up on most recent automation technologies and acquire implementation services from experts. Naturally, by the way it emerged, digitalization of production usually considers highly automated facilities combined with high labor costs.

I) Digitalization whatsoever does not necessarily need automation but brings the opportunity to skip, some of the steps usually mentioned as industrial revolution [25]. Thus, breaking with rules of the well acknowledged decomposition of the automation hierarchy – the automation pyramid [4].

II) Apart from industry, production also takes place in non-industrialized settings: On the one hand a non-neglectable part – 12% for Germany - of production is carried out by craftspeople [26]. On the other hand, developing countries are characterized by their mostly non-industrialized creation of value. Non-industrial hereby means either the absence of division of labor (as it can also be observed for craft professions) or less capitalization as might be commercially feasible. Nevertheless, for large parts of the population in developing countries the potential gain in standard of living from any production efficiency increase is much higher than a similar measure would allow for in an industrialized setting. Furthermore, crafts keeps artisan knowledge alive and is widely seen as a cultural heritage, worth to sustain [22].

Apart from the experienced neglection of both aspects in CPPS conceptions so far, further similarities can be observed between productive crafts and value creation in less-developed regions. While industrialization has unbound workplace and family ties in most developed countries by paid labor, family businesses are especially often found in craft branches. The same holds true for most developing countries, where knowledge of workmanship is passed on to the next generation. Especially when economic security during retirement relies on the succeeding descendants. For both parties a well-developed awareness for traditions can be observed.

Even though, machines are widely used by craftspeople in industrialized regions, their professions are usually still known as physically challenging. Meanwhile, a lack of production means in developing countries leads to higher shares of manual work.

Nevertheless, broadening recent SCPPS-modelling approaches for those alternative settings with limited infrastructure seems increasingly relevant. SCPPS can be used to conceptually consider the strong focus on human interactions, which herein occur in a much more characteristic manner than they do for an industrial setting.

III) In order to make these considerations about reasonable SCPPS integration more conceivable, value creation was modeled in Figure 4 for three scenarios: The left reflects the usually highly automated, high labor cost scenario of an industrialized country. Meanwhile the middle presents the craftspeoples approach of value creation for a functionally similar product. Concluded by right, representing a less developed region.

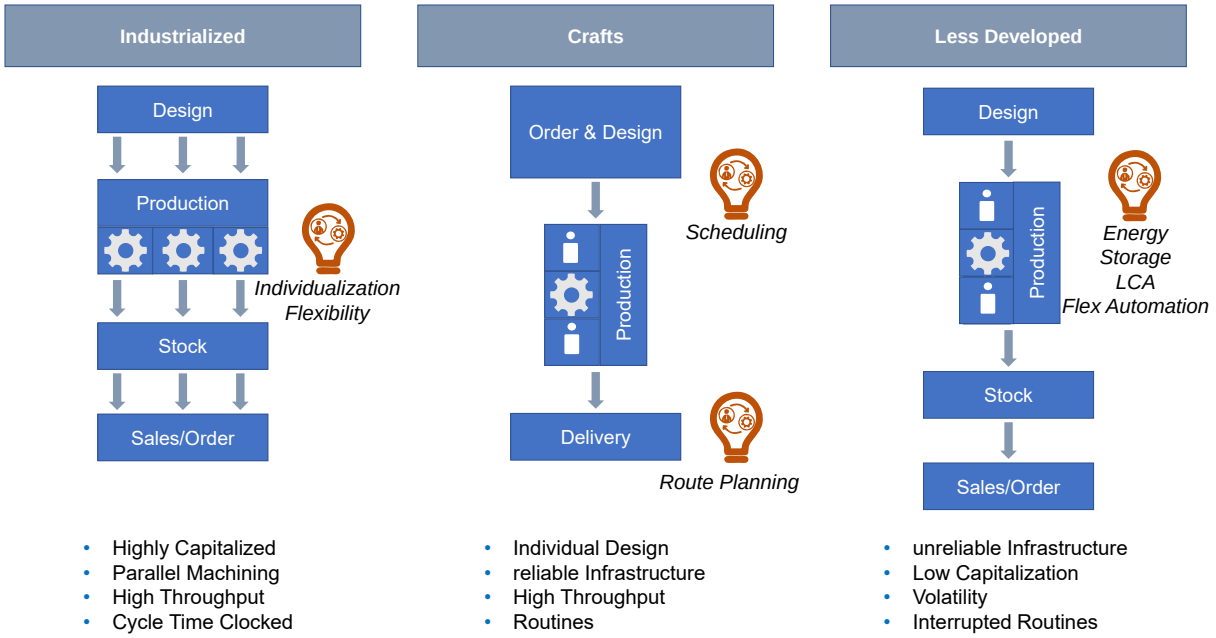

Figure 5. (S)CPPS Usage scenarios.

As mentioned, potential industrial use cases for CPPS or respective SCPPS are dominated by enabling individualization and product flexibility, as well as process flexibility. Such production is usually clocked by corresponding cycle times in order to synchronize parallel machining, allowing high throughputs, that are needed for the amortization of machinery. Productive crafts can easily be imagined to conclude individual contracts. The order is then produced usually with man power of the executing personal as bottle neck, while machinery is mostly not working full capacity but is frequently confronted with usage peaks and other organizations hazards [27]. SCPPS could help to schedule orders, so that synergies can be used and peaks of machine usage are avoided, while waiting times can be minimized. Production can follow the contract because of reliable infrastructure. Stock of raw material can easily be restored, a more or less steady flow of sales can be achieved through distance selling. Most important for a successful implementation is the ease of use. For less developed regions, in which infrastructure is insufficient, a make-to-stock model seems to be the pragmatic path, as individualization is not so advanced and it offers a steadier capacity usage. Furthermore, scarce capital will be rather be used for machinery than for floating assets, preventing large stocks and steady utilization of machinery. Bottle necks can mostly be traced back to the insufficient infrastructure affecting the supply chain. Once input factors are accumulated, machinery briefly becomes the bottleneck, as labor is usually flexible available at low cost. Energy is an input factor that is easily neglected in the western hemisphere. For regions heavily affected by shortages or low degrees of availability, this becomes another determinant for production. Autarkic systems as proposed by Reiff-Stephan et al. can level such effects out [28]. Whereas autarkic systems than need to be user friendly for usage as well as maintenance –a speaker, signaling when production is energetically feasible could benefit the mentioned system. Same holds true for low cost

automation (LCA), as a digital image can support intuitive reconfiguration, e.g., by a flow programming scheme, like the popular node-RED [29].

Conclusion and Summary

Competition between innovation driven extension of industrial production towards individualized produce and productive crafts may intensify. CPPS could be seen as a major driver of this development. Nevertheless, crafts offer a unique production structure that is unlikely to be made completely redundant and “producing” self-actualization for the people carrying out the profession, which industrial structures are less capable of. Both sectors could benefit from SCPPS in this regard. In a rather abstract manner starting points of SCPPS implementation have been shown for the discussed scenarios. Furthermore, it became clear that SCPPS are not solely a technical solution but during development and implementation sociological aspects embedding the stakeholders need to be considered as well.

Further research could benefit from exemplarily implementation and empirical observations that ought to support the deduced statements.

Acknowledgement

This publication was made possible through the funding of the PhD program *Innovation and Career Center - Integrated Engineering* by the state of Brandenburg’s Ministry of Research, Education and Culture (Germany).

References

[1] Hermann M, Pentek T, Otto B. Design principles for industrie 4.0 scenarios. *Proceedings of the Annual Hawaii International Conference on System Sciences*. 2016;2016-March:3928-3937. https://doi.org/10.1109/HICSS.2016.488

[2] Buer S, Strandhagen JO, Chan FTS. The link between Industry 4.0 and lean manufacturing: mapping current research and establishing a research agenda. *International Journal of Production Research*. 2018;56(8):2924-2940. https://doi.org/10.1080/00207543.2018.1442945

[3] Gassmann O, Csik M. Change a Running System. In: *Die Kunst der Innovation*. Gabler Verlag; 2012:41-49. https://doi.org/10.1007/978-3-8349-7188-3_3

[4] Monostori L. Cyber-physical production systems: Roots, expectations and R&D challenges. *Procedia CIRP*. 2014 Jan, 9-13. https://doi.org/10.1016/j.procir.2014.03.115

[5] Niggemann O, Lohweg V. *Proceedings of the AAAI Conference on Artificial Intelligence*. 2015 Mar.

[6] Thiede S, Juraschek M, Herrmann C. Implementing Cyber-physical Production Systems in Learning Factories. *Procedia CIRP*. 2016 Jan, 7-12. https://doi.org/10.1016/j.procir.2016.04.098

[7] Rudtsch V, Gausemeier J, Gesing J, Mittag T, Peter S. Pattern-based business model development for cyber-physical production systems. *Procedia CIRP*. 2014 Jan, 313-319. https://doi.org/10.1016/j.procir.2014.10.044

[8] Cabeza LF, Ürge-Vorsatz D, Ürge D, Palacios A, Barreneche C. Household appliances penetration and ownership trends in residential buildings. *Renewable and Sustainable Energy Reviews*. 2018 Dec 1;98:1-8. https://doi.org/10.1016/j.rser.2018.09.006

[9] *Das große Ding: Handwerk 4.0 Wie Betriebe und Beschäftigte erfolgreich den digitalen Wandel meistern Die Gewerkschaft für das Handwerk,*. IG Metall; 2015.

[10] Günther N, Reiff-Stephan J. Future Skills für die Produktion von Morgen. *AALE 2019*. 2019.

[11] Prescher T, Hellriegel J, Schön M, Baumann A, Heil M, Schulz F. Digitalisierung im Handwerk als Lernprozess fördern. *CEUR Workshop Proceedings*. 2016;1669(DeLFI):209-215.

[12] Günther N, Reiff-Stephan J. Prescriptive Education im Zuge der Industrie 5.0. In: Jäkel J, Thiel R, eds. *AALE*. Leipzig: VDE Verlag; 2020:315-320. https://doi.org/10.1007/978-3-642-51663-4_17

[13] Hipp C. *Innovationsprozesse im Dienstleistungssektor: Eine theoretisch und empirisch basierte Innovationstypologie*. Physica-Verlag HD; 2000.

[14] Gracia VB, Winkelheus K. The Next Revolution in Mass Customization : An insight into the sneaker market . La Próxima Revolución en la Personalización Masiva : Una visión en el mercado de las zapatillas de deporte .. 2016;4(June):85-104.

[15] Saldivar AAF, Goh C, Chen WN, Li Y. Self-organizing tool for smart design with predictive customer needs and wants to realize Industry 4.0. *2016 IEEE Congress on Evolutionary Computation, CEC 2016*. 2016;:5317-5324. https://doi.org/10.1109/CEC.2016.7748366

[16] McDermid CD, McDermid, D. C. How Money motivates Men. *Business Horizons*. 1960;3(4):93-100.

[17] Maslow AH. A theory of human motivation. *Psychological Review*. 1943 Jul;50(4):370-396. https://doi.org/10.1037/h0054346

[18] Schumann M. Industriearbeit zwischen Entfremdung und Entfaltung. *SOFI-Mitteilungen*. 2000;28(2000):103-112.

[19] Dörre K. Gewerkschaftseliten nach 1945 – Kontinuität und Wandel der Führungsgruppen deutscher Gewerkschaften: Das wiederbelebte Interesse an den gewerkschaftlichen Führungsgruppen. . Accessed 2006.

[20] Picot A, Dietl H, Franck E, Fiedler M, Royer S. *Organisation : Theorie und Praxis aus ökonomischer Sicht*. Stuttgart : Schäffer-Poeschel; 2012.

[21] Blankenberg A, Binder M. Göttingen: Volkswirtschaftliches Institut für Mittelstand und Handwerk an der Universität Göttingen (ifh); 2020. https://doi.org/10.3249/2364-3897-gbh-42

[22] Lahner J. *Innovationsprozesse im Handwerk, Göttinger handwerkswirtschaftliche Studien, No. 69*. Duderstadt: Mecke Druck und Verlag; 2004.

[23] Dörre K. Industrie 4.0 - Neue Prosperität oder Vertiefung gesellschaftlicher Spaltungen? Sechs Thesen zur Diskussion. 2016;:15.

[24] Ullrich O. Das Produktivistische Weltbild..

[25] Welzbacher C, Pirk W, Osterheimer A, Bartelt K, Bille J, Klemmt M. Digitalisierung der Wertschöpfungs- und Marktprozesse – Herausforderungen und Chancen für das Handwerk. *Eine Vorstudie im Rahmen der Konzeption eines Demonstrations- und Kompetenzzentrums im Handwerk*. 2015;:49.

[26] Zentralverband des deutschen Handwerks. Kennzahlen des Handwerks. . Accessed 2018.

[27] Kazaz A, Ulubeyli S, Acikara T, Er B. Factors Affecting Labor Productivity: Perspectives of Craft Workers. *Procedia Engineering*. 2016 Jan, 28-34. https://doi.org/10.1016/j.proeng.2016.11.588

[28] Reiff-Stephan J. Solar power in product development. In: Reiff-Stephan J, Amouzou K, Adanlete A, eds. *1st German-West African Conference on Sustainable, Renewable Energy Systems SusRes : 1st July 2020 - Kara, Togo*. Wildau: TH Wildau; 2020:55-65.

[29] Gokalp MO, Kayabay K, Akyol MA, Eren PE, Kocyigit A. Big data for Industry 4.0: A conceptual framework. *Proceedings - 2016 International Conference on Computational Science and Computational Intelligence, CSCI 2016*. 2017;:431-434. https://doi.org/10.1109/CSCI.2016.0088

2nd German-West African Conference on Sustainable, Renewable Energy Systems SusRes – Kara 2021

CPS & IOT (IIOT)

https://doi.org/10.52825/thwildauensp.v1i.19

Published: 15 June 2021

Implementation of a machine tool retrofit system

Alexander Dietrich[1][https://orcid.org/0000-0002-2482-7948], Ron van de Sand[1][https://orcid.org/0000-0002-8975-4030], and Jörg Reiff-Stephan [1][https://orcid.org/0000-0003-4176-6371]

[1] Technische Hochschule Wildau, Germany

Abstract. Small and medium-sized companies increasingly turning their attention towards the fourth industrial revolution. In order to increase their own long-term competitiveness, there is a growing desire to make production smarter, more efficient, safer and more sustainable through new technologies. Often, however, existing plants cannot be easily replaced by modern equipment. The reasons for this can be high investment costs, excessive downtimes or the unavailability of an equivalent machine. An alternative solution to the purchase of new equipment is the modernisation or expansion of existing systems, also called retrofitting. Thus, this paper deals with the retrofit process of a machine tool, whereby the software architecture of the control unit is the primary concern of this work.

Keywords: Retrofitting, CPS, Machine tool, Software Architecture

Introduction

Since the introduction of the fourth industrial revolution, the shape of the industry is changing and individual customer requirements become the focus of attention more than ever before. This paradigm shift from conventional production strategies towards fully connected value-adding processes places new demands on small and medium-sized companies (SME). To cope with this, Industry 4.0 (I4.0) enables more individual, flexible, efficient and sustainable production through the intelligent networking of machines and processes with the help of information and communication technologies [1]. Another concept that has recently come to the fore, are systems in which virtual and physical processes merge and interact, known as Cyber-Physical Systems (CPS) [2]. CPS can be seen as a technology for upgrading production for Industry 4.0. and consist of sensors, actuators, embedded systems, control, computing and communication devices that collect data and enable their availability [3]. However, implementing conventional machine tools into a CPS environment is not a trivial task, as these systems often do not provide adequate sensors or communication standards and mostly rely on proprietary system architectures, which inhibits the interconnection with other devices.

With machine tools, raw material is processed into a saleable product. These systems are part of the inventory of every company and impress with large quantities and high resource consumption [4]. They often constitute a high proportion of a company's capital. For this reason, a work life of 20-30 years is common for such machines [5]. Due to the paradigm shift in the course of Industry 4.0, older machine tools may no longer meet the requirements for quality or connection ability. Retrofitting offers an alternative solution to the purchase of a new machine.

Retrofitting can be divided into two categories, namely: traditional and smart retrofitting. Traditional retrofitting is the replacement of components to optimise accuracy, speed, maintainability and ease of use [5]. Upgrading the drive and control elements of an old machine is one way to extend work life. But often, when the machine is about to reach its payback point, the drive and control elements still meet the quality requirements but they do

not fit into modern production systems [4]. Therefore, smart retrofitting focuses on adapting existing equipment at a low-cost level. By adding smart sensors inside the old machine tool, relevant data will be generated. Both the historical and real-time data can be used to access status and condition of the system. The data can be, for example, further processed into a cloud service and also provides a decision-making basis for the plant control [5]. It should be noted that, for successful modernisation according to the idea of Industry 4.0, both types of retrofitting are necessary.

An important point that should be considered when retrofitting existing machinery is the control software of Programmable Logic Controllers (PLC). Due to the increasing functionality, higher availability as well as the higher degree of automation through modernisation, the demands on the PLC software are increasing [6]. Therefore, the development costs of the software contribute a not negligible share to the total costs of the retrofit project [7]. Especially when it comes to sustainability, it is important that the software has a modular structure and thus allows it to be extended, easy maintainable or individual modules to be tested at an early stage of development. For the reasons mentioned above, this paper describes both the hardware retrofitting process and the PLC software architecture.

Related Works

Stock and Seliger (2016) [8] describes various ways of realising sustainable manufacturing in Industry 4.0. The authors identify retrofitting as one opportunity for sustainable manufacturing. In a case study, retrofitting is applied to a machine tool. Therefore, the retrofit process is divided into four essential steps: situation analysis, defining of the monitoring strategy, data processing and implementation of the equipment in a CPS. As a result of the case study a milling machine has been extended by an acceleration sensor. Although their approach shows the fundamental steps of the retrofitting process, they leave open the question of how connectivity can be achieved.

A first retrofitting approach which is independent of the type and model of equipment is highlighted by the authors of Baker et al (2016) [9]. The authors are mainly concerned with requirements engineering for the technology applied in the modernisation process of subsea equipment used in offshore deepwater operations. To objectively define the requirements, they use a Model-Based Systems Engineering framework, which is basically the application of models to support product development at any stage of development or life cycle. Even though they do not devote to a specific type or model of equipment, their approach is limited subsea equipment. In addition, their work concentrates on the definition of requirements for this particular use case.

Arjoni et al. (2017) [10] propose retrofit techniques and focus on keeping the cost factor as low as possible. These developed techniques are demonstrated on three machines forming an academic plant. All three retrofit processes are about establishing intelligent and remote communication, as the scoped machines are outdated and do not allow communication with modern equipment. As a result, the authors present the Raspberry Pi 3 boards as a cost-effective tool in the retrofit process due to their versatility and stable operation.

Ehrlich et al. (2015) [11] consider the modernisation of a production line in terms of the potential offered by modern Industry 4.0 technologies. They conclude that the replacement of a whole production line by I4.0 technology at once is not financially feasible and they do not see the retrofit process as a “knee-jerk” action but more as a progressive process. The authors also present a new business model called Retrofitting as a Service. The retrofit process itself is divided into four steps, but the approach is limited to production lines.

Al-Maeeni et al. (2020) [5] show one way in which augmented reality (AR) can be used to increase the ease of use as well as reduce costs and processing times of existing machines and equipment. They use AR as a tool to help the machine operator to do the right

thing in the right sequence. In a case study, the authors use a navigation aid displayed on a Google HoloLens to improve orientation on a rotary bending machine due to an unstructured and unclear process flow. With this, they demonstrate a new technology or tool in the context of retrofitting.

In [12] and [13], Lins et al. deal with the topic of retrofitting in the context of Industry 4.0. These papers aim to develop a universal approach to transform industrial equipment into a CPS. In the latter contribution, a retrofitting platform is presented resp. developed, which provides resources for integrating old equipment in I4.0, regardless of the model or type. Inspired by the Reference Architectural Model for Industry 4.0, the developed retrofitting platform consist of three layers: infrastructure, communication and application. Furthermore, requirements, components and technical necessities to assist the implementation of the proposed platform were defined.

Friesen et al. (2020) [14] published a guide for retrofitting that applies regardless of the model and type of equipment used, similar to the work of Lins et al. (2020) [13]. This work is specifically aimed at companies that want to practise retrofitting. In addition to a detailed introduction to the field of retrofit, the authors present a multi-stage retrofit model. The multi-stage model shows users their current progress in the Industry 4.0 retrofitting as well as the stages and the order in which they need to be passed through. Subsequently, the universal approach is presented, which is split into 10 steps. Although the work of Friesen et al. gives a very detailed overview about the retrofitting process, they leave open the question of integration into Industry 4.0 architectures.

Lins et al. (2020) [13] and Friesen et al. (2020) [14] introduce an approach for retrofitting that can be applied regardless of the model and type of equipment. However, for the implementation of retrofit, it is beneficial to use the work of Lins et al. (2020) [13] as a basis, as this work clearly defines various requirements, components, methods and resources.

Related work on retrofit only show the upgrading process of the hardware, while the software is often left out of the discussion. In addition, the implementation is often not described in detail. The aim of this work is to look at the entire retrofit process from both the hardware and the software side in a case study.

Software Architecture

Software architectures describe a shared understanding of the design of a software application. Typically, an architecture describes how major components of a system interact with each other. The representations of software architectures are usually subjective, as the view of the significant architectural features may change during the life cycle [15].

A widely used architecture of software systems is the multitier architecture in which the software is subdivided into several layers. Each layer has a specific responsibility and contributes with its function to the overall application, whereby it provides and uses services. The basic principle of a multitier architecture is to allow only neighbouring layers to interact with each other. As a result, the system remains modular. This means that a layer can use the services of another layer without having to understand how this layer works [15]. This advantage is particularly useful in the development of standardised processes. However, layered architectures are not suitable for every application. A major disadvantage is that the software cannot be easily adapted to changing requirements. The reason for this is that the business logic is rooted in all layers. In addition, many layers harm the performance of a system.

This paper presents and applies a hexagonal architecture, also called *Ports and Adapters*, which was according to Litvinov (2020) [16] originally introduced by Alistar Cockburn in 2005. The idea is that users, programs, automated tests or batch scripts should drive the application equally. Furthermore, this and other approaches are the consequence of the desire for more flexibility, adaptability, maintainability and testability in software

development [16]. The hexagonal architecture consists the three layers: domain, application and framework. Compared to multitier architectures, in here the business logic is strictly separated from other logic elements. Consequently, the hexagonal architecture departs from the conventional multitier models and introduces ports and adapters. Ports define the protocol in which an interaction with the domain layer is allowed. In other words, they specify how the communication with the outside world can be established [17]. Adapters, on the other hand, form the bridges between the outside world and all ports. They convert incoming signals into a protocol-specific form so that the domain layer is capable of interpreting the signals and vice versa [16].

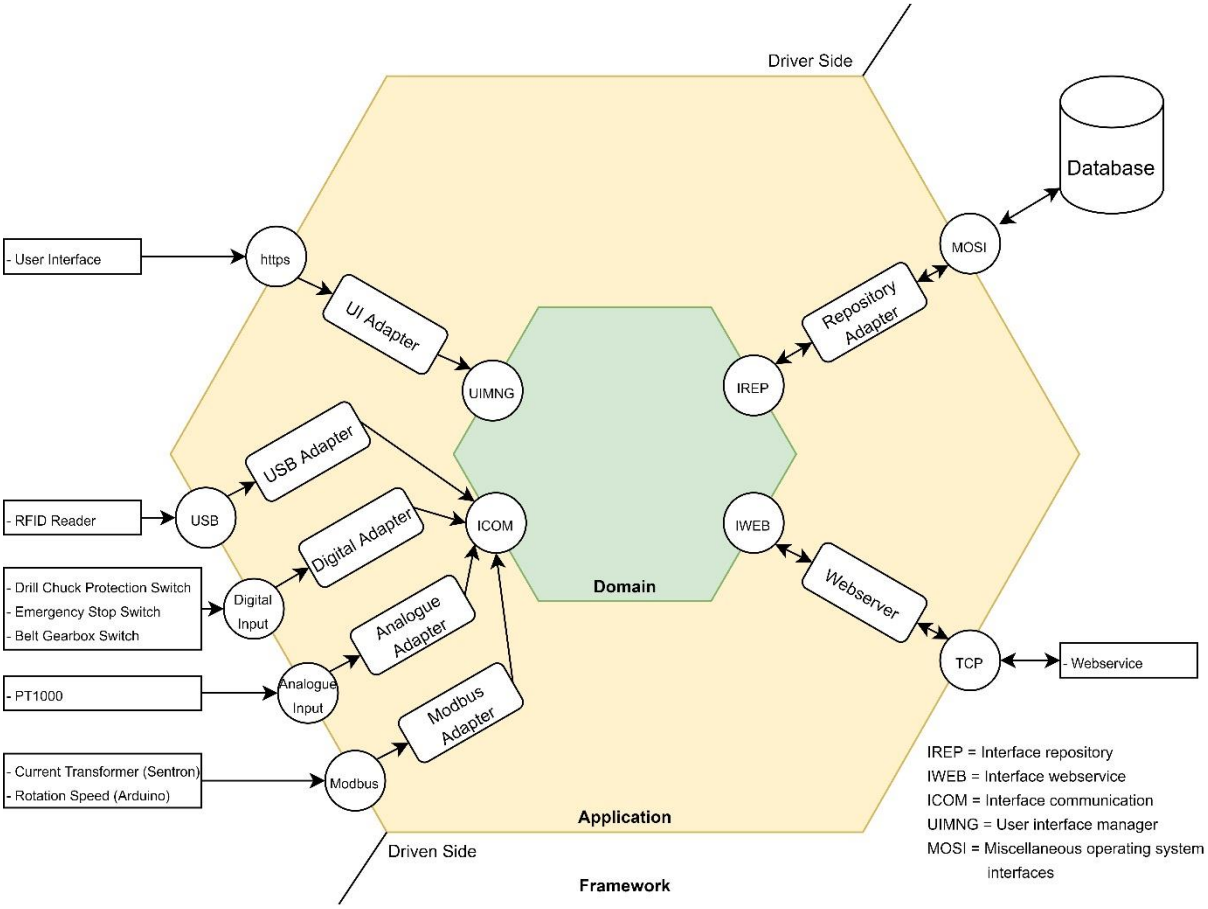

Figure 1. Software architecture

Figure 1 shows the architecture of the developed software. In the middle of the abstract diagram is the domain layer. The domain is the central part of the software and contains the business logic. Summarised, the business logic describes the behaviour and constraints of the application. In addition, the domain layer acts as a supervisor and throws errors if there is incorrect communication with the domain. In the figure shown, the circle elements describe the ports. There is a difference between inner and outer ports. The outer ports are the interfaces between the outside world and the application itself, whereas inner ports are the interfaces to the domain layer. Between the inner and outer ports the application layer is rooted and links the framework to the domain layer. All adapters are embedded in the application layer. The adapters convert the input of the outer ports into a shape that can be understood by the domain. As shown in figure 1, the entire application is surrounded by the framework layer. This outermost layer contains all input and output devices, other applications, external libraries or third-party services.

Use Case

According to the universal approach given by Lins et al. [13], the retrofit procedure begins with the mapping of all existing resources and the definition of new resources. For the implementation of the resources and the achievement of all functionalities, various components have to be added to the system. All available components are divided into three structural layers. The layers are interconnected and each component has access to information and functions of other components [13]. The infrastructure layer covers the support and connection of the components to the industrial equipment. The communication layer is responsible for integration into an industrial network and communication with other network participants. Finally, the application layer enables interaction with other applications within the industrial network. Figure 2 shows the relationship between the added components and the bench drill.

Existing resources. The bench drill used in this case study is an OPTIdrill D17 Pro made by Optimum. It is a hand-operating bench drill with a maximum power of 500W. Between the motor and the spindle, there is a belt drive. By changing the drive ratio of the belt, the spindle speed can be regulated between 500 and 2520 min^{-1}. An inductive sensor is used to detect the speed. A metallic object is attached to one pulley on the spindle so that a signal is triggered with each full revolution. In addition to the speed, the machine also detects the height of the drilling tool. A potentiometer is mounted on the feed lever, which changes its resistance (and hence the voltage) equivalent to the height of the drilling tool. The machine's digital display contains a HT46R54A 8-bit microcontroller that processes the signals of the speed and drilling tool height as well as visualising them on the display. The machine is also equipped with an emergency stop switch, a switch for the drill chuck protection and a magnetic switch for the belt gearbox. Each of these switches can interrupt the power supply to the motor and consequently stop the machine.

Defining new resources. Following the description of the Lins et al. 2020 [13], the new resources must be defined. In addition to the drilling tool height and the spindle speed, the motor temperature, the room temperature, the motor current and the motor voltage needs to be measured too. The positions of the three safety switches also need to be digitized. Adding an RFID identification enables the assignment of process data to the current job and the user working on it. The data collected shall be stored in a database. For communication with other Industrial Internet of Things (IIoT) devices, the CPS needs to be extended by an interface to an Industry 4.0 network. Furthermore, relevant information must be visualised via a user interface directly on the drilling machine and remotely via a web service. Table 1 shows a list of all resources.

Infrastructure and Communication

Embedded Board. The main component of the infrastructure layer is the embedded board, which receives the signals of all sensors. Such a board requires the support of various connections, buses and interfaces [13]. In this case study, a Revolution Pi Connect+ is used. The Revolution Pi is a programmable logic controller made by Kunbus. The PLC supports several industrial bus systems such as Modbus and RS485 and others like USB. Furthermore, extension modules allow the use of additional communication interfaces. Since the embedded system of the drilling machine does not offer a communication interface, the sensor signals must be captured separately. With the extension modules DIO (Digital In- and Output) and AIO (Analogue In- and Output), the signals of the integrated sensors of the machine tool can be received and processed by the PLC. The DIO module adds 16 individual digital inputs and outputs to the PLC. With the AIO module, up to 6 analogue signals can be captured and up to 2 analogue outputs can be controlled. The DIO module is responsible for monitoring the safety switches, while the AIO module monitors the temperature sensors and the potentiometer. All inputs and outputs on the PLC and the extension modules are read cyclically every 20ms.

Power Monitoring Device. As the PLC and the expansion modules only work up to a maximum of 24VDC, the additional power monitoring device Sentron PAC3200 from Siemens is used. The Sentron PAC3200 measures the supply voltage (≈230VAC), measures the current at the motor and sends the information to the PLC via the Modbus TCP/IP interface, where the PLC software can compute the power from these two values. However, instead of the primary current of the motor, a secondary current is measured, which is generated by an AX-0500 current transformer. The current transformer has a transmission ratio of 500:1.

Temperature sensor. A complete representation of the physical machine in the virtual world also includes the monitoring of temperatures. Since the AIO module of the PLC has two inputs especially programmable for resistance temperature detectors (RTD), two PT1000s are used to detect the room and motor temperatures. The AIO module automatically computes a temperature from the analogue signal.

Microcontroller. The PLC with a cycle time of 20ms is not fast enough to capture the signal peaks of the inductive sensor for the rotational speed. For this reason, an Adafruit Feather M0 Bluefruit microcontroller is used. The microcontroller measures the time difference between two signal peaks and sends this value periodically to the PLC via the RS485 bus.

USB RFID Reader. The bench drill is equipped with two USB EM 4100 radio-frequency identification (RFID) readers. One RFID reader is responsible for the user access identification. This means that registered users can only start the machine. Otherwise, relays interrupt the power supply. Another reader is responsible for identifying the current job. By scanning the RFID tag, the system searches for the route card belonging to the current job and displays it on the monitor.

Communication. The integration of a network component is an essential part of retrofitting. The network component is responsible for integrating the industrial equipment into an Industry 4.0 communication network. The PLC attached to the drilling machine still has an unused Ethernet port. A static IP address is set for this port so that other network participants can access the historical and live data via TCP IP protocol.

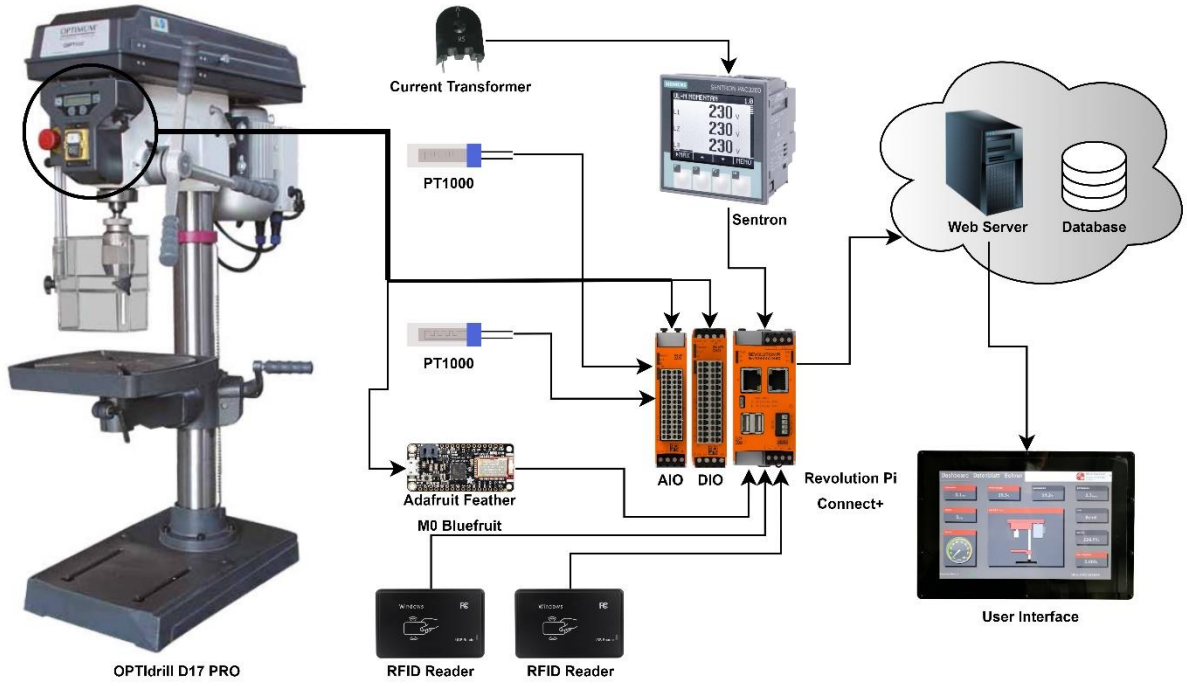

Figure 2. Retrofitted bench drill

Application

Database. By using a database component, historical process data can be stored and retrieved. Also, user-specific information for machine access and job details are stored. A SQLite database is used for this purpose. Another advantage of using a database is that the recorded process parameters are linked to the respective job and the machine user. This improves and simplifies the evaluation of the dataset.

Webserver. In general, the purpose of a web service component is to provide quick and easy access to relevant data. The web server is built with the web framework Flask. Flask is suitable for simple applications and supports simple URL routing.

Visualising Component. The visualization component works in cooperation with the webserver. The user interface is accessible via a website. For this purpose, a 10.1-inch capacitive touch Liquid Crystal Display (LCD) is equipped on the drilling machine, which displays relevant information to the user. The user interface only visualizes the process and cannot affect the physical process itself.

Results and Conclusion

In this paper, a traditional drilling machine, commonly encountered in industry, was equipped with modern acquisition and communication technologies (retrofitting). For this purpose, different approaches from the literature were presented and analysed for their suitability. By using a universal approach, the machine tool was upgraded for integration into I4.0 systems. Besides the integration itself, further functionalities were added. Table 1 shows the results of the retrofitting process and compares the before and after state.

Table 1. Retrofitting results.

Resource	Before	After	Description
Network	-	Ethernet, Wi-Fi	The use of Wi-Fi or Ethernet makes data available to other devices inside the network
Database	-	Local network	Stores historical data and makes information available to network participants
RFID User Identification	-	Machine-User assignment	Make the machine available only for trained and instructed employees
RFID Job Identification	-	Machine-Job assignment	By scanning the RFID tag, the monitor shows the route card of the current job
Measure motor temperature	-	Local network	System is able to measure motor temperature and provide data to other network participants
Measure Room Temperature	-	Local network	System is able to measure room temperature and provide data to other network participants
Webserver	-	Local network	Webserver provides data for user interface
Motor power consumption	-	Local Network	System is able to measure motor power consumption and provide data to other network participants

Drilling tool height	Display at the machine	At the machine and accessible via local network	System is able to measure drilling tool height and provide data to other network participants
Rotating spindle speed	Display at the machine	At the machine and accessible via local network	System is able to measure rotating spindle speed and provide data to other network participants
Display Parameters	Digital Display	Digital Display and LCD Monitor	Relevant data is displayed on an additional monitor in a user interface
Checking the positions of the safety switches	-	Local network	System is able to identify the positions of the safety switches and provide data to other network participants

Furthermore, the architecture of the control software is presented in this paper. The presented software departs from the conventional layered architecture and builds on a hexagonal architecture. Due to the principle of ports & adapters, it is possible to separate the business logic from the rest of the logic. As a result, the domain becomes independent of the rest of the application. Thus, the system can easily be extended by further components. This only requires the creation of an adapter, which communicates with the domain via the defined ports. An additional effect, individual software elements can be tested independently of the entire system.

Future Works

As future work, it is intended to implement an Open Platform Communications Unified Architecture (OPC-UA) component. This will standardise the data transfer and ensure interoperability between the communication participants. On the basis of this paper, a digital twin will be built for a complete representation of the machine in virtual world. In addition, the system will be extended by an AR application.

Acknowledgement

This project was realised within the framework of the Kompetenzzentrum Cottbus (Project number 01MF17001C), a joint project between BTU Cottbus, HNE Eberswalde, IHK Cottbus, IHP Frankfurt (Oder) and TH Wildau, which is part of the funding initiative “Mittelstand Digital” and supported by the German Federal Ministry of Economics and Energy (BMWi).

References

[1] Kagermann H, Wahlster W, Helbig J. *Recommendations for implementing the strategic initiative industrie 4.0: Final report of the industrie 4.0 working group*. Berlin, Germany: Forschungsunion; 2013.

[2] Lee EA. Cyber Physical Systems: Design Challenges. *2008 11th IEEE International Symposium on Object and Component-Oriented Real-Time Distributed Computing (ISORC)*. 2008 11th IEEE International Symposium on Object and Component-Oriented Real-Time Distributed Computing. 2008 05. https://doi.org/10.1109/isorc.2008.25

[3] Jazdi N. Cyber physical systems in the context of industry 4.0. 2008 11th IEEE International Symposium on Object and Component-Oriented Real-Time Distributed Computing (ISORC). 2008, 363–369.

[4] Lange G. Modernisierung von Brownfield-Anlagen. *P&A*. 2020;17(7):12-15.

[5] Al-Maeeni SSH, Kuhnhen C, Engel B, Schiller M. Smart retrofitting of machine tools in the context of industry 4.0. *Procedia CIRP*. 2020;88:369-374. https://doi.org/10.1016/j.procir.2020.05.064

[6] Zaeh MF, Poernbacher C. Model-driven development of PLC software for machine tools. *Production Engineering*. 2008 02 19;2(1):39-46. https://doi.org/10.1007/s11740-008-0083-7

[7] Weck M. *Werkzeugmaschinen 4: Automatisierung von Maschinen und Anlagen*. 6th ed.. Berlin-Heidelberg: Springer; 2006.

[8] Stock T, Seliger G. Opportunities of Sustainable Manufacturing in Industry 4.0. *Procedia CIRP*. 2016;40:536-541. https://doi.org/10.1016/j.procir.2016.01.129

[9] Baker J, Ferraioli P, Pereira LR, Hudson A, Barton G, Bhatt S, Fritz M, Odegard R. Requirements Engineering for Retrofittable Subsea Equipment. *2016 IEEE 24th International Requirements Engineering Conference (RE)*. 2016 IEEE 24th International Requirements Engineering Conference (RE). 2016 09. https://doi.org/10.1109/re.2016.44

[10] Arjoni DH, Madani FS, Ikeda G, Carvalho GDM, Cobianchi LB, Ferreira LFLR, Villani E. Manufacture Equipment Retrofit to Allow Usage in the Industry 4.0. *2017 2nd International Conference on Cybernetics, Robotics and Control (CRC)*. 2017 2nd International Conference on Cybernetics, Robotics and Control (CRC). 2017 07. https://doi.org/10.1109/crc.2017.46

[11] Ehrlich M, Wisniewski L, Jasperneite J. Usage of Retrofitting for Migration of Industrial Production Lines to Industry 4.0. *KommA 2015 – Jahreskolloquium Kommunikation in Der Automation, Magdeburg, 2015*..

[12] Lins T, Augusto Rabelo Oliveira R, H. A. Correia L, Sa Silva J. Industry 4.0 Retrofitting. *2018 VIII Brazilian Symposium on Computing Systems Engineering (SBESC)*. 2018 VIII Brazilian Symposium on Computing Systems Engineering (SBESC). 2018 Nov. https://doi.org/10.1109/sbesc.2018.00011

[13] Lins T, Oliveira RAR. Cyber-physical production systems retrofitting in context of industry 4.0. *Computers & Industrial Engineering*. 2020 01;139:106193. https://doi.org/10.1016/j.cie.2019.106193

[14] Friesen A, Flatt H, Jasperneite J. *Leitfaden Retrofit für Industrie 4.0*. (VDMA, Fraunhofer-IOSB-INA, eds). VDMA Verlag GmbH; 2020.

[15] Fowler M. *Patterns of Enterprise Application Architecture*. Addison-Wesley; 2012.

[16] Litvinov AA. ON BUSINESS LOGIC LAYER DESIGN AND ARCHITECTURE. *System technologies*. 2020 03 27;1(126):86-95. https://doi.org/10.34185/1562-9945-1-126-2020-09

[17] Pirker A, Lechner N. Designing Secure Architecture of Health Software using Agile Practices. Central European Conference on Information and Intelligent Systems, Faculty of Organization and Informatics Varazdin. 2019, 269-280.

2nd German-West African Conference on Sustainable, Renewable Energy Systems SusRES – Kara 2021

CPS & IOT (IIOT)

https://doi.or/10.52825/thwildauensp.v1i.35

Published: 15 June 2021

Challenges of IoT deployment in the context of developing countries

Bernardo Y. León-Ávila[1] [https://orcid.org/0000-0001-7985-0224], Yunior R. Hernández-Cabrera[1], Luis A. Quintero-Domínguez[1] [https://orcid.org/0000-0002-3527-0516], Felipe Hernández Pentón[1], and Frank R. Quesada Espinosa[1] [https://orcid.org/0000-0002-1576-6733]

[1] Universidad de Sancti Spíritus José Martí Pérez, Cuba

Abstract. The concept of the Internet of Things (IoT) is not exactly a novelty, even if it has not burst out yet with all the force that the market expected. The 5th generation of mobile telephony (5G) is rushing to deploy in the midst of a real trade war, and intends to get one's own way on this and others fronts. This paper analyses how to overcome the challenges of an IoT deployment, which can be too complex to fulfil its promise of massification and ubiquity. This analysis is primarily intended to identify whether 5G will be the key to a current IoT deployment in all contexts, or whether it is wise to pursue other development paths first.

Keywords: 5G, IoT, Road to Development

Introduction

Although all the current development of communication technologies has been oriented mainly to communication between people, new trends are encouraging machines and devices to connect massively, giving rise to Internet of Things (IoT). The IoT represents an ecosystem that is expected to be made up of 100 billion devices by 2025: sensors, alarms, wearables, mobile phones, household appliances, code readers, etc. According to Huawei's estimations, on this date only 10% of the total connections will be between humans; the rest will be between devices in autonomous way.

Technologically speaking, when dealing with the IoT there are three layers or levels. The first corresponds to devices, sensors and actuators whose main function is to capture different variables such as temperature or light, which are converted into electrical impulses (data). The second level is the "IoT gateway" or gateway, which includes the hardware and software components that serve as a connection point between the cloud and the controllers, sensors and intelligent devices. This level

configure the architecture required for data processing. Finally, the third layer of the IoT platform is where business, consumer applications and services are located [1].
The International Telecommunication Union (ITU) has created the overall roadmap for the development of 5G mobile technology and has defined the term "IMT-2020" to designate it. Following the completion of its work on the 5G "Vision" at the ITU Radiocommunication Section (ITU-R) 5D Working Party meeting in San Diego, California, the ITU defined the overall objectives, process and time frame for the development of 5G mobile systems [2].
To fulfil its promise of massification and ubiquity, IoT requires an infrastructure deployment that industry has been unable to supply, and 5G promises to deliver. This paper attempts to analyze whether 5G will be the key to a current IO deployment in all contexts, or whether it is wise to pursue other development paths first.

5G for IoT

One of the strongest reasons to think about revolutionizing mobile telecommunications is the IoT. The 5G is intended for this purpose, and its architecture has been redesigned by up to 36% to support the news requirements [3]
In the words of Asha Keddy, general manager of mobile standards for advance tech at Intel, "we'll see computing capabilities getting fused with communications everywhere, so trillions of things like wearable devices don't have to worry about computing power because network can do any processing needed" [4].
The IHS Markit consulting firm has conducted a forecasting exercise through 2035 based on knowledge of the impact of previous generations of wireless technologies and forecasts of the enormous opportunities. One of their conclusion was that "5G value chain will generate a return of $3.5 trillion and 22 million jobs. This figure is larger than the value of today's entire mobile value chain" [5].
The basic performance criteria for 5G systems have been established by the ITU in its Recommendation IMT-2020. ITU-R M.2083 describes three general usage scenarios for 5G systems [6]:

- Enhanced Mobile Broadband, to cope with vastly increased data volumes, global data capacity and user density
- Massive machine type communications. This use case is characterized by a very large number of connected devices typically transmitting a relatively low volume of non-delay sensitive data. Devices are required to be low cost, and have a very long battery life
- Ultra-reliable and low latency communications to support mission-critical and safety-critical applications

At this definition stage, one might ask whether the work teams will make the standardization and regulatory decisions that make it feasible to meet these expectations.
Figure 1 shows the increase in 5G network capabilities with respect to LTE-Advanced, technology for 4G by the 3GPP group.

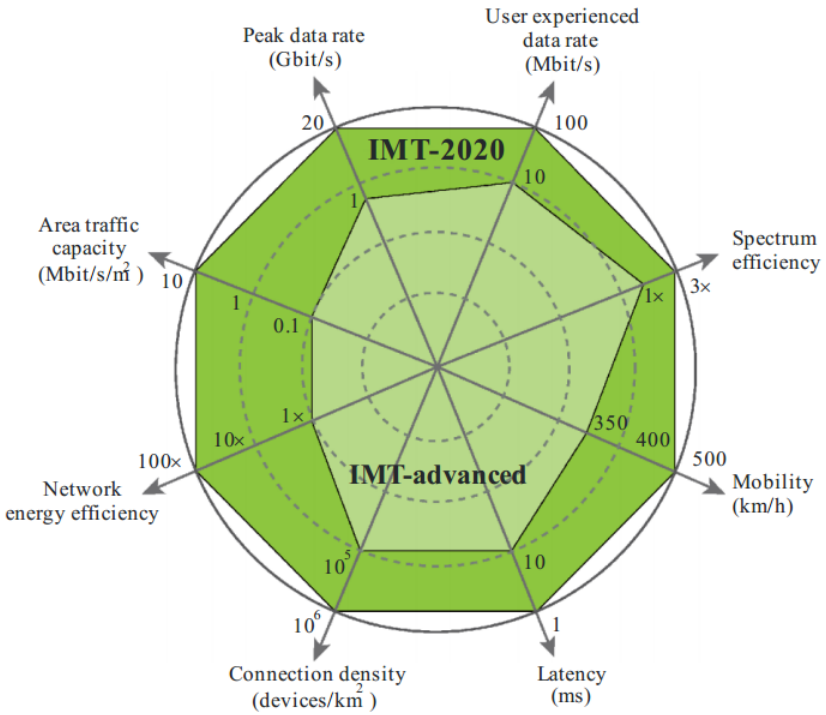

Figure 1. Enhancement of key capabilities from IMT-Advanced to IMT-2020 [6].

The 5G still has several major challenges to overcome that may slow down its massive deployment. The most illustrative are:

- **The radio spectrum:** This is probably the most important technological challenge facing 5G communications [7]. Brett Tarnutzer, director of the Spectrum GSMA, says "Operators urgently need more spectrum to deliver the endless array of services that 5G will enable (...) Without strong government support to allocate sufficient spectrum to next generation mobile services, it will be impossible to achieve the global scale that will make 5G affordable and accessible for everyone [7]. According with this goal, the GSMA has published the 5G Spectrum GSMA Public Policy Position [8].

  In order to support all expected performance, the ITU proposes to use the frequency bands above 24 GHz [8]. This means that operators will need to deploy thousands (or perhaps millions) of small cells throughout the territory: on streetlights and urban layouts, on the facades of buildings, and even inside individual homes, a deployment process that will be slow and require multi-million dollar investments.
- **Security issue:** More data means more challenges. Let's add that the 5G is the first generation of mobile networks designed for M2M machine-to-machine communication. The biggest security challenge posed by 5G networks is privacy. 5G networks will enable new types of applications and allow us to connect more

devices to the network (and each other), encouraging us to capture and share more and more of our personal data. Some of which may never have been captured digitally before. In this regard, the 5G Americas group makes an analysis of the emerging threats facing 5G and the different mitigation mechanisms [9]. Threats that are not exactly new, but of a greater scope, so potentially more invasive and with catastrophic effects.

- **Money Matters:** All the promises of 5G will not exactly be painless for mobile ISPs. The 5G requires that the deployment of the networks responds to the ambition of those who have designed the new technology, multiplying several times the number of antennas and modifying their topology. The key is that, with 5G, ISP networks can be used for functions that are now impossible, significantly extending their range of use and therefore also increasing, at least theoretically, revenue. However, the high cost of deploying these new networks in all their magnitude is a great challenge especially for telecommunication operators who have to bear it, especially when the differential economic return, although intuited, isn't yet evident.

IoT Deployments for Developing Countries

5G promises many technological advances and a great economic boost; but without a clear business model for all, and a prohibitive deployment cost for many economies. Maybe this new revolution in the field of mobile technology will have to wait for better times.

The biggest impact expected for 5G is on services and manufacturing. 5G's main customers are machines and objects, so in economies with weak and obsolete industry, based on infrastructures with very poor or no automation, you will have very few customers to help you with ROI (Return on Investment). In the end, the funds for deployment will be taken from the development of other sectors that also need it, sectors whose activity will be reversed in development in a faster and more objective way.

So, if it is not wise to think about the deployment of 5G for now, it could be thought, do we have to postpone the IoT as well? Of course not.

Although the 5G's sellers show it as the key piece for the massive deployment of the IoT, this concept has its own live, and has been born from several previous technologies and paradigms, so there are always excellent options.

LPWAN

LPWA (Low Power Wide Area) or LPWAN (Low Power Wide Area Network) for many authors. These terms do not denote any particular technology, but can be use as generic term to refer to any network designed perfom a low-power wireless communication with other networks, such as telephony, satellite communications or WiFi networks.

There are several technologies based on open or proprietary standards, such as LoRaWAN, Telensa, Sigfox, Igenu Networksentre's Random Phase Multiple Access (RPMA) and others. In a general sense LPWANs provide long range, promising

coverage up to 15 Km in open environments and up to 2 Km in urban environments. They are designed to give access to a potentially high number of devices that have to transmit small amounts of data (few bytes) sporadically (e.g. every few minutes), mostly to the server.
LPWA networks are used almost exclusively in the field of IoT devices and M2M communications. Its applications are in remote meter reading, public lighting control, theft alarms or control systems in infrastructure, crop irrigation system, unattended weather stations, animal control, and many others.
Another great advantage of these technologies is the use of unlicensed spectrum, although it is not in the classic 2.4GHz and 5GHz. The chips typically offer channels in the 867 and 869 MHz bands (Europe), 902 and 928 MHz (America and Asia). The regulations on this subject should be reviewed for non-invasive use of licensed frequencies.

NB-IoT

Taking care your own network infrastructure, especially when there are nodes in the field, can be quite problematic for companies that don't want to have too large an IT structure. It would be desirable if our mobile provider have solutions that do not include the trauma of paying for a SIM card for hundreds of devices. The solution has been NarrowBand - Internet of Things or NB-IoT for short.
The GSMA's initiative, NB-IoT uses the mobile phone bands and is designed to operate in several ways, including the use of the GSM band replacing the current deployment (standalone). Also uses the LTE band and therefore sharing it (in-band), or even using the spacing between LTE channels to maximize the communications spectrum (guard-band).
NB-IoT is a half-duplex technology that enables efficient uplink communication, that is, it allows the establishment of connection to the cellular network, the allocation of network resources to the node (known as User Equipment or UE) and the transmission of data (MT Data). In the most typically application, an UE will remain disconnected from the network and, when it has data to transmit, e.g. a meter reading, it will establish the connection, transmit the data and disconnect as soon as it receives confirmation of delivery [10].
NB-IoT is reliable because it guarantees the data delivery. This is significant if is compare with other LPWAN technologies based on an ALOHA access. Also, the use of a licensed band makes it more reliable due it does not coexist with other technologies. However, using a licensed band has implications such as being dependent on an operator and therefore subject to a service and coverage model beyond control of the application. E. g. if LoRaWAN used, and there is little coverage, an extra Gateway can always be deployed; but with NB-IoT, all is on the operator's hands.

LLNs

Like LPWA, LLNs (Low-power Lossy Network) is a set of technologies that include devices with very limited resources, both energy, computing performance and embedded memory. The main different with LPWA is the coverage area, just a few meters (around 200 m). This networks are formed in multi-hop meshes to connect to

the Internet. This idea follows the principle that multiple short jumps within a mesh are much more energy efficient than a single jump to a sink (gateway).
As in engineering, what is usually earned in one hand is sacrificed in the other. In an LLN, finding neighbors and then having them find a route to the gateway is not exactly a simple task. In LLNs, nodes (known as motes) must enter their work area, recognize their neighbors, and collaboratively find their way to the sink.
IEEE 802.15.4 is the standard for Low-Rate Wireless Personal Area Networks or simply Low-Rate Wireless Networks from 2015. The reduction of the acronym is due to the fact that its uses, potentialities and expectations began to go beyond the personal area to endorse the IoT's lines.
An important step towards the robustness of these networks was the 802.15.4e amendment [11] which specifies the TSCH (TimeSlotted Channel Hopping) mechanism within the multi-channel mechanism to mitigate the effects of multi-path fading and interference generated by different commercial devices.

Conclusions

For the first time, objects are the primary customer of a commercial telecommunications network. This is undoubtedly the most revolutionary contribution of the 5G, which expects to deploy the massive IoT and applications with critical performance and delay requirements. Its gradual implementation of 5G will have an economic impact on all industrial sectors.
However, it should be keep in mind that any forecast will depend on the implementation timetable, national regulations and the possibility of consolidating the new business models. For now, its cost and deployment challenges are not justified in economies with a underdeveloped infrastructure that will presumably not exploit the capabilities and benefits of this new generation of mobile telephony.
But the IoT is not intrinsically linked to 5G. There are several solutions that can be deployed by both public operators and other companies that wish to expand their service portfolio using a more competitive model.

References

1 W. Dargie and C. Poellabauer, *Fundamentals of Wireless Sensors Network, Theory and Practice*. John Wiley and Sons, Ltd., 2010, ISBN: 978-0-470-99765-9.

2 ITU, *ITU defines vision and roadmap for 5G mobile development*, (accessed 2018-04-06), 2015. [Online]. Available: http://www.itu.int/net/pressoffice/press_releases/2015/27.aspx (visited on 04/06/2018).

3 E. Obiodu and M. Giles, *The 5G era: Age of boundless connectivity and intelligent automation*, 2017. [Online]. Available: https://www.gsmaintelligence.com/research/?file=0efdd9e7b6eb1c4ad9aa5d4c0c971e62&download.

4 K. Kaplan, *The plans for 5G to power the internet of things*, en, (accessed 2019-06-11), 2014. [Online]. Available: https://qz.com/179980/the-plans-for-5g-to-power-the-internet-of-things/ (visited on 06/11/2019).

5 K. Campbell, J. Diflfey, B. Flanagan, B. Morelli, B. O'Neil, and F. Sideco, *The 5G economy: How 5G technology will contribute to the global economy*, (accessed 2020-06-11), 2017. [Online]. Available: https://cdn.ihs.com/www/pdf/IHS-Technology-5G-Economic-Impact-Study.pdf.

6 ITU-R, *Recommendation ITU-R M.2083-0. IMT Vision – Framework and overall objectives of the future development of IMT for 2020 and beyond*, (accessed 2020-04-21), 2015. [Online]. Available: https://www.itu.int/dms_pubrec/itu-r/rec/m/R-REC-M.2083-0-201509-I!!PDF-E.pdf.

7 A. Ilyas, *5G at Risk if Mobile Operators Don't Get Access to the Right Spectrum - Newsroom*, Oficial Web Site, (accessed 2020-02-11), Nov. 2018. [Online]. Available: https://www.gsma.com/newsroom/press-release/gsma-5g-at-risk-if-mobile-operators-dont-get-access-to-the-right-spectrum/ (visited on 05/20/2019).

8 GSMA Association, *5G Spectrum GSMA Public Policy Position*, en-US, (accessed 2020-03-19), 2018. [Online]. Available: https://www.gsma.com/latinamerica/resources/5g-spectrum-gsma-public-policy-position-2/ (visited on 03/19/2020).

9 5G Americas, *The Evolution of Security in 5G*, en-US, (accessed 2020-03-11), Jul. 2019. [Online]. Available: https://www.5gamericas.org/the-evolution-of-security-in-5g-2/ (visited on 03/19/2020).

10 P. Tuset-Peiró, B. Martinez, and X. Vilajosana, *Qué es NB-IoT?* es, (accessed 2019-06-13), Nov. 2018. [Online]. Available: http://informatica.blogs.uoc.edu/2018/11/22/que-es-nb-iot/ (visited on 06/13/2019).

11 "IEEE Standard for Low-Rate Wireless Networks," *IEEE Std 802.15.4-2015 (Revision of IEEE Std 802.15.4-2011)*, pp. 1–709, Apr. 2016. DOI: 10.1109/IEEESTD.2016.7460875.

2nd German-West African Conference on Sustainable, Renewable Energy Systems SusRes – Kara 2021

Poster Contributions

https://doi.or/10.52825/thwildauensp.v1i.23

Published: 15 June 2021

Design and simulation of an MPPT charge controller for a PV application

Bidjagare Akiza[1], Edjadessamam Akoro[1], and Dam-Bé L. Douti[1]

[1] Laboratoire Matériaux et Energie Renouvelable, Université de Kara, UK

Abstract. In this document, we propose an MPPT charge controller based on the two-phase charging method proposed by the datasheet of the battery under test. Also, for efficient and optimal charge the charge controller reacts with better exploitation of the available photovoltaic (PV) power by means of a maximum power point tracking (MPPT) technique employed in the control algorithm especially the Perturb and observe (P&O) techniques; when threshold voltage reach, the regulation phase start. The MPPT and converter efficiency are respectively 98.7% and 98.2% at the standard test condition (STC).

Keywords: photovoltaic, MPPT, battery

Introduction

Autonomous photovoltaic systems with storage have become more and more widespread in recent years, especially in rural areas isolated from the local energy distribution network. The type of storage generally used in these systems are lead-acid batteries. The maturity of this technology and its low cost are the main reasons[1]. Also, lead-acid batteries have a high number of cycles and represent about 15% of the initial investment but over an operating lifetime of twenty years, they could exceed 50% of the overall cost of the system ; it is therefore important to increase the life of the component to lower the cost of the energy produced[2]. And to get there, it requires an optimal use of these batteries, that is to say a charge/discharge controller. It is in this sense that we present in this document an algorithm for charging a lead-acid battery based on the (maximum power point tracking) MPPT method. This algorithm allows us to reach a state of charge of 100% while not exceeding the charge threshold voltage.

Principle of an MPPT

To optimize the power available from the panels we need an MPPT. The MPPT commands will continuously adjust the duty cycle associated to the static converter that charges the battery. Different MPPT methods have been published in the literature in order to obtain an optimal functioning. Many researchers are interested in recalling and comparing the different MPPT techniques that exist in the literature [3, 4]. BELKAID ABDELHAKIM shows in his thesis that there are about thirty MPPT techniques[5]. These MPPT command can be compared according to their dependencies on the parameters of the solar panels and their complexities and the type of implementation according to whether it is analogue, digital or mixed[3, 6, 7]. Among these commands the most knows are : the command called perturb and observed (P&O), the incrementation of the conductance (IncCond), the approach of the constant current, the constant voltage[7] and in recent years the approach to fuzzy logic and the neuron network. Only the P&O will be presented in this document.

Principle of P&O command

As its name indicates it is based on the disturbance of the system through the increase or decrease of V_{ref} or by acting directly on the duty cycle of the DC-DC converter, then by the observation of the effects of these disturbances on the panel output power. If the value of the current power P (k) of the panel is greater than the previous value P (k-1) then we reverse the direction of the disturbance. The algorithm flowchart is given below:

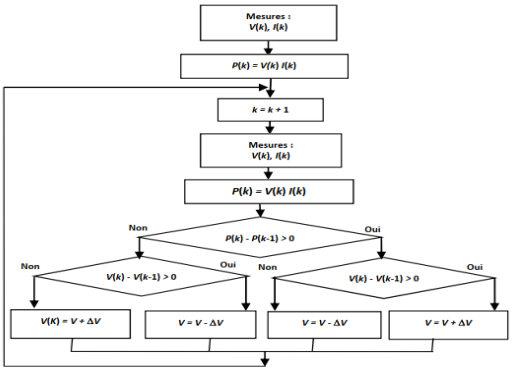

Figure 1. P&O command flowchart[8].

Design and sizing of a PV system charge controller

The conversion chain of a PV system with storage is presented as illustrated in the figure 2. It consists of a solar panel which acts as a generator, a DC-DC converter which ensures an adaptation between the generator and the battery, a charge controller that regulate the converter and finally the lead-acid battery which represents the charge.

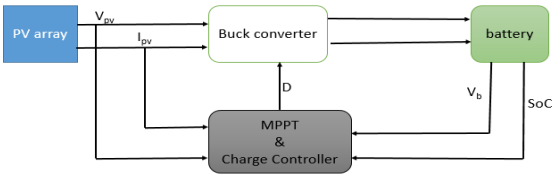

Figure 2. Battery charging system

The solar panel and the DC-DC converter

For the simulation we have used the “aleo solar A18.240” panel in the matlab library. The main electrical characteristics are maximal power, maximal voltage and maximal current which is respectively equal 240W, 30.1V and 8A.

The choice of buck DC-DC converter is motivated by the fact that the panel voltage is higher than one of the battery, and we need to lower it before charging the battery.

The equation (1) are given for the sizing of the filter at the output of the converter which limit current and voltage ripples. [8-10] :

- $L \geq \frac{\mathrm{Ve}}{\Delta Is * fc} \mathrm{D}(1-\mathrm{D})$ $\qquad$ $C \geq \frac{(1-\mathrm{D})}{8 * L * fc * fC} \left(\frac{Vs}{\Delta Vs}\right)$ $\qquad$ (1)

V_e: Maximal input voltage (30V), V_s: Maximal output voltage (12V), f_c: Switching frequency (750 Hz), ΔIs: Ripples output voltage and current (5% of V_s and of I_s), D: Duty cycle.

The choice of the switching frequency is crucial. The larger it is, smaller is the core of the inductor and greater the switching losses of power[11].

The algorithm of the MPPT charge regulator

The charging of a battery follows two basic steps for an efficient charge without the risk of damaging the battery and also optimized a battery life time[2, 8]. The charging mode is represented by the following curve:

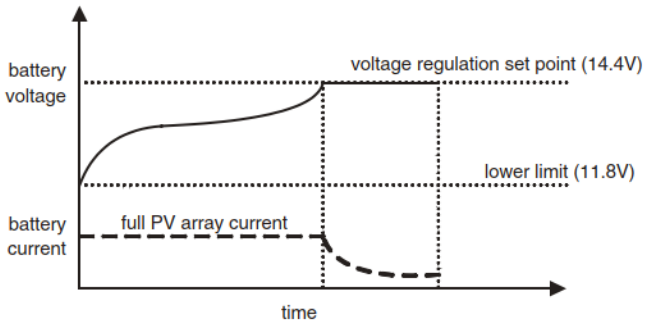

Figure 3. two-phase charging mode.

First, the battery is charged at constant current of around C/5 of its nominal capacity until the voltage at the battery terminal reaches the charging threshold voltage (14.4 V); then in a second charging phase, the voltage is kept constant at its threshold value until it is fully charge (100%) with a progressive decrease of charge current. Starting from the charge principle described above the flow chart of the MPPT regulator is presented below:

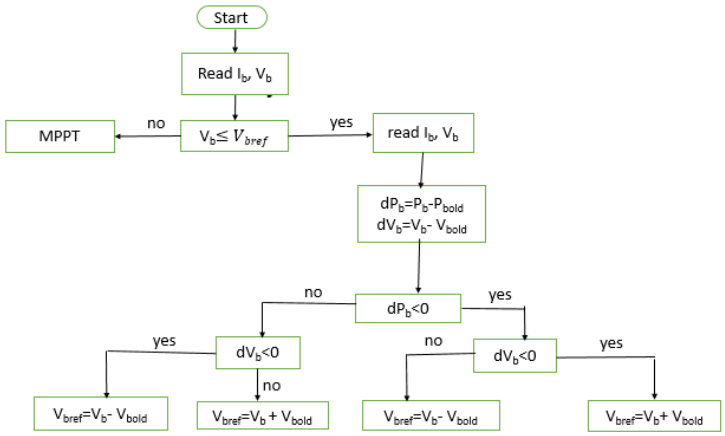

Figure 4. MPPT charge controller algorithm.

Simulation : results and analyses

For the simulations, we used the matlab/Simulink software. The capacity of battery over charge is 200Ah with nominal voltage at 12V. The test is done at STC condition.

At start of the charge, the maximum available PV power is transferred to the battery, according to the MPPT algorithm (Figure 6). Then the battery voltage progressively increase until it reaches 13.4V (Figure 5). Then the charge-regulation phase is initiated (Figure 5) and the battery charging current is progressively reduced to the defined value. Figure 6 shows the charging power variation when the regulation phase start. The efficiency of the converter and MPPT during all the charging process is lying between 97.3% and 98.7%. We can see on figure 6a that MPPT response is less than 0.01s.

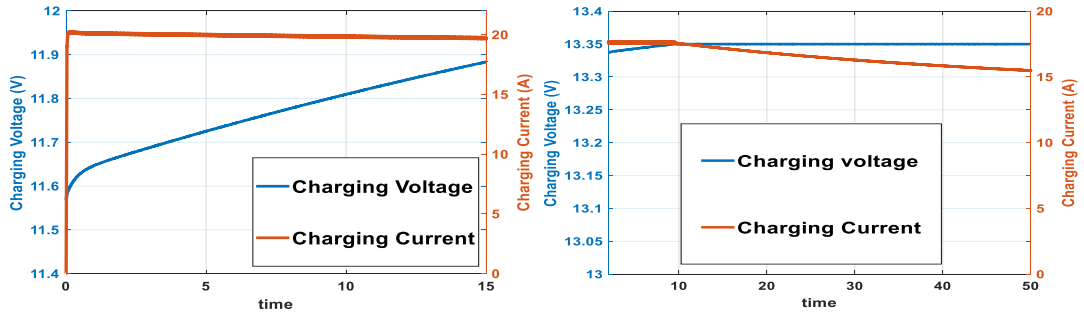

Figure 5. Voltage and current charging curve at the beginning and regulation phase.

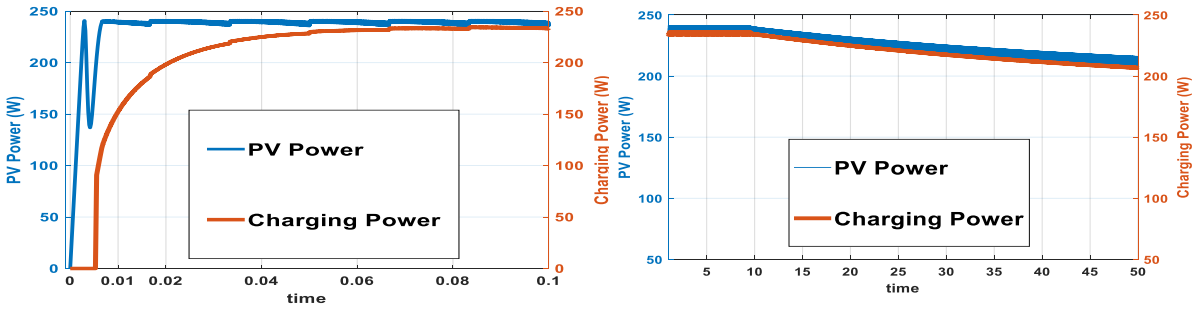

Figure 6. PV Power and charging Power at the beginning and regulation phase

Conclusion

In this document, we have studied the implementation of a two-phase MPPT charge controller with the aim of making an efficient charge allowing to prolong the life of the battery and other side save forward the fact that the use of an MPPT charge regulator reduces battery time charge for photovoltaic application by providing the maximum available power with an efficiency over 98%.

References

[1] Mohammed B. Modeling the parameter of a lead-acid battery and it integration into an autonomous photovoltaic system. Université Abou Bekr Belkaid Tlemcen; 2015, p.8.

[2] MERROUCHE W, MALEK A. Development under PROTEUS of a regulator based on an eficient charging algorithm safe for lead acid batteries in a system photovoltaic. 2ème International seminaron new Energies and renewables. 2012, 8.

[3] Cédric C. Energy optimization of the electonic adaptation stage dedicated to photovoltaic conversion. Université de Toulouse; 2008, p. 162.

[4] Reza Reisi A, Hassan Moradi M, Jamasb S. Classification and comparison of maximum power point tracking techniques for photovoltaic system: A review. Renewable and Sustainable Energy Reviews. 2013 03;19:433-443. https://doi.org/10.1016/j.rser.2012.11.052

[5] ABDELHAKIM B. Design and implementation of an MPPT control of high performance for a conversion chain autonomous photovoltaic system. Université Ferhat Abbas setif1; 2015, p. 99.

[6] TAFTICHT T. Analysis and control of a hybrid system wind photovoltaics. Université du Québec à Trois-Rivières; 2006, pp.1-74.

[7] Ajaamoum, M. Comparison of the takagi-sugeno fuzzy controller and "P&O"command for extracting the maximum power from a photovoltaic system. International Journal of Innovation and Applied Studies. 2015;10(1):192-206.

[8] Souleyman F, Omar E. Study and realization of a commanded boost chopper by the microcontroller arduino in order to implement MPPT orders. Université Ahmed Draia Adrar; 2019, p. 67.

[9] Omar M. Design and production of a photovoltaic generator fitted with an MPPT converter for better energy management. Université Abou Bekr Belkaid Tlemcen; 2011.

[10] Amine M. The sliding mode control of two-level boost chopppers. ESSA; 2019, p.52.

[11] Abdellatif M. Study and optimization of a hybrid wind-photovoltaic system. Université Ferhat Abbas setif1; 2014, p.100.

2nd German-West African Conference on Sustainable, Renewable Energy Systems SusRES – Kara 2021

Poster Contributions

https://doi.org/10.52825/thwildauensp.v1i.22

Published: 15 June 2021

Technical Condition Management for a PV-based Distributed Energy System

Sebastian Schulz [1] and Jörg Reiff-Stephan [1][https://orcid.org/0000-0003-4176-6371]

[1] Technical University of Applied Sciences Wildau, Germany

Abstract. Distributed energy systems are a key success factor for the future and self-determined living in undeveloped or emerging regions. Education, culture and economic growth are significantly influenced by energy processes. In order to be able to use a built-up infrastructure, maintenance and condition control of the systems along their entire life cycle are indispensable. However, this can only be achieved if an independent technical condition management system can be established. Event-based data and warnings can be transmitted or retrieved at any time. Due to this, decisions can be made on the basis of the information obtained, which then lead to the maintenance of the targeted functional scope of the power systems. In the following paper, a TCM for pv-based distributed energy systems is presented. It consists of a low performance single board computer which can be connected to a cloud system with mobile communication and transmits essential data.

Keywords: Technical Condition Management, MRO, pv-system

Introduction

Due to the continuing growth in global energy demand, the dilemma of extraction available energy sources and using them efficiently must also be solved especially in rural areas. Decentralized, distributed solutions based on renewable energy systems can provide a remedy and drive regional development. For several years, utility concepts for renewable energy systems have been designed for the sub-Saharan region of West Africa and pv (photovoltaics)-based energy supplies have been established, especially for powering elementary schools [1, 8].

A barrier to the readiness of a more widespread use of these technologies is often due to the fact that, due to a lack of means of communication, it was not possible to guarantee support for the plants by maintenance and repair (MRO) teams. This is where new technological enablers come in, offering the possibilities of health monitoring and alarm event management [3, 4, 5].

Data-driven information processing and decision support, especially through a transcript of historical data about the operating conditions on site, are an advantage for an efficient and long-lasting operation that should not be underestimated [6, 9]. Sophisticated applications have been set up as part of various project work on decentralized energy supply based on the use of regenerative energy systems. Since access to the systems is often difficult, maintenance and possible error analysis should be made possible remotely.

Architecture and Entities

Due to the described challenge, a holistic approach as well as a prototypical realization for a Technical Condition Management (TCM) is presented for pv-based distributed energy

systems. The core architecture consists of an inexpensive, commercially available single board computer (Raspberry PI 3 B) with various interoperable interfaces and additional PCBs for special sensors like as follows (hardware architecture see figure 1):

- temperature sensor DHT22
- current sensor ACS712-5
- voltmeter unit ADS1115 (M5Stack) as well as
- GSM GPRS module with antenna SIM800L GSM for mobile communication.

The system is used to health monitor and log the states of the energy system and to provide event-based decisions on its adapted continued operation. Regularities for the demand of provided energy resources are collected in order to enable an optimized utilization of existing capacities at any time. Furthermore, an escalating alarm management is presented to operators and MRO service providers on the basis of collected data. The data processing is enabled by the opensource software NodeRED and the communication via GSM/Internet protocol.

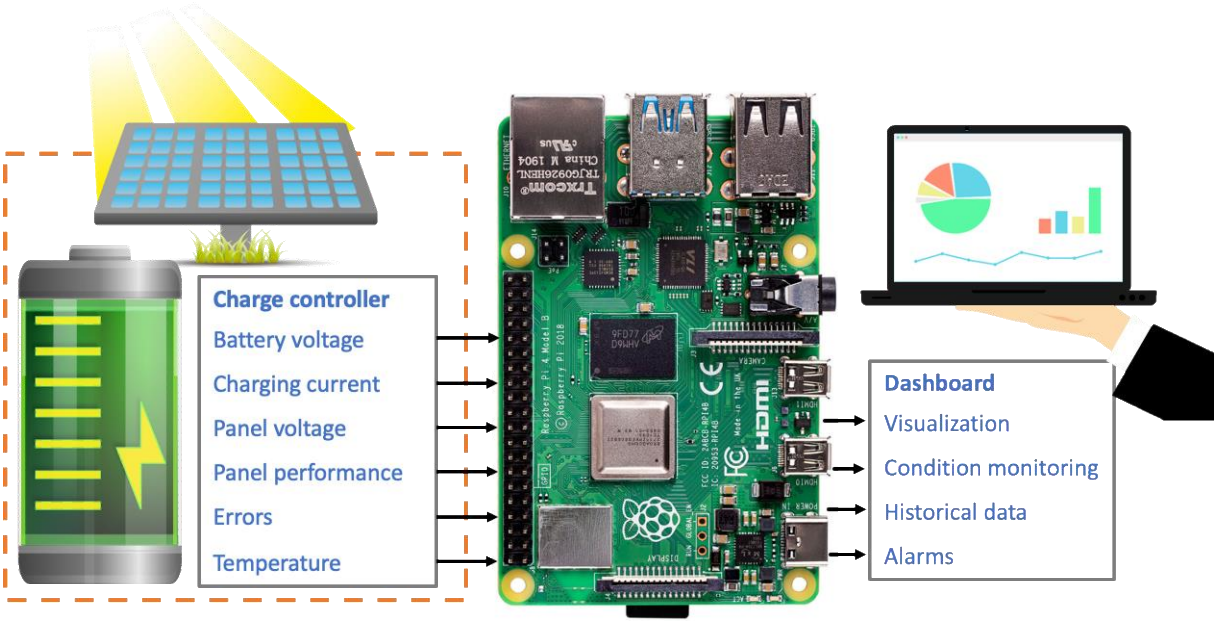

Figure 1. Architecture of the TCM system.

The innovation value of the TCM system lies in the distributed information provision across the application limits of the power systems. Here, the priority is to find a lightweight data structure that makes use of a narrow transmission bandwidth. A program for M2M communication and historical data acquisition was set up and implemented on NodeRED. By using common M2M protocols such as MQTT, the cloud infrastructure can be applied for external access to the distributed energy systems. Different architectural approaches for centralized and decentralized data storage as well as testing the use of an edge server for pre-processing the data have been examined.

Prototypical Realisation

An initial trial installation was carried out on the basis of the Roadshow logistics system in place at TH Wildau to raise the digital awareness of companies. Here, an overall package was designed and the basic feasibility is demonstrated. It is essential that the data of the system are transmitted mobile parallel to their use in the whole of Brandenburg region and reflect a constant overview of the state of the energy supply. For the frequently changing operators of the roadshow, the display elements were provided with a traffic light system.

This allows the operator to see quickly whether the actual values are within the required range (green) or whether a deviation is occurring.

As part of the development of the *Center for Renewable Energy Systems* (CenRES) at Kara University, a follow-up installation will be made on the Mobile Energy System of the BONITA House built in 2016. A prototype implementation of the graphical user interface of TCM especially for condition monitoring can be seen in figure 2. The data is transmitted collectively to the cloud server at TH Wildau in Germany. Event-driven applications are then mapped on the basis of self-analyzing process chains.

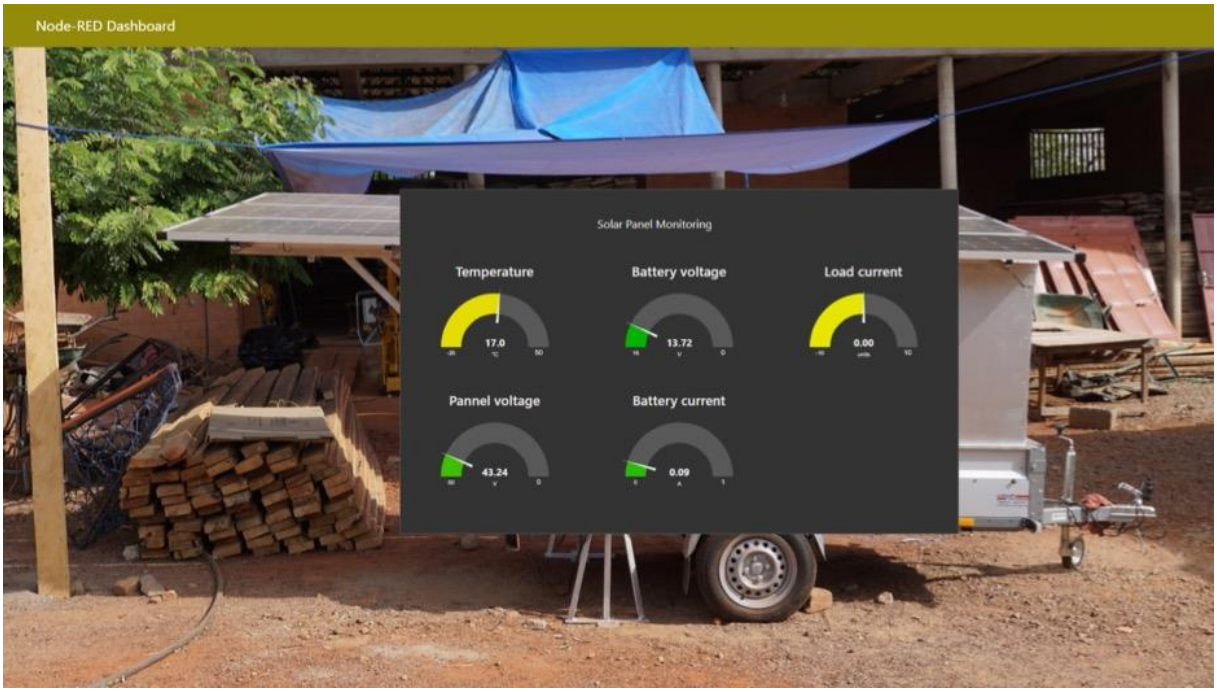

Figure 2. TCM-dashboard

Based on the cloud data storage, trend analyses can be prepared that provide an optimal insight into the energy system’s condition. In this way, deviations from target states can be identified at an early stage and alarms triggered. Before a failure of subsystems such as the batteries occurs, maintenance can be initiated or replacement prepared. It is also possible to implement a billing system based on the actual times consumers are switched on. This makes the economic viability of such solutions for use in the savannah possible.

Conclusions

Technical condition management enables a holistic view on the ability of the equipment to fulfil the customer needs. Finally, the following key enablers for future TCM systems can be derived from the approaches presented:

- The development of smart sensors, and other low-cost on-line monitoring systems that will permit the cost-effective continuous monitoring of key equipment items
- The increasing provision of built-in sensors as standard features in complex controlling items,
- The acceptance of Condition Monitoring within the "mainstream" of operations and maintenance, with service operators increasingly utilizing this technology as part of their day-to-day duties
- An increasing focus on the business implications and applications of Condition Monitoring technologies, leading to the utilization of TCM-technologies to improve equipment reliability and performance, rather than to merely predict component failure.

- A reduction in the cost-per-point of applying TCM technologies.

Ultimately, event-based alerting ensures high availability of the technique. Planned downtimes for maintenance tasks can be minimized and the safe use of the energy supply can be ensured.

Acknowledgement

This paper presents research results that are basically demonstrated in the Center of Renewable Energy Systems (CenRES) at University of Kara, Togo. The CenRES is partially supported by the German Academic Exchange Service (Project-ID: 57509668).

References

[1] Bullinger H, ed. Technology Management. Dordrecht, Heidelberg, London, New York: Springer; 2009.

[2] Uhlmann E, Laghmouchi A, Hohwieler E, Geisert C. Condition Monitoring in the Cloud. Procedia CIRP. 2015;38:53-57. https://doi.org/10.1016/j.procir.2015.08.075

[3] Reiff-Stephan J, Richter M, von Lipinski R. Intelligent sensor systems for self-optimising production chains. Proceedings of the 1th International Conference and Exhibition on Fu-ture RFID Technologies Eszterhazy Karoly University of Applied Sciences and Bay Zoltán Non-profit Ltd. for Applied Research Eger. 2014 November, pp. 115–125.

[4] Kumar NP, Jatoth RK. Development of cloud based light intensity monitoring system using raspberry Pi. 2015 International Conference on Industrial Instrumentation and Control (ICIC). 2015 International Conference on Industrial Instrumentation and Control (ICIC). 2015 05. https://doi.org/10.1109/iic.2015.7150959

[5] Heuberger A, Gamm E. Software Defined Radio-Systeme für die Telemetrie. Berlin Heidelberg: Springer; 2017.

[6] Dable E. Construction of PV Systems for Elementary Schools in the Savannah of Togo. 1st German-West African Conference on Sustainable, Renewable Energy Systems SusRes. 2020 July, pp. 111-115. https://doi.org/https://doi.org/10.15771/978-3-9819225-5-4

[7] Lee E. The Past, Present and Future of Cyber-Physical Systems: A Focus on Models. Sensors. 2015 02 26;15(3):4837-4869. https://doi.org/10.3390/s150304837

[8] Reiff-Stephan J. Solar power in product development. 1st German-West African Conference on Sustainable, Renewable Energy Systems SusRes; Kara, Togo. 2020 July, pp. 55-65. https://doi.org/https://doi.org/10.15771/978-3-9819225-5-4

[9] van de Sand R, Schulz S, Reiff-Stephan J. Smart Process Communication for Small and Medium-Sized Enterprises. In: Enterprise Interoperability VIII. Proceedings of the I-ESA Conferences. Springer International Publishing; 2019:pp. 411-420.

2nd German-West African Conference on Sustainable, Renewable Energy Systems SusRes – Kara 2021

Poster Contributions

https://doi.org/10.52825/thwildauensp.v1i.21

Published: 15 June 2021

Education 4.0: An remote approach for training of intelligent automation and robotic during COVID19

H. Smajic [1][https://orcid.org/0000-0002-0669-1979], T. Duspara [1][https://orcid.org/0000-0002-6985-5950]

[1] Technische Hochschule Köln

Abstract. The COVID-19 pandemic confronts universities with great challenges to maintain research and teaching activities with as little contact as possible. Lecturers currently have to migrate to Internet teaching. In most cases, e-learning and digital tools are used to continue online courses to replace classroom teaching. But current online approaches are limited to just lectures and theoretical mathematical exercises. In this paper it will be shown how practical exercises can be carried out remotely via internet in a real technical environment. Experimental laboratory equipment for automation technology and mechatronics is always associated with high costs. The reason for the high investments are the costs for different intelligent devices within an automation solution and the costs for extensive engineering. Beyond the costs, the number of workstations usually does not correspond to the required number of students to be trained. In this case, the same exercises have to be repeated several times, which also leads to in-creased personnel costs.

Remote laboratories are a very cost-effective solution for these problems. This paper describes how this goal can be achieved by implementing a WBT server (WBT - Web-Based Training Server) and a Java-based client-server architecture. The idea behind a remote controlled laboratory is to use web technologies and the Internet as communication infrastructure to perform an experimental part of the training with programmable automation devices. First of all, a detailed requirement profile for the laboratory was developed. Primarily technical, didactical and organizational requirements are concerned. In addition, the laboratory is to improve the education of the students by interactive, problem-oriented learning on real industrial automation components. The aim of the training is to learn suitable working methods for the design (engineering) of complete automation solutions starting from simple to medium complex machines and plants.

Keywords: Education 4.0, Remote Lab, IIoT, COVID-19

Introduction

The use of online automation engineering in general has thus far not found any sweeping acceptance on the operating side. The engineering capable of being performed via world-wide data paths and by means of multi-media tools are thus far advances of innovative manufacturers of capital goods who, in this way, ensure themselves new unique selling points compared with their competitors.

This type of manufacturer-driven approach neglects important customer interests through the proprietary design and the differing manners of communication of the systems. The reasons for this trend lie in the fact that many manufacturers have initially striven for support by their own service personnel, especially during the commissioning phase. The finding phase of the suppliers with respect to online engineering that is still continuing makes the path towards a uniform communications standard for use in the industrial environment more difficult. The latter has been prevented in particular through the rapid changes in the field of various information and communication technologies [1].

Some concepts for the provision of diverse machine-related services via remote control of these machines by humans with information technology tools have already been developed. These constitute comprehensive solutions for IT-assisted service scenarios with the involvement of the organizational structures of manufacturer and operating company that above all make clear the complete host of services that can be reproduced on the basis of modern-day information and communication technologies [2]. The use of the communications infrastructure of the Internet itself is becoming increasingly established in this field and, as a result, will develop far-reaching potential for the future online engineering.

Nevertheless, the introduction of online engineering brings with it major challenges for the companies. Many of these companies are placing their faith in differing suppliers in the field of machines and machine control, with the result that the large number of heterogeneous components and online service solutions offered, prevents any efficient organization of remote access that represents a further precondition for a comprehensive, inter-compatible and future-oriented introduction of online service in the field of remote control access. Operating companies of Online supportable, production systems are consequently faced with high infrastructure and organizational costs as they constantly have to administer the large number of different systems in order to keep them available for possible use.

In this respect, the world-wide operating, major manufacturers of online engineering systems offer comprehensive services that have already been taken into consideration in the planning of the installations, however, the well-known problems of the proprietary solutions and the difficulty with integration into company infrastructures continue to exist. In detail the following weaknesses of current remote. In detail the following weaknesses can be shown:

- Users are confronted with different online service solutions.
- Insufficient compatibility to allow in-house usage of proprietary systems.
- High requirements for safety of operator and machine.
- High requirements for security of system access and network.
- Version conflicts due to different software updates.
- Current complexity allows operation by experts only.

Available automation concepts

In process and manufacturing automation, the demands for increasing productivity and flexibility while maintaining consistently high quality standards are constantly growing in the face of intensifying competition. This development leads to increasingly complex requirements for control concepts and implies a further increase in the complexity of automation tasks. In order to meet these continuously changing requirements, decentralized control concepts are subject to constant change towards distributed systems with open interfaces. This change is also favored significantly by the daily growing performance potential of microelectronics and information technology [3, 4]. As a result, numerous centralized and decentralized control concepts have emerged in automation technology, which can be classified primarily according to their topological, functional and communication aspects (Figure 1).

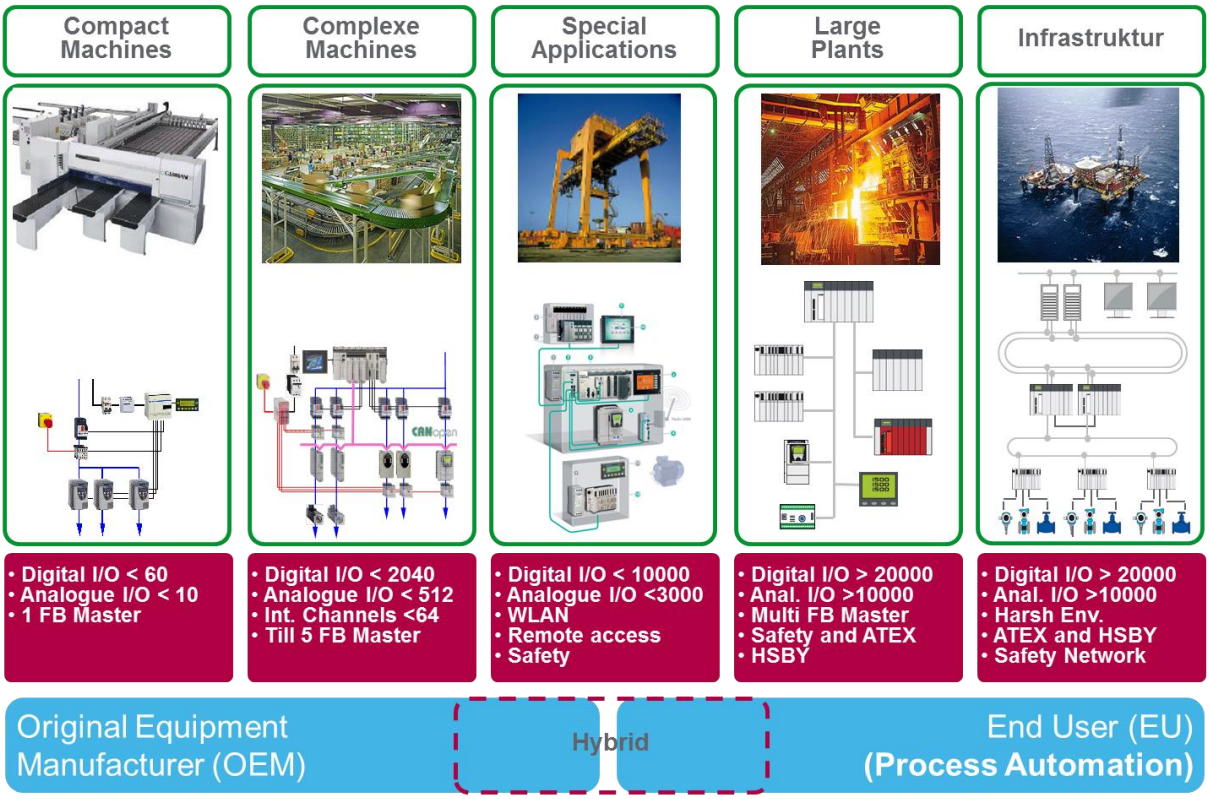

Figure 1. Available automation concepts for machine and plants

For the control tasks of simple machines, which predominantly require binary signal processing in the form of logic or sequence control, central programmable logic controllers are still used. In complex machines and plants, a decentralized and modular network of individual controllers is increasingly replacing centralized structures. These are usually small and medium-sized control systems or intelligent sensors and drives directly on the machine or plant, which are networked with each other via appropriate field buses. In order to protect employees and the environment, safety-oriented control components and safety-oriented communication systems are used in complex plants and in the field of infrastructure applications. A continuous process is guaranteed by the use of redundant and highly available systems (HSBY).

A new generation of decentralized control systems is significantly influenced by the spread of industrial Ethernet and web technologies. By consistently integrating these technologies, various problems of existing fieldbuses, such as openness and manufacturer independence, can be solved. These protocols have been successfully introduced right down to the control level. It is undisputed that this trend towards further integration will continue right into the field level. The introduction of Ethernet and the shifting of control functionalities to the field devices and drives requires further functional changes to the controllers and control systems when they are integrated into the higher automation structures, which consequently also affects the engineering and thus their software tools. The specification of different device descriptions (FDT, GDS, EDS, etc.), which are made available to the user by corresponding user organizations, is particularly helpful for the integration of these technologies.

The design of an automation solution depends of machine size and market segment, where automated equipment can be applied. The main criteria for building of automation architecture are: number of digital and analogue Inputs/Outputs, intelligent channels, type of fieldbus, remote access, high availability and safety.

Training in real and virtual environment

The currently most widespread model for knowledge transfer at European universities is still characterized by passive lectures and exercises. However, such knowledge transfer through theoretical input in engineering courses always suffers from a low recall rate. At the Faculty of Vehicle Systems and Production, application-oriented teaching is provided with the support of practical exercises and group work. Although the recall rate with this approach is as high as 32% after three months, the number of dropouts is still too high. One of the main reasons for this dropout rate is an excessively high level of abstraction in the transfer of knowledge in mechatronic modules. This problem makes it increasingly difficult to find candidates who can carry out internal project work in the form of individual projects, interdisciplinary projects and master projects. The current shortage of skilled workers in Germany is also intensify-ing the competition between universities and industry, since even the few existing candidates with specialist knowledge prefer to write their theses in industry.

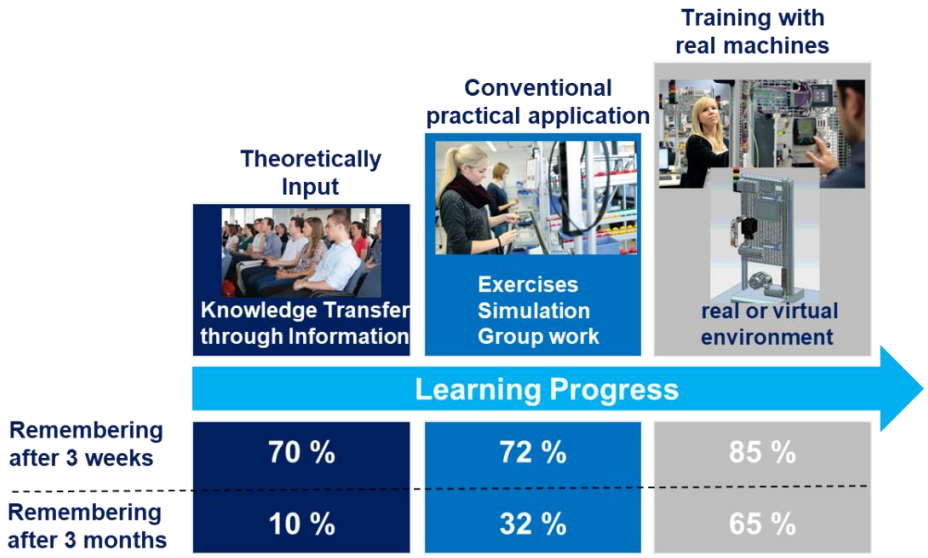

Figure 2. Various training opportunities in higher education

The main focus of this project is the development of teaching content with a high practical relevance for areas of automation technology. The previous rather passive and theoretical learning should be supplemented by the experience in the practical environment and would lead to essentially better and more efficient learning results.

For this purpose, technical workstations have been developed which enable active experience and experimentation. Such an approach can make the level of abstraction of complex programming tasks much more comprehensible through personal experience with all sensory organs and through cooperation and communication with others. It can even increase the above-mentioned recall rate to 65% and thus lead to significantly better learning outcomes.

Design of an automation solution for practical education

With the aim of providing students with a modern education in the field of automation technology, the Cologne University of Applied Sciences and Schneider Electric GmbH have designed a range of equipment to meet the needs of the students. Care was taken to ensure that as many and innovative automation technologies as possible were taken into account. Because of the investment security, the selected components should not be on the market

for longer than two years. A classification of these technologies, which had to be considered, is shown in Figure 3.

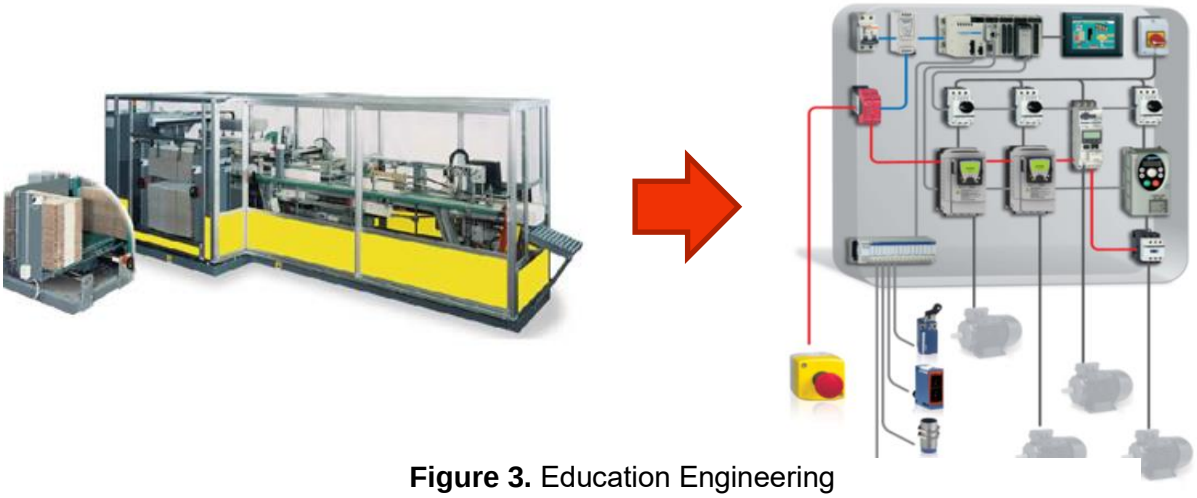

Figure 3. Education Engineering

Inductive and capacitive sensors, optical encoders and data carriers for radio frequency identification (RFID) are provided for the acquisition of binary and analogue process signals and are connected to the programmable logic controller (PLC). A modern mid-range PLC with numerous external modules was selected for processing the process signals. For the tasks "operating and monitoring", sophisticated HMI touch panels with colour display are used. Each station is equipped with modern electronic drive components. A frequency converter is used to practice clockwise and counter-clockwise rotation and commands for constant speeds and constant torque. A linear axis with servo motor and servo controller can be used to perform various tasks with positioning control. All components are networked via CANOpen fieldbus. Profibus DP is also available as an option. In this way, students can configure field buses and learn about their communication protocols. All stations are connected to each other via Industrial Ethernet, so that access to web servers of individual components and technologies of web-based automation can be explained.

The Cologne University of Applied Sciences is one of the first universities in Germany that would like to sensitize its students to the efficient use of electrical energy as part of their university education. For this purpose, appropriate measuring devices were installed at each station, with which all energy data of three consumers are continuously recorded and stored. Subsequently, these data are to be evaluated and analysed by the students. After the analysis, proposals for measures to be introduced to save energy will be developed. For training of automation engineering skills we designed a suitable working stations, which consider those commonly technologies. One workstation contains following equipment:

- Sensors, detectors, encoders and RFID switches for data detection
- Programmable logic control (PLC) for data processing
- Human Machine Interface
- Velocity speed driver and Motion driver
- Smart meter for energy efficiency
- Ethernet Network and CANOpen as machine bus
- Programming and SCADA software

In order to increase the motivation of the students for the education in the field of automation technology even more, technologies were also procured with which young people can identify more easily today. This makes it possible for students to complete certain parts of the exercises from their own smartphones using Java Apps. An overview of this is shown in Figure 3. For example following exercises can be performed:

- Command for motor via Bluetooth
  - Left turn and Right turn
  - Change velocity
- Commands vie GSM Modem
  - Email sending from process
  - Alarm per SMS receive and email

In addition to the hardware, appropriate site licenses were provided for the complete engineering (programming, visualization with SCADA, simulation, etc.). The entire apparatus equipment of the Laboratory for Automation Technology at the Cologne University of Applied Sciences comprises 20 modern workstations of identical design. A large number of practical exercises can be carried out in the teaching environment. The training of students in the areas of control, drive and communication technology is thus decisively improved and made much more clearly understandable.

IIoT architecture for remote education

The concept presented above was built identically at 20 workstations in the laboratory. At each station, two students work in a team, so the capacity for training is 40 participants. In order to use the potential of the equipment also outside, the approach of IoT was implemented. At each workstation 10 global IP addresses were implemented. A WBT server manages an Ethernet network of more than 200 addresses. The Internet-based architecture allows remote access to the automation technology modules for exercises and practical training. The resources of the laboratory can be used as "Distance Learning" for location-independent training. This technology offers an enormous advantage, especially in the global pandemic period due to COVID-19. Students do not have to be present at the university, but are able to carry out their automation tasks (programming, visualization, parameterization etc.) online via re-mote access. The equipment is also available to our external partners from industry and other universities.

In the middle of the remote architecture is a server that manages the entire information content of the individual stations. The server controls remote access and routing to individual workstations as well as authentication (user name and password) of the users. Various SQL databases for archiving access protocols are implemented on the server. Remote access from the global network is established via a VPN connection. In this step the external computer becomes part of the laboratory network and is assigned an IP address via the DHCP server.

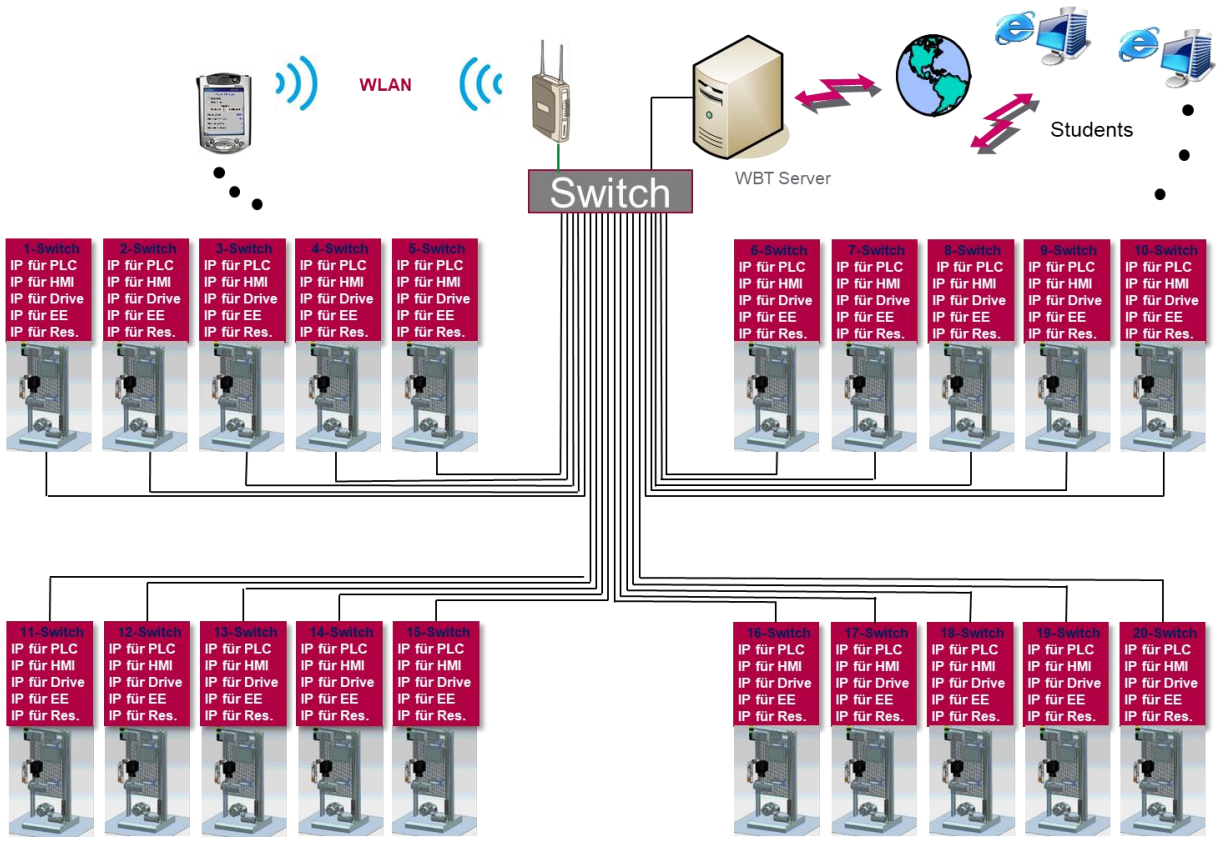

Figure 4. IoT architecture for practical exercises

In the next step, a connection to a virtual computer from the computer pool is created by establishing a remote desktop connection according to previously defined rules. This computer provides a working environment with all software components required for programming. After a "user name and password" query, access is gained to all programming software for PLC, HMI and drives. The user can observe the downloading and testing of the programs written on the automation components via a standard webcam.

Once a student has logged on to a remote computer, he can use all of Toll's soft-ware to program the platforms. In figure 4 on the left side is the software for configuring and programming the PLC. Five different languages (LD, FBD, SFC, IL, ST) according to IEC 61131-3 are available for programming the tasks. When the tasks have been programmed, the participant can test and validate his solutions in a de-bugging process before the project is remotely transferred to the hardware. Tools for diagnostics and online services are then also available. Following a similar pattern, students also use the software to create the screens on the HMI device. Objects are defined in a graphic editor and linked to control variables.

HMI software uses Ethernet TCP/IP connectivity and is therefore able to support decentralized WEB gate access as well as the exchange of application data between terminals, the transfer of recipes and protocols for variables and much more.

For the developed application, a simulation of the PLC variables (I/O, internal bits and words) and the graphical application can be performed with a RunTimer, before downloading the application to the device. This creates a condition window (top right) where all the exercise programs are validated. A webcam (bottom left) shows all activities on the unit.

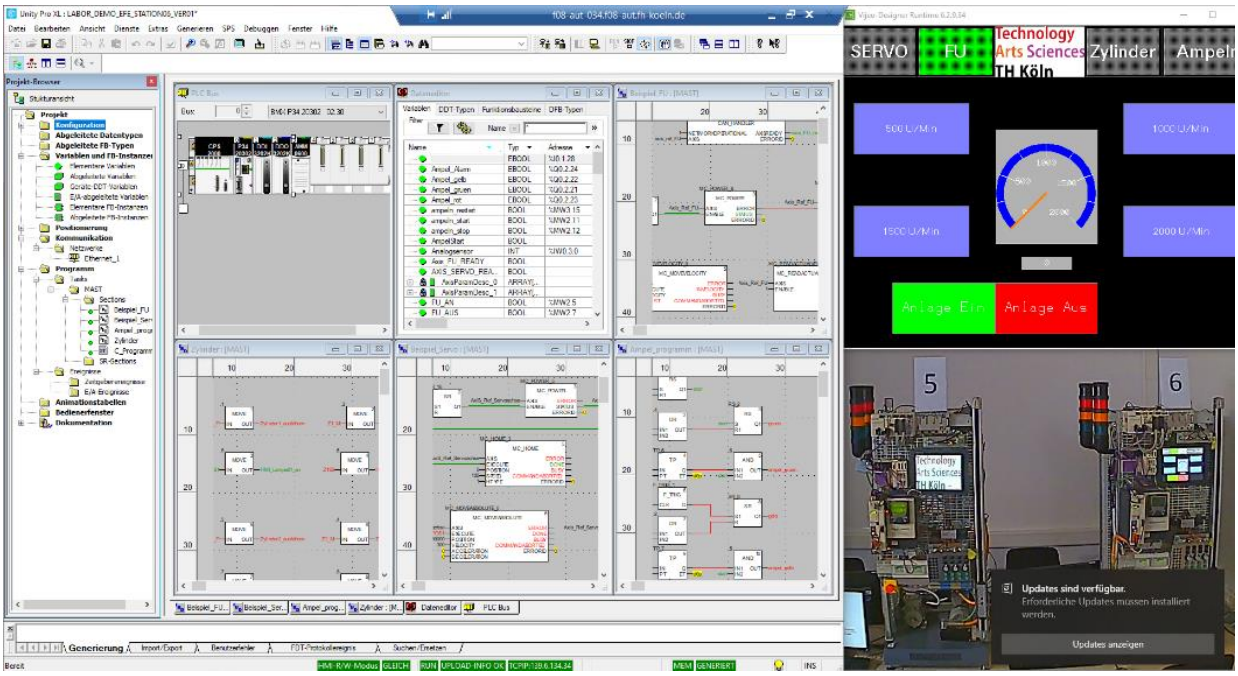

Figure 5. Software tools, testing and validation of programs remotly

Conclusion and future challenge

The first experiences have shown that the interest and motivation of students for the tasks of automation engineering has increased significantly. Varied exercises reduce the degree of abstraction in programming tasks significantly and lead to a significant improvement of the examination results.

The developed internet-based architecture with its WEB server provides a good basis for location-independent access to all resources of the laboratory. The challenges of digitization in teaching is another focus of current research at the faculty. Re-search projects include, for example, the development of innovative assistance systems for evaluating learning progress based on artificial intelligence approaches and the introduction of an automatized booking service (Scheduler Tools). The resources of the laboratory are currently also being used by partners from industry and partners from universities as "Distance Learning".

References

[1] Restivo M, Mendes J, Lopes A, Silva C, Chouzal F. A Remote Laboratory in Engineering Measurement. *IEEE Transactions on Industrial Electronics*. 2009 Dec;56(12):4836-4843. https://doi.org/10.1109/tie.2008.2011479

[2] Niedersteiner S, Lang J, Pohlt C, Schlegl T. Klassifikation des Arbeitsfortschritts. *atp magazin*. 2017 Nov 17;59(11):58-66. https://doi.org/10.17560/atp.v59i11.1911

[3] Osinde NO, Byiringiro JB, Gichane MM, Smajic H. Process Modelling of Geothermal Drilling System Using Digital Twin for Real-Time Monitoring and Control. *Designs*. 2019 08 17;3(3):45. https://doi.org/10.3390/designs3030045

[4] Smajic H, Bosco J. SIMULATION TOOLS FOR VIRTUAL PLC-TESTING IN EXTRUSION PROCESS. *University of Banja Luka*. DEMI 2019; Bosnia and Hercegovina. 2019 May.

[5] Falkman P, Helander E, Andersson M. Automatic generation: A way of ensuring PLC and HMI standards. *ETFA2011*. Factory Automation (ETFA 2011). 2011 09. https://doi.org/10.1109/etfa.2011.6059201

2nd German-West African Conference on Sustainable, Renewable Energy Systems SusRES – Kara 2021

Poster Contributions

https://doi.org/10.52825/thwildauensp.v1i.20

Published: 15 June 2021

Planning and optimization of a multipurpose farm using renewable energies (solar) in Yaoundé (Cameroon).

Bertold Damesse[1], Francois Damesse[2], Roland Kirchberger[1], Kevin Wamba[3] and Markus Sperka

[1] Beuth University of Applied Sciences, Germany

[2] Multipurpose Farmer, Yaounde, Cameroon

[3] Technical University of Munich, Germany

[4] MSP-Institute, Berlin, Germany

Abstract. The instability of Cameroon's electricity network leads to recurrent power outages, which constitute a significant obstacle to socio-economic activity in the region [3]. This is also the case for the agricultural activities carried out by the GIC PROSER in the MEYO area of Yaoundé. The main objective of this work is to demonstrate a solution approach for an ecologically sustainable and relatively self-sufficient solar energy supply by GIC-PROSER, thus creating a prototypical model for other farms. For this purpose, a detailed calculation of the annual energy demand was performed. A first investigation was done in order to find out the potential of wind energy, but the wind speeds are not sufficient to provide enough electrical energy due to the location of the farm. Subsequently, a thorough and optimized planning of a solar generator was made, taking into account the solar radiation data of the area. Finally, an approximate of the economic efficiency calculation of this ecological generator was shown. This results in an annual demand of 25,647 kWh/a with a peak load of 12.8 kW. On the roofs of two farm buildings, 49 solar modules with 600 W each are to be installed, resulting in an output of about 29.4 kW. The solar generator (AC grid) provides an annual energy of almost 38,794 kWh. About 32% of this energy is consumed directly by the electrical equipment on the farm. About 55% can be used for battery charging. The annual surplus of produced energy, about 4,131.90 kWh, is fed directly into the grid. This leads to a degree of autonomy of 90%. This solar system costs about 16,000,000 FCFA (24,425 EUR) and it is amortized 11 years after its installation.

Keywords: Cameroon, multipurpose farm, planning, renewable energies.

Introduction

Today, the multipurpose space MEYO has several units such as: a nursery with 5,000 trees, two poultry production units with 2,000 chickens per 45-day wave, a banana plantation, one hectare of fruit trees, a feed production unit, a pigsty and a three-story residential building. All of these units are now operational. But the normal operation of the multipurpose farm depends on a sufficient and permanent supply of electrical energy. This is not the case in the multipurpose farm as well as in several small farms in the region. The direct consequences that can be identified are:

- Rapid aging of the multipurpose farm's electrical equipment.
- High electricity costs.
- Slowing down the economic dynamics of the multipurpose farm [4].

In addition, one of the current major difficulties is the planned relocation of the company from the current production site to a new and larger site, which is not yet covered by the electric utility. In order to overcome the various electrical problems of the multi-purpose enterprise of the GIC PROSER, different renewable energy systems have been implemented in this work. The drawing below shows an overview representation of the agro-complex of Meyo Farm. Here it is worth **mentioning** that the renewable energy sources drawn in Figure 1 are not yet present.

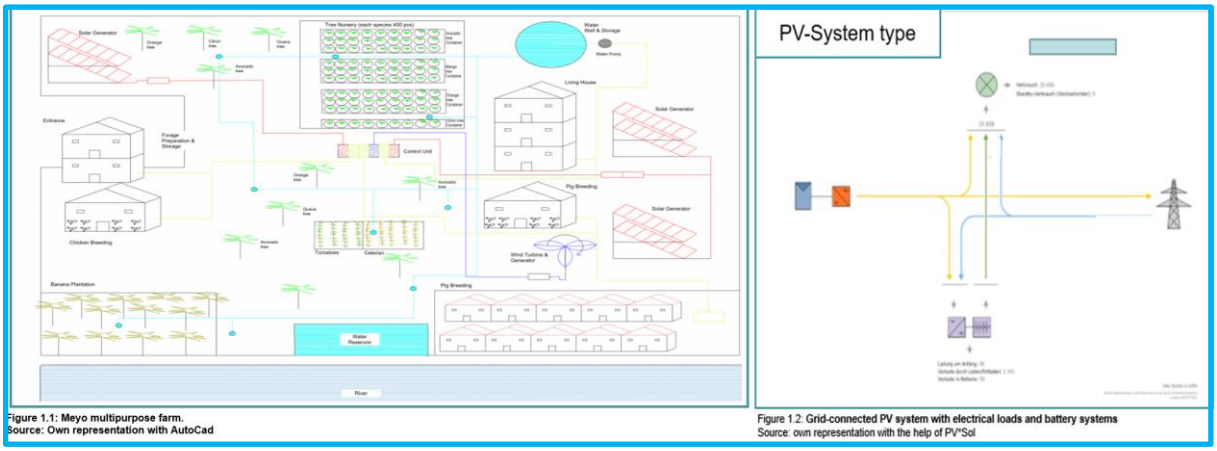

Figure 1. Meyo multipurpose farm and system type of solar generator.

Requirements

Calculation of the energy demand of the multi-purpose farm.

In the initial planning phase, all the equipment that consumes electrical energy was listed and classified according to the production unit of the multipurpose farm and the power of this equipment. The maximum average daily energy consumption of the multipurpose farm was approximately 70 kWh, considering the operating time of these devices. Then, the load management including the simultaneity factor was performed with the PV*Sol program, which reduced the peak power by about 8 kW. The PV*Sol simulation program was used to determine the annual energy demand of about 25,650 kWh and the peak power of 12.8 kWp for the multipurpose operation. In Figure 2.2 below, in addition to the annual energy demand, the distribution of the consumptions according to the production unit of the multipurpose farm over the months can be seen. It can be seen that in January, for example, about 1,300 kWh are consumed by the feed production compared to the energy demand of the pig production, which is about 150 kWh in this month.

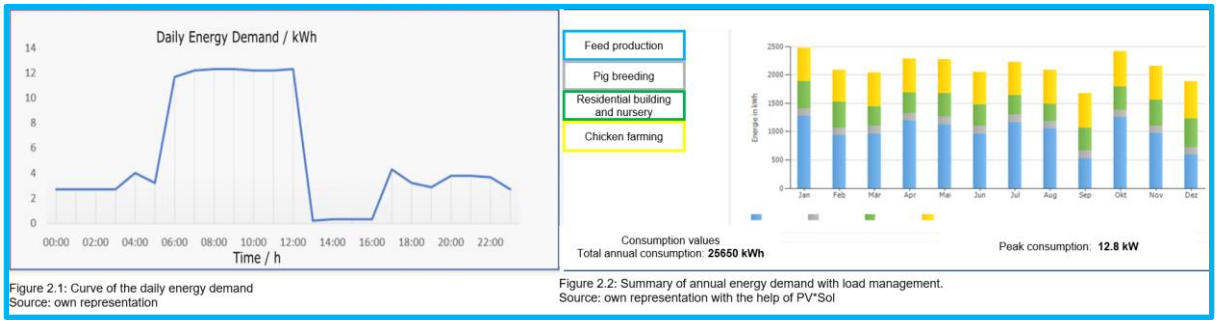

Figure 2. Summary of daily and annual energy demand with load management.

Planning of the energy supply of the multipurpose farm with the help of solar energy (simulation with PVSOL).

Solar radiation spectrum and global radiation in Yaoundé.

The average global radiation in Cameroon is just over 3,000 hours of sunshine per year. In the more humid southern area (Yaoundé) of Cameroon, the average incident global radiation is about 1,600 kWh/m². For the planning of the solar power plant, data on solar radiation in Cameroon were imported into the simulation software PV*Sol.

The system type used in this was a grid-connected PV system with electrical loads with battery storage. The battery systems increase the degree of self-sufficiency of the whole system and in case of power failures an emergency power supply will continue to run for a certain time. The selected system is shown in Fig. 1.2.

Selection of the material, design of the modules and module interconnection.

On the roof of one of the company buildings, 28 solar panels with a nominal line 600 W rated power from Sun Day were installed, giving a solar generator power of about 16.8 kW. This power is much higher than the peak power required by the operation, which is 12.8 KW. An 18.7 kW- 3-phase inverter was used to interconnect the module (due to the existing three-phase machines for feed production). To support or increase the degree of self-sufficiency of the system was used three 48 V/200 Ah battery systems from the company Shenzhen UFO.

Dimensioning of the cables and circuit of the system

The program PV*Sol made it possible to enter the following information in the circuit during the simulation: (the length of the cable, the cable material, a variety of safety devices SS, LS, FI-S, TS, ÜSS, as well as the meters (one or two-sided). Then the cable cross-section (DC or AC side) and the cable losses are calculated automatically.

Economic efficiency calculation

For an efficient calculation of the profitability of a PV system, cost balance, investment costs, financing, taxes, operating and transport costs have been taken into account. The feed-in concept was not integrated in the economic efficiency calculation, since there is still no law in Cameroon for compensation for electricity fed into the public grid [1],

Result

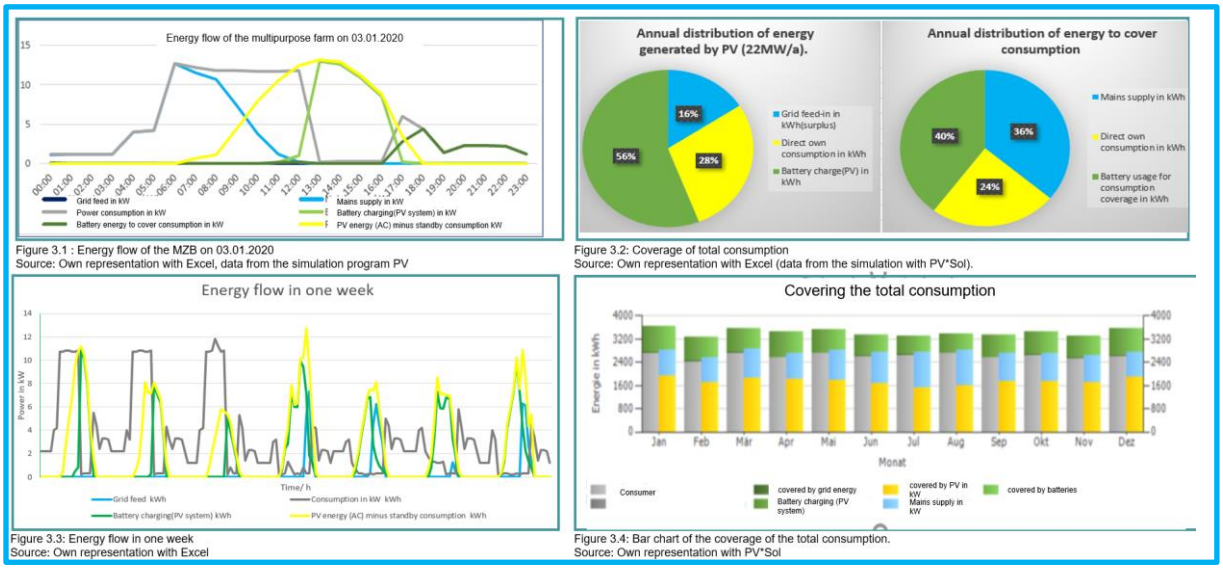

Figure 3.1 : Energy flow of the MZB on 03.01.2020
Source: Own representation with Excel, data from the simulation program PV

Figure 3.2: Coverage of total consumption
Source: Own representation with Excel (data from the simulation with PV*Sol).

Figure 3.3: Energy flow in one week
Source: Own representation with Excel

Figure 3.4: Bar chart of the coverage of the total consumption.
Source: Own representation with PV*Sol

Figure 3. Compilation of results.

This system generates 22,123 kWh per year, which is 86.6% of the farm's energy needs. 28.23% of this energy is used directly to meet demand. 55.9% is used to charge the batteries. Approximately 9,300 kWh of energy from the grid is used to power the photovoltaic

system. The system costs about 10,000,000 FCFA (15,260 EUR) and will be paid back 8.5 years after its implementation.

Planning of the energy supply of the multipurpose farm with the help of wind power.

A small wind turbine with a power of 10 kW was chosen as the second energy source. To determine the height at which the wind turbine should be planned, the first step was to determine the wind data at 10 m and 50 m above ground using wind atlas online tools. The results of the simulation allowed to make a calculation of the annual mean wind speed at 30 m height using the logarithmic boundary profile and the roughness factor. Then it was possible to determine the wind distributions (frequency Weibull and Rayleigh distributions) at this height. These wind turbines installed at 30 m height produce 24,496 kWh of energy in this region. Due to the poor wind data in the Meyo area, the planning of the wind turbine in island mode was no longer carried out, as it is very difficult to show a payback.

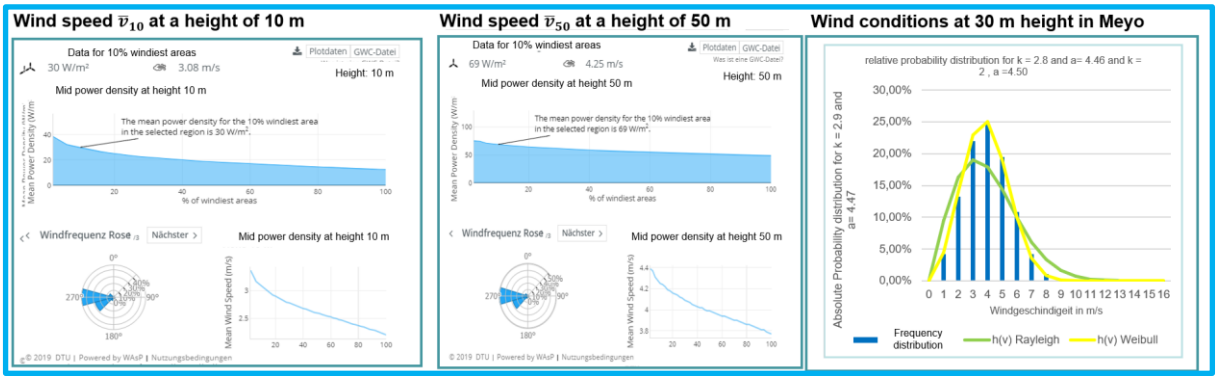

Figure 4. Wind conditions of the operating site

Optimization of the solar system

For the optimization, two three-phase inverters with 18.7 kW were used, a new south roof is equipped with 21 PV modules with a total power of 12.6 kWp. The total solar system has an output of 29.4 kWp with 21 modules each on the south roof and 28 modules on the north roof. For load optimization, the highest energy demand has a peak power of 12.8 kWp, which was between 07:00 and 13:00, was shifted by 3 hours, which seems feasible in terms of work organization. This can be seen from the red arrows in Figure 5.1 und 5.2.

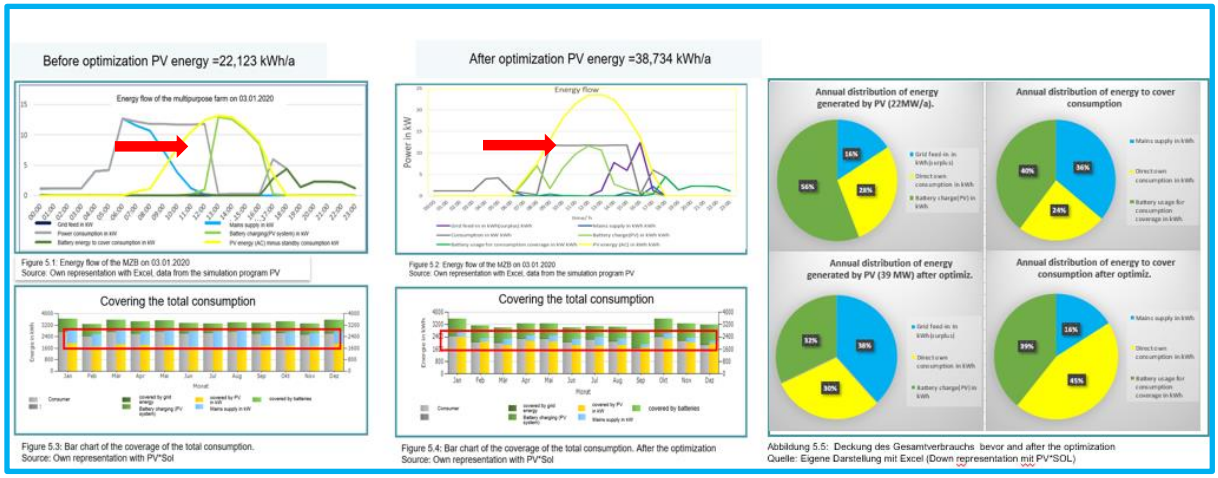

Figure 5. Compilation of results after the optimization

Simulation result after optimization

The simulation results show that the direct energy consumption of the technical equipment in multifunctional operation almost doubled. It increased from 6,246 kWh/a to 11,515 kWh/a. The system generates 38,734 kWh. 29.7% of this energy, i.e., 45% of the energy demand of the multifunctional operation, this energy is used directly to meet the demand. 32% of the generated energy is used to charge the batteries. The energy purchase from the grid decreased from 9,301.60 kWh to 4,131.90 kWh (from 36% to 16%). This leads to an increase in the degree of autonomy from 66.6% to 90%. This solar system costs about 16.000.000 FCFA (24.425 EUR) and will be paid back after about 11 years after its commissioning.

Conclusion

The solar planning approach optimized in this work would have positive impacts on the multipurpose farm. These impacts are as follows: annual savings of about 1,700,000 FCFA (2,594 EUR), increased productivity which will help in the fight against malnutrition in the region, in increased economic efficiency, in diversification of production units, in rapid growth of the business, in increasing the number of trainees and in improving competitiveness.

References

[1] D. M. I. Adolphe, „Problèmes d'électrification urbaine au Cameroun: diagnostic et proposition de solutions curatives,“ 02 03 2017. [Online]. Available: https://www.researchgate.net/publication/314154283_Problemes_d'electrification_urbaine_au_Cameroun_diagnostic_et_proposition_de_solutions_curatives. [Zugriff am 06 11 2020].
[2] H. Best , „Die Umstellung auf ökologische Landwirtschaft,“ Springerlink , Nr. 60, pp. 315-339, 20 08 2008.
[3] Deutsche Energie-Angentur GmbH (dena), „Länderprofil Kamerun,“ Bundesministerium für Wirtschaft und Energie, Berlin , 2014.
[4] B. N. Tansi, „MASTER THESIS: AN ASSESSMENT OF CAMEROON’S RENEWABLE ENERGY RESOURCE POTENTIAL AND PROSPECTS FOR A SUSTAINABLE ECONOMIC DEVELOPMENT,“ Cottbus, 2011.
[5] Eneo Cameroon S.A, „Rapport annuel 2018,“ Douala, 2018.
[6] F. Konrad, Planung von Photovoltaik-Anlagen, Wisbaaden: Vieweg+Teubner, 2008.
[7] European Communities, „EU SCIENCE HUB,“ PVGIS, 13 02 2020. [Online]. Available: https://re.jrc.ec.europa.eu/pvg_tools/en/tools.html#PVP. [Zugriff am 28 07 20].
[8] European Communities, „PVGIS users manual,“ PVGIS, 13 02 20. [Online]. Available: https://ec.europa.eu/jrc/en/PVGIS/docs/usermanual. [Zugriff am 13 07 20].
[9] ub.de Fachwissen GmbH, „Photovoltaik.org,“ [Online]. Available: https://www.photovoltaik.org/photovoltaikanlagen/solarmodule. [Zugriff am 31 07 2020].
[10] P. Guibert, „Master energétique et environement: TP Energie Solaire,“ Paris, 2012.